STRUCTURAL AND THERMAL EVOLUTION OF THE NORTHERN SELKIRK MOUNTAINS, SOUTHEASTERN CANADIAN CORDILLERA: TECTONIC DEVELOPMENT OF A REGIONAL-SCALE COMPOSITE STRUCTURAL FAN

by

H. Daniel Gibson, B.A., M.Sc.

A thesis submitted to the Faculty of Graduate Studies and Research

in partial fulfillment of the requirements for the degree of Doctor of Philosophy,

Department of Earth Sciences

Carleton University

Ottawa, Ontario

May, 2003

The undersigned hereby recommend to the Faculty of Graduate Studies and Research acceptance of the thesis,

STRUCTURAL AND THERMAL EVOLUTION OF THE NORTHERN SELKIRK MOUNTAINS, SOUTHEASTERN CANADIAN CORDILLERA: TECTONIC DEVELOPMENT OF A REGIONAL-SCALE COMPOSITE STRUCTURAL FAN

Submitted by H. Daniel Gibson, B.A, M.Sc., in partial fulfillment of the requirements for the degree of Doctor of Philosophy

____
Dr. Richard L. Brown
Thesis Co-Supervisor

____
Dr. Sharon D. Carr
Thesis Co-supervisor

____
Dr. Michael L. Williams
External Examiner

____
Dr. George Dix
Chair, Department of Earth Sciences

Carleton University
May, 2003

"Nature uses only the longest threads to weave her patterns, so that each small piece of her fabric reveals the organization of the entire tapestry".

Richard Feynman, Messenger Series Lectures, Cornell University (1964)

FRONTISPIECE

The impressive peaks of Argonaut Mountain as viewed looking toward the southeast from the Bigmouth pluton. This spectacular vista affords a profile view of the Selkirk fan axis, whose northwest trending surface trace passes through Argonaut Mountain. Structures within the highest peak to the left are orientated near vertical, whereas to the right (i.e., southwest), they dip moderately to the northeast.

ABSTRACT

In the southern Canadian Cordillera, the transition from the penetrative ductile deformation, medium- to high-grade metamorphism and plutonism of the hinterland, to the "thin-skinned" style of deformation in the foreland is marked by a zone of structural divergence. This northwest trending zone extends from northeastern Washington to east-central Alaska. In the northern Selkirk Mountains of southern British Columbia, within the southern Omineca belt, part of the zone coincides with a regional-scale structure termed the Selkirk fan. The fan is composed of low- to high-grade metamorphic rocks, and comprises at least three generations of superposed structures. Southwest verging, second generation folds (F_2) with shallow dipping axial surfaces (S_2) dominate the west flank of the fan, which become near vertical towards the fan axis. East of the fan axis, second (F_2) and third generation folds (F_3) are northeast verging with moderate dipping axial surfaces that become progressively overturned eastward near the Rocky Mountain Trench as they converge with structures in the Foreland belt.

The kinematic significance of the Selkirk fan is controversial, and its correct interpretation is essential for construction of tectonic models of the southern Cordillera. Thus, the tectonic development of the Selkirk fan has been the focus of considerable debate, but most researchers concluded that fan formation occurred primarily in the Middle Jurassic. However, U-Th-Pb geochronologic data obtained in this study by Isotope Dilution Thermal Ionization Mass Spectrometry (IDTIMS) and Sensitive High Resolution Ion Microprobe (SHRIMP) analyses indicate a more complex and protracted origin for the fan. The data demonstrate that the thermo-structural development and exhumation of the west flank of the fan occurred principally in the Middle Jurassic (ca. 172-167 Ma). In contrast, east of the fan axis significant Cretaceous deformation (104-84 Ma) and Cretaceous to Paleocene metamorphism (144-56 Ma) were superimposed on an early transposition fabric. This was followed by or partly concomitant with Late Cretaceous to Early Tertiary exhumation.

Refinement of the metamorphic age constraints was also facilitated by chemical mapping for Y, Th and U coupled with the *in situ* U-Th-Pb SHRIMP analyses. This revealed the link between age domains and zones of relative yttrium (Y) depletion or enrichment within monazite that were correlated with metamorphic reactions involving garnet. The Y maps generally provided the best indication of growth or recrystallization domains, and were critical for targeting SHRIMP analyses. Moreover, the Y domains consistently correlated with distinct age domains, with up to three or more in some crystals. These data clearly illustrate the cause of age dispersion within the analyzed monazites, and ubiquity of multiple age domains in metamorphic monazite. Furthermore, previous studies have demonstrated that the production and consumption of monazite is sensitive to the availability of Y, and that garnet exerts considerable control over the Y budget available during metamorphism in pelitic rocks. Thus, precise ages of Y domains within monazite provided by *in situ* SHRIMP analyses were correlated with metamorphic reactions involving garnet, and assigned to points along the P-T path.

Based on the data produced in this study a revised tectonic model is proposed in which the Selkirk fan developed within a critically tapered orogenic wedge that evolved diachronously in response to changing boundary conditions associated with periods of terrane accretion on the western margin of North America. During the Early to Middle

Jurassic accretion of the Intermontane Superterrane, a proto-F_{1-2} fan developed above a singularity where oceanic or marginal basin lithosphere was subducted eastward beneath continental lithosphere. Subsequently, the fan decoupled along a basal décollement system and was transferred northeastward, as rocks to the east were progressively incorporated into the orogenic wedge. The mid-Cretaceous accretion of the Insular Superterrane resulted in rejuvenation of compressional forces. This gave rise to out-of-sequence deformation that thickened the tectonic pile to reestablish critical taper and the continued eastward propagation of folding and faulting within the foreland to the east. Thus, the Selkirk fan may be thought of as a composite structure of juxtaposed Middle Jurassic and Cretaceous structures and metamorphism, rather than a singular fan that developed during one progressive event.

ACKNOWLEDGMENTS

Many people from close and afar supported me in countless ways throughout the course of my Ph.D. It is impossible to keep track of all the scientific input, acts of kindness, hospitality, generosity, and the little things that add up to big things through the years. For all of this I will always be indebted and grateful. It is equally impossible to thank every person who falls under this umbrella of support. Thus, special thanks are extended below to a limited number of exceptional people who were especially helpful during the course of my Ph.D.

Richard Brown is gratefully acknowledged for first proposing this project and fostering my love for the Selkirk Mountains. Fieldwork and laboratory procedures were supported by NSERC operating grants held by R.L. Brown and S.D Carr. Richard Brown and Sharon Carr are thanked for their patience and excellent co-supervision of the thesis. Both provided exceptional insight, guidance, input and critical reviewing of the thesis. The quality and clarity of this thesis are in large part a product of their unparalleled excellence in supervision. Their willingness to let me explore my curiosities and allowing me the liberty to carry out my research at my discretion is gratefully acknowledged. Special thanks are extended to Sharon Carr and "Father" John Blenkinsop who very patiently guided me through all the geochemical and mass spectrometry aspects of the study, and provided much insight that helped with the geochronologic interpretations made in this study. Chris Taylor is recognized for providing excellent assistance in the field and in the lab, and for his stimulating conversations. Paul Williams and Richard Brown are thanked for their sagacious and sometimes amusing outcrop discussions; I am most certainly a better person for it. The interpretations made in this thesis also benefited a great deal from discussions with Phil Simony, Ed Ghent, Jim Crowley, Paul Williams, Maurice Colpron and Ray Price.

I am grateful for the expert helicopter support provided by Matt Calligan and Stan Smith at Canadian Helicopters, Revelstoke, BC. I am thankful for the insightful discussions, tea, and storage of essential equipment provided by Bill and Ruby Cameron. Drs. Sid McKnight and Mary Johnston are also thanked for their kind hospitality during my time in Revelstoke. Special thanks are extended to Canadian Mountain Holidays and the staff at the Adamant Lodge for their logistical support and incredible generosity. Eric Unterberger is specifically thanked for his expert mountaineering advice and his steadfast friendship.

Many, many people at Carleton University deserve special acknowledgement for their friendship and support during the tenure of my Ph.D. Specifically, I would like to thank Mike Jackson and Peter Jones for their technical support and occasional comic relief. All faculty members and fellow graduate students whom I have relied upon intermittently for their intellectual input are acknowledged.

I am indebted to my friends, fellow students and colleagues who have provided excellent intellectual support, scientific discussions and critical social relief. In specific Maurice Colpron, Jim Crowley, Eric deKemp, Laurent Godin, Mike Hamilton, Brad Johnson, Dennis and Gretchen Johnston, Yvette Kuiper, Paul McNeil, Joe Pyle, Leslie Reid, Chris Taylor, and The Firebirds are gratefully recognized.

I especially thank George and Leita Gibson, my mom and dad, for their patience, understanding, kind words and learned advice. Peter and Corinne Cheney are also gratefully acknowledged for their support, generosity, hearty meals and insightful discussions at the dinner table through the years.

Last, I would like to extend very special thanks and gratitude to Yolande Gibson for her unwavering love and support, for her patience, for being my muse, and for providing me with the impetus to finish this endeavor.

ORIGINAL CONTRIBUTIONS

During six months of fieldwork in the summers of 1998, 1999 and 2000 I mapped lithostratigraphy, structures and metamorphic assemblages within the northern Selkirk Mountains of southern British Columbia. Mapping was done at a 1:20 000 scale in parts of the following 1:20 000 BC TRIM sheets (North American Datum 1983, UTM zone 11): 82M.068, 82M.069, 82M.070, 82M.078, 82M.079, 82M.080, 82M.088, 82M.089, 82M.090, 82M.098, 82M.099, 82M.100, 83D.008 and 83D.009. These data were compiled with previous results in the region to produce a composite geologic map and a number of cross sections for the northern Selkirk Mountains. Samples were also collected for U-Th-Pb geochronology, as well as structural analysis and metamorphic petrography back at Carleton University.

For the geochronologic component of this study, I carried out U-Pb Isotope Dilution Thermal Ionization Mass Spectrometry (IDTIMS) analyses on 22 samples that included variably deformed leucocratic dykes, monzonitic plutons, and pelitic schists from which a total of 111 fractions of monazite and zircon were analyzed. All stages of sample preparation, which included crushing, grinding, and mineral separation, were done at Carleton University. The picking of fractions, U-Pb chemistry, and mass spectrometry were completed by myself at Carleton University under the guidance of Drs. Sharon Carr and John Blenkinsop. Additional U-Th-Pb *in situ* Sensitive High mass Resolution Ion Microprobe (SHRIMP) analyses were carried out at the Geological Survey of Canada (GSC) in Ottawa. The U-Th-Pb data produced by the IDTIMS and SHRIMP analyses in this study greatly refined the age constraints for deformation and metamorphism within the northern Selkirk Mountains (Chapters 2 and 3).

In addition, prior to the SHRIMP analyses, the internal chemical morphology of the monazite and zircon were imaged by backscattered electron (BSE) and cathodoluminescence (CL) at the GSC. The monazite crystals were also imaged by Dr. Mike Jercinovic at the University of Massachusetts using X-ray elemental mapping for yttrium (Y), thorium (Th) and uranium (U). This revealed complex zoning in many of the monazites. In specific, the Y maps generally provided the best indication of growth or recrystallization domains, and were critical for targeting SHRIMP analyses. This relatively novel approach allowed me to make the link between age domains and zones of relative Y depletion or enrichment within monazite with metamorphic reactions involving major pelitic minerals like garnet and kyanite (Chapter 4). This is considered a significant contribution because prior to this study ambiguities persisted with regard to the assignment of monazite ages to specific metamorphic reactions that could be used as absolute timing constraints in P-T-t space.

The data produced in this study require significant revision of previous models proposed for the tectonic evolution of this region, most specifically the Selkirk fan. As a result, I formulated a conceptual tectonic model for the development of the Selkirk fan. The fan is modeled within a critically tapered orogenic wedge that evolved diachronously in response to changing boundary conditions associated with periods of terrane accretion on the western margin of North America.

TABLE OF CONTENTS

LIST OF FIGURES AND MAPS

LIST OF TABLES

LIST OF APPENDICIES

CHAPTER 1

GENERAL INTRODUCTION

The mountainous topography of the Canadian Cordillera marks the westward transition from the peneplained Canadian prairies that sit on the Canadian shield to the exotic terranes that were accreted to the western margin of North America. Understanding the orogenic processes that were responsible for creating the dramatic landscape we see today is the focus of intense investigation that is ever evolving, and was the major impetus for my Ph.D. research.

The Canadian Cordillera has been divided into five morphogeologic belts based on their distinct physiographic and geologic characteristics (Fig. 1.1a) (see Monger and Price, 1979; Monger et al., 1982; Gabrielse and Yorath, 1991 and references therein). From east to west, the Foreland, Intermontane and Insular belts represent the suprastructure of the Cordillera in which low-grade and unmetamorphosed rocks are situated. Separating these three belts are the high-standing metamorphic and plutonic welts that characterize the Omineca and Coast belts. Monger et al. (1982) concluded that they were formed during the compression and tectonic overlap that accompanied the Mesozoic accretion and obduction of two large composite, allochthonous terranes termed the Intermontane and Insular Superterranes (Gabrielse and Yorath, 1991) that were amalgamated outboard of the western margin North American.

In general, the boundary between the accreted terranes and the rocks of known North American cratonic affinity is marked by a regional zone of structural divergence that extends from northeastern Washington to east-central Alaska (Fig. 1.1a; Eisbacher et al., 1974; Price, 1986). Within the southern Omineca belt this zone coincides with the transition from rocks that were affected by deep-seated ductile and metamorphic processes to the "thin-skinned" deformation characteristic of the Foreland belt. As such, understanding the development of this orogen-scale feature is fundamental to elucidating the transition from hinterland to foreland tectonics in the Cordillera.

Research for this thesis focussed on part of the zone that trends through the northern Selkirk Mountains within the southern Omineca belt, where there is excellent exposure of a regional-scale structure termed the Selkirk fan (Wheeler, 1963, 1965; Price and Mountjoy, 1970; Brown and Tippett, 1978; Fig. 1.1b). Trending northwest for more than 120 km, the fan is composed of low- to high-grade metamorphic rocks, and comprises at least three generations of superposed structures. The west flank of the fan is dominated by southwest verging, second generation folds (F_2) with shallow dipping axial surfaces (S_2) that become near vertical towards the fan axis. Structures east of the fan axis comprise northeast verging second (F_2) and third generation folds (F_3) with moderate to shallow dipping axial surfaces, concordant with structures in the Foreland belt to the east.

The kinematic development of the Selkirk fan has been the focus of considerable debate from which two principal tectonic models have emerged. Brown et al. (1993) presented a finite-element model, where the fan developed in the Middle Jurassic above a singularity marking the transition between eastward subducting oceanic or marginal basin lithosphere beneath continental lithosphere. This is analogous to the doubly vergent structures produced in mechanical models of Malavieille (1984) and Willet et al. (1993). Alternatively, Price (1986) ascribed the development of fan to be the result of tectonic wedging of an allochthonous terrane between the cratonic basement and the overlying miogeoclinal cover. Colpron et al. (1998) expanded on this model by including an inherited basement ramp that impeded the eastward propagation of southwest verging structures that were developing above the wedge in the Middle Jurassic. In the Late Jurassic the wedge overrode and cannibalized the ramp after it had attained sufficient gravitational potential, resulting in the eastward propagation of northeast verging deformation into the Foreland belt.

In both models the fan developed primarily in the Middle to Late Jurassic as constrained by a limited number of meaningful U-Pb and $^{40}Ar/^{39}Ar$ ages for plutons sampled exclusively within the west side of the fan (e.g., Shaw, 1980a, 1980b; Brown et al., 1992; Colpron et al., 1996). However, to the northwest in the northern Monashee Mountains U-Pb and $^{40}Ar/^{39}Ar$ data strongly suggest that a significant episode of deformation and metamorphism occurred in the Early to Late Cretaceous (e.g., Sevigny et al., 1989, 1990; Scammell, 1993; Digel et al., 1998; Crowley et al. 2000). This presents a contradiction because stratigraphy, and the Cretaceous metamorphic and structural elements of the northern Monashee Mountains were mapped uninterrupted across the Columbia River into the northernmost Selkirk Mountains (e.g., Simony et al., 1980) where deformation and metamorphism have been interpreted to be Middle Jurassic (e.g., Brown et al., 1992; Parrish, 1995). Furthermore, geochronology by Crowley et al. (2000), which included the northernmost Selkirk Mountains near Mica Creek Village, strongly suggest a significant component of Cretaceous strain and metamorphism.

Research presented in this thesis reconciles this apparent contradiction by providing significantly refined timing constraints for deformation (Chapter 2) and metamorphism (Chapters 3 and 4) associated with the development of the Selkirk fan. Furthermore, the U-Th-Pb geochronologic data obtained by Isotope Dilution Thermal Ionization Mass

Spectrometry (IDTIMS) and Sensitive High Resolution Ion Microprobe (SHRIMP) analyses indicate a complex and protracted origin for the fan. As such, the Selkirk fan cannot be thought of as developing during one progressive event in the Jurassic, but is the result of the juxtaposition of at least two temporally and tectonically distinct domains. Thus, the Selkirk fan is a composite structure rather than a singular fan that developed during one progressive event. Based on the data presented in this thesis, a revised tectonic model is proposed (Chapter 5) in which the Selkirk fan developed within a critically tapered orogenic wedge that evolved diachronously in response to changing boundary conditions associated with periods of terrane accretion on the western margin of North America.

It should be noted that the next four chapters presented herein were written as separate papers to expedite submission to scientific journals, and therefore contain sections that are somewhat repetitious.

Figure 1.1. (a) Morphogeologic belts of the Canadian Cordillera. (b) Tectonic assemblage map of southeastern Omineca belt (modified after Wheeler and McFeely, 1991) showing lithologic map units of autochthonous Monashee complex (North American basement) and overlying Selkirk allochthon. ADP = Adamant pluton; AS = Albert stock; BMP = Bigmouth pluton; BR = Battle Range batholith; CS = Clachnacudainn Slice; FP = Fang pluton; GP = Goldstream pluton; GS = Goldstream Slice; IS = Illecillewaet Slice; KB = Kuskanax batholith; PC = Pass Creek pluton

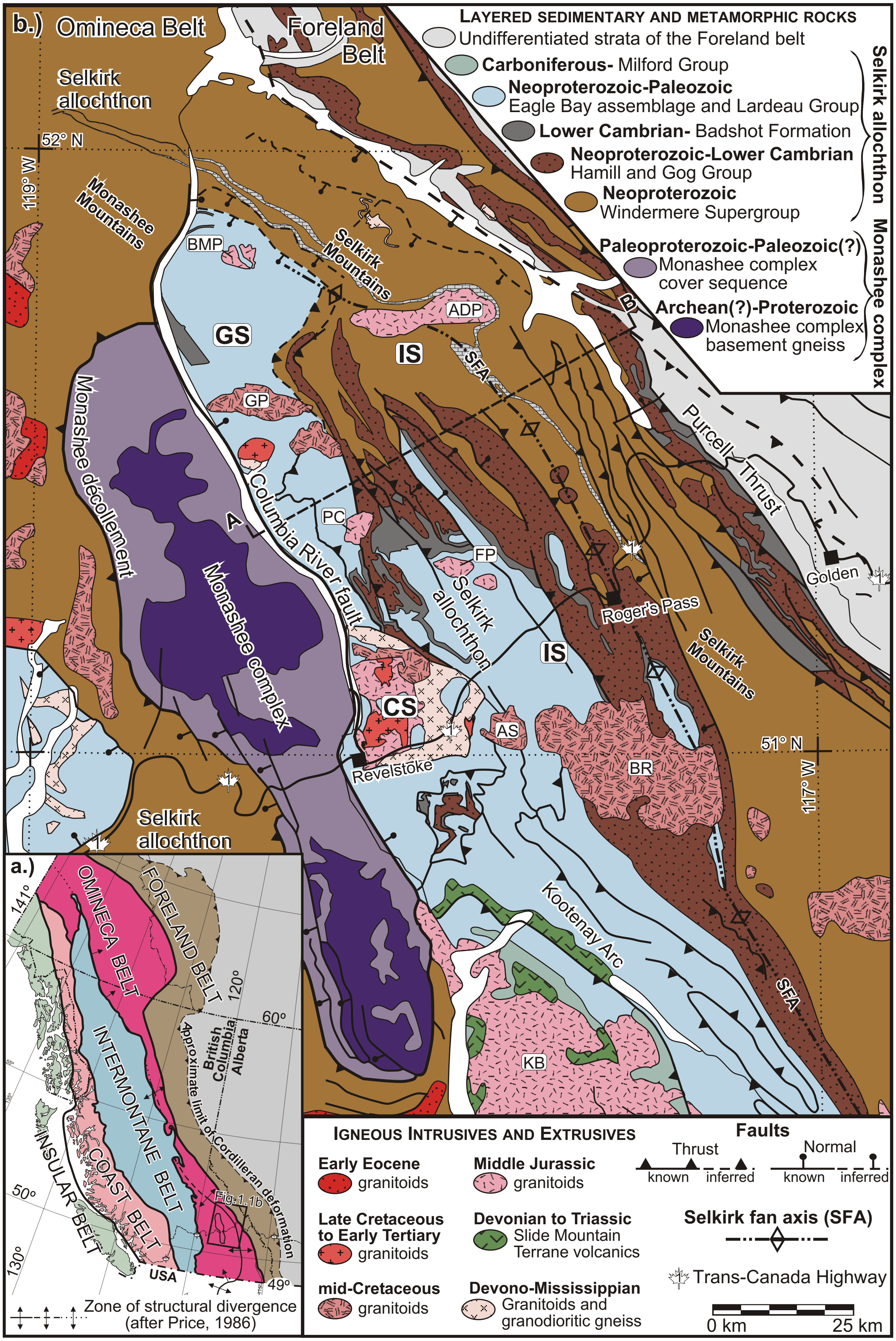

b.) Omineca Belt
Foreland Belt
Selkirk allochthon
52° N
119° W
Monashee Mountains
Selkirk Mountains
BMP
GS
ADP
IS
SFA
B
GP
Purcell Thrust
Monashee décollement
Columbia River fault
A
PC
FP
Monashee complex
Selkirk allochthon
Golden
Roger's Pass
IS
Selkirk Mountains
CS
AS
51° N
BR
117° W
Revelstoke
Selkirk allochthon
Kootenay Arc
SFA
KB
LAYERED SEDIMENTARY AND METAMORPHIC ROCKS
Undifferentiated strata of the Foreland belt
Carboniferous- Milford Group
Neoproterozoic-Paleozoic Eagle Bay assemblage and Lardeau Group
Lower Cambrian- Badshot Formation
Neoproterozoic-Lower Cambrian Hamill and Gog Group
Neoproterozoic Windermere Supergroup
Selkirk allochthon
Paleoproterozoic-Paleozoic(?) Monashee complex cover sequence
Archean(?)-Proterozoic Monashee complex basement gneiss
Monashee complex
a.)
141°
OMINECA BELT
FORELAND BELT
120°
60°
INTERMONTANE BELT
Approximate limit of Cordilleran deformation
British Columbia
Alberta
INSULAR BELT
COAST BELT
50°
Fig.1.1b
130°
USA
49°
Zone of structural divergence (after Price, 1986)
IGNEOUS INTRUSIVES AND EXTRUSIVES
Early Eocene granitoids
Late Cretaceous to Early Tertiary granitoids
mid-Cretaceous granitoids
Middle Jurassic granitoids
Devonian to Triassic Slide Mountain Terrane volcanics
Devono-Mississippian Granitoids and granodioritic gneiss
Faults
Thrust
known
inferred
Normal
known
inferred
Selkirk fan axis (SFA)
Trans-Canada Highway
0 km
25 km

Figure 1.1.

CHAPTER 2

STRUCTURAL EVOLUTION AND U-TH-PB GEOCHRONOLOGIC CONSTRAINTS OF THE SELKIRK FAN, NORTHERN SELKIRK MOUNTAINS, SOUTHEASTERN BRITISH COLUMBIA

Abstract

In the southern Canadian Cordillera, the transition from the penetrative ductile deformation, medium- to high-grade metamorphism and plutonism of the hinterland, to the "thin-skinned" style of deformation in the foreland is marked by a zone of structural divergence. This northwest trending zone extends from northeastern Washington to east-central Alaska. In the northern Selkirk Mountains of southern British Columbia, within the southern Omineca belt, part of the zone coincides with a regional-scale structure termed the Selkirk fan. The fan is composed of low- to high-grade metamorphic rocks, and comprises at least three generations of superposed structures. Southwest verging, second generation folds (F_2) with shallow dipping axial surfaces (S_2) dominate the west flank of the fan, and become progressively steeper towards its axis. To the east of the fan axis, second (F_2) and third generation folds (F_3) are northeast verging with axial surfaces that become increasingly overturned eastward toward the Rocky Mountain Trench as they converge with structures in the Foreland belt. The kinematic significance of the Selkirk fan is controversial, and its correct interpretation is essential for construction of tectonic models of the Cordillera.

New data provide U-Th-Pb geochronologic constraints on timing of deformation associated with the development of the Selkirk fan via small-fraction Isotope Dilution Thermal Ionization Mass Spectrometry (IDTIMS) and Sensitive High Resolution Ion Microprobe (SHRIMP) analyses. The data suggest that there has been juxtaposition of higher structural levels with an older deformation history in the west flank relative to lower levels with a younger deformation history in the east. Dated monazite and zircon from variably deformed leucocratic dykes and granodioritic- monzonitic plutons indicate that the thermo-structural development of the west flank of the fan occurred principally in the Middle Jurassic (ca. 172-167 Ma). In contrast, data from east of the fan axis demonstrate that there has been significant mid- to Late Cretaceous (ca. 104-84 Ma) deformation superimposed on an early transposition fabric. Thus, the Selkirk fan may be thought of as a composite structure of juxtaposed Middle Jurassic and Cretaceous structures, rather than a singular fan that developed during one progressive event. As such, these data indicate a complex and protracted origin for the Selkirk fan, requiring significant revision of previous models.

2. 1. Introduction

The Omineca belt of the Canadian Cordillera (Fig. 2.1a) was the locus of penetrative ductile deformation, metamorphism, plutonism, and significant uplift during the Mesozoic accretion of the Intermontane and Insular superterranes to the western margin of the North American craton (Monger et al., 1982; Murphy et al., 1995; Colpron et al. 1996). In general, the boundary between the accreted terranes and the rocks of known North American cratonic affinity is marked by a regional zone of structural divergence that extends from northeastern Washington to east-central Alaska (Eisbacher et al., 1974; Price, 1986; Fig. 2.1a). From west to east, this zone represents the change in orientation of structures that are southwest vergent to northeast vergent, respectively. Within the southern Omineca belt this zone also coincides with the eastward transition from rocks that were affected by deep-seated ductile and metamorphic processes to the “thin-skinned” deformation characteristic of the Foreland belt (Fig. 2.1a). As such, understanding the development of this orogen-scale feature is fundamental to elucidating the transition from hinterland to foreland tectonics in the Cordillera.

In the Selkirk Mountains of southern British Columbia, within the southern Omineca belt, part of the zone of structural divergence coincides with a regional-scale structure termed the Selkirk fan (Wheeler, 1963, 1965; Price and Mountjoy, 1970; Brown and Tippett, 1978; Fig. 2.1b). The fan trends northwest-southeast for more than 120 km, is composed of low to high-grade metamorphic rocks, and comprises at least three generations of superposed structures. The kinematic development of the Selkirk fan has been the focus of considerable debate from which two principle tectonic models have emerged. Brown et al. (1993) presented a finite-element model, where the fan developed in the Middle Jurassic above a singularity that marks the eastward subduction of oceanic or marginal basin lithosphere beneath continental lithosphere (Fig. 2.2a). This is analogous to the doubly vergent structures produced in mechanical models of Malavieille (1984) and Willet et al. (1993). Alternatively, Price (1986) ascribed the development of the fan to be the result of tectonic wedging of an allochthonous terrane between the cratonic basement and the overlying miogeoclinal cover. Colpron et al. (1998) expanded on this model by including an inherited basement ramp that impeded the eastward propagation of southwest verging structures that were developing above the wedge in the Middle Jurassic. In the Late Jurassic the wedge overrode and cannibalized the ramp after it had attained sufficient gravitational potential, resulting in the eastward propagation of northeastward verging deformation into the Foreland belt (Fig. 2.2b).

In both models the fan developed primarily in the Middle to Late Jurassic as constrained by a limited number of meaningful U-Pb and $^{40}Ar/^{39}Ar$ ages for plutons sampled exclusively within the west side of the fan (e.g., Shaw, 1980a, 1980b; Brown et al., 1992; Colpron et al., 1996; a summary is provided in Table 2.1). However, to the northwest in the northern Monashee Mountains (Fig. 2.1b) U-Pb and $^{40}Ar/^{39}Ar$ data strongly suggest that a significant episode of deformation and metamorphism occurred in the Early to Late Cretaceous (e.g., Sevigny et al., 1989, 1990; Scammell, 1993; Digel et al., 1998; Crowley et al. 2000). This presents a contradiction because Cretaceous metamorphic and structural elements, and the stratigraphy of the northern Monashee Mountains were mapped uninterrupted across the Columbia River into the northernmost Selkirk Mountains (e.g., Simony et al., 1980; Fig. 2.4), where deformation and metamorphism have been interpreted to be Middle Jurassic (e.g., Brown et al., 1992;

Parrish, 1995). Furthermore, recent geochronology by Crowley et al. (2000), which included the northernmost Selkirk Mountains near Mica Creek Village (Fig. 2.3, Table 2.1), strongly suggest a significant component of Cretaceous strain and metamorphism. This study provides additional geochronologic data from samples collected across the entire width of the northern Selkirk Mountains that are used to reconcile this apparent geochronologic contradiction.

In this communication, new U-Th-Pb isotopic data provide timing constraints for deformation associated with the development of the Selkirk fan via small-fraction isotope dilution thermal ionization mass spectrometry (IDTIMS) and Sensitive High Resolution Ion Microprobe (SHRIMP) analyses. Dated monazite and zircon from variably deformed leucocratic dykes and monzonitic-granodioritic plutons indicate that the Selkirk fan is a composite of Middle to Late Jurassic (ca. 172-156 Ma) and Early to Late Cretaceous (ca. 104-81 Ma) structures. As such, the Selkirk fan cannot be thought of as developing during one progressive event in the Jurassic, but is the result of the juxtaposition of at least two temporally and tectonically distinct domains.

2. 2. Geologic Setting

The Late Proterozoic to Paleozoic metasedimentary and metavolcanic rocks of northern Selkirk Mountains were originally deposited along the rifted western paleo-margin of the North American craton (see Gabrielse and Campbell, 1991 and references therein). During the Middle Jurassic to Paleocene these rocks were displaced northeastward along a basal shear zone ~250-300 km (Price and Mountjoy, 1970; Brown et al. 1993; Parrish, 1995) as part of the Selkirk allochthon (Read and Brown, 1981). During this time (ca. 100 My), the allochthon is interpreted to have experienced protracted and diachronous internal deformation and metamorphism (Parrish, 1995). Subsequent Early Tertiary normal faulting along the Columbia River and Okanagan Valley fault systems has served to dissect and expose all levels of the allochthon, as well as exposing the Precambrian cratonic basement of the Monashee complex through a tectonic window (Fig. 2.1b).

The complexly deformed rocks within the northern Selkirk Mountains were subjected to at least three generations of superposed folding (Fig. 2.5), and have been metamorphosed at low to high grade. Bounding the eastern flank of this region is the southern Rocky Mountain trench, which is part of a >2300 km long lineament. The trench also represents the boundary between the southern Omineca and Foreland belts. The trace of a major out-of-sequence, northeast verging Cretaceous contractional fault, the Purcell thrust, is mapped within the trench, but is transected and obscured at the latitude of this study by an *en echelon* series of down-to-the-west Tertiary normal faults (Simony et al., 1980). The western flank of the area is situated within the immediate hanging wall of the Columbia River fault, a crustal-scale, Eocene normal-sense shear zone. This NNW-striking fault separates upper amphibolite-facies footwall rocks of the Monashee complex interpreted to be autochthonous North American basement (Armstrong et al., 1991; Parkinson, 1991; Crowley, 1999) from greenschist-facies rocks within the Selkirk Mountains that are part of the Selkirk allochthon. The surface trace and magnitude of displacement of this fault disappear just south of 52ºN latitude at the confluence of Birch Creek and the Columbia River (Figs. 2.1, 2.3 and 2.4; Map 2). North of this point, the regional northwest trending stratigraphy, structures, and isograds are mapped uninterrupted across the Columbia River into the northern Monashee Mountains (e.g., Simony et al., 1980; Raeside and Simony, 1983; Scammell, 1993; Crowley et al., 2000; Figs. 2.3 and 2.4, Map 2).

2.2.1. Stratigraphy

Unraveling the complex lithostratigraphic elements has been an important contribution to understanding the tectonic development of the region; a summary is provided below. A more thorough treatment of the stratigraphy can be found in Brown et al. (1977, 1978), Poulton and Simony (1980), Perkins (1983), Pell and Simony (1987), and Logan and Colpron (1995).

The most widespread unit in the area is a clastic turbidite sequence of the Late Proterozoic Windermere Supergroup (Wheeler 1965; Brown et al., 1977, 1978; Perkins, 1983). It is overlain by the Eocambrian Hamill Group quartzites, the Lower Cambrian archaeocyathid-bearing marbles of the Badshot Formation, and the basinal deep-water facies carbonates, calc-silicates, metavolcanics, and schists of the Lower Paleozoic Lardeau Group. Establishing stratigraphic control in the area is difficult due to the lithologic similarity, lack of exposure in valley bottoms, and the complexity imposed by penetrative deformation and metamorphism. This has resulted in discrepancies in terminology and assignment of lithologic units amongst previous workers. Initially, regional correlations were made with the Horsethief Creek Group of the Windermere Supergroup within in the Monashee and Purcell Mountains, and Kootenay Arc to the south (e.g., Evans, 1933; Fyles and Eastwood, 1962; Wheeler, 1963, 1965; Simony and Wind, 1970; Brown et al., 1977, 1978; Poulton and Simony, 1980; Simony et al. 1980; Perkins, 1983; Brown and Lane, 1988). However, mapping in the northern Monashee and Cariboo Mountains by Pell and Simony (1987), and compilations by McDonough et al.

(1992) have demonstrated that most of the lithostratigraphy of the northern Selkirk and Monashee Mountains actually underlies the type- Horsethief Creek Group section located within the Windermere map area of southern British Columbia (Walker, 1926). As such, it is considered to be the lowest exposed subdivision of the Late Proterozoic Windermere Supergroup in the region (McDonough et al., 1992). Brown et al. (1978) subdivided the lithostratigraphy of the northern Selkirk Mountains into three members, the Lower Pelite, Middle Marble, and Upper Pelite. Here the same subdivisions are used, except that the distinctive Semipelite–Amphibolite (SPA) unit is considered separately, rather than as a part of the Lower Pelite member. This is consistent with subdivisions proposed by Poulton and Simony (1980) and Perkins (1983), and by other workers in the northern Monashee Mountains (e.g., Simony et al., 1980; Raeside and Simony, 1983; Scammell, 1993). It should be noted that the Lower Pelite, Middle Marble, and SPA units are now referred to as the Mica Creek Succession (McDonough et al., 1992), and that the Upper Pelite has been correlated with the Lower Grit unit of the Kaza Group in the southern Cariboo Mountains (Pell and Simony, 1987).

2.2.2. Structural Setting

The structural style in the northern Selkirk Mountains is dominated by northwest-southeast trending folds and faults (Figs. 2.3 and 2.4, Map 2). The change in vergence of these structures from southwestward to northeastward defines the geometry of the Selkirk fan (Fig. 2.6). Four generations of structures have been recognized based on overprinting and geometric observations (e.g., Brown and Tippett, 1978; Simony et al., 1980; Perkins, 1983), and are summarized below. It is important to note that in this study reference to fold and fabric generations does not necessarily imply regional timing correlations, especially across the fan axis.

2.2.2.1. First Generation: F_1 Carnes nappes

The earliest folds, F_1, and associated axial planar foliation, S_1, are found primarily in the west flank of the fan. Here there is a km-scale, southwest vergent, isoclinal recumbent fold termed the Carnes nappe (Brown and Lane, 1988; see also Fig. 3 of Brown and Lane for cross section of Carnes nappe). Identification of this and smaller parasitic F_1 folds, with shallow to horizontal hinge lines and gently dipping axial planar S_1 foliation defined by the alignment of muscovite and biotite (mineral abbreviation after Kretz, 1983), is complicated due to the pervasive and intense coaxial overprint of F_2 folds. However, recognition of regionally overturned stratigraphy (Read and Brown, 1979; Brown et al., 1983) interpreted as the inverted limb of the Carnes nappe (Brown and Lane, 1988; Brown, 1991), and the rare preservation of rootless isoclines and refolded S_1 foliation by F_2 folds (Brown and Tippett, 1978; Colpron et al., 1998) provide evidence for D_1 in the field. The Carnes nappe is correlated with the anticlinal Scrip nappe documented in the northern Monashee Mountains (Raeside and Simony, 1983) that has an overturned limb length of approximately 50 km. These macroscopic F_1 folds are interpreted to be correlative with similar nappes mapped to the south in the Kootenay arc (Fyles, 1964; Read and Wheeler, 1976; Höy, 1977), and to the north in the Cariboo Mountains (Murphy, 1986, 1987). Both the Carnes and Scrip nappe are thought to have originated at shallow crustal levels, and were progressively tightened and overturned as the result of subsequent deformation and burial (e.g., Raeside and Simony, 1983; Brown et al., 1986; Brown and Lane, 1988). These folds must have developed prior to the onset of peak metamorphism because metamorphic isograds are not folded by F_1, but are found to cut across axial surfaces at high angles (Wheeler, 1965; Brown and Tippett, 1978; Simony et al., 1980; Brown and Lane, 1988).

2.2.2.2. Second Generation: F_2 Folds and S_2 Transposition Foliation

Kilometer-scale to outcrop-scale, tight to isoclinal folds that are axial planar to the regional transposition fabric constitute the second generation of structures observed throughout the region (see Figs. 2.5 and 2.8). These folds (F_2) and the associated transposition foliation (S_2) are pervasive and dominate the structures observed at outcrop-scale. On both sides of the fan axis, F_2 can be characterized as Class 2 similar folds or Class 3 folds according to the scheme of Ramsay (1967). These folds typically have thickened hinge zones with highly attenuated to dismembered limbs, characteristic of folds in transposed terrane (e.g., Hobbs et al., 1976). In the vicinity of the fan axis of this study, which includes French Glacier and Argonaut Mountain (Fig. 2.3, Map 2), S_2 axial planes and the associated S_2 schistosity have a near-vertical dip toward either the southwest or northeast. In the French Glacier area, S_2 also dips steeply toward the southeast or northwest; the change in orientation is interpreted to be a result of the deflection of D_2 structures around the western margin of the Adamant pluton (Brown and Tippett, 1978; Shaw, 1980b). West of the fan axis, F_2 folds become increasingly overturned toward the southwest with axial planes that dip 10-20°. F_2 hinge lines generally have a shallow plunge of ~5-25° toward the northwest or southeast. Conversely, to the east of the fan axis near Mud Glacier, S_2 has a moderate to steep dip of ~50-80° toward the southwest. Further east toward Warsaw Mountain and the Rocky Mountain Trench, F_2 folds have moderate southwest-dipping (~25-50°) axial planes and associated transposition foliation, S_2, that bisect fold hinges. Throughout the region, F_2 is interpreted to be synchronous with regional metamorphism (e.g., Brown and Tippett, 1978; Perkins, 1983 and references therein). This is based on the observed alignment of kyanite, sillimanite, biotite and muscovite within S_2, and the preferred orientation of their long axes of within the L_2 lineation. However, metamorphism outlasted or subsequently overprinted D_2 at a later time because porphyroblasts such as garnet, kyanite and staurolite are also found to have overgrown F_2 and S_2 (Fig. 2.7). In addition, the map trace of regional isograds cut obliquely across the trend of F_2 structures south of the Bigmouth pluton where the structures have been deflected around the western margin of the Adamant pluton (cf. Leatherbarrow, 1981; Simony et al. 1980; Figs. 2.3 and 2.4, Map 2).

2.2.2.3.Third Generation: F_3 folds, L_3 crenulations, and S_3 crenulation cleavage

Outcrop- to km-scale third generation folds (F_3) are found primarily east of the fan axis where they refold earlier F_2 and S_2 structures. Northeast verging F_3 folds are generally more upright than F_2, and have moderate dipping axial planes (~40-80°) that tend to be less inclined (~15-40°) adjacent to the Rocky Mountain Trench. The F_3 fold style is typically Class 1B or Class 1C, with a close to tight geometry. Development of F_3 is interpreted to be the result of compressive buckling orthogonal to layering (Simony et al., 1980) during the late stages of, and/or following, regional metamorphism (e.g., Brown and Tippett, 1978; Simony et al., 1980; Perkins, 1983). These folds are generally coaxial with F_2, which resulted in Type-3 interference patterns (Ramsay, 1967). West of the fan axis, D_3 is less well developed; it is interpreted to be present mainly as near upright, shallow plunging L_3 crenulations and S_3 crenulation cleavage that transect the S_2 transposition foliation at a high angle (Brown and Tippett, 1978).

2.2.2.4. Fourth Generation of Structures (D_4): Southwest Dipping Normal Faults

Three southwest dipping normal faults have been mapped within the northeastern flank of the fan (e.g., Leatherbarrow, 1981; Perkins, 1983; Figs. 2.3, 2.4, and 2.8), and are interpreted to post-date the development of F_2 and F_3 structures as well as most of the metamorphism. These faults, which include the Bigmouth, Birch Creek, and Northeast faults (Figs. 2.3, 2.4, and 2.8), were interpreted on the basis of stratigraphic omission, and/or zones of localized strain (cf. Perkins, 1983; this study). The magnitude of displacement is uncertain due to a lack of piercing points. Estimates of 3-7 km of throw have been made for the Birch Creek fault based on arguments of stratigraphic omission (Perkins, 1983) and geobarometric data (Leatherbarrow, 1981; see Metamorphism section below). A similar amount of displacement may be interpreted for the Bigmouth fault, where the Lardeau Group has been dropped down in contact with the Upper Pelite of the Windermere Supergroup (Figs. 2.3 and 2.4). The stratigraphic omission of the Hamill Group, which is ~2.5 km thick in northern Selkirk Mountains (Wheeler, 1963), and the Badshot Formation (~300 m; Logan et al., 1996) suggests ~3 km of throw, and possibly more if there has been some omission of the Upper Pelite unit. Throw associated with the Northeast fault is difficult to assess, but a similar magnitude of displacement of ~3-7 km seems likely based on structural sections of Perkins (1983) and this study (Fig. 2.8).

2.2.3. Metamorphism

In the study area, sillimanite and Sil-Kfs grade rocks core the fan structure, and are flanked on either side by progressively lower grade assemblages (Fig. 2.3). A set of northwest trending regional isograds have been established based on the appearance or disappearance of the pelitic index minerals biotite, garnet, staurolite, kyanite, and sillimanite (Wheeler, 1965; Campbell, 1968; Ghent et al., 1977; Leatherbarrow and Brown, 1978; Simony et al., 1980; Leatherbarrow, 1981). In general, the isograds trend northwest-southeast parallel to the structural grain of the region, except where they crosscut the trace of F_2 structures south of the Bigmouth pluton (Fig. 2.3, Map 2). The lowest grade assemblages in the Chl-zone are located on the west flank of the fan in the immediate hanging wall of the Columbia River fault (Fig. 2.3). The metamorphic grade progressively increases eastward until the Sil-Kfs-melt zone is encountered near the fan axis, and then decreases to the northeast where Ky-St assemblages occur adjacent to the Rocky Mountain Trench (Fig. 2.3).

The peak metamorphic pressures and temperatures estimated for the region vary across the fan. Specifically, Leatherbarrow (1981) estimated that to the southwest of the fan axis in the vicinity of French Glacier, peak pressures and temperatures were 5 kbar and 500-550 °C (St-Ky-zone). To the northeast within the Sil-Kfs-zone, pressures were estimated to have reached 7 kbar and temperatures as high as 650 °C. The apparent 2 kbar difference was interpreted to be the result of normal faulting along the Birch Creek fault, with a vertical component of displacement of ~7 km down to the southwest. Geothermobarometric studies to the north in the Mica Creek area, within the northeast flank of the fan, agree well with those of Leatherbarrow. Ghent et al. (1979, 1982, and 1983) estimated peak conditions of 540 to 700 °C and 5.6 to 7.2 kbar (lower P-T estimates for Ky-zone, higher for Sil-Kfs-zone). Readers are referred to Chapter 3 for a detailed description of the geochronologic timing constraints for metamorphism in the region.

2.2.4. Plutonic Rocks

A suite of Middle Jurassic, km-scale monzonitic to granodioritic plutons and subordinate stocks is found within the northern Selkirk Mountains (Figs. 2.1 and 2.3). The SW-verging folds and faults of the region are truncated by most of the plutons, such as the Pass Creek and Fang plutons (Brown and Tippett, 1978; Brown et al., 1992; Colpron et al. 1996). However, SW-verging structures also appear to be deflected around the Adamant pluton (e.g., Brown and Tippett, 1978; Shaw, 1980b; Logan and Colpron, 1995; Logan et al., 1996; Colpron et al. 1996; this study; Figs. 2.1, 2.3 and 2.4; Map 2). Thus, the Middle Jurassic plutons were interpreted to be either: 1) Late syn- to post tectonic with respect to the development of SW-verging structures and the growth of peak metamorphic minerals that are aligned within their axial planes (Brown and Tippett, 1978; Brown et al. 1992), or 2) emplaced late in the development of SW-verging structures, where the SW-verging structures continued to form for a short period following pluton emplacement (Colpron et al., 1996 and references therein). U-Pb crystallization ages and $^{40}Ar/^{39}Ar$ cooling ages from the plutons and their aureoles were used to provide the Middle Jurassic age constraints for deformation, metamorphism, and exhumation throughout the northern Selkirk Mountains (e.g., Shaw, 1980a; Brown et al., 1992; Colpron et al., 1996, and references therein; see Table 2.1). However, all plutonic samples dated were situated within the southwest flank of the fan, and extrapolation of these ages was used to constrain the timing of structures northeast of the fan axis.

2. 3. Previous Timing Constraints for Deformation

2.3.1. Southwest-verging Structures: D_1 and D_2

In regions adjacent to the northern Selkirk Mountains, Murphy et al. (1995) constrained the timing for the development of SW-verging F_1 and F_2 folds to be ca. 185-174 Ma. The lower age limit is based partly on the age of the ca. 187-185 Ma Hall Formation in the Kootenay Arc (Tipper, 1984 based on the time scale of Harland et al., 1990). The Hall Formation is located within the hanging wall of the Stubbs thrust, which was subsequently folded by F_1. The upper age limit of ca. 174 Ma for both D_1 and D_2 was constrained by the Hobson Lake pluton (Gerasimoff, 1988) in the Cariboo Mountains to the north; this was the oldest pluton interpreted to truncate all SW-vergent structures.

Age constraints for SW-verging deformation and associated metamorphism in the northern Selkirk Mountains was primarily provided by U-Pb analyses of zircon and titanite from Middle Jurassic plutons (Shaw, 1980a; Brown et al., 1992; Logan and Friedman, 1997; Marchildon, 1999). Shaw (1980a) analyzed zircon from the southwestern part of the Adamant pluton (Figs. 2.3 and 2.4). He concluded that the ca. 169 Ma U-Pb ages represented the timing of metamorphic zircon growth concomitant with D_2, as opposed to pluton emplacement because the zircon could be found only in the outer hydrated zone of the pluton. U-Pb analyses of zircon and titanite by Brown et al. (1992) produced an age of ca. 168 Ma for the Fang and Pass Creek plutons, interpreted to post-date the development of SW-verging structures and regional metamorphism. Thus, in the northern Selkirk Mountains D_1 and D_2, and regional metamorphism were interpreted to have occurred prior to and possibly during 169 Ma, but no later than 168 Ma.

Based on structural and geochronologic evidence Colpron et al. (1996, 1998) argued that the F_1 Carnes nappe and the second generation SW-vergent folds and faults were part of a progressive deformation that occurred between ca. 173-168 Ma. This was interpreted to have post-dated the initial obduction of the Intermontane Superterrane and the associated development of ca. 187-173 Ma NE-verging folds and faults within the Quesnel Terrane of the Kootenay Arc. The age constraints proposed by Colpron et al. were provided by: 1) The reinterpreted age of deposition of the Hall Formation, ca. 190-187 Ma (according to the time scale of Gradstein et al., 1994). 2) A suite of syntectonic intrusive rocks deformed by east-vergent folds in the Quesnel Terrane that were emplaced ca. 183-178 Ma (Klepacki 1985; Andrew et al. 1990; T. Höy, 1995 pers. comm. to M. Colpron). 3) The intrusion of the ca. 173 ± 5 Ma Kuskanax batholith (Parrish and Wheeler, 1983), which postdated the earliest NE-verging deformation, but was emplaced prior to or early in the development of the SW-verging structures (Read, 1973). 4) The intrusion of the Kaslo River suite, ca. 173 ± 5 Ma (Smith et al., 1992), during the development of SW-verging deformation within the Kootenay Arc (Fyles, 1964, Warren, 1997). 5) The emplacement of the Fang pluton at 168 ± 2 Ma (Brown et al., 1992) immediately prior to the cessation of SW-verging deformation in the northern Selkirk Mountains. Also, by integrating thermochronometric and thermobarometric data, Colpron et al. (1996) were able to demonstrate that there was at least 10 km of exhumation within the Illecillewaet synclinorium during the development of SW-verging structures.

In the field area for this study, Marchildon (1999) interpreted the Bigmouth pluton and surrounding area to have been affected by two metamorphic events, M_1 and M_2, separated by an intervening period of decompression. This is based on thin section observations from the host rocks surrounding the Bigmouth pluton indicating that retrograde chlorite replaced M_1 garnet and was then overprinted by a second generation (M_2) of garnet growth (Plate 1b and 2 of Marchildon, 1999, p.105 and 107, respectively). The ductile deformation associated with development of the transposition foliation in the area, referred to as S_T by Marchildon, was interpreted to have been a protracted and ongoing process that began prior to M_1 and continued post-M_2. Marchildon concluded that the intrusion of the pluton was coeval with the M_1 metamorphism, at a depth >20km based on the presence of magmatic epidote (see Zen and Hammarstrom, 1984, and Zen, 1985). A linear regression through normally discordant IDTIMS zircon data produced a lower intercept age of ca. 157 ± 3 Ma with an elevated MSWD[1] of 182. This was interpreted to constrain the timing of pluton emplacement and M_1 metamorphism, which post-dated the initiation of the transposition-forming event. Two fractions of titanite analyzed by Marchildon gave $^{206}Pb/^{238}U$ ages of 140.5 ± 0.8 Ma and 137.4 ± 1.4 Ma with normal discordance (~6-16%). The younger titanite crystals were interpreted to have been reset during M_2 following post-M_1 decompression, and pre-dated the end of the transposition-forming event. Thus, S_T was considered to be older than ca. 157 Ma, and continued to develop after ca. 140 to 137 Ma.

Lastly, U-Pb analyses of zircon from the Goldstream pluton (Logan and Friedman, 1997) and the Albert stock (Crowley and Brown, 1994) both yielded an age of 104 Ma. Both intrusive bodies are situated within the west flank of the fan (Fig. 2.1) where they truncate all structures in the country rock, contain foliated xenoliths of the host bedrock,

[1] MSWD = Mean Squared Weighted Deviates = measure of data scatter about a linear regression

and are surrounded by a contact aureole. Thus, in the western flank development of SW-vergent structures and metamorphism occurred prior to ca. 104 Ma.

2.3.2. Northeast-verging structures: D_2 and D_3

Relative timing constraints for NE-verging structures in the northern Selkirk Mountains were initially put forward by Brown and Tippett (1978) and Brown et al. (1992). They speculated that the development of F_2 was closely related to regional metamorphism that predated the emplacement of the Middle Jurassic Fang and Pass Creek plutons (ca. 168 Ma). However, the deflection of F_2 structures around these igneous bodies was interpreted to be associated with F_3 (Brown et al., 1992). Thus, F_3 was constrained to be post- Middle Jurassic. Additional timing constraints for NE-vergent D_3 structures were presented by Colpron et al. (1998). They proposed that the development of NE-vergent structures in the Dogtooth Range on the east side of fan coincided with the Late Jurassic (ca. 154 Ma) loading of the foreland basin to the east marked by the accumulation of the 154-151 Ma Passage beds of the Fernie Group.

The only absolute timing constraints for the formation of NE-verging structures in the northern Selkirk Mountains come from Crowley et al. (2000; see Table 2.1). Based on IDTIMS U-Pb analyses of monazite and zircon from variably deformed and post-tectonic leucocratic dikes collected along Highway 23 near Mica Village and Mica Dam (Fig. 2.3), Crowley et al. constrained the timing of fold and foliation development to be ca. 122-58 Ma. This agreed well with ages previously provided by other studies to the west and northwest in the northern Monashee Mountains (Sevigny et al., 1989, 1990; Scammell, 1993; Digel et al., 1998). However, Crowley et al. also produced ages between ca. 170-58 Ma for the development of NE-verging structures and metamorphic assemblages in the northern Monashee Mountains. The implications for these data are considered below in the Discussion section.

2. 4. U-Th-Pb Geochronology: New Timing Constraints on Deformation

Zircon and monazite U-Th-Pb isotopic data are reported for 14 samples that include variably deformed leucosome, leucogranitic dikes, and plutons (Figs. 2.9a-s). The geochronologic data are presented in Tables 2.2, 2.3 and 2.4, and on concordia diagrams (Figs. 2.10a-l), and the results are projected along strike into a regional cross section (Fig. 2.11). The study area, which transects the fan (Figs. 2.3, 2.4 and 2.8), has been broadly divided into three domains (Figs. 2.4, 2.8 and 2.11) according to the lithostratigraphic, structural, metamorphic and geochronologic elements that characterize portions of the fan. Domain 1 is located in the west flank of the fan where SW- verging folds (F_2) with shallow dipping axial planes and transposed foliation (S_2) dominate. This domain is interpreted to represent the highest structural level in the study area, comprised primarily of Lardeau Group and Badshot Formation stratigraphy that was metamorphosed at chlorite to sillimanite grade, and intruded by Middle Jurassic (ca. 169 Ma) plutons. Deformation and metamorphism are constrained to be Middle to Late Jurassic in age (ca. 172-156 Ma; this study), with a minor overprint at ca. 91 Ma (this study). Domain 2 occupies the zone where the trace of the fan axis is mapped (Figs. 2.3 and 2.4), and is cored by Sil-grade rocks of the Windermere Supergroup. Axial planes of folds and transposition foliation have a near-vertical orientation (Fig. 2.8 and 2.11) that generally strike to the northwest or southeast. Domain 2 is termed the ‘Transition Zone’ because the isotopic data suggest evidence for Middle Jurassic structures that have been substantially overprinted during the mid- to Late Cretaceous (ca. 104-81 Ma). Domain 3 is located within the eastern flank of the fan where NE-vergent folds (F_2 and F_3) and transposed foliation dominate at all scales of observation. The east flank is composed of Windermere Supergroup rocks that progressively change from Sil-Kfs near the fan axis to Ky-St grade adjacent to the Rocky Mountain Trench. In Domain 3, thermo-structural age constraints range between Early Cretaceous to Early Tertiary (ca. 144-63 Ma, Chapter 3). It is important to reiterate that assignment of fold and fabric generation, as discussed below, is based on local overprinting and geometric observations; no regional timing correlation is implied, especially across the fan.

2.4.1. Analytical Methods

Geochronologic methods include U-Pb IDTIMS and U-Th-Pb SHRIMP analyses accompanied by backscattered electron (BSE) and cathodoluminescence (CL) imaging, and high-resolution X-ray compositional maps of dated minerals. Integration of these techniques was necessary to resolve such complexities as multiple age domains within single crystals and young monazites with Th disequilibrium.

U-Pb IDTIMS geochronology at Carleton University followed procedures outlined by Parrish et al. (1987). Mineral separates were obtained by standard crushing, grinding, Rogers Gold™ table, heavy liquid, and Frantz™ magnetic separation techniques. When possible, the clearest, crack- and inclusion-free crystals were selected for analysis. All zircon, with the exception of some <74 μm grains, were abraded according to Krogh (1982). Teflon® microcapsules (Parrish, 1987) were used for mineral dissolution with a mixed ^{233}U-^{235}U-^{205}Pb tracer (Parrish and Krogh, 1987). Ion exchange column chemistry (Parrish et al., 1987) facilitated U-Pb element separation. U-Pb isotopes were analyzed using a multicollector mass spectrometer (Finnagan MAT 261 as described by Roddick et al., 1987), and estimation of errors was based on numerical error propagation (Roddick, 1987). Decay constants used are those recommended by Steiger and Jagër (1977). Discordia lines through analyses were calculated using a modified York (1969) regression (Parrish et al., 1987). Typically, procedural U blanks were less than 5 pg and Pb blanks less than 10 pg. Common Pb corrections were made assuming model Pb compositions derived from the growth curves of Stacey and Kramers (1975).

Ion microprobe analyses of monazite and zircon grains in a polished araldite resin mount, using the SHRIMP II at the Geological Survey of Canada in Ottawa, were carried out according to the methods outlined by Stern (1997), Stern and Sanborn (1998), and Stern and Berman (2000). A full description of the SHRIMP II instrument may be found in Stern (1997), Williams (1998), and De Laeter and Kennedy (1998). The grain mount was polished using 9, 6, and 1 μm diamond polishing compound to reveal grain centers, and coated with 5.8-6.0 nm of Au (99.9999%). BSE and CL images were obtained using a Cambridge Instruments S360 scanning electron microscope operating at 20 kV accelerating potential and using an electron beam current of 2-5 nA. Chemical maps of Y, Th, and U of strategically selected monazites were made using a Cameca SX-50 electron microprobe at the University of Massachusetts (see Williams et al., 1999), using a high sample current (>200 nA), small step sizes (~0.5 μm), and rastering the electron beam. Obtaining chemical maps of monazite prior to SHRIMP II analyses is unique to this study, and proved to be very effective for elucidating age domains within the analyzed monazite (see Chapter 4, Gibson et al. 2002).

Target locations for U-Th-Pb SHRIMP analysis on selected zircon and monazite were chosen using the BSE, CL, and X-ray images. Targeted areas were sputtered using a mass-filtered O_2^- primary beam operating in Kohler illumination mode to effect even sputtering. All samples were analyzed using the K120 Kohler aperture setting, which yielded an approximate beam diameter of 22 x 31 μm. For zircon, the primary ion beam current was typically 15-16 nA for standards and ~10 nA for unknowns. For monazite, the primary beam current was ~2-2.3 nA for both standards and unknowns. The operational mass resolution (1% peak height) over the course of the analyses was 5550-5700. Instrumental bias in the measured Pb/U and Pb/Th ratios was corrected by an empirically-derived calibration of the linear relationships between $^{206}Pb^+/UO^+$ vs. UO_2^+/UO^+, determined on natural monazite and zircon standards (GSC samples 3345, 4170, and BR266, respectively). Isotopic ratios were corrected for common Pb using Stacey-Kramers ^{204}Pb. Errors assigned to SHRIMP U-Th-Pb ages were determined using numerical propagation of all known sources of error as outlined by Stern (1997), Stern and Sanborn (1998), and Stern and Berman (2000). Uncertainties for SHRIMP isotopic ratios and ages listed are presented at 1σ in Table 2.4, whereas the error ellipses in Figs. 2.10a-l, and any quoted weighted mean ages, are presented at 2σ. The ^{204}Pb correction can impart significant error on the calculated age for SHRIMP data due to extremely low ^{204}Pb counts (see Stern, 1997). The propagation of the statistical error associated with this usually has the most impact on the $^{207}Pb/^{235}U$ age, because of low ^{207}Pb counts in relatively young minerals (i.e., Jurassic-Tertiary). This can cause an "artificial" disagreement between the calculated $^{207}Pb/^{235}U$ age and ages calculated using the other isotopic systems. Thus, the isotopic systems for monazite and zircon that include the highest Pb counts, the $^{208}Pb/^{232}Th$ and $^{206}Pb/^{238}U$ chronometers, respectively, are considered most accurate and are used when quoting SHRIMP ages in the text and figures unless otherwise noted. U-Th-Pb concordia plots have been included only for monazite SHRIMP analyses, but not for zircon because of very low the ^{208}Pb counts.

2.4.2. Guidelines for age interpretations

The IDTIMS data in many of the samples yielded an age range of a few million years or more, well outside analytical uncertainty, which is attributed to the presence of two or more age domains within the analyzed monazite or zircon. Causes for the spread of ages include inherited cores, partial recrystallization, and/or secondary growth. Additional complexities included unsupported ^{206}Pb in monazite resulting from the incorporation of excess ^{230}Th upon crystallization (Schärer, 1984; e.g., sample DG22b and c, Figs. 2.10h-i), multiple ages of inheritance in zircon (sample DG150, Fig. 2.10a), and crystal alteration due to metamictization and/or hydrothermal fluids (sample DG69, Fig. 2.10g).

In this study diffusive Pb loss is considered unlikely for either zircon or monazite. Based on experimentally determined diffusion parameters, Cherniak and Watson (2000) and Cherniak et al. (2002) concluded that the mean closure temperature (Tc; see Dodson, 1973) for both zircon and monazite of typical size (10-100 µm) is in excess of 900º C. Furthermore, many *in situ* studies of monazite have also concluded that it is highly resistant to thermally induced volume diffusion, even under conditions of granulite facies metamorphism (e.g., DeWolf et al., 1993; Zhu et al., 1997; Braun et al., 1998; Cocherie et al., 1998; Crowley and Ghent, 1999; Zhu and O'Nions, 1999; Foster et al., 2002). Thus, Pb loss by volume diffusion is considered unlikely for both zircon and monazite under most geologic conditions.

In consideration of the complexities mentioned above, age interpretations were generally made based on both the IDTIMS and SHRIMP data when available. In general, the errors assigned to the IDTIMS data were an order of magnitude less than the SHRIMP data. Thus, concordant IDTIMS data should provide the most precise timing constraints; however, this was the exception to the norm. As such, interpretations benefited greatly from the *in situ* SHRIMP analyses, which were used to discern multiple age domains within single crystals or sample microcrystalline domains within significantly altered crystals. Additional confidence was gained when both monazite and zircon from the same sample could be analyzed, serving as a check against each other. Although many pegmatite and leucogranitic dike samples contained both minerals, the zircons were often difficult or impossible to analyze due to low Pb concentrations (e.g., <5 ppm), or were metamict and/or severely altered (Fig. 2.10g). In contrast, the monazites in these samples contained abundant Pb (e.g., >200-500 ppm; see Table 2.3), and were crystalline. However, most monazites produced reversely discordant data (i.e., $^{206}Pb/^{238}U$ ages > $^{207}Pb/^{235}U$ ages) due to unsupported ^{206}Pb (Schärer, 1984). The correction prescribed by Schärer (1984) has not been applied to these data because it is not considered appropriate for many of the monazite that have come from igneous rocks that were subsequently metamorphosed or thermally overprinted. This is supported by chemical maps, BSE images, and SHRIMP analyses that all strongly suggest the monazite analyzed likely contained variable degrees of secondary growth and/or recrystallization (see Figs. 2.10h-k). Parrish (1990) pointed out that it would be very difficult to determine the Th/U ratios of the fluids from which the secondary monazite grew. Thus, for IDTIMS data it is assumed that the $^{207}Pb/^{235}U$ chronometer, which is unaffected by ^{230}Th disequilibrium, is the best approximation for the timing of monazite crystallization (Schärer, 1984). Lastly, most of the IDTIMS monazite data is supplemented by $^{208}Pb/^{232}Th$ data provided by SHRIMP analyses, which is also considered to be unaffected by isotopic disequilibrium.

For some IDTIMS data, the $^{207}Pb/^{235}U$ age for reversely discordant monazite data is considered a good approximation of the timing of primary growth, especially when fractions are tightly clustered above the concordia curve. The analyses would not be expected to cluster if there was significant inheritance, overgrowths, or recrystallization domains, as it would be unlikely to get identical mixtures from grain to grain; however, minor amounts of mixing cannot be completely ruled out. Linear regressions through discordant monazite data are not considered reliable because intercepts will be offset at either end if any of the data contain a component of unsupported ^{206}Pb. For these data, the youngest $^{207}Pb/^{235}U$ age is considered the best approximation of the secondary growth event.

2.4.3. Isotopic Data and Age Interpretations

A summary of the ages, locations, hand sample and thin section descriptions, and geologic relationships can be found in Table 2.2.

2.4.3.1. Domain 1: Western Flank

DG150 – Bigmouth pluton (IDTIMS and SHRIMP)

The Bigmouth pluton (Fig. 2.9a) is a weakly deformed to undeformed coarse-grained Hbl-Bt-Qtz monzonite to granite intrusion. Mapping near the southwest contact has revealed that the shape of the Bigmouth pluton is that of a ~1 km-thick laccolith whose lower contact appears to dip shallowly to the northeast (Fig. 2.3; Map 2). The base of the pluton is in contact with marble and calcareous pelite, and can be viewed in valleys trending north into Bigmouth Creek, one of which dissects the pluton (Fig. 2.3; Map 2).

The upper contact was interpreted by mapping roof pendants of calcareous schist and marble along ridge tops (Map 2).

The pluton appears to truncate regional D_2 structures (Fig. 2.4; Map2). Xenoliths of foliated (S_2) country rock are found entrained near the contact (Fig. 2.9b), suggesting the main phase of transposition pre-dated the emplacement of the pluton. Van der Leeden (1976) interpreted the pluton to be post-D_2 and pre- to syn-D_3 because the pluton crosscut F_2 folds, but contains a weak foliation attributed to be S_3. However, the lack of strain-related structures such as deflection of foliation around megacrysts of microcline, and poor development of undulatory extinction and subgrains as observed in thin sections, suggest that the S_3 foliation may actually be magmatic flow banding. Nevertheless, weakly folded dikes and veinlets of apparent pluton affinity extending away from the contact do suggest some strain was imparted following pluton emplacement (Fig. 2.9d), but possibly not enough to develop a foliation within the pluton itself.

Both IDTIMS and SHRIMP analyses were carried out on euhedral, clear and crack-free zircon. Optically, some of the zircon appeared to have cores; thus one IDTIMS fraction (i.e., D) consisted only of tips to minimize the effect of the inherited cores. All IDTIMS fractions are normally discordant with significant scatter (Fig. 2.10a) and highly variable $^{207}Pb/^{206}Pb$ ages (ca. 1956-950 Ma; Table 2.3), indicating multiple ages of inheritance. This precluded the use of linear regression to determine an igneous age for the pluton, and brought into question the age assigned by Marchildon (1999) based on a linear regression of similarly dispersed data. The inheritance problem was clarified by the SHRIMP analysis of the cores; six spots on cores of six crystals produced a range in age between Early Proterozoic and Archean (ca. 2650-1655 Ma; Fig. 2.10a; Table 2.4).

Conversely, six spots targeted within the domains of pristine oscillatory zoning that mantled the inherited cores produced $^{206}Pb/^{238}U$ ages between 172-164 Ma (weighted mean of $^{206}Pb/^{238}U = 167 \pm 3$ Ma). The analyses all overlap concordia within error (Fig. 2.10a, inset of SHRIMP U-Pb concordia plot); the variable discordance associated with these analyses is likely attributable to the imprecision of the $^{207}Pb/^{235}U$ ratio due to low ^{207}Pb counts. The analyzed domains of oscillatory zoning within these zircons are interpreted to represent igneous growth (see Vavra, 1990; Pidgeon, 1992; Hanchar and Miller, 1993; Connelly, 2001). Therefore the $^{206}Pb/^{238}U$ SHRIMP ages of ca. 172-164 Ma are interpreted as the best approximation for the timing of crystallization of the Bigmouth pluton, and the age assigned by Marchildon (1999), 157 ± 3 Ma, is considered too young. Furthermore, pluton emplacement at ca. 172-164 Ma is interpreted to have post-dated most, if not all, of the development of the transposition fabric (S_2) in the area.

CT07 – Highly strained pegmatite (SHRIMP only)

Sample CT07 is from an isoclinally folded Ms-Bt bearing leucocratic pegmatite dike (Fig. 2.9c) that is hosted in marble approximately 1 km south of the Bigmouth pluton. The fold limbs are highly attenuated and dismembered, leaving rootless isoclinal hinges floating in the host marble, indicative of transposition. The axial planar foliation, found in fold hinges, dips shallowly to the northeast, parallel to the regional S_2 transposition foliation. Hence, this dike is thought to be pre- to syn-D_2. IDTIMS analyses were not carried out due to a paucity of zircon, most of which were turbid and sugary in texture indicative of having been severely altered (see inset of Zrn 8 in Fig. 2.10b). Instead, three euhedral, crack and inclusion free zircons and one altered zircon with clear tips were chosen for SHRIMP analyses. BSE images of the three relatively clear zircons revealed diffuse oscillatory zoning around inherited cores (inset Fig. 2.10b of Zrn's 1, 2 and 3). Three analyses in the cores yielded ages that range between Late Archean (2933 ± 6 Ma) and Early Proterozoic (1113 ± 41 Ma); this is a similar age range as was found in the inherited cores within zircons analyzed from the Bigmouth pluton. The oscillatory zones surrounding the cores are interpreted to represent igneous growth related to the crystallization of CT07. Thus, the igneous age of this dike is interpreted to be constrained by three SHRIMP analyses within the domains of oscillatory zoning of Zrn1, Zrn2 and Zrn3, and a spot in the tip of Zrn 8; the $^{206}Pb/^{238}U$ ages range between 171 to 167 Ma. None of the analyses were concordant in U-Pb space (Fig. 2.10b), but three of the analyses (1.3, 2.2, and 8.1) overlapped concordia within error. A discordia chord with a lower intercept anchored at 91 Ma, the probable age of recrystallization (see below), was regressed through the SHRIMP data. This produced a very imprecise upper intercept age of 244 ± 420 Ma, which is not duplicated in any of the other analyses of this study and is thus considered meaningless. A cause for the discordance observed in these analyses could be due to the SHRIMP spots overlapping the older cores, but this is considered unlikely because the placement of the spots as shown in the BSE images in Fig. 2.10b do not support this. As such, the discordance is interpreted to be the result of imprecision associated with the $^{207}Pb/^{235}U$ ages due to low ^{207}Pb counts, therefore, the age is interpreted using the $^{206}Pb/^{238}U$ chronometer.

In the BSE images, the domains of oscillatory zoning in Zrn1, Zrn2 and Zrn3 were partly resorbed and overgrown by brighter rims of homogeneous zircon (Fig. 2.10b). One SHRIMP spot placed entirely within the bright overgrowth rim of Zrn1 yielded a $^{206}Pb/^{238}U$ age of 90.7 ± 1.4 Ma, coincident with metamorphic ages produced within

Domains 2 and 3 of this study (see below, Table 2.2 and Chapter 3). This is interpreted to be the timing of a secondary thermal event that may also be responsible for the severe alteration (hydrothermal?) of the other zircons in this sample. This Late Cretaceous overprint has implications for the interpretation of the two titanite fractions analyzed by Marchildon (1999), that gave $^{206}Pb/^{238}U$ ages of 140.5 ± 0.8 Ma and 137.4 ± 1.4 Ma with normal discordance (~6-16%). The titanite crystals were interpreted to be reset during the second metamorphic event (M_2) that followed post-M_1 decompression. However, the younger, discordant titanite ages are re-interpreted to represent a mixture of primary titanite grown in the Middle Jurassic that was partially recrystallized or overgrown during a minor thermal overprint at ca. 91 Ma. The Late Cretaceous age may be the time of M_2 following post-M_1 decompression. However, this is considered somewhat tentative because the textural evidence in thin section presented by Marchildon is complicated by the overprinting effects of both pluton emplacement and subsequent retrograde growth of chlorite during final exhumation. It is only in the westernmost flank of the fan in the lowest grade rocks, furthest away from the pluton, that the transposed fabric, S_2, and the associated prograde assemblage are best preserved, and seemingly unaffected by subsequent overprints.

DG116 – Weakly folded pegmatite (IDTIMS and SHRIMP)

DG116 comes from a Ms-Bt bearing pegmatite dike that extends from the contact of the Bigmouth pluton into the host marble (Fig. 2.9d), and is interpreted to be a late stage phase of the pluton. The dike is weakly folded, with axial planes that strike 332° and dip at 44° to the northeast, which is slightly oblique to the foliation (strike/dip = 301/30° NNE) in the host marble. The zircons chosen for IDTIMS analysis included two fractions that were turbid and inclusion-rich, and two fractions that were clear and resinous brown with few inclusions. The brown crystals were quite enriched in uranium, making up ~2-5% of the total atomic abundance (Table 2.3). All but fraction A, a turbid inclusion-rich single-grain fraction, plotted above the concordia curve (Fig. 2.10c). Fraction A was closest to being concordant (3% discordant), with a $^{207}Pb/^{206}Pb$ age of 167 ± 22 Ma. The isotopic composition of fractions B, C, and D is enigmatic; the points are reversely discordant and lie in a line parallel with the $^{207}Pb/^{235}U$ axis. Interestingly, fractions B and C have $^{206}Pb/^{238}U$ ages within error of fraction A, possibly suggesting that the $^{207}Pb/^{235}U$ isotopic system has been disturbed either naturally or analytically.

Four SHRIMP analyses of four resinous brown zircons are normally discordant and lie along a discordia line that passes through the origin (Fig. 2.10c). A linear regression of the SHRIMP data and IDTIMS fraction A yields an upper intercept of 170.8 ± 4.6 Ma, interpreted to be the approximate age of this weakly deformed pegmatite, and the latter stages of deformation in the area. The intersection of the discordia line with the origin suggests these high-U zircons have lost Pb sometime near the present, possibly due to metamictization related to substatial alpha recoil damage. The crystals would then have been susceptible to low-temperature Pb loss by processes such as fluid mediated diffusion along microfractures.

DG129 – Undeformed pegmatite dike (IDTIMS and SHRIMP)

This sample comes from an undeformed, crosscutting pegmatite dike. Second generation folds and transposition foliation within the host calc-silicate are truncated by the highly discordant margins of the vertical dike (Fig. 2.9e). In thin section, there is little evidence of strain, with randomly oriented minerals showing good development of euhedral to subhedral grain boundaries and uniform extinction. IDTIMS analyses were carried out on multigrain fractions of clear, euhedral and prismatic crystals with few inclusions and no apparent cores as determined optically. The data are normally discordant with $^{207}Pb/^{206}Pb$ ages between ca. 487-178 Ma (Table 2.3), suggesting a component of older inheritance. BSE imaging revealed the presence of cores surrounded by a diffuse mantle of oscillatory zoning. A discordia line through the data produced a lower intercept of 162.3 ± 0.7 Ma (Fig. 2.10d), interpreted to reflect the igneous age of the dike, and an upper intercept of 2082 ± 64 Ma thought to approximate the age of inheritance. Four SHRIMP spots (2.1, 5.1, 7.1, and 13.1) targeted within the domains of oscillatory zoning of four zircons overlap the concordia curve (Fig. 2.10d - U-Pb SHRIMP plot), with $^{206}Pb/^{238}U$ ages that range between 171-167 Ma, and weighted mean of 169 ± 3 Ma. The age for a fifth spot, 12.1, is clearly discordant, and although it is not clear in the BSE image, it must represent partial sampling of an older inherited core. A linear regression through the SHRIMP data provided a lower intercept of 169 ± 2 Ma, which matches the weighted mean of other spot ages, and is interpreted to represent the igneous age of the dike. The upper intercept of 2289 ± 610 Ma is likely the age of inheritance affecting spot 12.1. The reason for the difference between the SHRIMP age determined for the dike, ca. 169 Ma, and the age determined using IDTIMS, ca. 163 Ma, is uncertain. Possibly the IDTIMS intercept ages have been influenced either by the Late Cretaceous overprint that affected CT07 (cf. image of Zrn7.1 in Fig. 2.9d), or variable ages of inheritance. An MSWD of 0.14 for the IDTIMS discordia chord suggests a good linear fit for the data, which would not be expected if there had been variable degrees of Late Cretaceous overgrowth or variable ages of inheritance. However, neither scenario can be ruled out based three data points, so the SHRIMP age of 169 ± 3 Ma is considered the most accurate for the age of post-tectonic dike emplacement.

In Domain 1 on the west flank of the fan, the ages for the analyzed dikes and the Bigmouth pluton appear to overlap within error. Thus, it is likely these intrusives were emplaced during and immediately following the waning stages of D_2, suggesting D_2 is at least as old as 172 ± 1 Ma.

DG169 - Adamant Pluton (IDTIMS and SHRIMP)

In map view the Adamant pluton is an elliptical (~27km x 6 km) east-trending composite intrusion (Fig. 2.3) that is cored by hypersthene-augite monzonite enclosed by quartz monzonite to hornblende-biotite granodiorite (Fox, 1969). It is highly discordant to the trend of regional D_2 structures, which were deflected around the southwest and northeast margins of the pluton (Shaw, 1980b). A weak fabric (S_2?) defined by the alignment of hornblende and biotite is observed within the pluton. Shaw (1980a) carried out IDTIMS U-Pb analyses on three multigrain fractions of zircon that yielded an average age of 169 ± 4 Ma. Shaw interpreted this age to constrain the time at which the pluton was metamorphosed rather than emplaced, because the zircons were confined to the hydrated outer zones of the pluton. However, Woodsworth et al. (1991) reinterpreted the Middle Jurassic age to be the time of pluton crystallization. Logan and Colpron (1995) concurred on the basis of mapping a contact aureole around the southwest margin of the pluton that overprinted regional fabrics.

In this study, four multigrain fractions of clear, euhedral, elongate and prismatic, inclusion-free zircons were analyzed by IDTIMS. The data cluster just below the concordia curve at 167 Ma (2-4% discordant; Fig. 2.10e); they have a weighted mean

$^{206}Pb/^{238}U$ age of 166.8 ± 0.3 Ma. The slight discordance is likely caused by the presence of very small xenocrystic cores that were not detected optically prior to the analysis, but were revealed, although rarely, in CL images of other apparently clear zircon crystals. Eight SHRIMP analyses on similar grains yielded $^{206}Pb/^{238}U$ ages between 170-163 Ma. Cathodoluminescence images of the interior of the zircon crystals displayed two types of zoning patterns. Some showed straight, elongate zones (e.g., Fig. 2.10e), while others had oscillatory zoning. The oscillatory zoned zircon tended to be more equant in shape, whereas the striped zoning was usually found in elongate (~1:5 aspect ratio) zircon, but not always. Both types of zircon were considered igneous in origin based on their distinct zoning and euhedral habit. The four SHRIMP spots within these zones yielded $^{206}Pb/^{238}U$ ages between 170-166 Ma. Truncating the interior zones are discordant, fairly homogenous low-U zones (i.e., brighter zones in CL equate to lower concentrations of U and Th; Fig. 2.10e), which produced slightly younger and more discordant ages between 165-163 Ma (Table 2.4; Fig. 2.10e). The increased discordance may be caused by analyzing zircon portions with lower ^{207}Pb concentrations. These younger, homogenous zones may represent an episode of metamorphic recrystallization, but this cannot be proven conclusively because they overlap within error with the ages produced from the interior zones. The weighted mean of all eight $^{206}Pb/^{238}U$ SHRIMP ages of 167 ± 2 Ma, which matches the IDTIMS weighted mean $^{206}Pb/^{238}U$ age of 166.7 ± 0.3 Ma. Therefore, 167 Ma is considered the best approximation for the igneous age of the Adamant pluton, which is interpreted to be late-syn to post-D_2, and pre-D_3.

2.4.3.2. Domain 2: Transition zone – fan axis

DG09 – Folded and boudinaged tonalite dike, French Glacier (IDTIMS and SHRIMP)

DG09 is a medium-grained leucocratic tonalite dike with subordinate-scale veins that are both folded by F_2 and boudinaged (Fig. 2.9g). The nearly vertical axial planes of the F_2 folds dip steeply to the south, concordant with the transposition fabric (S_2) in the host Sil-Grt-Ms-Bt pelitic schist. Veins that are oriented parallel to the S_2 flattening plane are boudinaged. Four multigrain zircon fractions were analyzed by IDTIMS (Fig. 2.10f, Table 2.3). Fractions A and B contained brownish-grey elongate and prismatic zircon with minor fractures. Zircons in fractions C and D were clear, elongate and prismatic. All data plot very close to 167 Ma, with Fraction A being most concordant (-1% discordant, Table 2.3) with ages of 167 ± 3 Ma for both the $^{206}Pb/^{238}U$ and $^{207}Pb/^{235}U$ ratios; thus, 167 ± 3 Ma is interpreted to be the igneous age of this pre- to syn-F_2 dike. The very slight negative discordance is enigmatic because it cannot be attributed to excess ^{206}Pb since zircon incorporates relatively minor amounts of Th when it crystallizes (see Schärer, 1984; Parrish, 1990). The low Th/U ratio of Fraction A, 0.007, supports this interpretation. Nevertheless, the fact that the next most concordant analysis, Fraction B (2.8% discordant), has a $^{206}Pb/^{238}U$ age of 166.4 ± 0.7 Ma strongly suggests 167 ± 3 Ma is the correct age for this dike.

One SHRIMP spot on a monazite picked from this sample produced an age of ca. 91 Ma, which coincides with the age of monazites dated nearby in a pelitic schist (DG01, Fig. 2.10f). This is thought to represent the time of a significant thermal overprint, possibly M2 of Marchildon (1999). Anchoring a regression line from 91 Ma through the zircon data described above yields an upper intercept of 167 ± 9 Ma (Fig. 2.10f), which lends further support for the interpretation that the igneous age for this dike is 167 ± 3 Ma.

DG02 – Crosscutting tonalite dike, French Glacier (IDTIMS)

DG02 is a tonalite dike that crosscuts the transposition foliation (S_2) and contains foliated xenoliths of the host Sil-Grt-Ms-Bt pelitic schist (Fig. 2.9h), suggesting dike emplacement post-dated the development of the transposition foliation. However, small apophyses extending from the dike margin appear to be weakly deformed, thus emplacement is interpreted to be post-D_2 but not completely post-tectonic, i.e., pre-D_3. Two single-grain monazite fractions were analyzed by IDTIMS. Single-grain zircon fractions were analyzed, but the data were meaningless due to their extremely low Pb concentrations (~0.3 – 8.0 ppm). The monazites analyzed were light yellow, clear, inclusion-free, with well-formed crystal faces that are indicative of igneous crystallization. BSE images of monazite from this sample display oscillatory zoning (see Fig. 2.10f inset), further suggesting they are igneous in origin (Pidgeon, 1992 and references therein). The two monazite fractions M1 and M2 are nearly concordant (i.e., 1.5 and 0.8% discordant, respectively), with essentially the same $^{207}Pb/^{206}Pb$ ages, ca. 156 Ma (Table 2.3). The most concordant fraction, M2, has a $^{207}Pb/^{235}U$ age of 155.5 ± 0.6 Ma. This is interpreted to be the igneous age of this dike, and is considered to constrain the time of post-D_2 and pre-D_3 at French Glacier.

DG70a – Folded (F_3) pegmatite dike, Argonaut Mountain (IDTIMS and SHRIMP)

DG70a is a discordant Grt-Ms pegmatite that truncates and entrains the S_2 transposition foliation in the host Sil-Grt-Bt-Ms pelitic schist, but is folded by F_3 (Fig. 2.9i). The F_3 folds are disharmonic with close to tight hinges and a Class 1C geometry

(Ramsay, 1967), and have axial surfaces that dip moderately (~50º) toward the northwest. Five single-grain monazite fractions were analyzed by IDTIMS. Zircon grains in this sample were too severely altered to be analyzed (Fig. 2.10g inset). The monazites were pale yellow, clear, inclusion-free and had a subhedral habit. Four fractions, M2, M3, M4 and M6, with minimal normal and reverse discordance between 3.0 to –6.2% plotted on the concordia curve at ca. 100 Ma, whereas fraction M5 with 10% normal discordance overlaps concordia at ca. 98 Ma (Fig. 2.10g). Monazites dated from the host pelitic schist (DG70b) also produced a similar range of U-Pb ages (see Chapter 3, p. 114). Five SHRIMP spots within variably zoned monazites, including oscillatory zoning, plotted on a U-Th-Pb concordia diagram between 106-102 Ma (Fig. 2.10g) with a $^{208}Pb/^{232}Th$ weighted mean age of 103.5 ± 2.7 Ma. The younger IDTIMS ages, especially for M5, likely resulted from analyzing igneous monazite crystals that had variable amounts of younger rim overgrowths similar to that illustrated in the Th map of Mnz4 of Fig. 2.10g. Thus, the weighted mean $^{208}Pb/^{232}Th$ SHRIMP age of 103.5 ± 2.7 Ma determined by analyzing the interior of the monazites, and presumably avoiding younger rim overgrowths, is interpreted to be the igneous age of this pre- to syn-F_3 dike.

DG69 – Undeformed, crosscutting pegmatite (IDTIMS)

DG69 is an undeformed, coarse-grained, Tur-Grt-Bt-Ms pegmatite dike that crosscuts both limbs of a 20m-scale F_3 fold (Fig. 2.9j), and contains foliated (S_2) xenoliths of country rock (Fig. 2.9k). Like DG70a, all zircons separated from this dike were too severely altered to analyze. Three single-grain monazite fractions were analyzed by IDTIMS (Table 2.3). The monazites were light yellow, clear, inclusion-free, and sub- to euhedral in habit. BSE imaging shows good development of sector zoning (Fig. 2.9g).

The fractions are reversely discordant and plot in a tight cluster above 81 Ma on the concordia curve. The weighted mean $^{207}Pb/^{235}U$ age for all three fractions, 80.8 ± 0.2 Ma, is considered to be the age of this post-tectonic dike.

2.4.3.3. Domain 3: East flank of fan

DG22c – folded (F_3) leucosome, Mud Glacier (IDTIMS)

DG22c is a medium-grained Ms-Bt-Grt-Pl-Qtz bearing leucosome hosted within Sil-Grt-Bt-Ms pelitic schist. The leucosome is concordant with the south to southwest moderate to steeply (~60°- 80°) dipping transposition foliation, S_2, that is defined by the alignment of the metamorphic minerals. Both the leucosome and S_2 have been folded and crenulated presumably by F_3 (Fig. 2.9l), with a hinge that plunges 48° to the southeast and an axial plane that dips 48° to the south-southwest. Three clear, xenoblastic monazites were dated by IDTIMS. The fractions are spread out slightly above concordia between 93-91 Ma (Fig. 2.10h), which likely reflects a mixture of ages within single-grains. Yttrium maps for two monazites that were analyzed by the SHRIMP demonstrate that there are at least two chemical domains within the monazites of this sample. Two SHRIMP spots within the darker, lower Yttrium interiors both produced a slightly older age, 104 ± 2 Ma, compared to the lighter, higher Yttrium exterior domains that have a weighted mean $^{208}Pb/^{232}Th$ age of 97 ± 2 Ma (Fig. 2.10h). The ages quoted above for the IDTIMS analyses are clearly younger, and actually match the SHRIMP ages produced in the zircon from this sample (see below). Perhaps the two monazite crystals chosen for SHRIMP analyses reflect incomplete recrystallization at ca. 92 Ma. The oldest 104 ± 2 Ma monazite cores likely grew during earlier stages of prograde metamorphism prior to leucosome production. The 97 ± 2 Ma age may represent analyses within domains of the older monazites that were partially recrystallized during leucosome generation associated with sillimanite-grade metamorphism at ca. 92 Ma (see Chapter 4; Foster et al. 2000; Foster et al. 2002).

BSE images of zircon display a diffuse and dark colored inner core surrounded by a lighter and fairly uniform mantle (Fig. 2.10h). The cores of three zircons analyzed by the SHRIMP are Archean in age (Table 2.4). Two spots within the mantles of Zrn10 and Zrn13 both produced an age of 92 ± 1 Ma, which is very similar to the IDTIMS analyses of the monazite, as well as the 94-92 Ma ages for monazites analyzed from the host pelitic schist (DG23, Chapter 3, p. 115). Thus, leucosome production is interpreted to have occurred at 92 ± 1 Ma.

It seems likely that the progressive development of S_2 transposition foliation was ongoing during leucosome production, which is considered to have occurred no earlier than 104 Ma, and that F_3 folding of the leucosome occurred sometime after 104 Ma and quite possibly after 92 Ma. Also, the range of ages documented above, 104-92 Ma, suggest that metamorphism in this area occurred over a period of at least 12 M.y.

DG22b – Undeformed, crosscutting pegmatite, Mud Glacier (IDTIMS)

DG22b is from a coarse-grained Tur-Ms bearing leucocratic pegmatite dike that crosscuts all fabrics (i.e., S_2, F_3) in the host pelitic schist, as well as a foliated (S_2) pegmatite (Fig. 2.9m). Three single-grain monazite fractions were analyzed by IDTIMS (Table 2.3). The monazites were medium yellow, clear, and inclusion free. Fraction M2 was euhedral with good crystal faces, whereas M3 and M4 were sub- to anhedral. The data plot in a line above the concordia curve between 67 and 63 Ma ($^{207}Pb/^{235}U$ ages; Fig. 2.10i). These data clearly demonstrate that there was a mixture of ages within single-grains. BSE images of monazite did not indicate the presence of cores; sector, and irregular nebulous zoning were observed (Fig. 2.10i). Nevertheless, the youngest $^{207}Pb/^{235}U$ age of 63.0 ± 0.6 Ma (M3) is interpreted to be least affected by inheritance problems, and is therefore considered the best approximation for timing of post-tectonic dike emplacement.

DG246 – Folded (F_3) Qtz-diorite dike, Warsaw Mountain (IDTIMS and SHRIMP)

DG246 is a medium-grained Qtz-diorite dike that displays similar field relationships to that described for DG70a (Fig. 2.9n). DG246 was folded by open F_3 folds, but is discordant to and truncates the S_2 foliation in the host Ky-Grt-Bt-Ms pelitic schist, and contains entrained foliated xenoliths of the schist. The S_2 foliation and associated leucosome in the schist is folded and crenulated within the hinges of the folded dike (Fig. 2.9o). These relationships suggest DG246 was post-S_2 and pre- to syn-F_3. Both monazite and zircon were analyzed by IDTIMS and SHRIMP. Three multi-grain zircon fractions were dated by IDTIMS. The zircons were euhedral, elongate and prismatic, and clear with very few inclusions. The data plot on a line immediately below the concordia curve (Fig. 2.10j). A best fit linear regression through the zircon data produced a discordia chord with imprecise lower and upper intercepts of 64 ± 11 Ma and 139 ± 65 Ma, respectively (MSWD = 0.07). A second regression line anchored at the origin produced an upper intercept of 84.1 ± 6.9 Ma (MSWD = 5.5), which is the same within error as the IDTIMS monazite ages from this sample (see below). BSE images of zircons in Fig. 2.10j display a consistent pattern where the interior is either oscillatory zoned, mottled, or both, and is surrounded by homogeneous zircon that lacks any zoning features. The diffuse and mottled pattern of the interior suggests that a strong thermal or hydrothermal overprint affected these zircons, and likely resulted in variable degrees of secondary recrystallization. Thus, the intercept ages quoted above are not considered to be meaningful. SHRIMP analyses of the zircon confirmed and resolved the suspected problem of age mixing (Fig. 2.10j). Four SHRIMP spots within the four zircon cores produced a weighted mean $^{206}Pb/^{238}U$ age of 90 ± 2 Ma, interpreted to reflect the igneous age of this dike. The outer, secondary portions of these zircons yielded a weighted mean $^{206}Pb/^{238}U$ age of 76 ± 2 Ma, interpreted to represent the age of metamorphic recrystallization.

The monazites analyzed by IDTIMS were large (+202 μm), clear, inclusion-free, euhedral crystals. All four fractions are reversely discordant and plot between 88-85 Ma (based on $^{207}Pb/^{235}U$ ages), indicative of mixing between at least two age domains. BSE and chemical maps shown in Fig. 2.10j revealed the monazites to have pristine, sector zoned interiors truncated and surrounded by a uniform rim. Eight SHRIMP analyses of the interior portion of six monazite crystals produced a tight cluster around a weighted mean $^{208}Pb/^{232}Th$ age of 92 ± 1 Ma, which is the same within error as the analyzed zircon interiors (90 ± 2 Ma). Thus, 92 ± 1 Ma is considered to be the best approximation for the timing of dike crystallization. The data from the monazite rims have a $^{208}Pb/^{232}Th$ weighted mean age of 80 ± 1 Ma; this is interpreted to be the timing of secondary crystallization of monazite, which is older than the ca. 76 Ma rims analyzed for the zircons. Possibly, this is the result of regrowth or recrystallization processes that differ for zircon compared to monazite; that at 80 Ma the appropriate fluid-mediated or solid-state reactions facilitated secondary monazite growth, but not zircon growth, and vice-versa for zircon but not monazite at 76 Ma. Also, considering the significantly altered nature of the zircons compared to the more pristine monazites, this suggests that the zircons were more susceptible to hydrothermal alteration. This could be related to the chemistry of the hydrothermal fluids that affected DG246, and/or the degree of metamictization of the zircons versus the monazites.

DG231 – Crosscutting, post-F_3 tonalite dike (IDTIMS)

DG231 is a medium-grained Ms-Pl-Qtz tonalite dike that crosscuts two, metre-scale F_2 folds that are gently refolded by F_3 (Fig. 2.9p and q). Thin section analysis revealed undulatory extinction, development of subgrains, and deformation twins, suggesting that the rock has undergone some strain ($D_{4?}$, see below) following emplacement. Four single-grain fractions, including two monazite and two xenotime, were analyzed by IDTIMS (Fig. 2.10k; Table 2.3). All fractions were large (+202 μm), pristine, clear, euhedral grains that were optically indistinguishable under the microscope. Two fractions, M1 and M4, are reversely discordant and have $^{207}Pb/^{235}U$ ages of 85.4 ± 0.1 Ma and 84.0 ± 0.2 Ma, respectively. The two normally discordant fractions, X2 and X3, are considered to be xenotime because they have Th/U values of 0.09 and 0.08, respectively, whereas monazite typically has Th/U >>1.0. The xenotime fractions, X2 and X3, have $^{207}Pb/^{206}Pb$ ages of 88.8 ± 1.6 Ma and 82.8 ± 2.1 Ma, respectively. The cause for the normal discordance in the xenotimes remains unclear; it is questionable whether it is due to Pb loss, recrystallization, or overgrowth. However, since the $^{207}Pb/^{206}Pb$ ages X2 and X3 closely match the $^{207}Pb/^{235}U$ ages of the monazites, recent Pb loss seems to be the most likely cause of normal discordance. Conversely, the spread observed in the monazite data may be due to some degree of inheritance and/or secondary growth because Pb loss would cause the fractions to plot much closer to the concordia curve (see Parrish, 1990).

Thus, the youngest, most reversely discordant monazite fraction, M4, at 84 ± 0.2 Ma is considered to be the best approximation for the age of this post-$F_{2\text{-}3}$ dike, because it was presumably least affected by inheritance, overgrowth or Pb loss.

DG235 – Highly strained Qtz-rich granitoid (IDTIMS)

DG235 comes from a set of intensely strained and sheared, medium-grained Qtz-rich granitoid lozenges that are hosted within a highly transposed Ky-Grt-Bt-Ms pelitic schist (Fig. 2.9r and s). There is a significant increase in strain observed at this location evidenced by the extreme dismemberment of the leucosome within the host schist (Fig. 2.9s). Perkins (1983) mapped the D_4, normal sense Northeastern fault through this area (see Fig. 2.3 and 2.8), which may explain the observed increase in strain. DG235 exhibits a pinch-and-swell structure, and contains a foliation ($S_{2?}$) parallel to that in the host schist (Fig. 2.9r). Four single-grain, euhedral, light yellow, clear, and inclusion-free monazites were analyzed by IDTIMS (Table 2.3). The fractions plot in a line above the concordia curve between ca. 84-76 Ma ($^{207}Pb/^{235}U$ ages), clearly indicative of age mixing. BSE images show that some of the monazites are homogeneous throughout, while others appear to have resorbed cores mantled by secondary monazite (Fig. 2.10l). It is difficult to determine the primary age of this dike. Monazite from the host pelitic schist (DG225) dated by IDTIMS and SHRIMP (Chapter 3, p. 122) may provide some insight (see Fig. 2.10l); three age domains were found, a ca. 105 Ma core, 100 Ma mantle, and 64 Ma rim overgrowth. The ca. 105 Ma age may approximate the primary age of DG235. The 64 Ma rim, which closely matches the age of the ca. 63 Ma crosscutting dike at Mud Glacier (DG22b), may be the age of an overprint facilitated by the D_4 shear zone acting as a conduit for hydrothermal fluids. Thus, the deformation of the dike associated with D_2

and/or subsequent strain reactivated parallel to S_2, may be as old as or even older than 105 Ma. Unfortunately, no SHRIMP work was done on this sample to corroborate these interpretations, so they are considered speculative.

2. 5. Discussion

The data presented in this chapter have provided timing constraints for deformation across the Selkirk fan at the latitude of this study. On the west flank of the fan, Domain 1, the development of SW-verging D_2 structures and transposition foliation (S_2) appear to be at least as old as ca. 172-167 Ma, which agrees well with timing constraints documented further south (e.g., Brown et al., 1992; Colpron et al., 1996; Table 2.1). A Late Cretaceous, ca. 92 Ma, overprint is interpreted to have affected the Bigmouth pluton area, but not enough to reset or erase the isotopic systems of the zircons analyzed. This overprint was not recorded in the area around Fang pluton, which is situated in a similar geologic setting ~60 km to the southeast in the Illecillewaet synclinorium. Based on $^{39}Ar/^{40}Ar$ analyses of hornblende, biotite, and muscovite, Colpron et al. (1996) concluded there was >10 km of exhumation by late Middle Jurassic time, and that the region remained at upper crustal levels until the present. The overprint at the Bigmouth pluton, which likely coincides with the M_2 metamorphism of Marchildon (1999), may indicate that the Bigmouth pluton was at a deeper crustal level in the mid- to Late Cretaceous relative to Fang pluton. Indeed, the Bigmouth pluton is interpreted by Marchildon (1999) to be situated within the same Sil-zone that is along strike from French Glacier and Argonaut Mountain of Domain 2 (Fig. 2.3). IDTIMS and SHRIMP analyses of monazites from Domain 2 strongly suggest that the M_2 assemblages, which includes the Sil-bearing schists, grew during the mid- to Late Cretaceous ca. 100-92 Ma (see Chapter 3, p. 112-

114). Unfortunately, the Grt-St-Bt schist sampled in the Bigmouth pluton area ~3 km south of its southeast margin was barren of monazite. However, another ~2.5 km due south, near Argonaut pass (Fig. 2.3), unpublished $^{40}Ar/^{39}Ar$ data provided muscovite and biotite cooling ages of 76 ± 0.8 Ma (M. Colpron, 1997, pers. comm.). Assuming this marks the time both muscovite and biotite cooled below their respective closure temperatures of 350ºC and 300ºC (Hanes, 1991), the above interpretation seems quite reasonable.

Within Domain 2, referred to as the Transition zone (fan axis), the U-Th-Pb isotopic evidence constrains D_2 to be Middle to Late Jurassic, ca. 167-156 Ma, and D_3 to be ca. 104-81 Ma. In addition, there has been a significant thermal overprint during the mid- to Late Cretaceous (ca. 100-92 Ma, see Chapter 3). The intensity of this overprint seems to be greater in Domain 2 than in Domain 1. For instance, the metamorphic grade is as low as chlorite grade in Domain 1, whereas it is Sil-grade in Domain 2 (Fig. 2.3). Secondly, there is excellent preservation of Middle Jurassic ages in Domain 1, with only a single Late Cretaceous SHRIMP spot age located on the thin rim of a zircon from CT07. Alternatively, in Domain 2 there was preservation of both Middle to Late Jurassic zircon and monazite (i.e., French Glacier), as well as an abundance of pristine mid- to Late Cretaceous metamorphic and igneous monazite. In addition, the absence of mid- to Late Cretaceous ages for leucocratic dikes in Domain 1 that are similar in composition to those found in Domain 2 at Argonaut Mountain suggests mid- to Late Cretaceous anatectic melting may have been a more prevalent process in Domain 2 than Domain 1.

The most pervasive mid- to Late Cretaceous strain and thermal overprint (Chapter 3) occurred within the east flank of the fan, in Domain 3, where the highest-grade rocks (e.g., Sil-Kfs grade) are situated. Within this part of the study area, the isotopic evidence for Middle Jurassic strain and metamorphism is absent, possibly due to subsequent recrystallization of the zircon and monazite during high-grade metamorphism in the Cretaceous. Conversely, the U-Th-Pb data provide excellent age constraints for D_3, which is interpreted to be ca. 104-84 Ma. This is interpreted to be a function of structural level and metamorphic grade, such that the isotopic evidence for older structures and metamorphism coincides with the highest structural and stratigraphic levels, and lowest metamorphic grade. Conversely, an apparent progressively stronger overprint of Early to Late Cretaceous strain and metamorphism (Chapter 3) affected rocks found in both the fan axis (Domain 2: Transition zone) and the eastern flank (Domain 3) where the highest grade rocks (Sil-Kfs-melt) are found, and presumably the deepest structural levels. This concept is a recurring theme in the southeastern Canadian Cordillera. Studies to the west and south have also arrived at similar conclusions (e.g., Carr, 1991; Parrish, 1995; Gibson et al., 1999; Crowley et al., 2001).

In the northern Monashee Mountains, north of this study (Figs. 2.1, 2.3, and 2.4), Crowley et al. (2000) documented a similar transition. The oldest strain and metamorphism developed in the Middle Jurassic was preserved in the lowest grade rocks (Bt-Grt grade), presumably of the highest structural levels, and the youngest Cretaceous to Tertiary ages were found within the highest grade, deepest level rocks. A notable difference was that the oldest ages came from rocks adjacent to the trench within the eastern flank of Selkirk fan that were deformed by two generations of northeast vergent structures belonging to D_2 and D_3. This is very important because it suggests that there was concomitant development of both southwest and northeast vergent structures in

Middle Jurassic time. Yet, data from this study and others in the northern Monashee Mountains (e.g., Crowley et al., 2000; Sevigny et al., 1990; Scammell, 1993) demonstrate that the southwest dipping S_2 transposition fabric in the east flank was at deep levels during the Early Cretaceous to Early Tertiary. Thus, it seems reasonable to suggest the initial northeast verging Middle Jurassic S_2 transposition foliation in the east flank was progressively or episodically reactivated and recrystallized during the Cretaceous. Also, Crowley et al. (2000) document a significant variation in U-Th-Pb ages, ca. 163-58 Ma, recorded in a seemingly continuous package of rocks in the northern Monashee Mountains. This likely reflects local variations in the intensity and degree of the Cretaceous to Tertiary tectonic overprint in the east flank of the fan that is a function of structural level, asymmetric geometry of the isograds (e.g., Ghent et al., 1980), and hydrothermal perturbations (Digel et al., 1998).

The significance of the east-west orientation of the Adamant pluton such that it straddles both sides of the fan axis remains problematic (Figs. 2.1 and 2.3, Map 2). The Adamant pluton is found in all three domains distinguished in this study, yet the analyzed zircons from the western portion preserve Middle Jurassic ages. Perhaps zircons analyzed from the eastern part of the pluton would provide evidence of a significant Cretaceous overprint indicating that the west side was exhumed to higher levels prior to the east due to differential uplift and rotation of the pluton. It is worth noting that the zircons from both the Adamant and Bigmouth plutons retain pristine crystallinity, whereas the zircon from the sampled dikes did not. This may be telling us something about the insulating effect that larger intrusive bodies have against overprinting metamorphic and/or hydrothermal events that would otherwise reset, recrystallize, or alter the zircons. It is possible that the whole Adamant pluton was at moderate crustal depth and overprinted by Cretaceous metamorphism, but the isotopic systems of the zircons inside were not significantly affected. Interestingly, a very thin rim was found to truncate the outer zones of some Adamant pluton zircons, but was too small to analyze. This rim may represent the same Late Cretaceous overprint that affected some of the zircons from the dikes of the Bigmouth pluton area. Further detailed geochronologic work in the area surrounding the Adamant pluton may clarify these uncertainties.

Lastly, a suite of Paleocene, post-tectonic pegmatites, commonly Tur-Ms bearing with or without biotite, intrude the east flank (this study; Crowley et al., 2000; Tables 2.1 and 2.2). It seems reasonable to infer that the emplacement of these dikes was facilitated by the late extensional structures that transect the east flank (Fig. 2.4 and 2.8). Regionally, this closely coincides with the onset of Early Eocene crustal-scale extension (e.g., Columbia River fault) that tectonically denuded a series of core complexes throughout the southeastern Canadian Cordillera (see Parrish et al., 1988).

The U-Th-Pb data presented above have significant implications for tectonic models previously proposed for the development of the Selkirk fan. First, the data demonstrate that significant Early to Late Cretaceous tectonism has affected the east flank of the fan. Furthermore, it seems reasonable to propose that there has been juxtaposition of higher structural levels with an older deformation history in the west flank relative to lower levels with a much younger deformation history in the east. This concept was not specifically considered in the models proposed by Price (1986), Brown et al. (1993), or Colpron et al. (1998). Although, the data in this study and that presented in Crowley et al. (2000) do indicate the concomitant development of southwest and northeast verging structures in the Middle Jurassic, which seems to fit the model of Brown et al. (1993; Fig. 2.2). Nevertheless, in light of the new U-Th-Pb data these models require a critical reexamination. Readers are referred to Chapter 5 for a more rigorous treatment of this topic.

2. 6. Conclusions

New data provide U-Th-Pb geochronologic constraints for deformation associated with the development of the Selkirk fan. The data suggest that there has been juxtaposition of higher structural levels with an older deformation history in the west flank relative to lower levels that record a younger deformation history in the east. Dated monazite and zircon from variably deformed leucocratic dykes and granodioritic-monzonitic plutons indicate that the thermo-structural development of the west flank of the fan occurred principally in the Middle Jurassic (ca. ≥172-167 Ma). In contrast, data from east of the fan axis demonstrate that there has been substantial Early to Late Cretaceous (ca. 104-84 Ma) deformation superimposed on an earlier Middle Jurassic transposition fabric, and that significant exhumation did not occur until the Late Cretaceous-Early Tertiary. Thus, the Selkirk fan should be thought of as a composite structure of Middle Jurassic and Cretaceous strain, rather than a singular fan that developed during one progressive event. As such, these data indicate a complex and protracted origin for the Selkirk fan, requiring significant revision of previous models.

Table 2.1. Summary of Previous U-Pb Age Constraints for Deformation in the Northern Selkirk Mountains, British Columbia[a]

Crowley et al. (2000) East flank of fan

Sample	Lithology	Mineralogy[b]	Texture/Fabric/Structural Interpretation	Interpreted Age[c]	Location (UTM)
2	Pegmatitic leucosome in migmatitic Ky-schist	Ms, Bt, Tur, Kfs, Pl, Qtz	Coarse-grained, lacking planar or linear fabric; interpreted as leucosome boudin parallel to the transposed fabric (S_{1-2})	Igneous Mnz and Zrn **60.7 ± 0.5 Ma** Interpreted to constrain late development of S_{1-2} fabric or reactivation parallel to S_{1-2}	E 393200 N 5770350
4	Pegmatite dike	Ms, Kfs, Pl, Qtz	Undeformed vertical dike, highly discordant, truncates transposed fabric	Igneous Mnz **58.4 ± 0.5 Ma** Post-dates deformation	E 393200 N 5770800
6	Leucogranite	Ms, Bt, Kfs, Pl Qtz	Concordant layer with S_{1-2} in host migmatitic Ky-schist; has a weak layer-parallel foliation and is boudinaged	Igneous Zrn **122.0 ± 1.0 Ma**, possibly constrains (late?) development of S_{1-2} Mnz and Xen **98.7-95.3 and 92.1 ± 0.3 Ma**; interpreted as metamorphic overprint	E 392500 N 5760000
7	Pegmatite dike	Ms, Kfs, Pl, Qtz	Undeformed vertical dike, highly discordant, truncates transposed fabric	Igneous Mnz **62.7 ± 0.5 Ma** Post-dates deformation	E 392500 N 5760000
24	Pegmatite dike	Ms, Bt, Tur, Kfs, Pl, Qtz	Coarse-grained, lacking planar or linear fabric; beaded (i.e. pinch and swell) parallel to the transposed fabric (S_{1-2}); also discordant to S_{1-2} in places, and contains foliated xenoliths of country rock (this study)	Igneous Mnz **63.5 ± 0.5 Ma** Interpreted to constrain late development of S_{1-2} fabric or reactivation parallel to S_{1-2}	E 395000 N 5772100

Marchildon (1999) Big Mouth Pluton (BMP) – West flank of fan

Sample	Lithology	Mineralogy	Texture/Fabric/Structural Interpretation	Interpreted Age	Location (UTM)
BMP	Kfs-megacrystic, Hbl-Bt bearing, Qtz-monzonite	Hbl, Bt, Kfs, Pl, Qtz, Ep,	Coarse grained; weak foliation defined by alignment of Kfs-megacrysts and Hbl; xenoliths of transposed country rock entrained near margin	Zrn w/ Precambrian xenocrystic cores: Lower intercept = **157.4 ± 3.3 Ma,** interpreted as age of pluton, syn- tectonic and M_1 metamorphism Ttn ca. **139 Ma –** interpreted as time of thermal resetting of Ttn during M_2 metamorphism	E 401700 N 5741100

Shaw (1980) Adamant Pluton (AP) – Southwest corner of pluton within west flank of fan

Sample	Lithology	Mineralogy	Texture/Fabric/Structural Interpretation	Interpreted Age	Location (UTM)
Group C	Hyp-Aug core, enclosed by Hbl-Qtz monzonite and Bt-Hbl granodiorite	Bt, Hbl, Pl, Kfs, Qtz, Ep	Sample collected within Bt-Hbl granodiorite zone; weak fabric developed; F_2 and S_2 mapped in outer zone of pluton; pluton interpreted to be emplaced pre-tectonic	Zrn age of **169 ± 4 Ma** interpreted as time of metamorphic recrystallization of outer zone of pluton, which is thought to be late D_2 and pre-D_3	E 421885 N 5729200

[a]Summary is presented in geographic order from north to south

[b]Mineral abbreviations after Kretz (1983); only major rock forming minerals listed

[c]Quoted monazite (Mnz) ages are based on $^{207}Pb/^{235}U$ isotopic ratio; Zircon (Zrn), titanite (Tnt) and xenotime (Xno) are based on $^{206}Pb/^{238}U$ isotopic ratio

Table 2.1. (concluded).

Logan and Friedman (1997) Goldstream Pluton – West flank of fan

Sample	Lithology	Mineralogy	Texture/Fabric/Structural Interpretation	Interpreted Age	Location (UTM)
94-MC0-9-306	Hbl-Bt monzodiorite	Hbl, Bt, Pl, Kfs, Qtz	Massive, homogeneous, no penetrative foliation, and primary igneous textures are well preserved; contains xenoliths of foliated country rock; has contact aureole	Five concordant Zrn at **ca. 104 ± 1.6 Ma**, interpreted as age of crystallization for post-tectonic pluton	E 396000 N 5718600

Brown et al. (1992) Fang and Pass Creek Plutons – West flank of fan

Sample	Lithology	Mineralogy	Texture/Fabric/Structural Interpretation	Interpreted Age	Location (UTM)
RB 21 Fang Pluton	Kfs-megacrystic, Hbl-Bt bearing, Qtz-monzonite	Hbl, Bt, Kfs, Pl, Qtz, Ep	Coarse-grained; no apparent foliation; xenoliths of foliated (S_2) phyllites entrained near margin; emplacement interpreted to post-date D_2; F_2 axial surfaces appear to be deflected around pluton, thought to be related to subsequent D_3 strain, thus, pre-dated D_3	Igneous Zrn with xenocrystic cores (≥1950 Ma) crystallized **ca. 168 ± 2 Ma**, interpreted as age for pluton that post-dates peak metamorphism and D_2 deformation, but pre-dates, in part, D_3	E 436600 N 5684600
R502 Pass Creek Pluton	Kfs-megacrystic, Hbl-Bt bearing, Qtz-monzonite	Hbl, Bt, Kfs, Pl, Qtz, Ep	Coarse-grained; no apparent foliation; stratigraphy and structures truncated at contact; emplacement interpreted to post-date D_2; strat. contacts and traces of normal faults appear to be deflected around pluton, possibly related to subsequent D_3 strain	Zrn contain xenocrystic cores (≥1950 Ma); Concordant Ttn at **168 ± 3 Ma** interpreted as age of emplacement for post-tectonic pluton following the peak of greenschist facies metamorphism	E 419000 N 5692000

Crowley and Brown (1994) Albert Stock – West flank of fan

Sample	Lithology	Mineralogy	Texture/Fabric/Structural Interpretation	Interpreted Age	Location (UTM)
AS-1	Bt-Hbl bearing, Qtz-monzonite	Hbl, Bt Pl, Kfs, Qtz	Complete preservation of igneous textures; truncates stratigraphy and structures; interpreted to post-date all ductile deformation in region; has a contact aureole	**ca. 104 ± 1 Ma** is the interpreted age of the post-tectonic pluton, based on three sub-concordant Zrn analyses	E 445300 N 5653700

Table 2.2. This Study: Summary of U-Th-Pb Age Constraints for Deformation in the Northern Selkirk Mountains, British Columbia[a]

Sample	Lithology[b]	Mineralogy[c]	Texture/Fabric/Structural Interpretation	Interpreted Age[d]	Location (UTM)
Domain 1: West flank of fan - Bigmouth Pluton (BMP) area					
DG150 BMP	Kfs-megacrystic, Hbl-Bt bearing, Qtz- monzonite	Hbl, Bt, Kfs, Pl, Qtz, Ep, Ttn	Coarse grained; weak foliation (flow banding?) of aligned Kfs-megacrysts, Hbl, and Bt; xenoliths of wall rock containing S_2 entrained near margin	Igneous Zrn **ca. 172-164 Ma; Wt. mn. = 167 ± 3 Ma;** Interpreted to constrain latest stages of deformation in the area	E 402125 N 5739400 2370 m
CT07	Pegmatite dike	Bt, Ms, Kfs, Pl, Qtz, Cal	Intensely strained dike, with rootless fold hinges, dismembered limbs, and axial planes parallel to S_2	Igneous Zrn **ca. 171-167 Ma; Wt. mn. = 169 ± 3 Ma**; Pre- to syn-D2	E 402750 N 5738310 2410 m
DG116	Pegmatite dike	Ms, Bt, Chl, Kfs, Pl Qtz	Weakly deformed dike that extends from contact of BMP into marble; interpreted to possibly be latest F_2	Igneous Zrn **171 ± 5 Ma**, possibly constrains latest development of F_2	E 402100 N 5739050 2260m
DG129	Leucogranitic dike	Ms, Bt, Chl, Kfs, Pl Qtz	Undeformed vertical dike, highly discordant, truncates transposed fabrics and folds in host calc-silicate	Igneous Zrn ca. **169 Ma**; Post-dates deformation	E 402540 N 5738650 2395 m
West flank - Adamant Pluton					
DG169	Hyp-Aug core, enclosed by Hbl-Qtz monzonite and Bt-Hbl granodiorite	Bt, Hbl, Kfs, Pl, Qtz, Hyp*, Aug*; *Px's mantled by Hbl	Coarse-grained; weak foliation (S_2?) defined by alignment of Hbl and Bt; margin highly discordant to regional structures (D_2), which deflect (by D_3?) around SW and NE corners of pluton; contact aureole interpreted to overprint regional fabrics (Logan and Colpron, 1995)	Igneous Zrn **ca. 171-167 Ma;** Interpreted to possibly constrain latest development of S_2 fabric and pre-D_3	E 422100 N 5727300 2200 m
Domain 2: Transition zone (fan axis) - French Glacier area					
DG09	Medium-grained tonalite dike	Ms, Grt, Pl, Qtz	Folded and boudinaged dike, with axial planes parallel to S_2 transposition; somewhat discordant margins suggest transposition was ongoing when dike was emplaced	Igneous Zrn **ca. 167 Ma;** syn-D_2 Thermally overprinted at 91 ± 2 Ma, same age as Mnz in host pelitic schist	E 414710 N 5735940 2040 m
DG02	Medium-grained tonalite dike	Bt, Ms, Chl, Pl, Qtz	Crosscutting dike with entrained xenoliths of transposed (S_2) pelitic schist; small apophyses appear to be slightly strained; subgrains and undulose extinction in Qtz and Pl in thin section	Igneous Mzn **ca. 156 Ma;** youngest age constraint for D_2 in this area; however there appears to have been some degree of subsequent deformation (D_3?)	E 415160 N 5734820 1865 m

[a]Summary is presented in geographic order from west to east across the fan

[b]Assignment of igneous rock lithology according to the IUGS classification system

[c]Mineral abbreviations after Kretz (1983); only optically identified major rock forming minerals listed

[d]Quoted monazite (Mnz) ages are based on $^{207}Pb/^{235}U$ (IDTIMS) or $^{208}Pb/^{232}Th$ (SHRIMP) isotopic ratios; Zircon (Zrn) are based on $^{206}Pb/^{238}U$ isotopic ratio; Wt. mn. = Weighted Mean

Table 2.2. (concluded).

Sample	Lithology	Mineralogy	Texture/Fabric/Structural Interpretation	Interpreted Age	Location (UTM)
Domain 2 cont.: Transition zone (fan axis) - Argonaut Mountain area					
DG70a	Pegmatite dike	Bt, Grt, Kfs, Pl, Qtz	Folded (F_3?) pegmatite that is discordant to the transposition foliation (S_2); thin section indicates some static recrystallization	Igneous Mnz **ca. 104 ± 3 Ma**; Post –F_2, pre- to syn-D_3	E 410730 N 5738180 2460 m
DG69	Tur-Grt-Bt-Ms pegmatite dike	Tur, Grt, Bt, Ms, Kfs, Pl, Qtz	Undeformed pegmatite that crosscuts both limbs of large (~20 m scale) F_3 folds (Fig. 2.9j) ; contains entrained xenoliths of foliated (S_2) country rock (Fig. 2.9k)	Igneous Mnz **ca. 81 ± 0.2 Ma**; Youngest age constraint for D_3 in this area	E 411300 N 5738125 2470 m
Domain 3: East flank of fan - Mud Glacier area					
DG22c	Leucosome	Ms, Bt, Grt, Pl, Qtz	Folded (F_3?) leucosome within a Sil-Grt-Bt pelitic schist; peak metamorphic minerals (Sil and Bt) in S_2 are folded and crenulated around hinge of the folded leucosome	Mnz = **104 ± 2 Ma** (primary? interior?) surrounded/overprinted by **97.1 ± 1.5 Ma** (secondary exterior); Zrn = **92 ± 1** Ma interpreted as metamorphic overprint	E 400325 N 5755000 2150 m
DG22b	Coarse-grained pegmatite	Tur, Ms, Pl, Kfs, Qtz	Essentially undeformed (thin section does show undulatory extinction and development of subgrains in Qtz); crosscuts all folds and fabrics in country rock; contains xenoliths of foliated (S_2) country rock	Mnz = **63 ± 1 Ma**; Interpreted as post-dating most if not all strain at this location; possibly minor strain imparted by D_4 faulting in the area	E 400350 N 5755000 2150 m
East flank - Warsaw Mountain area					
DG246	Medium-grained Qtz-diorite dike	Ms, Pl, Qtz	Folded (F_3) dike that is discordant to the transposed foliation (S_2); S_2 foliation and associated leucosome folded around F_3 fold hinges in dike; nearby dike of similar composition, fold geometry, and geologic relationships contains xenoliths of foliated (S_2) country	Igneous Mnz **ca. 92 ± 1 Ma** with secondary overgrowth at **80 ± 1 Ma;** Primary (?) Zrn **ca. 90 ± 2 Ma** with secondary overgrowth at **76 ± 2 Ma;** Ages interpreted as post-D_2 (S_2), pre- to syn-D_3	E 402667 N 5763431 2268 m
DG231	Medium-grained tonalite dike	Ms, Pl, Qtz	Dike crosscuts both limbs of two m-scale F_3 folds (Figs. 9p and q); minerals are randomly oriented in thin section and hand sample, with only minor evidence for strain (e.g. undulatory extinction, minor subgrain development)	Mnz **ca. 84 ± 0.2 Ma**; Age of dike interpreted to post-date development of F_3	E 402320 N 5764259 2485 m
DG235	Qtz-rich granitoid	Ms, Ky, Pl, Qtz	Part of a foliated ($S_{2?}$ or S_4?) and significantly strained set of intrusive granitoids within intensely transposed country rock (Figs. 9r and s); Alignment of Ms defines foliation which parallels foliation (S_2 or S_4?) in country rock	Mnz spread out above concordia from **84 to 76 Ma; 76 ± 0.3 Ma** possibly the age of dike emplacement during D_4, or the data may represent mixed ages between ca. 104 Ma and 64 Ma (i.e. ages determined for Mnz in nearby Ky-Grt-Bt schist)	E 401775 N 5764050 2280 m

Table 2.3 IDTIMS U-Pb Analytical Data for Northern Selkirk Mountains, British Columbia

Analysis[a]	Wt.[b] (µg)	U (ppm)	Pb*[c] (ppm)	^{206}Pb/^{204}Pb[d]	Pb[e] (pg)	^{208}Pb (%)[f]	^{206}Pb/^{238}U[g]	^{207}Pb/^{235}U[g]	^{206}Pb/^{238}U[h] (Ma)	^{207}Pb/^{235}U[h] (Ma)	Corr. Coeff.[i]	^{207}Pb/^{206}Pb[g]	^{207}Pb/^{206}Pb[h] (Ma)	Disc.[j] (%)
DG150 Bigmouth pluton								***Domain 1: West flank of fan***						
A* 149-202	60	591	39	4553	32	8.4	0.062718 ± 0.91%	1.03751 ± 0.92%	392.1 ± 6.9	722.7 ± 9.5	1.00	0.11998 ± 0.05%	1955.9 ± 1.9	82.3
B* 149-202	30	452	26	1426	34	10.2	0.054985 ± 0.10%	0.72145 ± 0.21%	345.1 ± 0.7	551.5 ± 1.8	0.65	0.09516 ± 0.17%	1531.3 ± 6.3	79.5
C* 149-202	50	394	29	3793	24	8.7	0.071706 ± 0.21%	0.93889 ± 0.22%	446.4 ± 1.8	672.3 ± 2.2	0.94	0.94963 ± 0.08%	1527.3 ± 2.9	73.2
D* 149-202	30	801	29	1433	41	6.3	0.036670 ± 0.12%	0.35774 ± 0.24%	232.2 ± 0.5	310.5 ± 1.3	0.61	0.07075 ± 0.19%	950.3 ± 8.0	76.9
E* 105-149	50	1235	78	2258	112	7.6	0.062244 ± 0.51%	0.81905 ± 0.51%	389.3 ± 3.8	607.5 ± 4.7	0.99	0.09544 ± 0.06%	1536.7 ± 2.3	76.9
DG116 Weakly folded ($F_{2?}$) pegmatite dike														
A 149-202	6	2546	58	609	41	0.01	0.025390 ± 0.40%	0.17294 ± 0.63%	161.6 ± 1.3	162.0 ± 1.9	0.67	0.04940 ± 0.47%	166.9 ± 21.8	3.2
B 105-149	6	15335	356	10930	14	0.01	0.025937 ± 1.42%	0.15354 ± 1.01%	165.1 ± 4.6	145.0 ± 2.7	0.69	0.04293 ± 1.03%	-171.6 ± 50.8	—
C* 149-202	7	46598	1088	23970	19	0.02	0.026135 ± 1.09%	0.14213 ± 0.84%	166.3 ± 3.6	134.9 ± 2.1	0.76	0.03944 ± 0.71%	-387.4 ± 36.9	—
D* 105-149	30	6322	136	506	600	-0.9	0.024356 ± 0.85%	0.12071 ± 1.22%	155.1 ± 2.6	115.7 ± 2.7	0.58	0.03594 ± 1.01%	-635.2 ± 54.2	—
DG129 Undeformed, crosscutting leucogranitic dike														
C* 105-149	20	292	7	633	15	0.6	0.025853 ± 0.65%	0.18024 ± 0.77%	164.5 ± 2.1	168.3 ± 2.4	0.66	0.05056 ± 0.60%	221.0 ± 27.4	25.9
D* <74	15	857	20	1412	15	0.6	0.025654 ± 0.15%	0.17563 ± 0.23%	163.3 ± 0.5	164.3 ± 0.7	0.55	0.04965 ± 0.19%	178.7 ± 8.9	8.7
E* 74-105	80	1302	34	1598	120	2.5	0.028040 ± 0.13%	0.21992 ± 0.19%	178.3 ± 0.5	201.8 ± 0.7	0.56	0.05688 ± 0.15%	487.0 ± 6.9	64.3
DG169 Adamant pluton, latest D_2, pre-D_3														
A* 149-202	90	703	20	3242	33	17.2	0.026188 ± 0.06%	0.17867 ± 0.17%	166.6 ± 0.2	166.9 ± 0.5	0.52	0.04948 ± 0.15%	170.8 ± 6.9	2.5
B* 149-202	210	814	24	5268	56	18.2	0.026230 ± 0.12%	0.17892 ± 0.14%	166.9 ± 0.4	167.1 ± 0.4	0.87	0.04947 ± 0.07%	170.2 ± 3.2	2.0
C* 149-202	460	554	16	5446	80	17.3	0.026237 ± 0.08%	0.17923 ± 0.10%	167.0 ± 0.3	167.4 ± 0.3	0.82	0.04954 ± 0.06%	173.6 ± 2.7	3.9
D* 105-149	230	706	20	3557	78	15.8	0.026227 ± 0.12%	0.17918 ± 0.15%	166.9 ± 0.4	167.4 ± 0.5	0.82	0.04955 ± 0.08%	173.9 ± 3.9	4.1
DG09 Folded (F_2) tonalite dike, French Glacier								***Domain 2: Transition zone (fan axis)***						
A* 74-105	4	22115	524	6306	23	21.8	0.026231 ± 0.99%	0.17853 ± 0.99%	166.9 ± 3.3	166.8 ± 3.3	0.99	0.04936 ± 0.11%	165.1 ± 5.2	-1.1
B* 74-105	2	17737	419	2672	22	20.2	0.026142 ± 0.23%	0.17838 ± 0.29%	166.4 ± 0.7	166.7 ± 0.9	0.65	0.04949 ± 0.22%	171.1 ± 10.3	2.8
C* 74-105	12	24201	571	5373	13	55.1	0.025980 ± 0.21%	0.18118 ± 0.23%	165.3 ± 0.7	169.1 ± 0.7	0.92	0.05058 ± 0.09%	221.8 ± 4.2	25.8
DG02 Crosscutting tonalitic dike, French Glacier														
M1 105-149	7	6367	408	3684	19	65.8	0.024176 ± 0.18%	0.16392 ± 0.23%	154.0 ± 0.5	154.1 ± 0.7	0.69	0.04918 ± 0.17%	156.3 ± 7.8	1.5
M2 105-149	5	7842	406	4529	13	57.3	0.024399 ± 0.20%	0.16547 ± 0.21%	155.4 ± 0.6	155.5 ± 0.6	0.68	0.04919 ± 0.16%	156.7 ± 7.7	0.8

[a]A-E in first column, fraction codes for zircon analyses; A* multi-zircon fraction; M1-M6, X1-X2 fraction codes for monazite and xenotime analyses, respectively; +74-105, size in µm. [b]Wt. = Weights, estimated from grain size measurements; uncertainty is 2 µg. [c]Radiogenic Pb. [d]Measured ratio, corrected for spike and Pb fractionation of 0.09 ± 0.03%/a.m.u. [e]Total common Pb in analysis, corrected for spike and fractionation. [f]Radiogenic ^{208}Pb, expressed as percentage of total radiogenic Pb. [g]Corrected for Pb and U laboratory blank where 208/204:207/204:206/204 = 19.01:15.64:38.23:1, and common Pb (Stacey-Kramers model Pb composition equal to interpreted age of analysis); errors are one standard error of the mean in percent. [h]Corrected for common Pb and laboratory blank; errors are two standard errors of the mean in Ma. [i]Corr. Coeff. = Correlation Coefficient. [j]Disc. = Discordance; values are reported when < -100.

Table 2.3. (concluded)

Analysis[a]	Wt.[b] (μg)	U (ppm)	Pb*[c] (ppm)	$\frac{^{206}Pb}{^{204}Pb}$[d]	Pb[e] (pg)	^{208}Pb (%)[f]	$\frac{^{206}Pb}{^{238}U}$[g]	$\frac{^{207}Pb}{^{235}U}$[g]	$\frac{^{206}Pb}{^{238}U}$[h] (Ma)	$\frac{^{207}Pb}{^{235}U}$[h] (Ma)	Corr.[i] Coeff.	$\frac{^{207}Pb}{^{206}Pb}$[g]	$\frac{^{207}Pb}{^{206}Pb}$[h] (Ma)	Disc.[j] (%)
DG70a F$_3$ pegmatite, Argonaut Mountain cont.							***Domain 2: Transition zone (fan axis) cont.***							
M2 105-149	5	10944	363	3114	17	57.3	0.015625 ± 0.18%	0.10319 ± 0.28%	99.9 ± 0.4	99.7 ± 0.5	0.59	0.04790 ± 0.22%	94.2 ± 10.6	-6.2
M3 105-149	8	9029	320	2832	25	59.8	0.015702 ± 0.22%	0.10377 ± 0.25%	100.4 ± 0.5	100.2 ± 0.5	0.74	0.04793 ± 0.17%	95.7 ± 8.1	-4.9
M4 105-149	5	5401	239	850	32	68.0	0.015633 ± 0.23%	0.10363 ± 0.53%	100.1 ± 0.5	100.1 ± 1.0	0.29	0.04808 ± 0.52%	103.1 ± 24.4	3.0
M5 105-149	3	5825	249	873	20	67.6	0.015252 ± 0.22%	0.10133 ± 0.42%	97.6 ± 0.4	98.0 ± 0.8	0.59	0.04818 ± 0.34%	108.3 ± 16.0	10.0
M6 105-149	4	4815	195	2170	9	64.9	0.015707 ± 0.19%	0.10370 ± 0.32%	100.5 ± 0.4	100.2 ± 0.6	0.39	0.04788 ± 0.30%	93.5 ± 14.3	-7.5
DG69 Undeformed, crosscutting pegmatite, Argonaut Mountain														
M1 105-149	5	27101	490	2840	39	36.0	0.012801 ± 0.30%	0.08292 ± 0.30%	82.0 ± 0.5	80.9 ± 0.5	0.85	0.04698 ± 0.16%	48.3 ± 7.9	-70.2
M5 105-149	4	13139	261	3073	14	41.4	0.012896 ± 0.16%	0.08291 ± 0.20%	82.6 ± 0.3	80.9 ± 0.3	0.67	0.04665 ± 0.15%	31.2 ± 7.2	——
M6 105-149	5	23071	432	4616	20	38.4	0.012800 ± 0.14%	0.08266 ± 0.16%	82.0 ± 0.2	80.6 ± 0.3	0.91	0.04684 ± 0.07%	40.9 ± 3.3	——
DG22c Folded (F$_{3?}$) trondhjemitic leucosome, Mud Glacier							***Domain 3: East flank***							
M2 149-202	17	5112	177	3124	26	62.1	0.014483 ± 0.09%	0.09360 ± 0.12%	92.7 ± 0.2	90.9 ± 0.2	0.71	0.04687 ± 0.08%	42.7 ± 3.9	——
M3 149-202	12	6225	305	3991	18	72.8	0.014718 ± 0.17%	0.09561 ± 0.18%	94.2 ± 0.3	92.7 ± 0.3	0.88	0.04712 ± 0.09%	55.0 ± 4.2	-71.7
M4 149-202	5	6131	326	2011	14	74.9	0.014719 ± 0.10%	0.09618 ± 0.17%	94.2 ± 0.2	93.2 ± 0.3	0.53	0.04739 ± 0.14%	68.9 ± 6.8	-37.0
DG22b Undeformed, crosscutting pegmatite, Mud Glacier														
M2 149-202	6	138180	2964	1479	63	55.8	0.010502 ± 0.20%	0.06689 ± 0.24%	67.3 ± 0.3	65.7 ± 0.3	0.85	0.04619 ± 0.13%	7.7 ± 6.1	——
M3 149-202	37	17781	326	2058	206	50.1	0.010119 ± 0.50%	0.06402 ± 0.51%	64.9 ± 0.6	63.0 ± 0.6	0.99	0.04589 ± 0.08%	-8.3 ± 3.6	——
M4 149-202	61	2005	251	1572	31	53.5	0.010773 ± 0.22%	0.06866 ± 0.27%	69.1 ± 0.3	67.4 ± 0.4	0.85	0.04622 ± 0.14%	9.3 ± 6.9	——
DG246 Folded (F$_3$) Qtz-diorite dike														
B* 74-105	105	8638	92	6047	112	0.15	0.011848 ± 0.28%	0.07799 ± 0.29%	75.9 ± 0.4	76.3 ± 0.4	0.99	0.04774 ± 0.04%	86.6 ± 2.0	12.4
C* 105-149	240	4181	43	5233	144	0.15	0.011460 ± 0.30%	0.07532 ± 0.30%	73.5 ± 0.4	73.7 ± 0.4	0.99	0.04767 ± 0.04%	82.6 ± 2.1	11.2
D* 105-149	80	11298	116	7140	94	0.15	0.011385 ± 1.32%	0.07478 ± 1.32%	73.0 ± 1.9	73.2 ± 1.9	1.00	0.04764 ± 0.06%	81.4 ± 2.6	10.4
M1 +202	50	6981	283	3736	22	70.1	0.013370 ± 1.05%	0.08698 ± 1.11%	85.6 ± 1.8	84.7 ± 1.8	0.97	0.04718 ± 0.27%	58.4 ±12.9	-47.0
M2 +202	39	6944	298	3769	97	70.8	0.013848 ± 1.88%	0.08987 ± 1.88%	88.7 ± 3.3	87.4 ± 3.1	1.00	0.04707 ± 0.06%	52.7 ± 2.8	-68.7
M3 +202	25	5462	291	3389	55	76.2	0.014000 ± 0.12%	0.09091 ± 0.14%	89.6 ± 0.2	88.3 ± 0.2	0.85	0.04710 ± 0.07%	54.0 ± 3.5	-66.4
M4 +202	40	12254	368	2906	231	57.8	0.013994 ± 0.08%	0.08887 ± 0.11%	89.6 ± 0.1	86.4 ± 0.2	0.83	0.04606 ± 0.07%	0.6 ± 3.2	——
DG231 Crosscutting tonalite dike, Warsaw Mountain														
M1 +202	26	15683	402	5182	68	52.0	0.013593 ± 0.06%	0.08772 ± 0.09%	87.0 ± 0.1	85.4 ± 0.1	0.88	0.04681 ± 0.04%	39.4 ± 2.1	——
M4 +202	32	12253	358	2512	207	57.9	0.013584 ± 0.09%	0.08630 ± 0.13%	87.0 ± 0.2	84.0 ± 0.2	0.84	0.04607 ± 0.07%	1.5 ± 3.5	——
X1 149-202	17	29819	369	59410	11	2.8	0.013359 ± 0.08%	0.08803 ± 0.09%	85.5 ± 0.1	85.7 ± 0.2	0.94	0.04779 ± 0.03%	88.8 ± 1.6	3.7
X2 +202	28	19078	210	6022	103	2.3	0.011934 ± 0.10%	0.07843 ± 0.11%	76.5 ± 0.1	76.7 ± 0.2	0.92	0.04767 ± 0.04%	82.8 ± 2.1	7.7
DG235 Highly strained Qtz-granitoid														
M1 +202	40	7439	269	2278	256	68.5	0.012583 ± 0.10%	0.08059 ± 0.14%	80.6 ± 0.2	78.7 ± 0.2	0.80	0.04645 ± 0.08%	21.0 ± 4.0	——
M2 149-202	23	10761	337	2099	140	64.8	0.012155 ± 0.23%	0.07768 ± 0.23%	77.9 ± 0.3	75.9 ± 0.3	0.75	0.04631 ± 0.16%	13.8 ± 7.8	——
M3 +202	30	8663	301	2172	154	65.7	0.013164 ± 0.07%	0.08460 ± 0.11%	84.3 ± 0.1	82.5 ± 0.2	0.73	0.04661 ± 0.08%	29.3 ± 3.9	——
M4 +202	30	12325	308	2166	222	52.1	0.013257 ± 0.08%	0.08572 ± 0.12%	84.9 ± 0.1	83.5 ± 0.2	0.81	0.04690 ± 0.08%	44.1 ± 3.7	-93.3

Table 2.4. SHRIMP U-Th-Pb Analytical Data, Northern Selkirk Mountains, British Columbia

Spots[a]	U (ppm)	Th (ppm)	Th/U	Pb*[b] (ppm)	^{204}Pb (ppb)	^{206}Pb/^{204}Pb	^{208}Pb/^{232}Th[c]	^{206}Pb/^{238}U[c]	^{207}Pb/^{235}U[c]
DG150 Bigmouth pluton								***Domain 1: West flank of fan***	
Z1.1m	539	67	0.13	13	2	6707	0.00945 ± 0.0007	0.02585 ± 0.0002	0.17748 ± 0.003
Z1.2c	413	139	0.35	106	4	24746	0.07160 ± 0.0008	0.24767 ± 0.0015	3.59788 ± 0.026
Z2.1m	875	159	0.19	23	2	12221	0.00853 ± 0.0003	0.02697 ± 0.0002	0.18462 ± 0.003
Z2.2c	186	173	0.96	96	3	19531	0.11801 ± 0.0016	0.41645 ± 0.0036	9.73370 ± 0.087
Z6.1c	49	15	0.33	16	2	5322	0.09169 ± 0.0027	0.31051 ± 0.0023	4.73971 ± 0.060
Z6.2m	634	31	0.05	15	2	7459	0.00748 ± 0.0013	0.02615 ± 0.0002	0.17796 ± 0.004
Z7.1c	238	100	0.43	116	2	48875	0.12079 ± 0.0017	0.43652 ± 0.0027	10.84364 ± 0.078
Z7.2m	867	115	0.14	21	2	8278	0.00792 ± 0.0004	0.02647 ± 0.0002	0.17539 ± 0.003
Z9.1m	193	13	0.07	5	3	1730	0.00098 ± 0.0029	0.02599 ± 0.0002	0.16385 ± 0.012
Z9.2c	127	149	1.20	46	0	268817	0.08637 ± 0.0012	0.28873 ± 0.0020	4.04819 ± 0.038
Z10.1c	273	126	0.48	87	2	33233	0.08735 ± 0.0013	0.29614 ± 0.0021	4.43644 ± 0.037
Z10.2m	431	29	0.07	10	2	3981	0.00749 ± 0.0010	0.02571 ± 0.0003	0.16797 ± 0.005
CT07 pre- to syn F_2 pegmatite dike									
Z1.1r	1637	19	0.01	21	1	17828	0.00553 ± 0.0014	0.01418 ± 0.0001	0.09461 ± 0.002
Z1.2c	121	59	0.50	75	3	20354	0.14579 ± 0.0021	0.53184 ± 0.0042	15.65961 ± 0.141
Z1.3m	412	23	0.06	10	0	19493	0.01028 ± 0.0015	0.02618 ± 0.0002	0.17962 ± 0.006
Z2.1c	48	42	0.90	11	2	3299	0.05986 ± 0.0018	0.19654 ± 0.0022	2.07768 ± 0.050
Z2.2m	677	39	0.06	17	2	8937	0.00852 ± 0.0011	0.02680 ± 0.0002	0.17899 ± 0.004
Z3.1m	76	2	0.02	2	0	100000	0.02809 ± 0.0046	0.02654 ± 0.0003	0.20067 ± 0.006
Z8.1m	2759	10	0.004	67	107	607	0.09206 ± 0.0351	0.02671 ± 0.0002	0.19208 ± 0.007
DG116 Weakly folded pegmatite dike									
Z1.1m	37984	73	0.002	726	1	892857	0.00660 ± 0.0005	0.02118 ± 0.0010	0.14499 ± 0.007
Z2.1m	43896	78	0.002	746	2	421941	0.00503 ± 0.0004	0.01897 ± 0.0009	0.12929 ± 0.006
Z8.1m	27652	37	0.001	603	2	255754	0.00788 ± 0.0010	0.02418 ± 0.0008	0.16447 ± 0.006
Z10.1m	21097	27	0.001	489	2	273973	0.00733 ± 0.0013	0.02570 ± 0.0007	0.17535 ± 0.005
DG129 Undeformed, crosscutting pegmatite dike									
Z2.1	15853	153	0.01	377	2	17391	0.00760 ± 0.0003	0.02630 ± 0.0007	0.17970 ± 0.005
Z5.1	874	186	0.22	22	2	11220	0.00851 ± 0.0002	0.02637 ± 0.0002	0.17726 ± 0.003
Z7.1	1190	104	0.09	30	2	17956	0.00867 ± 0.0003	0.02692 ± 0.0002	0.18334 ± 0.002
Z12.1	691	2	0.00	17	2	10735	0.00855 ± 0.0101	0.02764 ± 0.0002	0.20387 ± 0.003
Z13.1	857	92	0.11	21	1	21468	0.00881 ± 0.0008	0.02640 ± 0.0002	0.18269 ± 0.005
DG169 Adamant pluton									
Z12.1c	795	836	1.09	26	2	11450	0.00863 ± 0.0001	0.02678 ± 0.0002	0.17571 ± 0.003
Z12.2m	177	50	0.29	5	0	11310	0.01030 ± 0.0008	0.02587 ± 0.0002	0.18586 ± 0.012
Z20.1m	217	17	0.08	5	3	1592	0.00799 ± 0.0022	0.02593 ± 0.0003	0.15710 ± 0.011
Z20.2c	648	442	0.70	19	0	100000	0.00879 ± 0.0001	0.02618 ± 0.0002	0.18211 ± 0.002
Z24.1m	158	83	0.54	4	0	100000	0.00951 ± 0.0004	0.02604 ± 0.0003	0.19610 ± 0.004
Z24.2c	292	234	0.83	8	2	3712	0.00765 ± 0.0002	0.02582 ± 0.0002	0.17953 ± 0.007
Z34.1c	129	13	0.11	3	0	100000	0.01220 ± 0.0011	0.02562 ± 0.0005	0.18657 ± 0.007
Z34.2m	467	374	0.83	14	2	6845	0.00861 ± 0.0002	0.02641 ± 0.0002	0.17968 ± 0.007

[a]SHRIMP Spots: M1.1 = monazite and spot number; c = core, m = mantle and r = rim indicates the location of the spot in a zoned crystal when applicable, genetic origin is not implied. [b]Radiogenic Pb. [c]Corrected for common Pb according to Stern and Berman (2000); uncertainties are reported at 1 σ and are calculated by numerical propagation of all known sources of error; ^{207}Pb/^{206}Pb ages that are ≤0Ma are reported as 0 Ma.

Table 2.4. (continued)

Spots[a]	$^{207}Pb^{c}/^{206}Pb$	$^{208}Pb^{c}/^{232}Th$ (Ma)	$^{206}Pb^{c}/^{238}U$ (Ma)	$^{207}Pb^{c}/^{235}U$ (Ma)	Corr.[d] Coeff.	$^{207}Pb^{c}/^{206}Pb$ (Ma)	Disc.[e] (%)
DG150 Bigmouth pluton				***Domain 1: West flank of fan***			
Z1.1m	0.04980 ± 0.0008	190.0 ± 13.6	164.5 ± 1.0	165.9 ± 2.7	0.46	185.8 ± 36.8	12
Z1.2c	0.10536 ± 0.0004	1397.8 ± 14.8	1426.5 ± 7.5	1549.1 ± 5.8	0.87	1720.6 ± 6.5	17
Z2.1m	0.04965 ± 0.0008	171.8 ± 6.1	171.6 ± 1.0	172.0 ± 2.8	0.47	178.5 ± 36.7	4
Z2.2c	0.16952 ± 0.0003	2254.7 ± 29.6	2244.4 ± 16.4	2409.9 ± 8.3	0.99	2552.9 ± 2.5	12
Z6.1c	0.11071 ± 0.0010	1773.1 ± 50.3	1743.2 ± 11.2	1774.3 ± 10.6	0.68	1811.0 ± 17.1	4
Z6.2m	0.04936 ± 0.0011	150.7 ± 26.5	166.4 ± 1.2	166.3 ± 3.6	0.42	164.8 ± 51.6	-1
Z7.1c	0.18017 ± 0.0005	2304.8 ± 31.2	2335.0 ± 12.1	2509.8 ± 6.7	0.91	2654.4 ± 4.9	12
Z7.2m	0.04806 ± 0.0006	159.4 ± 7.7	168.4 ± 1.0	164.1 ± 2.3	0.49	102.2 ± 31.9	-65
Z9.1m	0.04573 ± 0.0034	19.8 ± 58.4	165.4 ± 1.3	154.1 ± 10.8	0.23	0.0 ± 0.0	——
Z9.2c	0.10169 ± 0.0006	1674.4 ± 22.9	1635.2 ± 10.0	1643.9 ± 7.7	0.81	1655.2 ± 10.4	1
Z10.1c	0.10865 ± 0.0004	1692.6 ± 23.5	1672.2 ± 10.6	1719.2 ± 7.0	0.91	1776.9 ± 6.3	6
Z10.2m	0.04738 ± 0.0013	150.9 ± 20.8	163.6 ± 1.9	157.7 ± 4.5	0.49	4.5 ± 63.3	——
CT07 pre- to syn F_2 pegmatite dike							
Z1.1r	0.04840 ± 0.0006	111.4 ± 29.0	90.8 ± 0.7	91.8 ± 1.4	0.61	118.9 ± 30.4	24
Z1.2c	0.21355 ± 0.0008	2750.9 ± 37.0	2749.2 ± 17.5	2856.3 ± 8.7	0.92	2932.7 ± 5.9	6
Z1.3m	0.04977 ± 0.0015	206.6 ± 30.2	166.6 ± 1.3	167.7 ± 4.9	0.38	184.2 ± 69.6	10
Z2.1c	0.07667 ± 0.0016	1175.1 ± 35.1	1156.7 ± 11.7	1141.5 ± 16.8	0.56	1112.6 ± 41.0	-4
Z2.2m	0.04844 ± 0.0009	171.5 ± 21.0	170.5 ± 1.1	167.2 ± 3.2	0.43	120.9 ± 44.9	-41
Z3.1m	0.05483 ± 0.0016	560.0 ± 91.1	168.9 ± 2.0	185.7 ± 5.5	0.47	405.3 ± 65.5	58
Z8.1m	0.05216 ± 0.0019	1780.0 ± 661.1	169.9 ± 1.2	178.4 ± 6.1	0.31	292.3 ± 83.7	42
DG116 Weakly folded pegmatite dike							
Z1.1m	0.04966 ± 0.00004	133.0 ± 10.2	135.1 ± 6.1	137.5 ± 5.9	1.00	179.0 ± 2.1	25
Z2.1m	0.04944 ± 0.00003	101.3 ± 7.2	121.1 ± 5.7	123.5 ± 5.5	1.00	168.7 ± 1.4	28
Z8.1m	0.04934 ± 0.00008	158.6 ± 20.1	154.0 ± 5.3	154.6 ± 5.1	1.00	164.1 ± 4.0	6
Z10.1m	0.04948 ± 0.00006	147.7 ± 25.9	163.6 ± 4.4	164.1 ± 4.1	1.00	170.9 ± 2.6	4
DG129 Undeformed, crosscutting pegmatite dike							
Z2.1	0.04955 ± 0.00004	153.1 ± 5.8	167.4 ± 4.2	167.8 ± 4.0	1.00	174.1 ± 2.1	4
Z5.1	0.04875 ± 0.0006	171.3 ± 4.5	167.8 ± 1.2	165.7 ± 2.3	0.61	135.7 ± 28.1	-24
Z7.1	0.04939 ± 0.0004	174.5 ± 5.7	171.3 ± 1.3	170.9 ± 2.0	0.72	166.3 ± 20.3	-3
Z12.1	0.05350 ± 0.0007	172.1 ± 200.9	175.8 ± 1.4	188.4 ± 2.9	0.57	350.0 ± 31.6	50
Z13.1	0.05018 ± 0.0012	177.3 ± 15.2	168.0 ± 1.1	170.4 ± 4.1	0.37	203.5 ± 57.4	18
DG169 Adamant pluton							
Z12.1c	0.04759 ± 0.0007	173.7 ± 1.6	170.4 ± 1.1	164.4 ± 2.4	0.51	78.9 ± 32.6	——
Z12.2m	0.05210 ± 0.0032	207.2 ± 16.0	164.7 ± 1.4	173.1 ± 10.1	0.26	289.9 ± 146.2	43
Z20.1m	0.04394 ± 0.0029	160.8 ± 44.3	165.0 ± 1.9	148.2 ± 9.3	0.29	0.0 ± 0.0	——
Z20.2c	0.05045 ± 0.0005	176.8 ± 2.8	166.6 ± 1.1	169.9 ± 2.0	0.65	216.0 ± 22.5	23
Z24.1m	0.05462 ± 0.0008	191.4 ± 7.5	165.7 ± 1.8	181.8 ± 3.3	0.66	396.6 ± 33.7	58
Z24.2c	0.05043 ± 0.0020	154.1 ± 4.5	164.4 ± 1.0	167.7 ± 6.2	0.28	214.6 ± 92.2	23
Z34.1c	0.05281 ± 0.0017	245.1 ± 22.9	163.1 ± 3.4	173.7 ± 6.4	0.62	320.7 ± 73.6	49
Z34.2m	0.04935 ± 0.0017	173.2 ± 3.8	168.0 ± 1.1	167.8 ± 5.6	0.30	164.3 ± 83.9	-2

[d]Corr. Coeff. = Correlation Coefficient. [e]Discordance = 100 x [1-($^{206}Pb/^{238}U$ age)/($^{207}Pb/^{206}Pb$ age)]; values are not quoted when < -100.

Table 2.4. (continued)

Spots[a]	U (ppm)	Th (ppm)	Th/U	Pb*[b] (ppm)	^{204}Pb (ppb)	$^{206}Pb/^{204}Pb$	$^{208}Pb/^{232}Th$ [c]	$^{206}Pb/^{238}U$ [c]	$^{207}Pb/^{235}U$ [c]
DG09 Folded (F_2) tonalite dike, French Glacier							***Domain 2: Transition zone (fan axis)***		
M1.1	28283	96277	3.4	739	55	6269	0.00448 ± 0.00007	0.01423 ± 0.0003	0.09436 ± 0.002
DG70a Folded (F_3) pegmatite, Argonaut Mountain									
M1.1c	42215	116090	2.75	1156	79	7492	0.00527 ± 0.00008	0.01634 ± 0.0003	0.10742 ± 0.003
M1.2c	21327	137676	6.46	913	73	4016	0.00503 ± 0.00008	0.01603 ± 0.0003	0.10589 ± 0.002
M3.1c	29040	201868	6.95	1358	86	4802	0.00523 ± 0.00008	0.01660 ± 0.0003	0.10918 ± 0.003
M3.2c	18145	107416	5.92	738	26	9626	0.00505 ± 0.00008	0.01615 ± 0.0003	0.10862 ± 0.003
M4.1c	13460	141921	10.54	827	90	2091	0.00511 ± 0.00008	0.01612 ± 0.0003	0.09510 ± 0.003
DG22c F_3 trondhjemitic leucosome, Mud Glacier								***Domain 3: East flank of fan***	
Z10.1r	647	5	0.008	8	3	2878	-0.00417 ± -0.0099	0.01440 ± 0.0001	0.08994 ± 0.005
Z10.2c	27	9	0.33	16	3	3571	0.14590 ± 0.0064	0.52703 ± 0.0061	13.62983 ± 0.294
Z13.1c	162	105	0.67	90	2	36483	0.13469 ± 0.0013	0.47194 ± 0.0026	11.34564 ± 0.076
Z15.1r	1020	6	0.006	13	2	5750	-0.00061 ± -0.0041	0.01437 ± 0.0001	0.09324 ± 0.002
Z15.2c	105	55	0.54	52	2	20855	0.13631 ± 0.0021	0.42071 ± 0.0025	10.92302 ± 0.088
M1.1c	30419	76718	2.52	800	94	4599	0.00517 ± 0.00008	0.01651 ± 0.0003	0.10542 ± 0.002
M1.2r	9032	116156	12.86	619	121	1011	0.00486 ± 0.00007	0.01554 ± 0.0003	0.07966 ± 0.005
M2.1c	22026	80189	3.64	685	91	3408	0.00515 ± 0.00008	0.01634 ± 0.0003	0.10703 ± 0.003
M2.2r	11972	148868	12.43	781	22	7079	0.00477 ± 0.00007	0.01523 ± 0.0003	0.10162 ± 0.004
DG246 Folded (F_3) Qtz-diorite dike, Warsaw Mountain									
Z1.1c	10102	55	0.006	132	9	14306	0.00278 ± 0.0009	0.01455 ± 0.0003	0.09519 ± 0.002
Z1.2r	4400	15	0.003	47	0	100000	0.00702 ± 0.0014	0.01184 ± 0.0001	0.07824 ± 0.001
Z5.1c	2975	11	0.004	37	1	30093	0.00587 ± 0.0028	0.01398 ± 0.0001	0.09116 ± 0.001
Z20.1c	6554	65	0.010	85	2	47529	0.00508 ± 0.0007	0.01442 ± 0.0002	0.09508 ± 0.001
Z20.2r	4343	14	0.003	45	1	40306	0.00619 ± 0.0021	0.01155 ± 0.0001	0.07601 ± 0.001
Z21.1c	3441	26	0.008	44	2	26567	0.00619 ± 0.0014	0.01418 ± 0.0002	0.09394 ± 0.001
Z21.2r	4402	15	0.004	47	3	13772	-0.00026 ± -0.0022	0.01180 ± 0.0001	0.07687 ± 0.001
Z29.1c	3113	9	0.003	36	3	11494	0.00132 ± 0.0035	0.01273 ± 0.0001	0.08270 ± 0.001
Z29.2r	3447	11	0.003	37	2	14278	0.00178 ± 0.0025	0.01191 ± 0.0001	0.07806 ± 0.001
M1.1c	17201	1200	13.97	1200	95	2323	0.00462 ± 0.00007	0.01493 ± 0.0003	0.09308 ± 0.004
M1.2r	22478	1124	9.42	1124	82	3419	0.00450 ± 0.00007	0.01453 ± 0.0003	0.09528 ± 0.004
M2.1r	66746	1338	2.46	1338	220	3350	0.00398 ± 0.00006	0.01280 ± 0.0002	0.07872 ± 0.002
M2.2c	15388	866	11.03	866	36	5270	0.00448 ± 0.00007	0.01448 ± 0.0003	0.09440 ± 0.002
M2.3c	30267	1597	9.98	1597	110	3448	0.00458 ± 0.00007	0.01452 ± 0.0003	0.09280 ± 0.003
M3.1r	56024	1288	3.47	1288	117	5179	0.00388 ± 0.00006	0.01256 ± 0.0002	0.07813 ± 0.002
M3.2c	16103	933	11.48	933	105	1920	0.00449 ± 0.00007	0.01451 ± 0.0003	0.08804 ± 0.004
M5.1c	23726	1202	9.32	1202	150	2011	0.00462 ± 0.00007	0.01471 ± 0.0003	0.08669 ± 0.003
M5.2r	43099	1446	5.14	1446	89	6129	0.00454 ± 0.00007	0.01471 ± 0.0003	0.09514 ± 0.004
M6.1c	24061	1331	10.33	1331	120	2545	0.00467 ± 0.00007	0.01474 ± 0.0003	0.09147 ± 0.004
M6.2m	39630	1452	5.60	1452	233	2252	0.00469 ± 0.00007	0.01532 ± 0.0003	0.09380 ± 0.002
M6.3r	68688	1381	2.42	1381	125	6127	0.00397 ± 0.00006	0.01301 ± 0.0002	0.08210 ± 0.002
M10.1r	45488	1381	4.50	1381	125	4498	0.00444 ± 0.00007	0.01437 ± 0.0003	0.09284 ± 0.002
M10.2c	24520	1199	8.96	1199	99	3114	0.00459 ± 0.00007	0.01458 ± 0.0003	0.09196 ± 0.004
M10.3r	45300	1516	5.00	1516	166	3523	0.00460 ± 0.00007	0.01498 ± 0.0003	0.09447 ± 0.002

Table 2.4. (concluded)

Spots[a]	$^{207}Pb^c/^{206}Pb$	$^{208}Pb^c/^{232}Th$ (Ma)	$^{206}Pb^c/^{238}U$ (Ma)	$^{207}Pb^c/^{235}U$ (Ma)	Corr. Coeff.	$^{207}Pb^c/^{206}Pb$ (Ma)	Disc. (%)
DG09 Folded (F_2) tonalite dike, French Glacier				***Domain 2: Transition zone (fan axis)***			
M1.1	0.04809 ± 0.0007	90.3 ± 1.4	91.1 ± 1.6	91.6 ± 2.1	0.81	103.5 ± 34.2	12
DG70a Folded (F_3) pegmatite, Argonaut Mountain							
M1.1c	0.04767 ± 0.0006	106.3 ± 1.6	104.5 ± 1.9	103.6 ± 2.3	0.85	82.8 ± 30.1	-26
M1.2c	0.04791 ± 0.0005	101.3 ± 1.5	102.5 ± 1.9	102.2 ± 2.2	0.88	94.7 ± 25.5	-8
M3.1c	0.04770 ± 0.0006	105.4 ± 1.6	106.1 ± 1.9	105.2 ± 2.3	0.85	84.3 ± 29.8	-26
M3.2c	0.04877 ± 0.0009	101.9 ± 1.6	103.3 ± 1.9	104.7 ± 2.7	0.76	136.9 ± 42.4	25
M4.1c	0.04280 ± 0.0012	103.0 ± 1.6	103.1 ± 1.9	92.2 ± 3.1	0.61	0.0 ± 0.0	——
DG22c F_3 trondhjemitic leucosome, Mud Glacier				***Domain 3: East flank of fan***			
Z10.1r	0.04531 ± 0.0023	0.0 ± 0.0	92.1 ± 0.7	87.5 ± 4.4	0.27	0.0 ± 0.0	——
Z10.2c	0.18757 ± 0.0032	2752.7 ± 113.8	2728.9 ± 25.9	2724.3 ± 20.6	0.63	2720.9 ± 28.0	——
Z13.1c	0.17436 ± 0.0005	2554.1 ± 23.0	2492.1 ± 11.5	2552.0 ± 6.3	0.89	2599.9 ± 5.2	4
Z15.1r	0.04707 ± 0.0007	0.0 ± 0.0	92.0 ± 0.6	90.5 ± 1.6	0.48	52.7 ± 37.3	-75
Z15.2c	0.18830 ± 0.0009	2582.8 ± 37.9	2263.7 ± 11.5	2516.6 ± 7.5	0.82	2727.4 ± 7.6	17
M1.1c	0.04632 ± 0.0004	104.3 ± 1.6	105.6 ± 1.9	101.8 ± 2.0	0.92	15.5 ± 17.9	——
M1.2r	0.03718 ± 0.0022	98.1 ± 1.5	99.4 ± 1.9	77.8 ± 4.9	0.40	0.0 ± 0.0	——
M2.1c	0.04750 ± 0.0007	103.8 ± 1.6	104.5 ± 1.9	103.2 ± 2.4	0.82	74.7 ± 33.1	-40
M2.2r	0.04840 ± 0.0018	96.2 ± 1.5	97.4 ± 1.8	98.3 ± 4.1	0.54	119.0 ± 90.3	18
DG246 Folded (F_3) Qtz-diorite dike, Warsaw Mountain							
Z1.1c	0.04745 ± 0.0002	56.1 ± 17.8	93.1 ± 2.0	92.3 ± 2.0	0.99	71.8 ± 8.4	-30
Z1.2r	0.04793 ± 0.0002	141.4 ± 27.5	75.9 ± 0.8	76.5 ± 0.8	0.93	95.9 ± 9.9	21
Z5.1c	0.04731 ± 0.0004	118.4 ± 57.2	89.5 ± 0.6	88.6 ± 0.9	0.69	65.0 ± 18.1	-38
Z20.1c	0.04781 ± 0.0002	102.4 ± 13.1	92.3 ± 1.0	92.2 ± 1.1	0.94	89.6 ± 10.3	-3
Z20.2r	0.04772 ± 0.0004	124.8 ± 43.1	74.0 ± 0.8	74.4 ± 1.0	0.83	85.4 ± 18.2	13
Z21.1c	0.04804 ± 0.0004	124.6 ± 28.7	90.8 ± 1.1	91.2 ± 1.3	0.87	101.1 ± 18.2	10
Z21.2r	0.04726 ± 0.0004	0.0 ± 0.0	75.6 ± 0.7	75.2 ± 1.0	0.82	62.5 ± 17.8	-21
Z29.1c	0.04713 ± 0.0004	26.6 ± 70.0	81.5 ± 0.8	80.7 ± 1.1	0.75	55.8 ± 22.4	-46
Z29.2r	0.04752 ± 0.0004	36.0 ± 49.9	76.3 ± 0.5	76.3 ± 0.8	0.72	75.5 ± 18.7	-1
M1.1c	0.04522 ± 0.0018	93.2 ± 1.4	95.5 ± 1.7	90.4 ± 3.9	0.51	0.0 ± 0.0	——
M1.2r	0.04755 ± 0.0018	90.7 ± 1.4	93.0 ± 1.7	92.4 ± 3.9	0.53	77.1 ± 86.5	-21
M2.1r	0.04462 ± 0.0005	80.3 ± 1.2	82.0 ± 1.6	76.9 ± 1.8	0.86	0.0 ± 0.0	0
M2.2c	0.04727 ± 0.0008	90.4 ± 1.4	92.7 ± 1.7	91.6 ± 2.3	0.79	62.7 ± 37.6	-48
M2.3c	0.04635 ± 0.0008	92.4 ± 1.4	92.9 ± 1.7	90.1 ± 2.4	0.77	17.0 ± 40.6	——
M3.1r	0.04511 ± 0.0008	78.2 ± 1.2	80.5 ± 1.5	76.4 ± 2.0	0.75	0.0 ± 0.0	——
M3.2c	0.04401 ± 0.0015	90.5 ± 1.4	92.9 ± 1.7	85.7 ± 3.4	0.55	0.0 ± 0.0	——
M5.1c	0.04274 ± 0.0009	93.1 ± 1.4	94.1 ± 1.7	84.4 ± 2.4	0.71	0.0 ± 0.0	——
M5.2r	0.04690 ± 0.0016	91.7 ± 1.4	94.2 ± 1.8	92.3 ± 3.7	0.55	44.2 ± 81.3	——
M6.1c	0.04502 ± 0.0016	94.1 ± 1.5	94.3 ± 1.7	88.9 ± 3.5	0.55	0.0 ± 0.0	——
M6.2m	0.04440 ± 0.0006	94.5 ± 1.4	98.0 ± 1.8	91.0 ± 2.1	0.84	0.0 ± 0.0	——
M6.3r	0.04575 ± 0.0005	80.2 ± 1.2	83.4 ± 1.5	80.1 ± 1.8	0.87	0.0 ± 0.0	——
M10.1r	0.04686 ± 0.0005	89.6 ± 1.4	92.0 ± 1.7	90.1 ± 1.9	0.90	42.0 ± 22.7	——
M10.2c	0.04574 ± 0.0019	92.5 ± 1.4	93.3 ± 1.7	89.3 ± 4.1	0.50	0.0 ± 0.0	——
M10.3r	0.04574 ± 0.0005	92.7 ± 1.4	95.9 ± 1.7	91.7 ± 1.9	0.89	0.0 ± 0.0	——

Figure 2.1. (a) Morphogeologic belts of the Canadian Cordillera. (b) Tectonic assemblage map of southeastern Omineca belt (modified after Wheeler and McFeely, 1991) showing lithologic map units of autochthonous Monashee complex (North American basement) and overlying Selkirk allochthon. Box outlined in the top left of the figure represents the location of Figs. 2.3 and 2.4. A-B is line of section for Fig. 2.6. ADP = Adamant pluton; AS = Albert stock; BMP = Bigmouth pluton; BR = Battle Range batholith; CS = Clachnacudainn Slice; FP = Fang pluton; GP = Goldstream pluton; GS = Goldstream Slice; IS = Illecillewaet Slice; KB = Kuskanax batholith; PC = Pass Creek pluton.

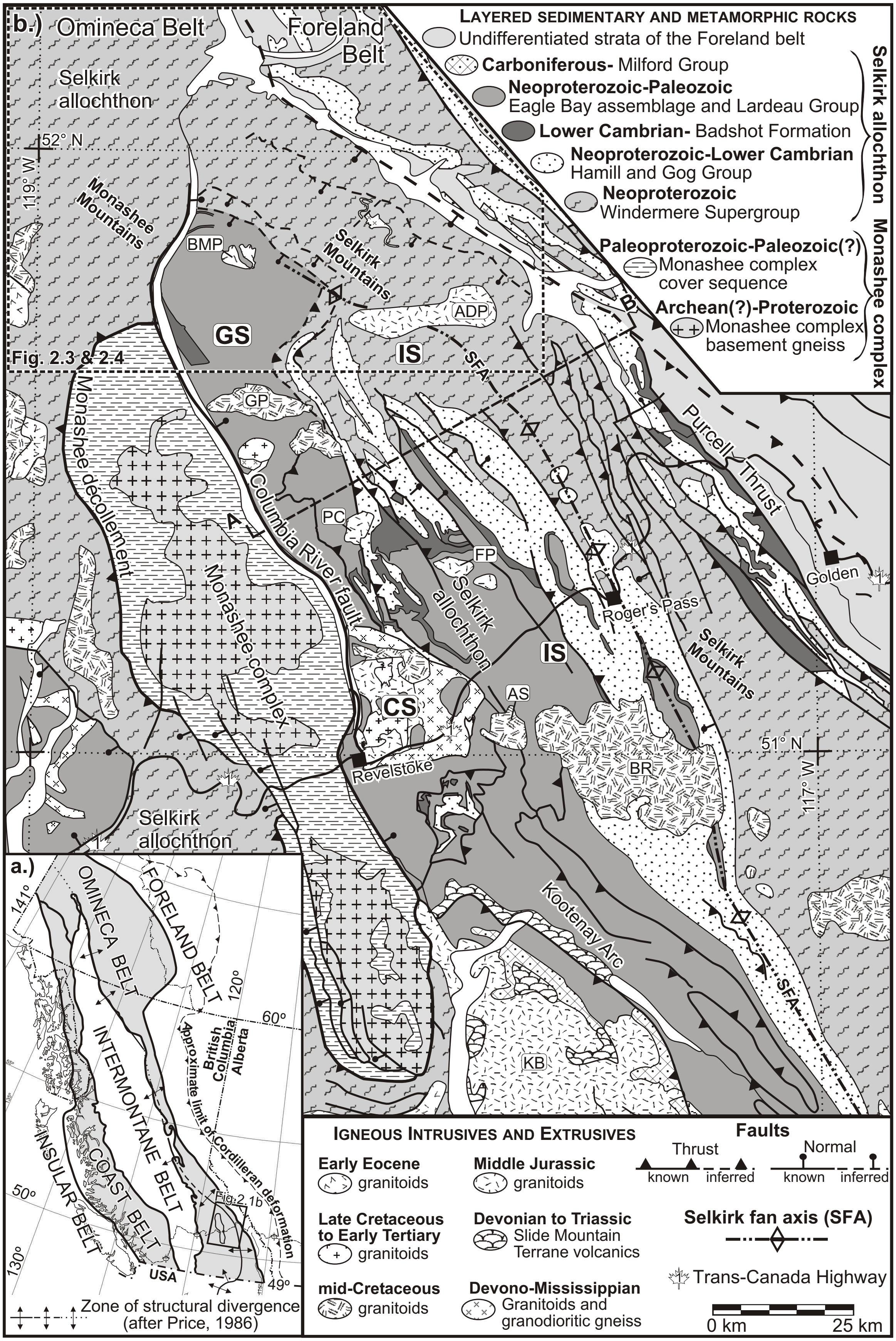
b.)
Omineca Belt
Foreland Belt
Selkirk allochthon
52° N
119° W
Monashee Mountains
Selkirk Mountains
BMP
GS
ADP
IS
SFA
Fig. 2.3 & 2.4
GP
Monashee decollement
Columbia River fault
Monashee complex
A
PC
FP
Selkirk allochthon
Roger's Pass
Golden
Purcell Thrust
B
CS
AS
Revelstoke
BR
51° N
117° W
Selkirk allochthon
Kootenay Arc
KB
LAYERED SEDIMENTARY AND METAMORPHIC ROCKS
Undifferentiated strata of the Foreland belt
Carboniferous- Milford Group
Neoproterozoic-Paleozoic
Eagle Bay assemblage and Lardeau Group
Lower Cambrian- Badshot Formation
Neoproterozoic-Lower Cambrian
Hamill and Gog Group
Neoproterozoic
Windermere Supergroup
Selkirk allochthon
Paleoproterozoic-Paleozoic(?)
Monashee complex cover sequence
Archean(?)-Proterozoic
Monashee complex basement gneiss
Monashee complex
a.)
141°
OMINECA BELT
FORELAND BELT
120°
60°
British Columbia
Alberta
Approximate limit of Cordilleran deformation
INTERMONTANE BELT
COAST BELT
INSULAR BELT
50°
130°
Fig. 2.1b
USA
49°
Zone of structural divergence (after Price, 1986)
IGNEOUS INTRUSIVES AND EXTRUSIVES
Early Eocene granitoids
Middle Jurassic granitoids
Late Cretaceous to Early Tertiary granitoids
Devonian to Triassic Slide Mountain Terrane volcanics
mid-Cretaceous granitoids
Devono-Mississippian Granitoids and granodioritic gneiss
Faults
Thrust
Normal
known
inferred
known
inferred
Selkirk fan axis (SFA)
Trans-Canada Highway
0 km
25 km

Figure 2.1.

Figure 2.2. Two principal tectonic models for the formation of the Selkirk fan.

a.) **Fan Formation Above Subduction Zone**

b.) **Fan Formation Resulting from Tectonic Wedging**

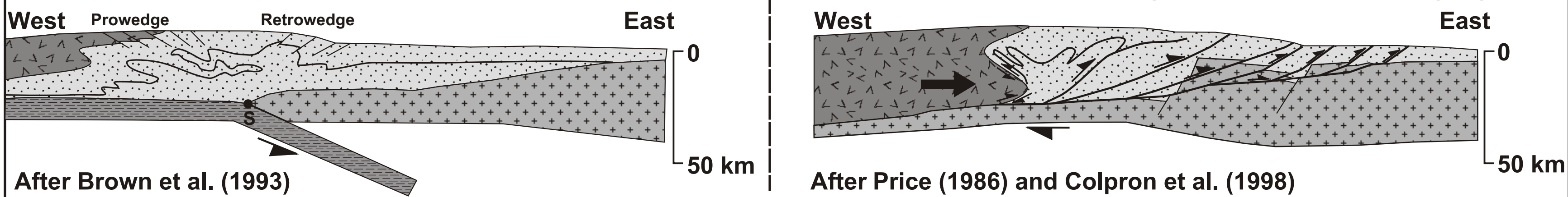

After Brown et al. (1993)

After Price (1986) and Colpron et al. (1998)

Early to Middle Jurassic accretion and obduction of Intermontane Superterrane

Singularity (S) represents point of detachment and underthrusting of oceanic or marginal basin lithosphere beneath continental lithosphere

Middle Jurassic development of southwest verging folds and faults in prowedge, northeast verging structures in retrowedge above singularity

Fan becomes detached and is carried along basal thrust toward foreland

Accreted terranes

Oceanic lithosphere

North American sediments

North American crust

Early to Middle Jurassic accretion and obduction of Intermontane Superterrane

Middle Jurassic tectonic wedging of allochthonous terrane between the North American basement and the overlying miogeoclinal cover resulted in backfolding and thrusting of cover rocks toward the southwest

A basement ramp inherited from Late Proterozoic rifting impeded the eastward propagating front of southwest verging structures above the wedge in the Middle Jurassic

In the Late Jurassic the wedge overrode and cannibalized the ramp after attaining sufficient gravitational potential, resulting in the eastward propagation of northeastward verging deformation into the foreland

Figure 2.2.

Figure 2.3. Generalized geologic map of the northern Selkirk Mountains illustrating lithostratigraphy, regional metamorphic isograds, and major structures. Compiled from mapping by Brown (1991), Brown and Tippett (1978), Colpron et al. (1995), Leatherbarrow (1981), Marchildon (1999), Perkins (1983), Poulton and Simony, (1980), Raeside and Simony (1983), Scammell (1993), Simony et al. (1980), and Wheeler (1965). Geochronologic sample locations within the studied area have also been included. Abbreviations: ADP = Adamant pluton; ADM = Adamant Mountain; AM = Argonaut Mountain; AP = Argonaut Pass; BMP = Bigmouth pluton; BCF = Birch Creek fault; BMF = Bigmouth fault; CRF = Columbia River fault; FG = French glacier; MC = Mica Creek village; MD = Monashee décollement; MN = Mount Nagle; MSF = Mount Sir Sanford; NEF = Northeastern fault; RP = Remillard Peak; TM = Trident Mountain. Abbreviations for metamorphic zones (e.g., Chl, Bt, Grt) based on mineral abbreviations after Kretz (1983).

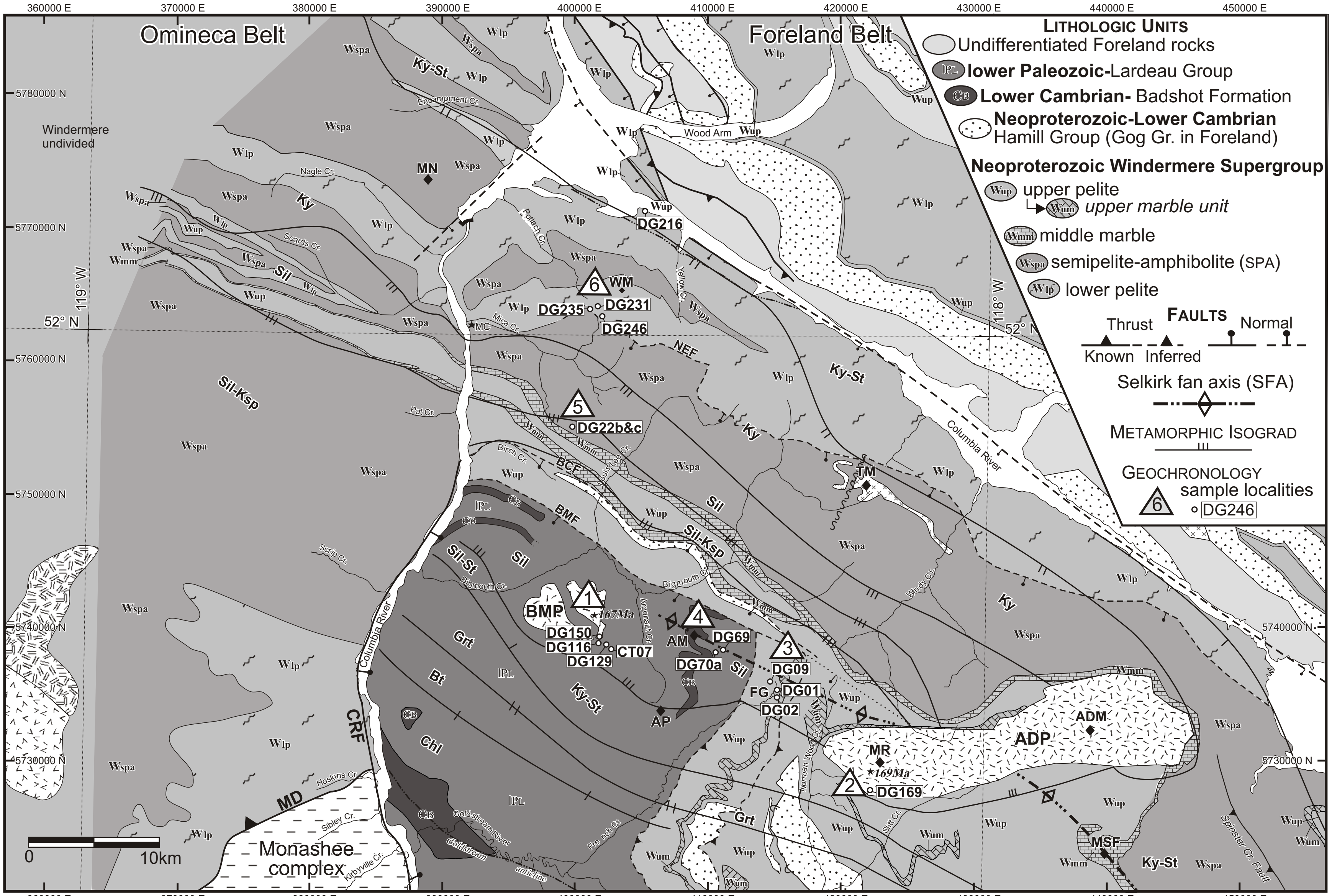

Omineca Belt
Foreland Belt
LITHOLOGIC UNITS
Undifferentiated Foreland rocks
lower Paleozoic-Lardeau Group
Lower Cambrian- Badshot Formation
Neoproterozoic-Lower Cambrian
Hamill Group (Gog Gr. in Foreland)
Neoproterozoic Windermere Supergroup
upper pelite
upper marble unit
middle marble
semipelite-amphibolite (SPA)
lower pelite
FAULTS
Thrust
Normal
Known
Inferred
Selkirk fan axis (SFA)
METAMORPHIC ISOGRAD
GEOCHRONOLOGY
sample localities
DG246
Windermere
undivided
360000 E
370000 E
380000 E
390000 E
400000 E
410000 E
420000 E
430000 E
440000 E
450000 E
5780000 N
5770000 N
5760000 N
5750000 N
5740000 N
5730000 N
52° N
119° W
118° W
MN
WM
TM
BMP
ADP
ADM
MR
AM
AP
FG
MSF
NEF
BCF
BMF
CRF
MD
DG216
DG235
DG231
DG246
DG22b&c
DG150
DG116
DG129
CT07
DG69
DG70a
DG09
DG01
DG02
DG169
167Ma
169Ma
Ky-St
Ky
Sil
Sil-Ksp
Sil-St
Grt
Bt
Chl
Wood Arm
Columbia River
Monashee
complex
0
10km

Figure 2.3.

Figure 2.4. Generalized structure map for the northern Selkirk and Monashee Mountains showing the axial surface traces of F_1, F_2, and F_3. Compiled from Brown and Tippett (1978), Colpron et al. (1995), Perkins (1983), and Simony et al. (1980). A-A', B-B', C-C', D-D', and E-E' represent the lines of cross sections drawn in Figs. 2.8 and 2.11.

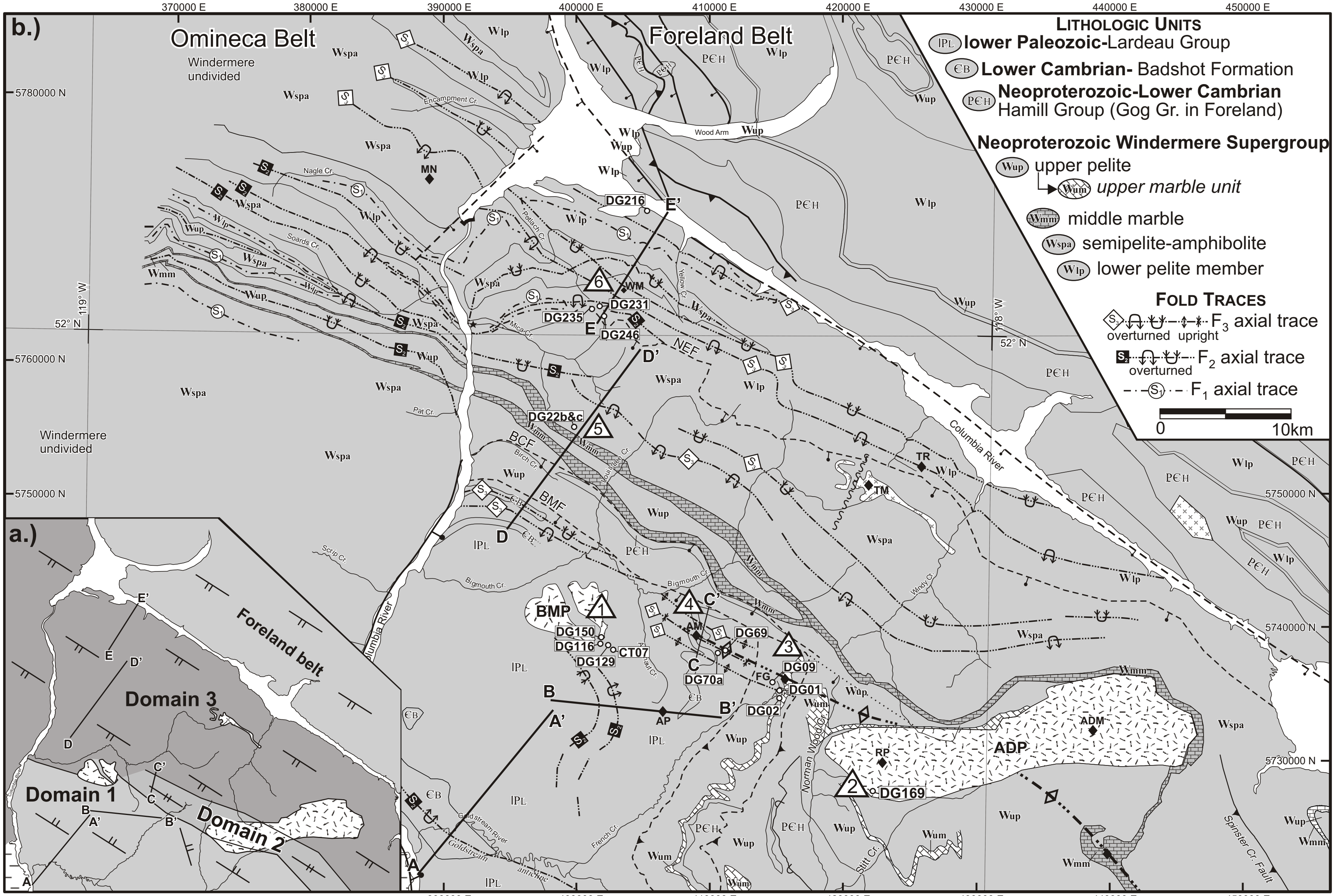

b.)
Omineca Belt
Foreland Belt
Windermere undivided
LITHOLOGIC UNITS
lPL lower Paleozoic-Lardeau Group
€B Lower Cambrian- Badshot Formation
P€H Neoproterozoic-Lower Cambrian
Hamill Group (Gog Gr. in Foreland)
Neoproterozoic Windermere Supergroup
Wup upper pelite
Wum upper marble unit
Wmm middle marble
Wspa semipelite-amphibolite
Wlp lower pelite member
FOLD TRACES
F3 axial trace
overturned
upright
F2 axial trace
overturned
F1 axial trace
0
10km
370000 E
380000 E
390000 E
400000 E
410000 E
420000 E
430000 E
440000 E
450000 E
5780000 N
5760000 N
5750000 N
5740000 N
5730000 N
52° N
119° W
118° W
Columbia River
Wood Arm
Goldstream River
Goldstream anticline
Norman Wood Cr.
Stitt Cr.
Spinster Cr. Fault
BMP
ADP
BCF
BMF
NEF
DG216
DG231
DG235
DG246
DG22b&c
DG150
DG116
DG129
CT07
DG69
DG70a
DG09
DG01
DG02
DG169
MN
TR
TM
AM
FG
AP
RP
ADM
WM
a.)
Domain 1
Domain 2
Domain 3
Foreland belt

Figure 2.4.

Figure 2.5. (a) Polydeformed marble at Argonaut Mountain with three generations of superposed folds, F_1, F_2, and F_3. (b) Line drawing superimposed on the photo to help illustrate the interference geometry of the superposed folding. The drawing is modified after an original field sketch by Paul Williams in the summer of 1998, and is featured on the cover of the 1998 GAC-NUNA Research Conference Abstract Volume.

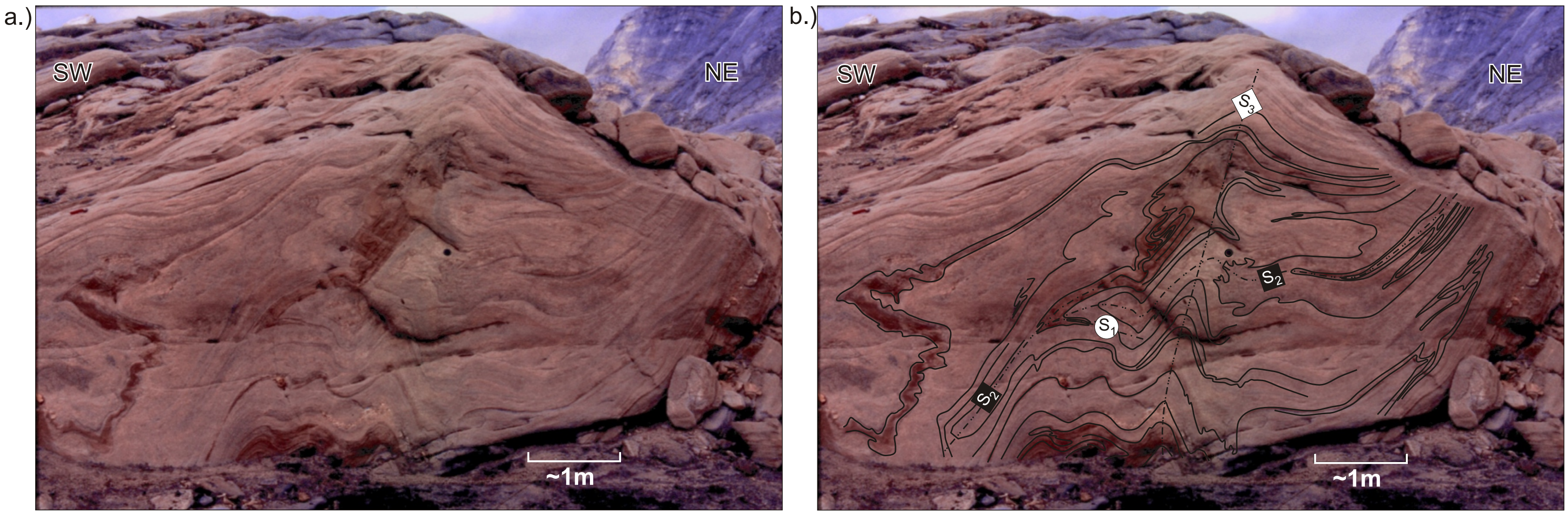

Figure 2.5.

Figure 2.6. Generalized cross section of the Selkirk fan for section line A-B of Fig. 2.1 (modified after Brown et al., 1993). CRF = Columbia River fault; MD = Monashee décollement; PT = Purcell thrust.

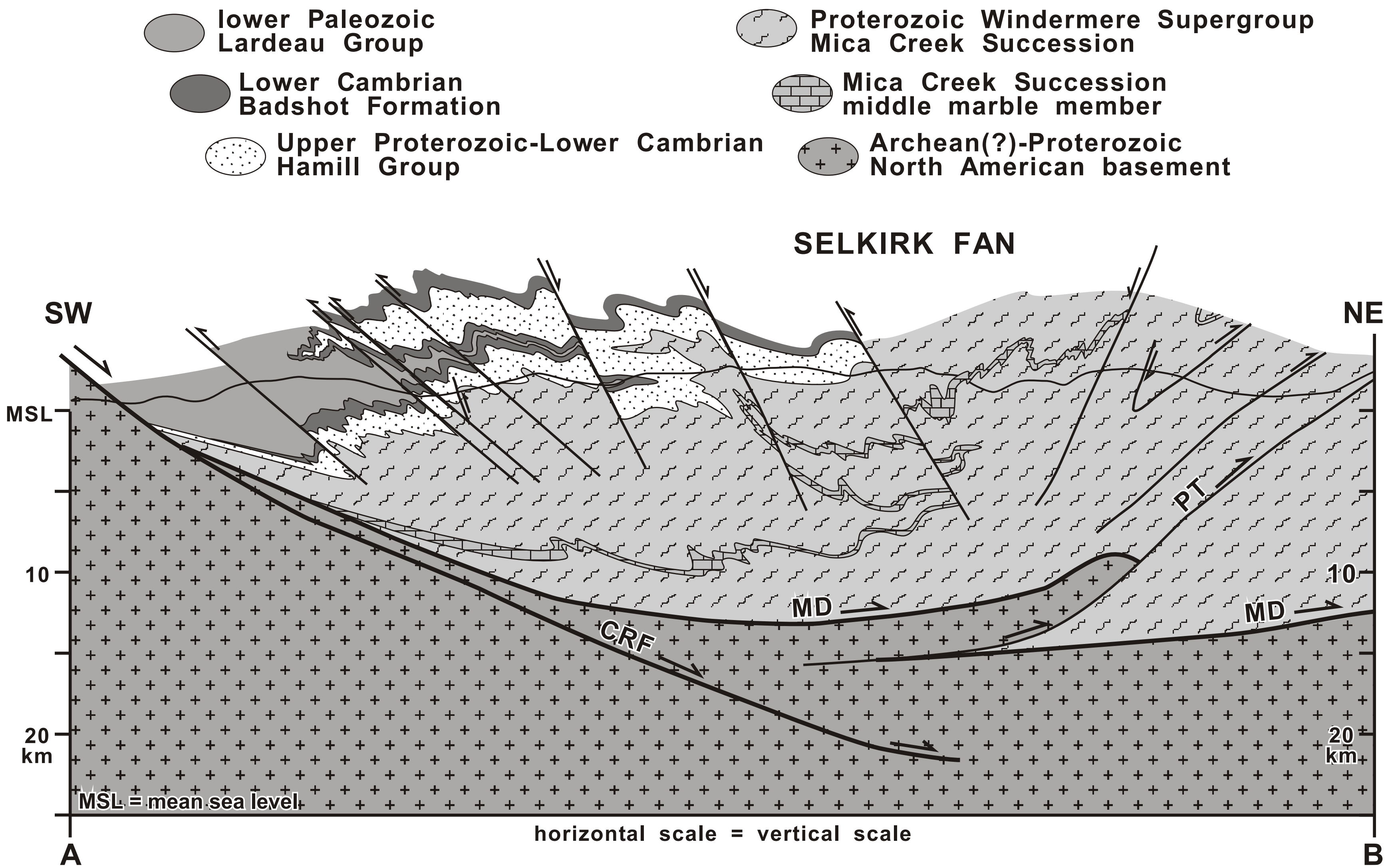

lower Paleozoic
Lardeau Group
Lower Cambrian
Badshot Formation
Upper Proterozoic-Lower Cambrian
Hamill Group
Proterozoic Windermere Supergroup
Mica Creek Succession
Mica Creek Succession
middle marble member
Archean(?)-Proterozoic
North American basement
SELKIRK FAN
SW
NE
MSL
10
20
km
PT
MD
MD
CRF
10
20
km
MSL = mean sea level
horizontal scale = vertical scale
A
B

Figure 2.6

Figure 2.7. (a) Photomicrograph of a St-Grt-Bt-Ms pelitic schist (DG216) from the east flank of the fan in the vicinity of Red Rock Harbour. This example illustrates the relationship between the metamorphic mineral assemblage and polyphase deformation (i.e., S_2 and S_3) commonly observed throughout most of the northern Selkirk Mountains. In (b) and (d) S_2 is preserved as Qtz inclusion trails (S_i), which was overgrown by anhedral M_1 garnet and staurolite cores. The external foliation, S_e, continued to develop following initial garnet and staurolite growth, and occurs at a high angle to S_i. S_e is thought to be a composite foliation, such that recrystallization and reactivation responsible for its development occurred progressively or episodically over an extended period of time. The data suggest that the original S_i fabric within the anhedral cores may actually be Middle Jurassic, whereas S_e continued to develop, at least in part, during the Cretaceous (see Discussion section in text). In (b), the anhedral M_1 cores are overgrown by uniform, inclusion-free, euhedral rims, M_2, that appear to truncate most of the S_e foliation which has been crenulated by F_3, suggesting that some of the staurolite recrystallization occurred during or after D_3. However, the deflection of Bt and Ms around the staurolite at the bottom of (b) near the scale bar, as well as around euhedral M_2 staurolite (c) and M_2 garnet (e) suggests D_3 continued to develop following the peak of M_2.

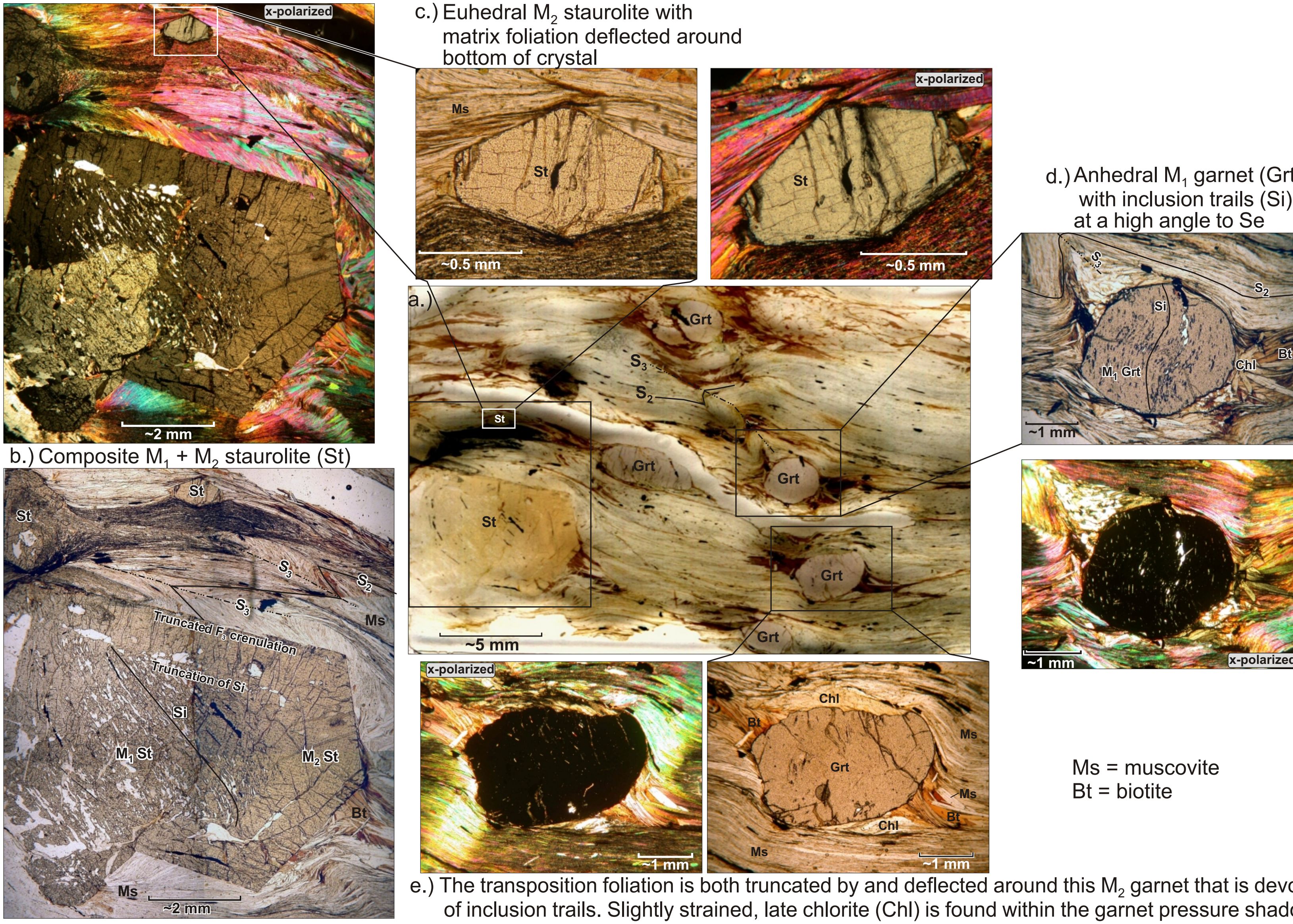

b.) Composite M_1 + M_2 staurolite (St)

c.) Euhedral M_2 staurolite with matrix foliation deflected around bottom of crystal

d.) Anhedral M_1 garnet (Grt) with inclusion trails (Si) at a high angle to Se

e.) The transposition foliation is both truncated by and deflected around this M_2 garnet that is devoid of inclusion trails. Slightly strained, late chlorite (Chl) is found within the garnet pressure shadows.

Ms = muscovite
Bt = biotite

Figure 2.7.

Figure 2.8. Composite structural cross section that transects the studied area, illustrating the geometry of the fan modified after Brown and Tippett (1978), Colpron et al. (1995), Perkins (1983), and Simony et al. (1980). Section lines are located in Fig. 2.4. Geochronology sample locations have been projected along strike into the line of section.

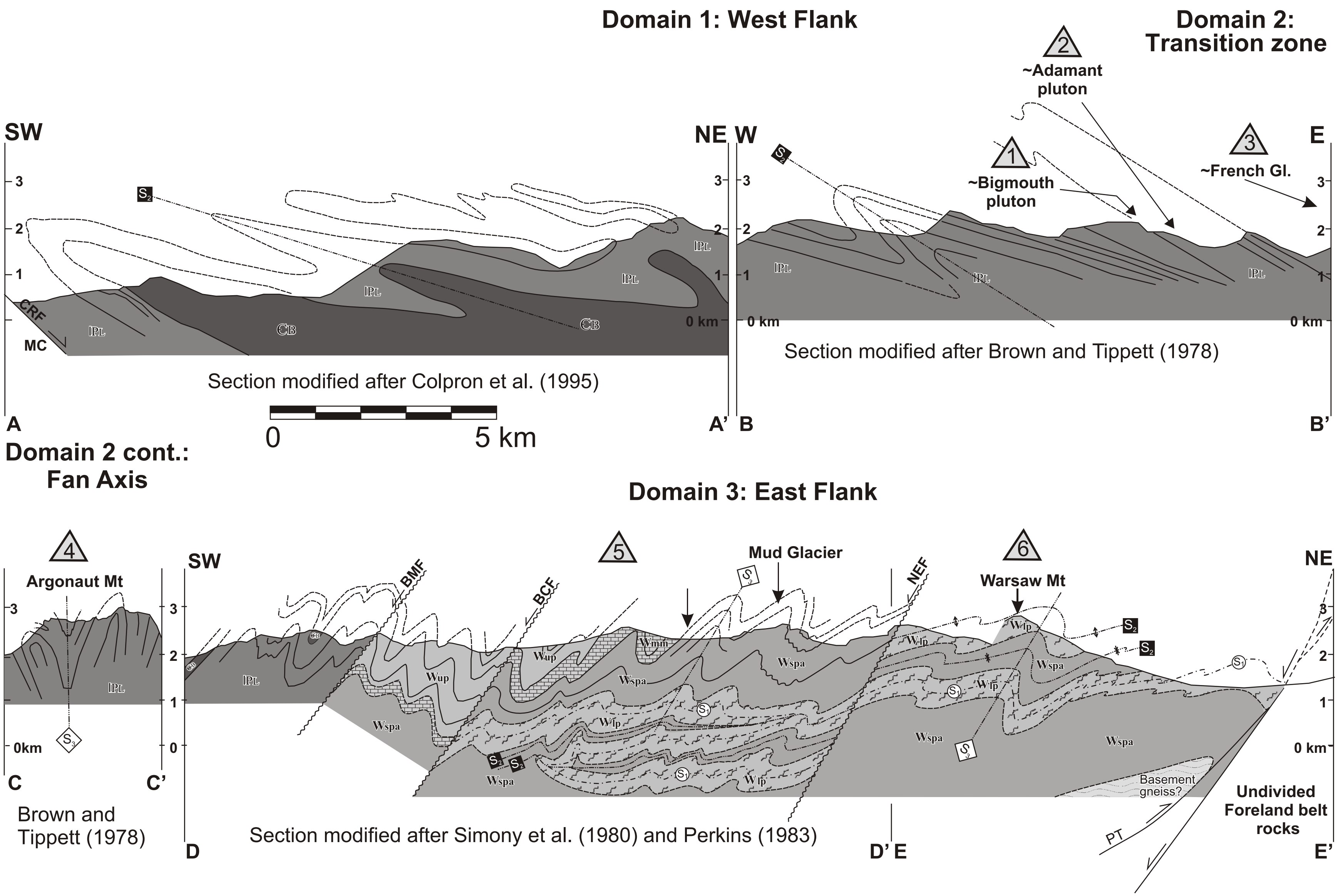
Domain 1: West Flank
Domain 2:
Transition zone
2
~Adamant
pluton
SW
NE
W
E
1
~Bigmouth
pluton
3
~French Gl.
S2
IPL
CB
CRF
MC
0 km
Section modified after Colpron et al. (1995)
Section modified after Brown and Tippett (1978)
A
A'
B
B'
0
5 km
Domain 2 cont.:
Fan Axis
Domain 3: East Flank
4
Argonaut Mt
0km
C
C'
Brown and
Tippett (1978)
5
Mud Glacier
6
Warsaw Mt
BMF
BCF
NEF
Wup
Wmm
Wspa
Wlp
S1
S2
S3
Basement
gneiss?
Undivided
Foreland belt
rocks
PT
Section modified after Simony et al. (1980) and Perkins (1983)
D
D'
E
E'

Figure 2.8.

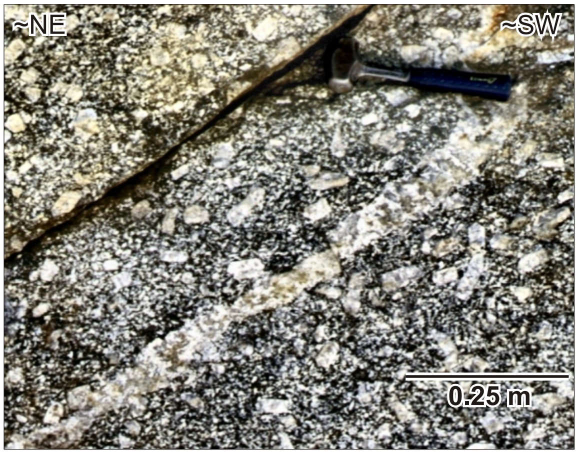

a.) DG150 - coarse-grained Hbl-Bt-Qtz monzonite of the ca. 172-164 Ma Bigmouth pluton (BMP)

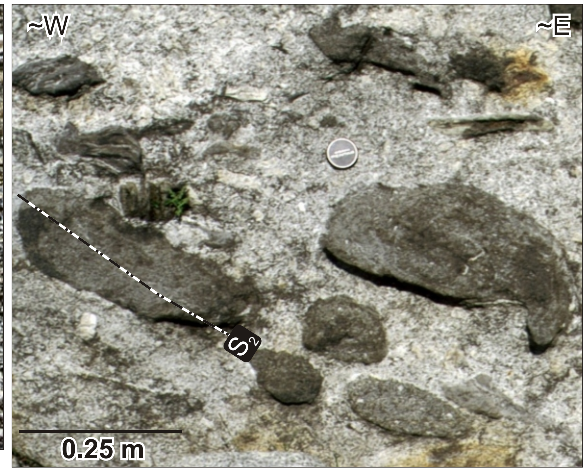

b.) DG150 (BMP) - foliated (S_2) xenoliths of host rock within BMP suggest emplacement post-dated most of the major S_2 transposition forming event

c.) CT07 - F_2 pegmatite; rootless fold hinges and sheared out limbs suggest this pegmatite is older than F_2

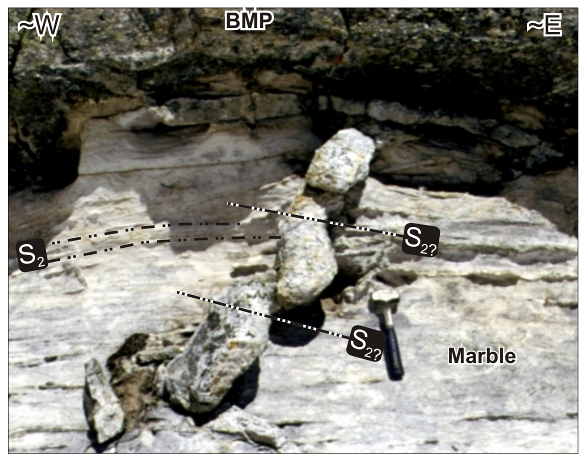

d.) DG116 - Late $F_{2?}$ pegmatite at contact between marble and BMP

e.) DG129 - highly discordant medium-grained, undeformed pegmatite in contact with a folded calc-silicate

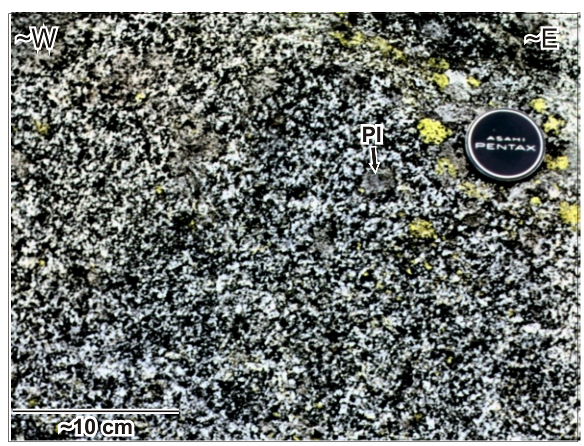

f.) DG169 - Bt-Hbl Qtz-monzonite of the ca. 170 - 166 Ma Adamant pluton

Figure 2.9a-f.

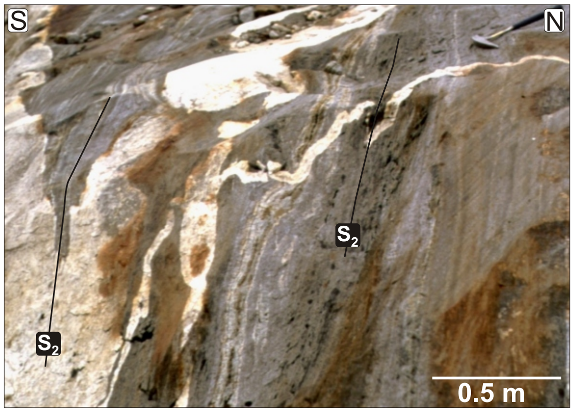

g.) DG09 - strained pegmatite with folded (F_2) and boudinaged veinlets

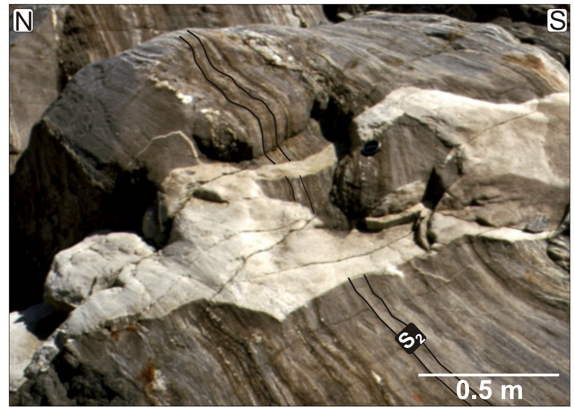

h.) DG02 - crosscutting, undeformed granodiorite; contains xenolith of transposed (S_2) host pelitic schist

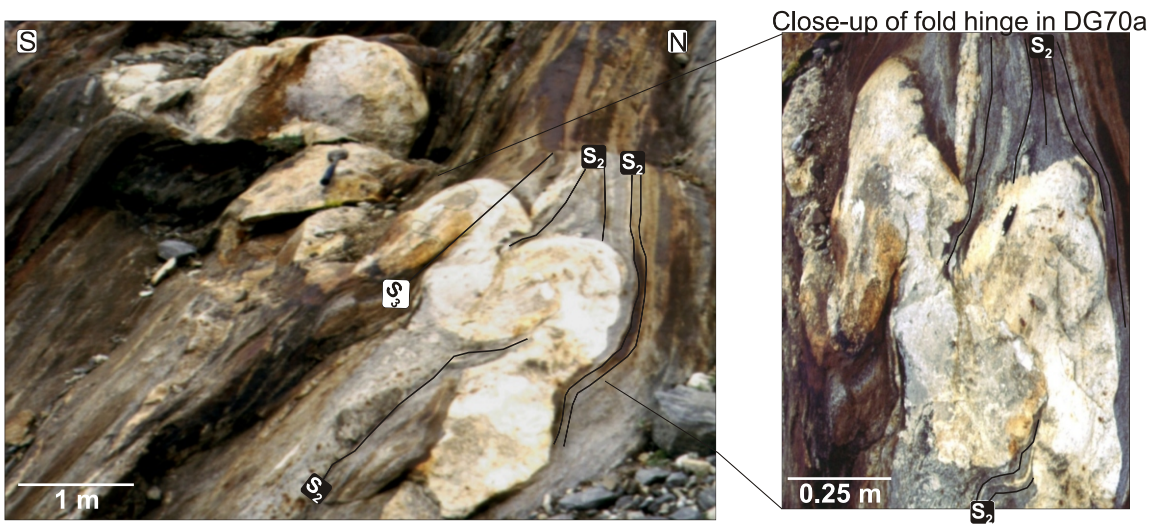

i.) DG70a - deformed pegmatite; axial planes (S_3) of folded pegmatite (F_3) are oblique to the transposition foliation (S_2) in the host pelitic schist; S_2 is truncated at the dike margins and is deflected into the fold hinges and into the boudin necks of the pegmatite; intrusion of this ca. 104 Ma pegmatite is thus interpreted to have occurred during D_3

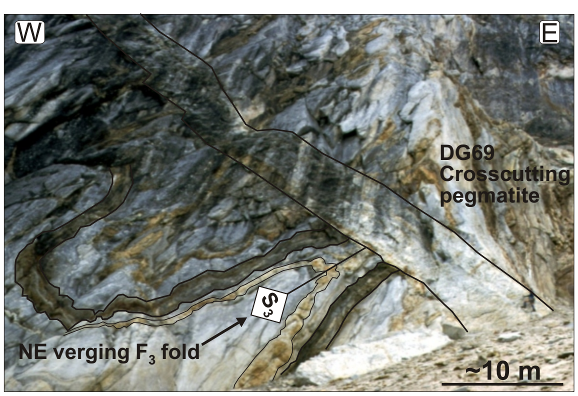

j.) DG69 - undeformed pegmatite cuts across both limbs of a large F_3 fold

k.) DG69 - close-up of undeformed pegmatite; contains xenoliths of foliated (S_2) country rock

Figure 2.9g-k.

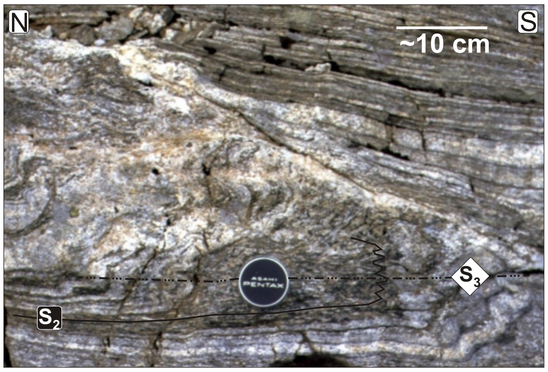

l.) DG22c - folded (F_3) leucosome within sillimanite pelitic schist; peak metamorphic minerals within S_2 (e.g. Bt, Sil) have been folded and crenulated

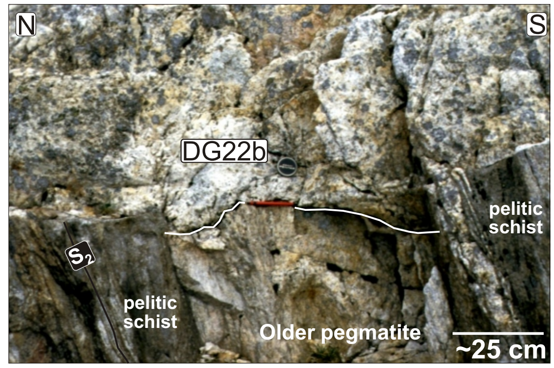

m.) DG22b - undeformed pegmatite crosscuts older, deformed pegmatite (below) that is concordant with S_2 foliation; the red pencil is aligned parallel to the contact between the two pegmatites

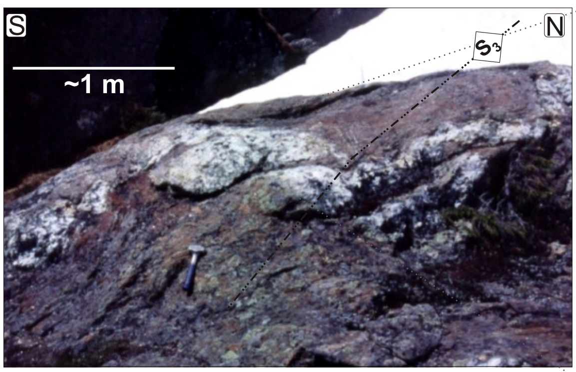

n.) DG246 - folded (F_3) pegmatite; S_2 is discordant to the dike margins and folded within the F_3 hinges

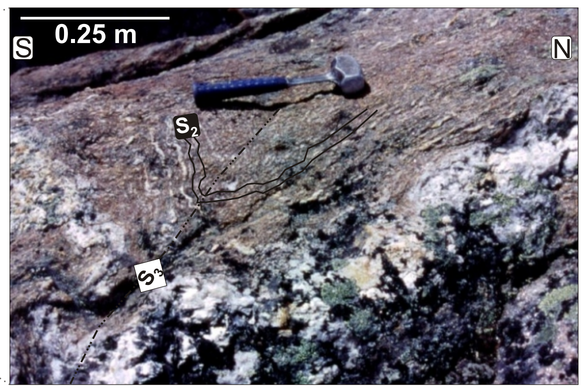

o.) DG246 - close-up view of a fold hinge (F_3) in which S_2 is folded

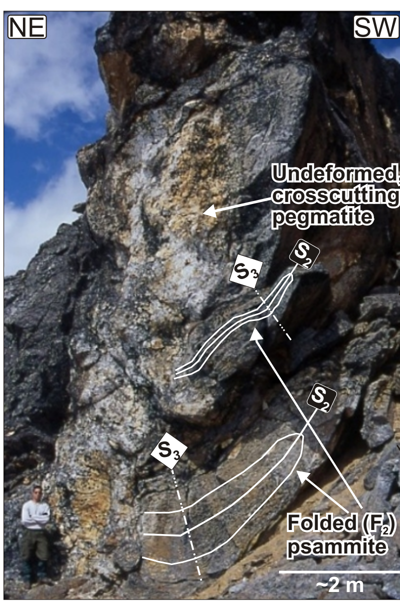

p.) DG231 - undeformed pegmatite that crosscuts both limbs of a refolded F_2 fold

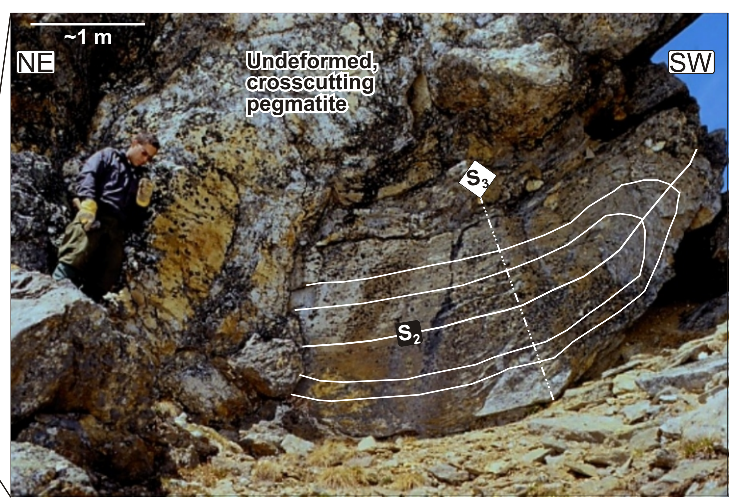

q.) DG231 - close-up of crosscutting relationship between DG231 and the polydeformed psammite

Figure 2.9l-q.

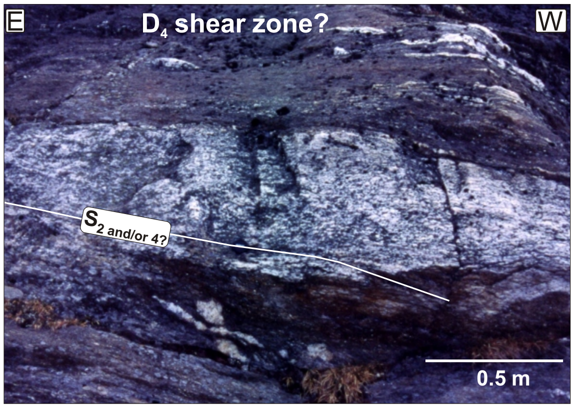

r.) DG235 - foliated (S_2 and/or S_4) Qtz-rich granitoid, within highly sheared Ky-pelitic schist

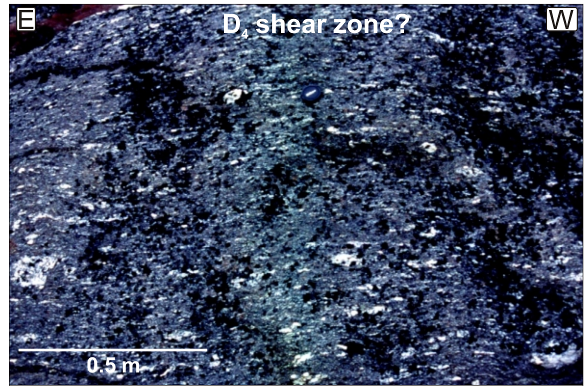

s.) DG235 - host Ky-schist which was severely strained, as seen by the extreme dismemberment of *in situ* leucosome

Figure 2.9r-s.

Figure 2.10a-b. U-Pb concordia diagrams for samples DG150 and CT07 that include IDTIMS and SHRIMP data with BSE and CL images of zircon, and spot locations for SHRIMP analyses.

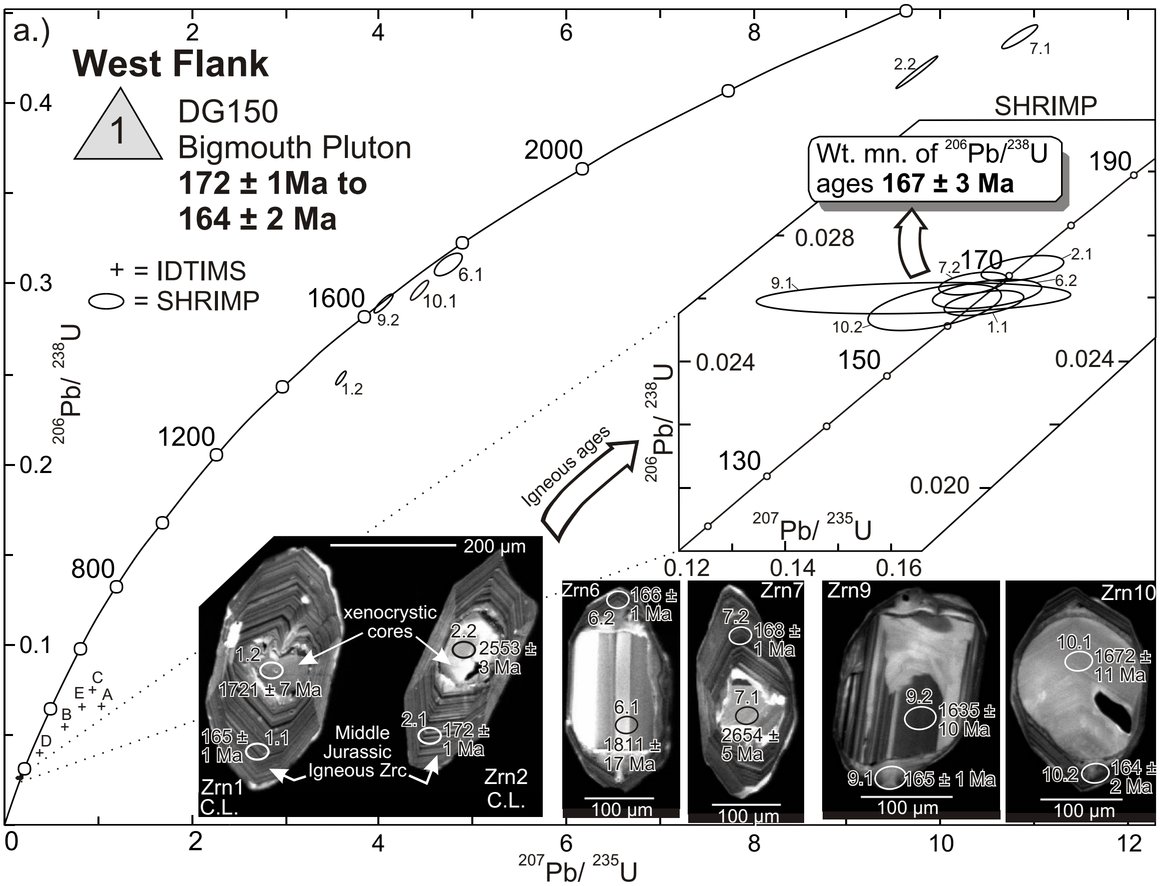

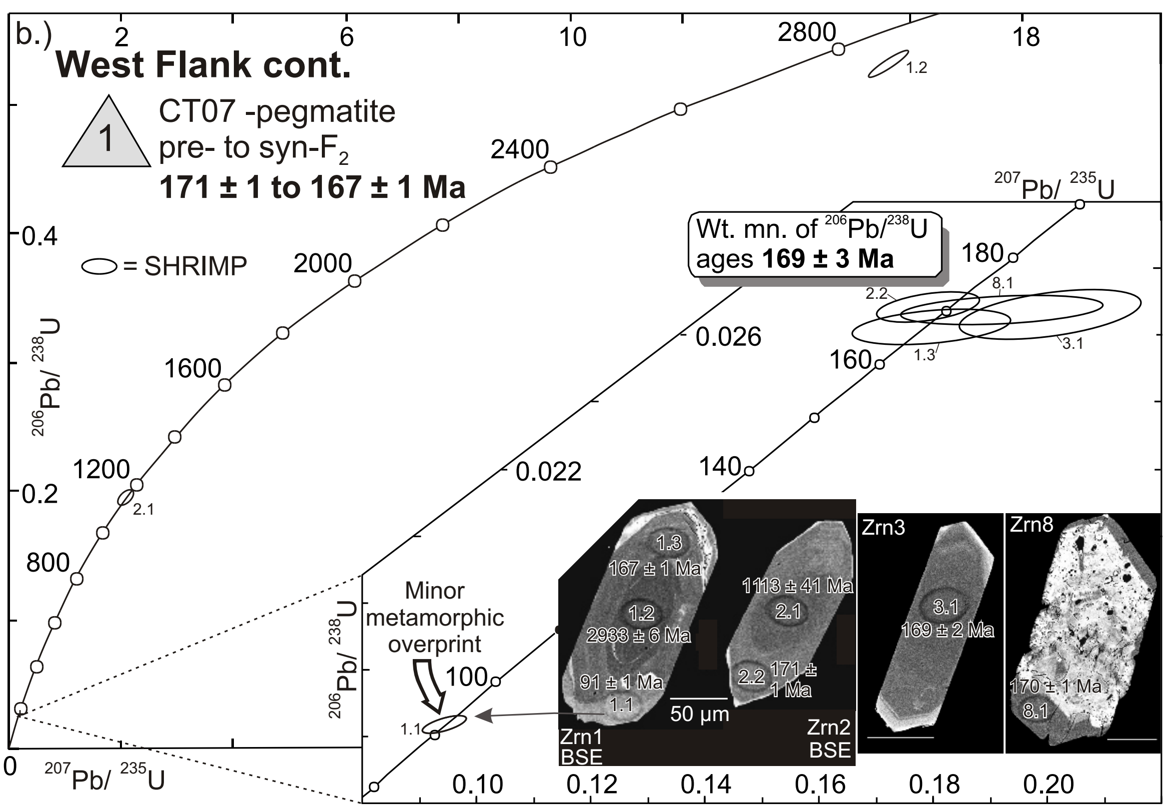

Figure 2.10a-b.

Figure 2.10c-e. U-Pb concordia diagrams for samples DG116, DG129 and DG169 that include IDTIMS and SHRIMP data with BSE and CL images of zircon, and spot locations for SHRIMP analyses.

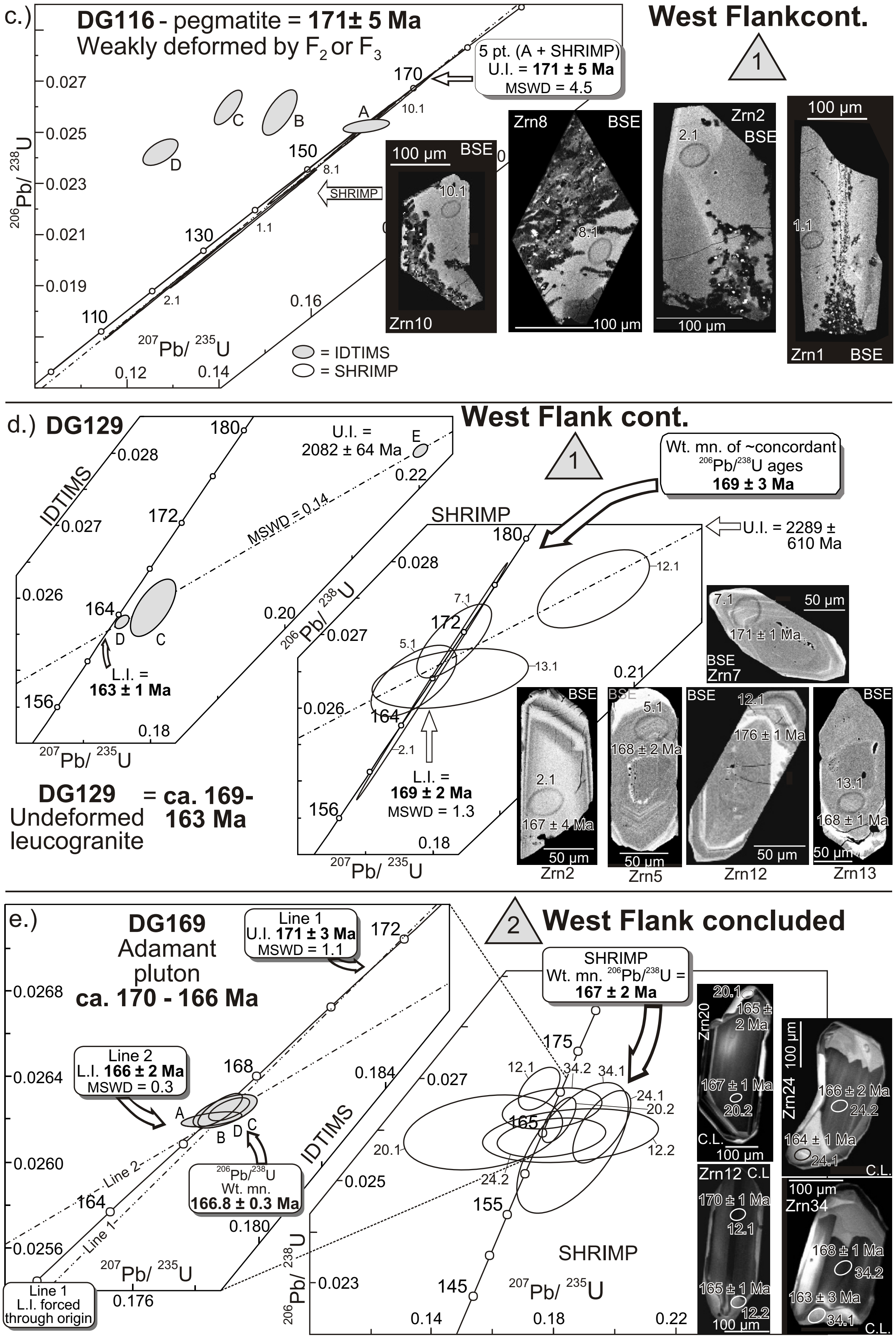

Figure 2.10c-e.

Figure 2.10f-g. U-Pb and U-Th-Pb concordia diagrams for samples DG09 and DG70a that include IDTIMS and SHRIMP data with BSE and chemical map images, and spot locations for SHRIMP analyses when applicable.

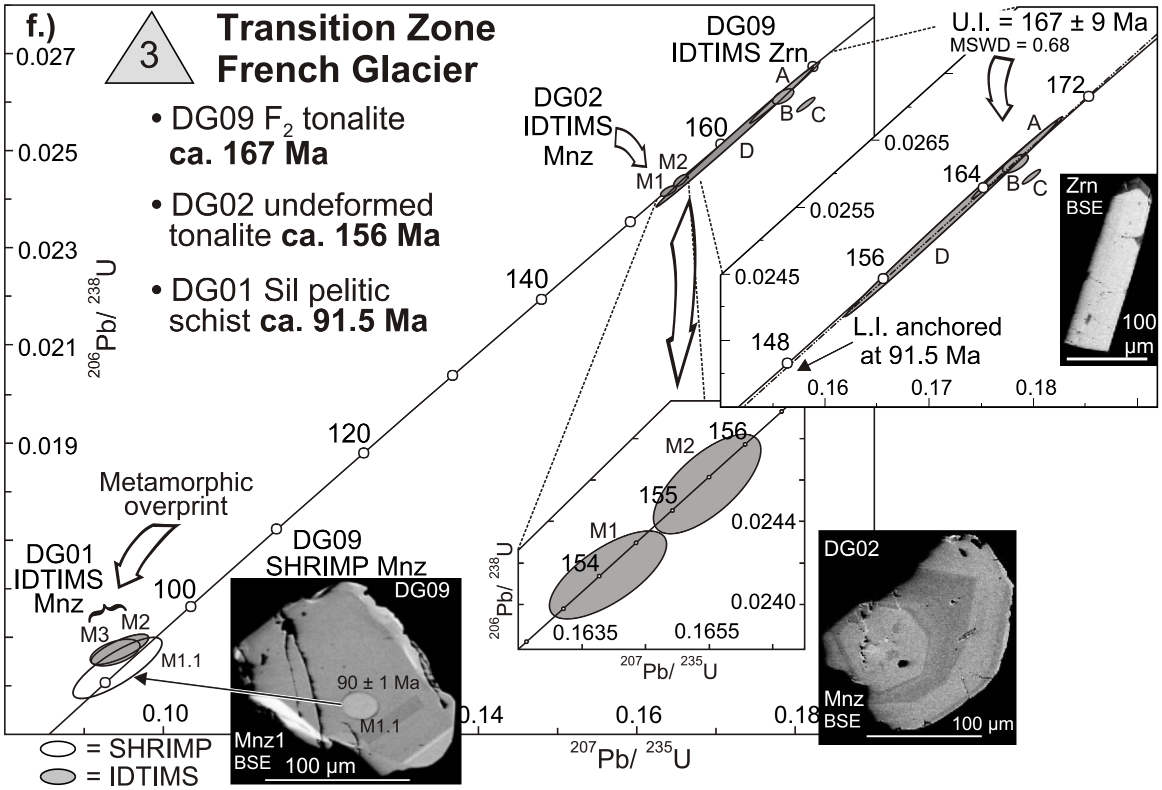

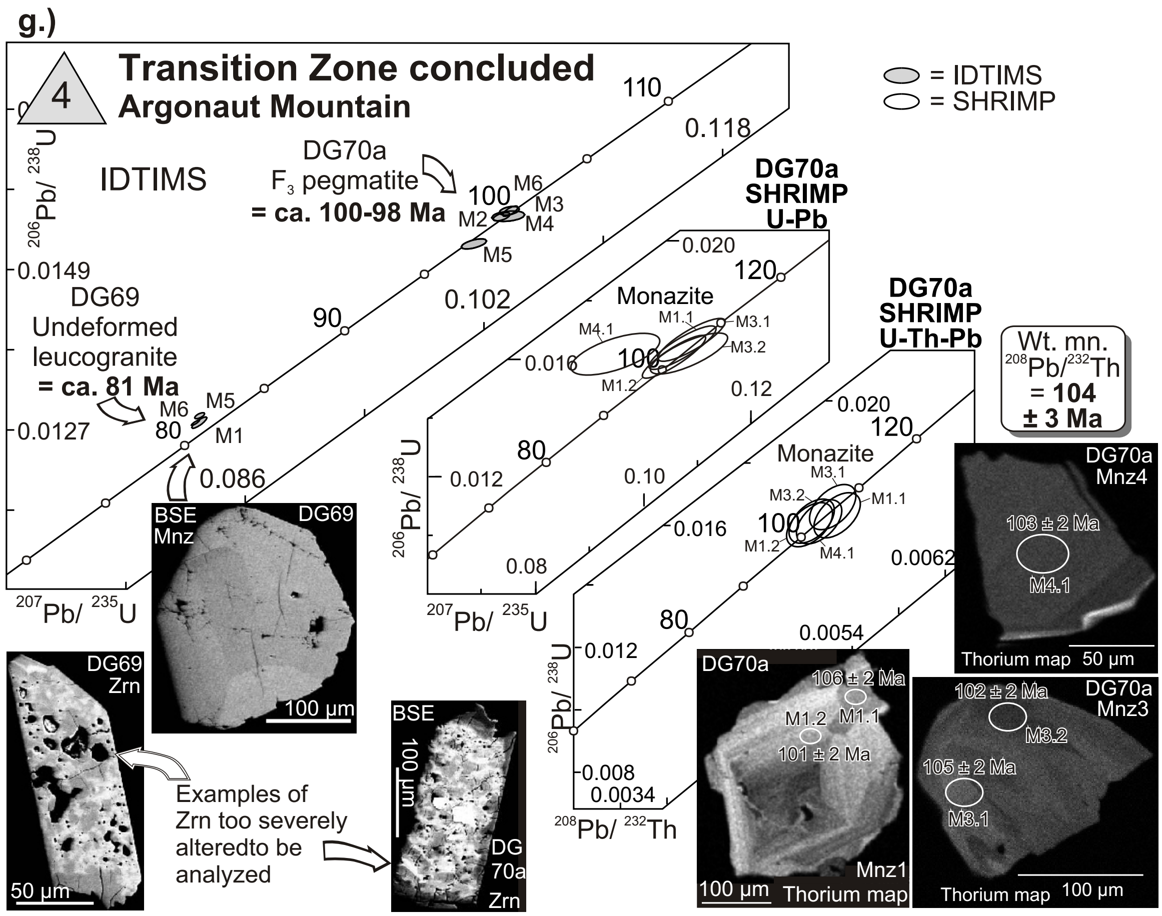

Figure 2.10f-g.

Figure 2.10h-i. U-Pb and U-Th-Pb concordia diagrams for samples DG22c and DG22b that include IDTIMS and SHRIMP data with BSE and chemical map images, and spot locations for SHRIMP analyses when applicable.

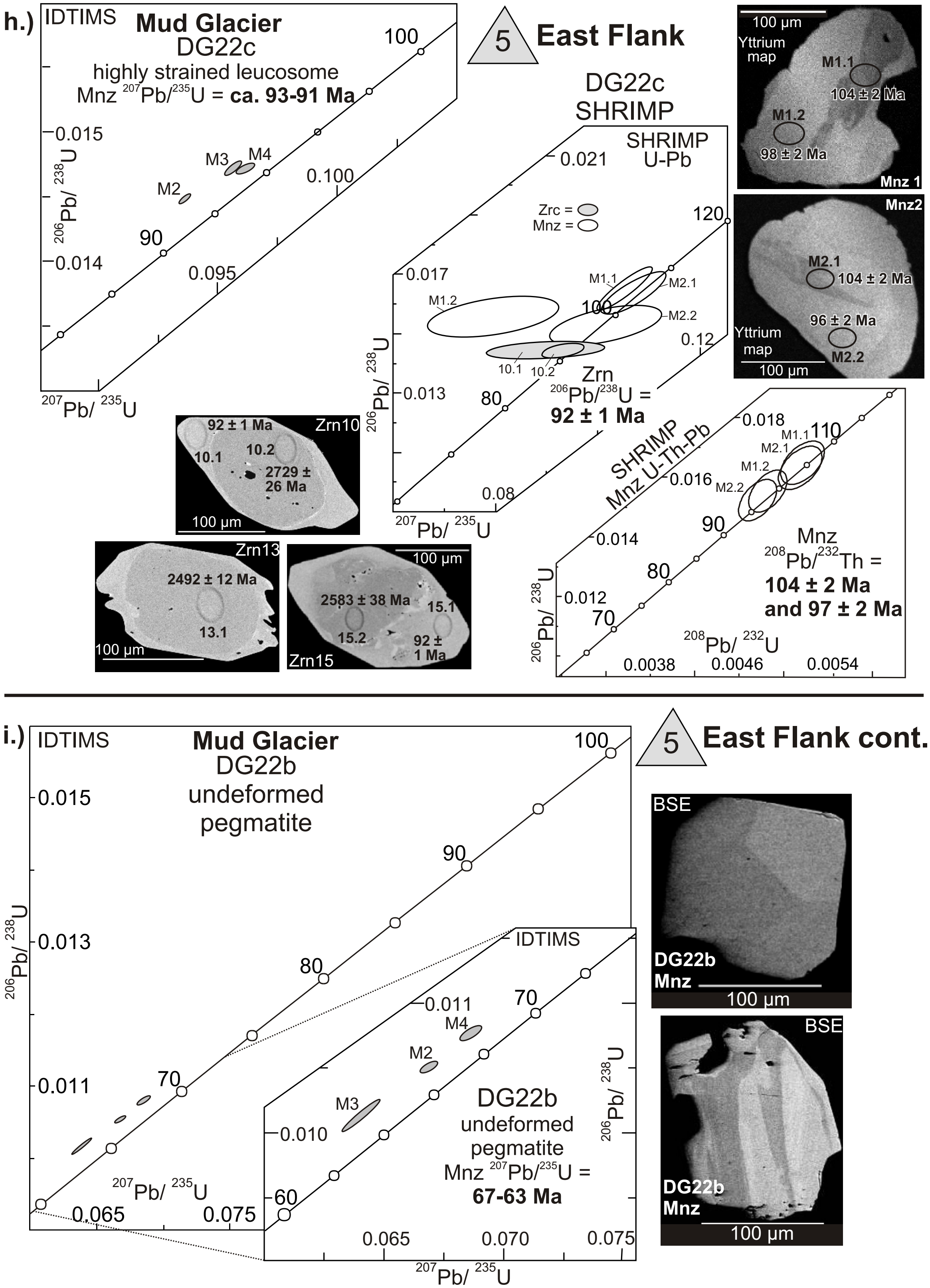

Figure 2.10h-i.

Figure 2.10j. U-Pb and U-Th-Pb concordia diagrams for samples DG246 that include IDTIMS and SHRIMP data with BSE, CL, and chemical map images and spot locations for SHRIMP analyses.

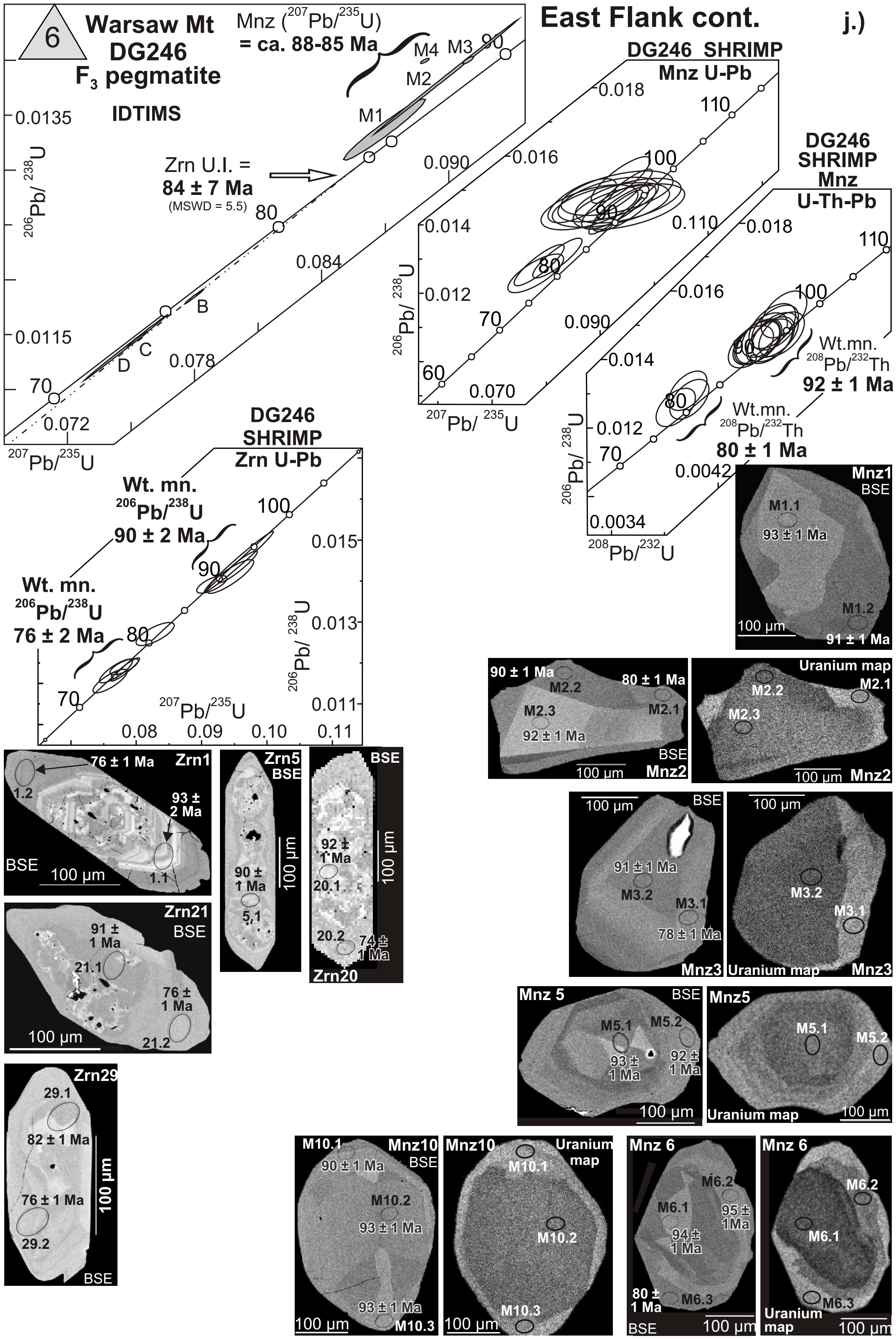
East Flank cont.
j.)
6
Warsaw Mt
DG246
F3 pegmatite
IDTIMS
Mnz (207Pb/235U)
= ca. 88-85 Ma
M4 M3
M2
M1
Zrn U.I. =
84 ± 7 Ma
(MSWD = 5.5)
206Pb/238U
207Pb/235U
DG246 SHRIMP
Mnz U-Pb
DG246
SHRIMP
Mnz
U-Th-Pb
Wt.mn.
208Pb/232Th
92 ± 1 Ma
Wt.mn.
208Pb/232Th
80 ± 1 Ma
208Pb/232U
DG246
SHRIMP
Zrn U-Pb
Wt. mn.
206Pb/238U
90 ± 2 Ma
Wt. mn.
206Pb/238U
76 ± 2 Ma
Mnz1
BSE
93 ± 1 Ma
91 ± 1 Ma
100 µm
Mnz2
Uranium map
90 ± 1 Ma
80 ± 1 Ma
92 ± 1 Ma
Mnz3
91 ± 1 Ma
78 ± 1 Ma
Mnz 5
93 ± 1 Ma
92 ± 1 Ma
Zrn1
76 ± 1 Ma
93 ± 2 Ma
Zrn5
90 ± 1 Ma
Zrn20
92 ± 1 Ma
74 ± 1 Ma
Zrn21
91 ± 1 Ma
76 ± 1 Ma
Zrn29
82 ± 1 Ma
76 ± 1 Ma
Mnz10
90 ± 1 Ma
93 ± 1 Ma
93 ± 1 Ma
Mnz 6
95 ± 1 Ma
94 ± 1 Ma
80 ± 1 Ma

Figure 2.10j.

Figure 2.10k-l. U-Pb concordia diagrams for samples DG231 and DG235 that include IDTIMS data with BSE images of monazites from those samples.

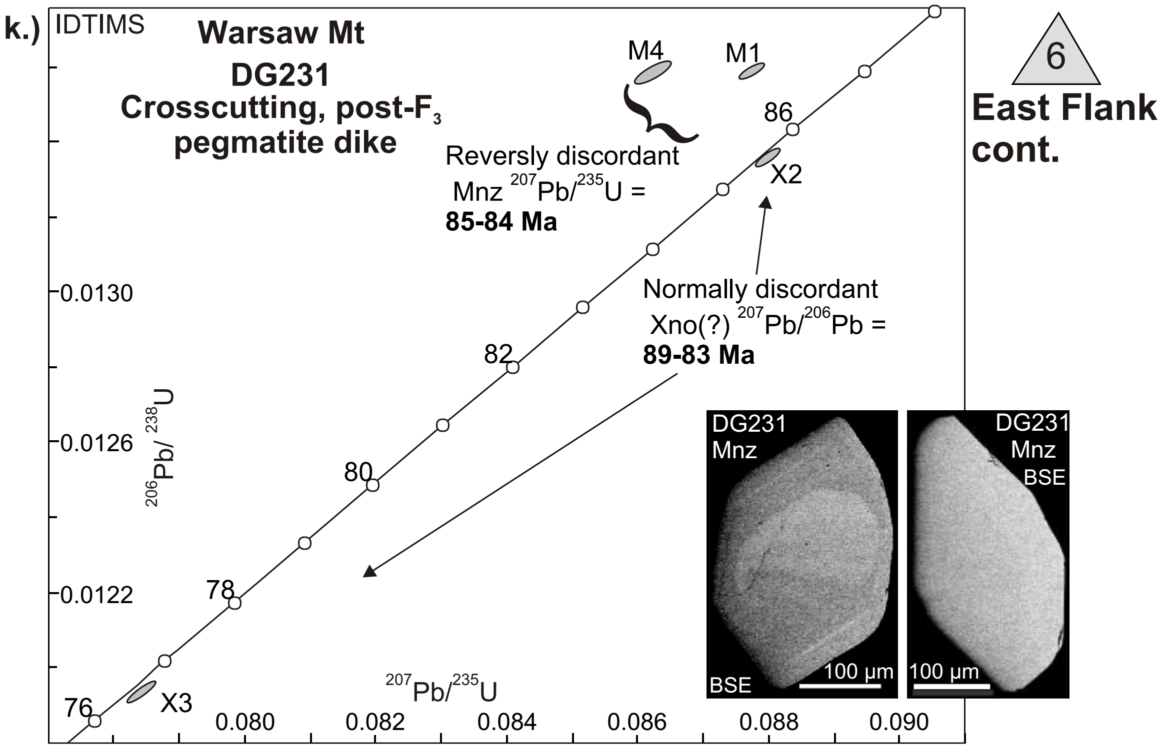

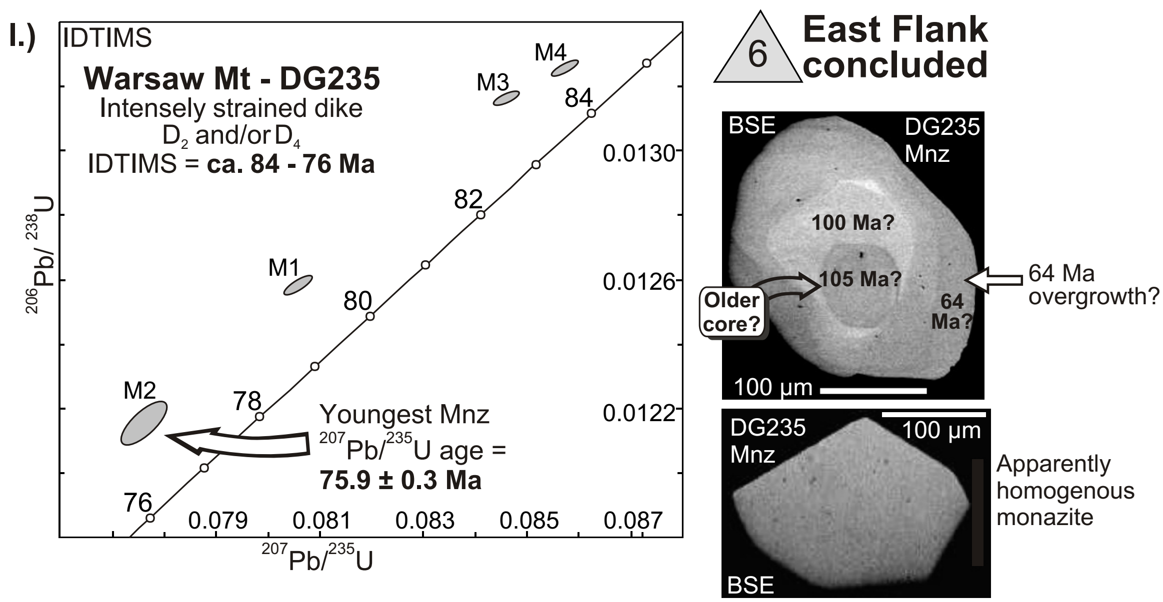

Figure 2.10k-l.

Figure 2.11. U-Th-Pb geochronologic constraints for timing of deformation projected into the composite structural cross section of Fig. 2.8.

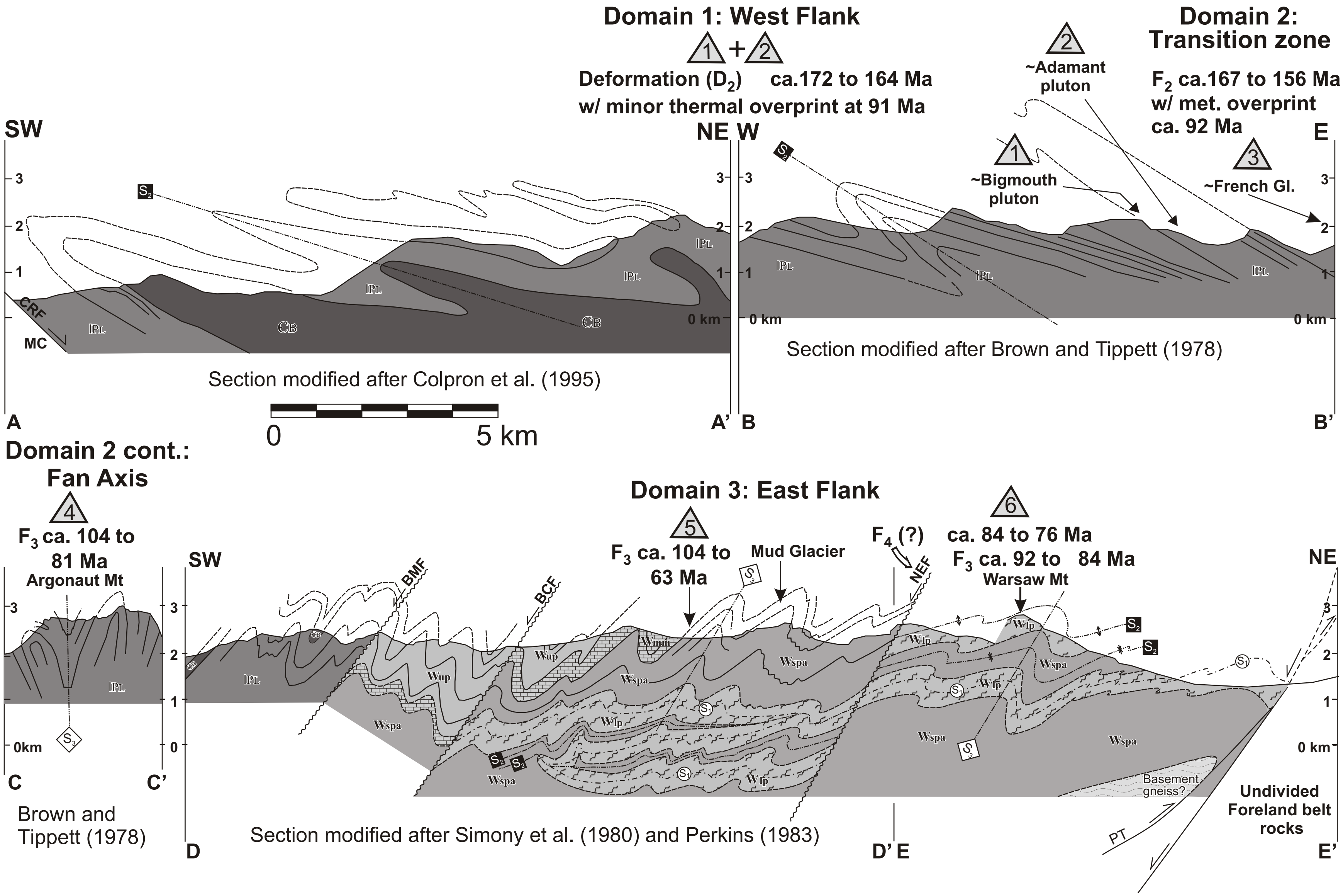
Domain 1: West Flank
1 + 2
Deformation (D_2) ca.172 to 164 Ma
w/ minor thermal overprint at 91 Ma
SW
NE
S2
CRF
MC
IPL
CB
Section modified after Colpron et al. (1995)
A
A'
0
5 km
W
E
Domain 2:
Transition zone
2
~Adamant
pluton
F_2 ca.167 to 156 Ma
w/ met. overprint
ca. 92 Ma
1
~Bigmouth
pluton
3
~French Gl.
0 km
Section modified after Brown and Tippett (1978)
B
B'
Domain 2 cont.:
Fan Axis
4
F_3 ca. 104 to
81 Ma
Argonaut Mt
0km
C
C'
Brown and
Tippett (1978)
Domain 3: East Flank
5
F_3 ca. 104 to
63 Ma
Mud Glacier
BMF
BCF
F_4 (?)
NEF
6
ca. 84 to 76 Ma
F_3 ca. 92 to 84 Ma
Warsaw Mt
Wup
Wmm
Wspa
Wlp
S1
S2
S3
Basement
gneiss?
PT
Undivided
Foreland belt
rocks
Section modified after Simony et al. (1980) and Perkins (1983)
D
D'
E
E'

Figure 2.11.

CHAPTER 3

THERMAL EVOLUTION OF THE NORTHERN SELKIRK MOUNTAINS, SOUTHEASTERN CANADIAN CORDILLERA: U-TH-PB IDTIMS AND SHRIMP AGE CONSTRAINTS ON DIACHRONOUS METAMORPHISM

Abstract

U-Th-Pb geochronologic data are presented that constrain the timing of metamorphism associated with the formation of the Selkirk fan within the northern Selkirk Mountains of the southeastern Canadian Cordillera. The U-Th-Pb isotopic data for metamorphic monazite were attained via small-fraction Isotope Dilution Thermal Ionization Mass Spectrometry (IDTIMS) and *in situ* Sensitive High Resolution Ion Microprobe (SHRIMP) analyses. The internal morphology of the monazite was imaged using back-scattered electron (BSE) imaging and X-ray elemental mapping for Y, Th and U. This revealed complex zoning in many of the monazites, which commonly correlated with distinct age domains, with up to three or more in some crystals. The integration of these techniques facilitated a significant refinement of metamorphic age constraints for medium- to high-grade rocks associated with the development of the Selkirk fan. The data also reconcile an apparent geochronologic contradiction between the northern Selkirk Mountains and adjacent northern Monashee Mountains to the west. The age constraints demonstrate that the metamorphic assemblage in the axis and east flank of the fan evolved over a protracted period of time, from at least the Early Cretaceous to Tertiary (144 to 56 Ma), and likely overprinted pre-existing Middle Jurassic structures and the associated metamorphic assemblage. The degree of overprinting appears to have been a function of structural level, and is interpreted to have been so severe in the deepest levels of the east flank that the isotopic evidence associated with the Middle Jurassic event was essentially erased.

These timing constraints coupled with those presented in Chapter 2 provide a more complete understanding of the tectonic processes involved in the formation of the Selkirk fan. The implications of these results require revision of previous tectonic models proposed for the Selkirk fan, and should also be taken into consideration with regard to other orogens where similar tectonic features are encountered.

3. 1. Introduction

In the southern Omineca belt the eastward transition from the ductile deformation, medium- to high-grade metamorphism and plutonism to the adjacent "thin-skinned" deformation of the Foreland belt is marked by a regional zone of structural divergence (Fig. 3.1a; Price, 1986; Colpron et al., 1998). Within the Selkirk Mountains of southern British Columbia, this zone coincides with the axis of a regional-scale structure termed the Selkirk fan (Wheeler, 1963, 1965; Price and Mountjoy, 1970; Brown and Tippett, 1978; Figs. 3.1b, 3.2). The tectonic development of the Selkirk fan has been the focus of considerable debate, but it is generally thought to have formed primarily in the Middle to Late Jurassic (e.g., Brown and Tippett, 1978; Brown et al., 1992, 1993; Colpron et al., 1996). However, the structural age constraints presented in Chapter 2 demonstrate that the development of the Selkirk fan was more complex and protracted; that it is a composite of Middle to Late Jurassic (ca. 172-156 Ma) and Early to Late Cretaceous (ca. 104-81 Ma) structures. In order to facilitate a more complete understanding of the thermotectonic processes involved in the formation of the Selkirk fan, this chapter presents new geochronologic data that better constrain the timing of medium- to high-grade metamorphism of this region.

U-Th-Pb isotopic data were attained via small-fraction isotope dilution thermal ionization mass spectrometry (IDTIMS) and Sensitive High Resolution Ion Microprobe (SHRIMP) analyses. Dated metamorphic monazites from pelitic schists (Figs. 3.4-3.9) located primarily in medium- to high-grade rocks within the axis and eastern flank of the fan (Fig. 3.3) range in age between ≥144 to 56 Ma. This suggests that metamorphism in this region was strongly diachronous and post-dated most of the Middle Jurassic (ca. 172-

163 Ma) deformation and metamorphism that affected the west flank of the fan (Shaw, 1980a, 1980b; Brown et al., 1992; Colpron et al., 1996; Chapter 2).

3. 2. Geologic Setting

The northern Selkirk Mountains are composed of Late Proterozoic to Paleozoic metasedimentary and metavolcanic rocks (Figs. 3.1a and b) that were initially deposited along the western paleo-margin of the North American craton (Monger et al., 1982). During Middle Jurassic to Paleocene contraction these rocks were displaced northeastward ~250-300 km (e.g., Price and Mountjoy, 1970; Brown et al., 1993; Parrish, 1995) as part of the Selkirk allochthon (Read and Brown, 1981). During this time the allochthon is interpreted to have experienced protracted and diachronous internal deformation and metamorphism (Parrish, 1995). Subsequent Tertiary normal faulting along the Columbia River and Okanagan Valley fault systems has dissected and exposed all levels of the allochthon.

The complexly deformed rocks within the northern Selkirk Mountains comprise at least three generations of superposed folding whose divergence from east to west defines the geometry of the Selkirk fan (Fig. 3.2; Brown and Tippett, 1978; Simony et al., 1980; Perkins, 1983). The eastern flank of this region is bounded by the southern Rocky Mountain Trench, which is part of an orogen-scale tectonic lineament that trends northwest-southeast for more than 2300 km along the strike of the Canadian Cordillera. The structural style in the east flank consists of moderate to shallow southwest dipping faults, transposition foliation (S_2), and second (F_2) and third generation folds (F_3) that become progressively overturned toward the northeast as the trench is approached.

The west flank is partly situated within the immediate hanging wall of the Columbia

River fault (Figs. 3.1b and 3.2), a northwest striking, crustal-scale, Eocene normal-sense shear zone (Parrish et al., 1988). This fault separates upper-amphibolite-facies footwall rocks of the Monashee complex, which includes autochthonous North American basement (see Armstrong et al., 1991; Parkinson, 1991; Crowley, 1999), from greenschist-facies rocks of the Selkirk allochthon (Fig. 3.3). The west flank of the fan is dominated by southwest verging, second generation folds (F_2) with shallow dipping axial surfaces (S_2) that become progressively steeper toward the fan axis. Identification of F_3 is generally restricted to crenulations that overprint the S_2 transposition foliation. The earliest folds, F_1, and associated axial planar foliation, S_1, are also found primarily in the west flank, but identification of F_1 and S_1 is complicated due to the pervasive and intense coaxial overprint of F_2. However, recognition of regionally overturned stratigraphy (Read and Brown, 1979; Brown et al., 1983) interpreted as the inverted limb of the km-scale, southwest vergent Carnes nappe (Brown and Lane, 1988; Brown, 1991), and the rare preservation of rootless isoclines and refolded S_1 foliation by F_2 (Brown and Tippett, 1978; Colpron et al., 1998) provide evidence for D_1 in the field.

Readers are referred to Chapter 2 for a more thorough discussion of the structural and lithostratigraphic elements found in the study area.

3. 3. Metamorphism

Sillimanite- and Sil-Kfs[1]-grade rocks core the central part of the study area, and are flanked on either side by progressively lower grade assemblages (Fig. 3.3). In some locations, complex textural relationships characteristic of polyphase metamorphism are

[1] Mineral abbreviations according to Kretz (1983); in this study and individual samples, sillimanite occurs both as fibrolite with a grain diameter <2μm (Pattison, 1992, p. 426), and as sillimanite with a grain diameter >2μm. Both are referred to collectively as sillimanite.

evident (see Marchildon, 1999). Notwithstanding, a set of northwest trending regional isograds (Fig. 3.3) parallel to the structural grain of the region have been established based on the appearance or disappearance of index minerals chlorite, biotite, garnet, staurolite, kyanite, and sillimanite in pelites (Wheeler, 1965; Leatherbarrow and Brown, 1978; Leatherbarrow, 1981; Simony et al., 1980). The lowest grade chlorite-in assemblage is located in the west flank of the study area, in the immediate hanging wall of the Columbia River fault (Fig. 3.3). Eastward, the metamorphic grade increases progressively to Sil-Kfs-melt and then decreases to the northeast where Ky-St assemblages are located adjacent to the southern Rocky Mountain Trench (Fig. 3.3).

The peak metamorphic pressures and temperatures estimated for the region vary from west to east. On the basis of geothermobarometry, Leatherbarrow (1981) documented that in the southwest flank of the fan, in the vicinity of French Glacier within the St-Ky-zone (Fig. 3.3) peak pressures and temperatures were 5 kbar and 500-550 °C. To the northeast within the Sil-Kfs-zone, pressures were estimated to have reached 7 kbar and temperatures as high as 650 °C. Geothermobarometric studies to the north in the Mica Creek area agree well with those of Leatherbarrow. Ghent et al. (1979, 1982, and 1983) estimated peak conditions of 540 to 700 °C and 5.6 to 7.2 kbar (lower P-T estimates for St-Ky-zone, higher for Sil-Kfs-zone).

Throughout the region a consistent relationship between microfabrics and the metamorphic assemblage has been documented in thin section (e.g., Franzen, 1974; Brown and Tippett, 1978; Leatherbarrow, 1981; Perkins, 1983). These studies demonstrated that most porphyroblast growth was synchronous with or postdated the late stages of transposition (S_2), but predated or was synchronous with the early stages of D_3.

For example, the anhedral cores of garnet and staurolite porphyroblasts commonly contain inclusion trails of S_2, which were statically overgrown by inclusion-free, euhedral rims, and S_2 within the surrounding matrix is crenulated (F_3) and deformed around the porphyroblasts (Fig. 3.4). Also, in the area south of the Bigmouth pluton the northwest trending metamorphic isograds are found to intersect the trace of north trending F_2 folds at a high angle, but do not display evidence that they have been significantly reoriented by these folds (Map 2).

3. 4. Previous Timing Constraints

U-Pb crystallization ages and $^{40}Ar/^{39}Ar$ cooling ages from plutons and their immediate aureoles were used to provide the Middle Jurassic age constraints for deformation, metamorphism, and exhumation throughout the northern Selkirk Mountains (e.g., Shaw, 1980a; Brown et al., 1992; Colpron et al., 1996, and references therein). A summary of previous timing constraints is provided in Table 3.1.

Shaw (1980a) analyzed zircon from the southwestern margin of the Adamant pluton (Figs. 3.1 and 3.3). He concluded that the ca. 169 Ma U-Pb ages represented the timing of metamorphic zircon growth concomitant with D_2, rather than pluton emplacement, because the zircon could be found only in the outer hydrated zone of the pluton, presumably the product of regional metamorphism. To the south, U-Pb analyses of zircon and titanite by Brown et al. (1992) produced an age of ca. 168 Ma for the Fang and Pass Creek plutons. These plutons were interpreted to post-date the development of southwest verging structures and regional metamorphism. In this region, Colpron et al. (1996) were able to demonstrate that there was at least 10 km of exhumation between ca. 173-168 Ma during the development of southwest verging structures by integrating hornblende, biotite and muscovite $^{40}Ar/^{39}Ar$ cooling ages with thermobarometric data. Thus, in the northern Selkirk Mountains southwest vergent deformation and regional metamorphism were interpreted to have occurred prior to and possibly during 169 Ma, but no later than 168 Ma.

Within the study area, Marchildon (1999) interpreted the Bigmouth pluton and surrounding area to have been affected by two metamorphic events, M_1 and M_2, separated by an intervening period of decompression. This is based on thin section observations from the host rocks surrounding the Bigmouth pluton that indicated retrograde chlorite replaced M_1 garnet and was then overprinted by a second generation (M_2) of garnet growth (Plate 1b and 2 of Marchildon, 1999, p. 105 and 107, respectively). Marchildon concluded that the intrusion of the pluton was coeval with the M_1 metamorphism, at a depth >20km based on the presence of magmatic epidote (see Zen and Hammarstrom, 1984, and Zen, 1985). Marchildon constrained the timing of pluton emplacement and M_1 metamorphism to be 157 ± 3 Ma based on a linear regression through normally discordant IDTIMS zircon data. This was interpreted to post-date the initiation of the transposition-forming event. Marchildon also analyzed two fractions of titanite that gave $^{206}Pb/^{238}U$ ages of 140.5 ± 0.8 Ma and 137.4 ± 1.4 Ma with minor normal discordance (~6-16%). The younger titanite crystals were interpreted to have been reset during M_2 following post-M_1 decompression, and pre-dated the end of the transposition-forming event. However, the SHRIMP data presented in Chapter 2 bring into question the validity of the timing constraints provided by Marchildon (1999). The SHRIMP data conclusively demonstrate that the pluton crystallization age is ca. 172-164 Ma, and that the titanites were likely affected by a minor thermal disturbance at ca. 92

Ma, rather than arguing for complete resetting at 140-137 Ma.

Crowley et al. (2000) provided timing constraints for metamorphism in the northernmost Selkirk Mountains for rocks located in the eastern flank of the Selkirk fan (Table 3.1). The age constraints range between ≥132-61 Ma based on IDTIMS and SHRIMP U-Th-Pb analyses of monazite crystals from migmatitic Ms-Grt-Ky-Bt schists collected along Highway 23 near Mica Village and Mica Dam (Fig. 3.3). This agrees well with additional ages produced by Crowley et al. and other studies to the west and northwest in the northern Monashee Mountains (Sevigny et al., 1989, 1990; Scammell, 1993; Digel et al., 1998). Interestingly, less than 5 km to the north in the northern Monashee Mountains, Crowley et al. (2000) also provided convincing evidence for Middle Jurassic metamorphism, ca. 163-160 Ma. The implications for these data are considered below in the Discussion section.

3. 5. U-Th-Pb Geochronology: New Timing Constraints on Metamorphism

U-Th-Pb isotopic data for metamorphic monazites are reported for eight medium-to high-grade metapelitic samples from the northern Selkirk Mountains (Fig. 3.3, Map 1). The geochronologic data are presented in Tables 3.2-3.4, in concordia diagrams (Figs. 3.5-3.9; errors for ellipses are presented at two standard errors, i.e., 2σ), assigned to points in P-T space (Fig. 3.10) and projected along strike into cross section (Fig. 3.11). BSE images and Y, Th and U maps are provided for each monazite analyzed by SHRIMP, and are accompanied by U-Th-Pb concordia plots (errors for ellipses are reported at 2σ). Figures 3.6-3.9 also include the $^{208}Pb/^{232}Th$ SHRIMP age beside each spot (errors are quoted at 1σ in Ma). In addition, each Y image has a corresponding gray value pixel profile that has been included to further illustrate the contrast between Y zones. The plots provide a means to qualitatively assess the Y concentrations within the zones in order to facilitate comparisons. In the following sections, references to element concentrations (e.g., Y concentration) are based on the original, unadjusted gray pixel values of the X-ray maps. This is considered a reasonable qualitative approach for estimating and comparing Y zone concentrations (M. Jercinovic EMP lab UMASS, 2002, pers. comm.). Some of the Y images have been adjusted slightly for contrast and brightness to enhance the zoning, but only after the gray value plots were created.

In Figs. 3.6-3.9, the SHRIMP data are also plotted in a Tera-Wasserburg diagram (Tera and Wasserburg, 1972; errors presented at 2σ), in which the $^{207}Pb/^{206}Pb$ ratio uncorrected for common Pb is plotted against the uncorrected $^{238}U/^{206}Pb$ ratio. Linear regressions were fitted through data that clustered in distinguishable groups. The age for a particular group was determined using the lower intercept of the regression line with the concordia curve. The upper end of the chord was anchored at the common $^{207}Pb/^{206}Pb$ composition based on the approximate age of each group using Stacey-Kramers (1975) model growth curves[2]. In theory, the ages derived from the lower intercepts of the regressions avoid the potentially large uncertainty imposed by the ^{204}Pb correction for common Pb (see below). Although the calculated ages may be affected by variable amounts of unsupported ^{206}Pb, the Tera-Wasserburg plot helps to highlight the age domains within individual monazite crystals.

The study area has been broadly divided into three domains (Fig. 3.3a; Chapter 2) according to the lithostratigraphic, structural, metamorphic and geochronologic elements that characterize portions of the fan. Domain 1 is located in the west flank of the fan

[2] It was not necessary to know the exact $^{207}Pb/^{206}Pb$ ages when calculating the Stacey-Kramer common Pb composition because there is <1% variation in the common $^{207}Pb/^{206}Pb$ ratio for Jurassic-Cretaceous ages.

where southwest verging folds (F_2) with shallow dipping axial planes and transposed foliation (S_2) dominate. This domain is interpreted to represent the highest structural level in the study area, comprised primarily of Lardeau Group and Badshot Formation stratigraphy that was metamorphosed at Chl- to Sil-grade, and intruded by the Middle Jurassic (ca. 167 Ma) Bigmouth pluton. Unfortunately, metamorphic monazite data were not acquired for Domain 1 due to the absence of monazite in the pelitic schist sampled for geochronology in this domain. However, deformation and metamorphism are constrained to be Middle to Late Jurassic in age (ca. 172-156 Ma) based on IDTIMS and SHRIMP analyses of zircon and monazite from variably deformed dikes and the pluton (Chapter 2). These data also indicated that there was a thermal overprint at ca. 91 Ma. The Cretaceous overprint in Domain 1 is considered in more detail in the Discussion section based on additional unpublished $^{40}Ar/^{39}Ar$ cooling ages that were produced in this region (Table 3.1).

Domain 2 occupies the zone where the trace of the fan axis is mapped (Fig. 3.3), and is cored by Sil-grade rocks of the Windermere Supergroup. Axial planes of folds and transposition foliation have a near vertical to vertical orientation (Fig. 3.11; Map 2) that generally strike to the northwest and southeast. Domain 2 is termed the ‘Transition Zone’ because the isotopic data provide evidence for Middle Jurassic structures that have been substantially overprinted during the mid- to Late Cretaceous (ca. 104-81 Ma, this study).

Domain 3 is located within the eastern flank of the fan where northeast vergent folds (F_2 and F_3) and transposition foliation dominate at all scales of observation. The east flank is composed of Windermere Supergroup rocks that progressively change in metamorphic grade from Sil-Kfs near the fan axis to Ky-St grade adjacent to the Rocky

Mountain Trench. In Domain 3, thermo-structural age constraints range between Early Cretaceous to Early Tertiary (ca. 144-56 Ma, this study).

3.5.1. Analytical Methods

Geochronologic methods included U-Pb IDTIMS and U-Th-Pb SHRIMP analyses accompanied by backscattered electron (BSE) imaging, and high-resolution Y-Th-U X-ray maps of metamorphic monazite crystals. U-Pb IDTIMS geochronology at Carleton University followed procedures outlined by Parrish et al. (1987). Mineral separates were obtained by standard crushing, grinding, Rogers Gold™ table, heavy liquid, and Frantz™ magnetic separation techniques. When possible, the clearest, crack- and inclusion-free crystals were selected for analysis. Teflon® microcapsules (Parrish, 1987) were used for mineral dissolution with a mixed ^{233}U-^{235}U-^{205}Pb tracer (Parrish and Krough, 1987). Ion exchange column chemistry (Parrish et al., 1987) facilitated U-Pb element separation. U-Pb isotopes were analyzed using a multicollector mass spectrometer (Finnagan MAT 261 as described by Roddick et al., 1987), and estimation of errors was based on numerical error propagation (Roddick, 1987). Decay constants used are those recommended by Steiger and Jagër (1977). Discordia lines through analyses were calculated using a modified York (1969) regression (Parrish et al., 1987). Typically, procedural U blanks were less than 5 pg and Pb blanks less than 10 pg. Common Pb corrections were made assuming model Pb compositions derived from the growth curves of Stacey and Kramers (1975).

Ion microprobe analyses of monazite grains in a polished mount using the SHRIMP II at the Geological Survey of Canada (GSC) in Ottawa were carried out according to the methods outlined by Stern (1997), Stern and Sanborn (1998), and Stern and Berman

(2000). A full description of the SHRIMP II instrument may be found in Stern (1997), Williams (1998) and De Laeter and Kennedy (1998). Monazite crystals from samples dated in this study were set in an araldite resin grain mount. The mount was polished using 9, 6, and 1 μm diamond polishing compound to reveal grain centers, and coated with 5.8-6.0 nm of Au (99.9999%). BSE and cathodoluminescence (CL) images were obtained at the GSC using a Cambridge Instruments S360 scanning electron microscope operating at 20 kV accelerating potential and using an electron beam current of 2-5 nA. Chemical maps of Y, Th and U of selected monazite grains were made using a Cameca SX-50 electron microprobe at the University of Massachusetts according to procedures outlined by Williams et al. (1999). High resolution X-ray maps of Y, Th and U were produced using a high sample current (>200 nA), small step sizes (~0.5 μm), and rastering the electron beam. Obtaining chemical maps of the monazite crystals prior to SHRIMP II analyses is unique to this study, and proved to be very effective for elucidating age domains within the analyzed monazite.

Target locations for U-Th-Pb SHRIMP analysis on selected monazite grains were chosen using the chemical maps. Targeted areas were sputtered using a mass-filtered O_2^- primary beam operating in Kohler illumination mode to effect even sputtering. All samples were analyzed using the K120 Kohler aperture setting, which yielded an approximate beam diameter of 22 x 31 μm. For monazite, the primary beam current was ~2-2.3 nA for both standards and unknowns. The operational mass resolution (1% peak height) over the course of the analyses was 5550-5700. Instrumental bias in the measured Pb/U and Pb/Th ratios was corrected by an empirically-derived calibration of the linear relationships between $^{206}Pb^+/UO^+$ vs. UO_2^+/UO^+, determined on natural monazite standards (GSC samples 3345 and 4170). Isotopic ratios were corrected for common Pb using ^{204}Pb. However, for SHRIMP data the ^{204}Pb correction can impart significant error on the calculated age due to extremely low ^{204}Pb counts (see Stern, 1997). The propagation of the statistical error associated with this presumably has the most impact on the ^{207}Pb/^{235}U age, because of low ^{207}Pb counts in Mesozoic or younger minerals. This may cause an "artificial" disagreement between the calculated ^{207}Pb/^{235}U age and the other isotopic systems. Thus, for monazite the ^{208}Pb/^{232}Th chronometer is considered most accurate because it includes the highest Pb counts, and is apparently unaffected by isotopic disequilibrium, such as unsupported ^{206}Pb (see Schärer, 1984). In the following sections and figures, quoted SHRIMP ages rely primarily on the ^{208}Pb/^{232}Th chronometer unless otherwise noted. Errors assigned to SHRIMP U-Th-Pb ages were determined using numerical propagation of all known sources of error as outlined by Stern (1997), Stern and Sanborn (1998), and Stern and Berman (2000).

3.5.2. Guidelines for age interpretations

The IDTIMS data in many of the samples yielded an age range of a few million years or more, which is attributed to the presence of two or more age domains within the analyzed monazites. Causes for the spread of ages include partial recrystallization and/or secondary growth. Additional complexities included unsupported ^{206}Pb in monazite resulting from the incorporation of excess ^{230}Th upon crystallization (Schärer, 1984; e.g., sample DG01, DG23 and DG70b, Fig. 3.5a-c). In this study diffusive Pb loss is considered unlikely for monazite. Based on experimentally determined diffusion parameters, Cherniak et al. (2002) concluded that the closure temperature (Dodson, 1973) for Pb in monazite is similar to that in zircon (Cherniak et al., 2000), and that thermally activated Pb diffusion in monazite is not a viable mechanism for Pb loss. They found that the closure temperature for a 10 µm monazite is >900 °C for a reasonable cooling rate of 10 °C/Ma. This corroborates conclusions reached in many *in situ* studies that demonstrate monazite is highly resistant to thermally induced volume diffusion, even under conditions of granulite facies metamorphism (e.g., DeWolf et al., 1993; Zhu et al., 1997; Braun et al., 1998; Cocherie et al., 1998; Crowley and Ghent, 1999; Zhu and O'Nions, 1999b; Foster et al., 2002). Thus, Pb loss by volume diffusion is considered unlikely for monazite under most geologic conditions.

Age interpretations made in this study were generally based on both the IDTIMS and SHRIMP data when available. Interpretations benefited greatly from the *in situ* SHRIMP analyses, which were used to discern multiple age domains within single crystals. Monazite data were often reversely discordant (i.e., $^{206}Pb/^{238}U$ ages > $^{207}Pb/^{235}U$ ages) due to unsupported ^{206}Pb (Schärer, 1984). The correction prescribed by Schärer (1984) has not been applied to these data because it is not considered appropriate for metamorphic monazite since the Th/U ratio of the medium from which the monazite grew is virtually impossible to determine (Parrish, 1990). Thus, for IDTIMS data it is assumed that the $^{207}Pb/^{235}U$ chronometer, which is unaffected by ^{230}Th disequilibrium, is the best approximation for the timing of monazite crystallization (Schärer, 1984). Furthermore, most of the IDTIMS monazite data are supplemented by $^{208}Pb/^{232}Th$ data provided by SHRIMP analyses; this chronometer is also considered to be unaffected by isotopic disequilibrium.

For some IDTIMS data, the $^{207}Pb/^{235}U$ age for reversely discordant monazite fractions is considered a good approximation of the timing of monazite growth, especially when tightly clustered above the concordia curve. The analyses would not be expected to cluster if there was significant inheritance, overgrowths, or recrystallization domains, as it would be unlikely to get identical mixtures from grain to grain; however, minor amounts of mixing cannot be completely ruled out. Linear regressions through discordant monazite data are not considered reliable because intercepts will be offset at either end if any of the data contain a component of unsupported ^{206}Pb. For these data, the youngest ^{207}Pb/^{235}U age is considered the best approximation of secondary growth-recrystallization events.

3.5.3. Isotopic Data and Age Interpretations

A summary of the ages, locations, hand sample and thin section descriptions, and geologic relationships are summarized in Table 3.2. Note that most of the Ky- and Sil-grade pelitic schists contain substantial volumes of leucosome, up to 40%. However, the restite portions of the outcrop were preferentially sampled in order to avoid leucosome that may have emanated from another source.

3.5.3.1. Domain 2: Transition Zone

DG01 – Ms-Grt-Sil-Bt pelitic schist (IDTIMS)

DG01 was sampled from a migmatitic Ms-Grt-Sil-Bt pelitic schist[3] located at the headwaters of French Creek, ~1 km southwest of the interpreted location of the trace of the fan axis (Fig. 3.3b, Map 2). The transposition foliation, S_2, is defined by the alignment of biotite and muscovite, and is steeply dipping at ~83° to the southeast. In hand sample, the garnets appear to be rimmed and sometime replaced by knots of sillimanite. In thin section, garnet poikiloblasts riddled with inclusion trails often have significantly embayed margins that suggest there has been considerable resorption and replacement by Bt-Sil-Qtz (Fig. 3.4a). Mats of sillimanite are commonly found to have preferentially nucleated on a biotite substrate, with splays of sillimanite appearing to be randomly oriented in many cases. However, some sillimanite crystals do appear to be deflected around hinges of F_3 crenulations (Fig. 3.4a), or are overgrown by euhedral, inclusion-free garnet rims (Fig. 3.4b). Most muscovite and some biotite laths are found to crosscut S_2, or appear to have grown mimetically within the S_2 foliation. The melt portion in this sample is predominantly quartz that appears to be annealed except where it is deformed by F_3 crenulations. Subhedral monazite grains are typically found within biotite, some of which are overgrown by sillimanite, or along biotite grain boundaries (Fig. 3.4c), and less commonly within sillimanite mats. BSE images of sectioned and polished matrix monazite grains lack evidence for multiple age domains, displaying either homogenous or diffuse zoning (Fig. 3.5a inset). Based on the BSE images and textures observed in thin section, most of the matrix monazite grains in this sample are interpreted to have grown primarily during the same metamorphic episode responsible for the formation of sillimanite. Although the exact relationship of monazite to F_2 and F_3 is unclear, its apparent paragenetic association with sillimanite suggests that it grew post-F_2 and syn- to post-F_3.

Two single-grain fractions of pale yellow, clear and inclusion-free subhedral monazite were analyzed by IDTIMS. Both fractions, M2 and M3, are reversely discordant (Table 3.3) and plot directly above the concordia curve at ca. 92 Ma (Fig. 3.5a). The mean $^{207}Pb/^{235}U$ age of 91.5 ± 1.7 Ma is interpreted to represent the time of monazite growth

---

[3] Minerals are listed by increasing modal abundance

associated with Sil-grade metamorphism, which post-dated the majority of the deformation observed in this area.

Interestingly, a deformed pegmatite, DG09, located ~800m to the northwest within the same pelitic schist unit is interpreted to be Middle Jurassic in age, as constrained by IDTIMS analysis of igneous zircon (Chapter 2, p.39). However, SHRIMP analysis of a monazite from this dike yielded an age of 90 ± 1 Ma; the SHRIMP spot was targeted within the homogenous interior of the monazite (Chapter 2, inset Fig. 2.10f). This monazite is interpreted to have grown during the same metamorphic event responsible for the growth of matrix monazite grains within the host pelitic schist.

DG70b - Grt-Sil-Bt-Ms pelitic schist (IDTIMS)

Sample DG70b comes from a migmatitic Grt-Sil-Bt-Ms pelitic schist located in a south-facing bowl below Jason Peak, immediately southeast of Argonaut Mountain (Fig. 3.3b). The metamorphic assemblage and textures in this sample are very similar to DG01 (see Fig. 3.4d and e), except there is more plagioclase in this sample and the quartz does not appear to be as completely annealed.

Five pale yellow, clear and relatively inclusion-free, subhedral monazite crystals were analyzed by IDTIMS. Although the BSE images do not provide evidence for chemical zoning within the monazites of this sample (see inset Fig. 3.5b), the monazites are interpreted to have undergone more than one period of growth. Four fractions with varying degrees of reverse discordance between –6.8% to –42.4% plot just above the concordia curve between 100-95 Ma. The spread in ages strongly suggests age mixing within the analyzed population. Thus, fraction M5, with the youngest $^{207}Pb/^{235}U$ age of 94.7 ± 0.5 Ma, is considered to be the closest approximation for the timing of the most recent period of monazite growth. Fraction M6, which is normally discordant with a $^{207}Pb/^{206}Pb$ age of 107.5 ± 10.8 Ma, is considered to be a minimum age estimate for the oldest episode of monazite crystallization. By volume the latest period of monazite growth, ca. 95 Ma, must have been most substantive since the data are closely grouped nearest this age, and most analyses are reversely discordant. Based on the textural evidence observed in thin section, this more recent period of monazite growth was likely associated with sillimanite metamorphism. The older age, ca. 107 Ma, may either represent an earlier stage in the prograde metamorphism of this assemblage, or a separate episode of metamorphism that was almost completely recrystallized during the sillimanite metamorphism in the Late Cretaceous. The earlier metamorphism may have been associated with the period of Middle Jurassic deformation whose U-Pb isotopic signature was preserved along strike at French Glacier.

3.5.3.2.Domain 3: East Flank

DG23 - Ms-Grt-Sil-Bt pelitic schist (IDTIMS)

Sample DG23 comes from a migmatitic Ms-Grt-Sil-Bt pelitic schist located ~3 km southwest of Mud Glacier, situated within the Sil-Kfs-zone on the east flank of the Selkirk fan (Fig. 3.3b). The moderate to steep southwest dipping transposition foliation, S_2, is defined primarily by the alignment of biotite, but is also crosscut by late euhedral porphyroblasts of biotite. Mats of sillimanite are commonly found on a biotite substrate in contact with or as a replacement of garnet, but are also overgrown by euhedral, homogenous garnet rims (Fig. 3.4g). Sillimanite appears to be aligned within S_2, but is also found to crosscut it. In hand sample, sillimanite often protrudes as knots having the appearance of faserkiesel. The leucosome can constitute up to 30-40% of the rock.

Monazite is commonly found within biotite and along its grain boundaries. A number of elongate monazite crystals are concordant with S_2 (Fig. 3.4f), suggesting that some monazite growth predated at least the latest development or reactivation of the transposition foliation. Late euhedral laths of muscovite crosscut S_2, and likely represent muscovite grown during melt crystallization following the most recent peak of metamorphism. In this sample, and more clearly in a nearby sample, DG26 (Map 1), crenulations interpreted to be associated with the development of F_3 deform all the minerals in the assemblage.

Four single-grain IDTIMS analyses of clear, pale yellow, inclusion-free monazite produced an age range between 94.2-91.6 Ma. Three of the fractions are reversely discordant, whereas one fraction, M6, is nearly concordant (1% discordant). Again, this sample is interpreted to contain monazite crystals that underwent more than one growth event. Monazite, M6, is interpreted to be a fortuitous mix between younger and older monazite components that yielded a nearly concordant data point. The youngest monazite fraction, M4, which is 91.4 ± 0.6 Ma is thought to be the maximum age for the most recent episode of monazite growth.

The interpretation of more than one episode of monazite growth in sample DG23 is corroborated by SHRIMP analyses of monazite grains from a leucosome located ~100m to the south that was deformed by F_3 (DG22c, Chapter 2, p. 42). Within the innermost core of the monazite crystals of DG22c, an age of ca. 104 Ma was produced, whereas analyses outside of this inner zone yielded a mean $^{208}Pb/^{232}Th$ age of ca. 97 Ma. In addition, SHRIMP analyses within metamorphic zircon rims that overgrew Archean detrital cores yielded an age of 92 Ma. These ages compare well with the results from

DG23, and support the interpretation that the discordance is due to age mixing, which is likely the consequence of a prolonged period of metamorphism at this location, ca. ≥104-91 Ma.

DG206 – Ms-Grt-Ky-Bt pelitic schist (IDTIMS)

Sample DG206 is from a migmatitic Ms-Grt-Ky-Bt pelitic schist that was collected on Fred Laing Ridge, within the Ky-zone on the east flank of the fan (Fig. 3.3b). The leucosome has a tonalite composition, and constitutes up to 40% of the rock. Alignment of kyanite, biotite and muscovite define the S_2 transposition foliation (Fig. 3.4h). Both kyanite and garnet have been variably resorbed, and replaced primarily by biotite and quartz. Most garnets have poikiloblastic cores filled with randomly oriented quartz inclusions, surrounded by homogenous, inclusion-free rims. Many garnets appear to be flattened into an oblate shape, with long axes concordant to S_2 (Fig. 3.4i). This is likely attributable to the preferential growth of the garnet rims parallel with the plane of flattening. Monazite grains are found mainly as inclusions in biotite and along biotite grain boundaries.

Four single-grain, pale yellow, clear and inclusion-free monazite grains were analyzed by IDTIMS. Two fractions, M2 and M4, have minor normal discordance of 5.1% and 1.5%, respectively, and M1 is nearly concordant with only 0.4% discordance. Conversely, fraction M3 has slight reverse discordance, i.e., -14.4%. The spread of these data in a chord near the concordia curve strongly suggests age mixing within this monazite population, and likely within individual crystals, as indicated by the zoning illustrated in the BSE images for two monazites from this sample (Fig. 3.5d inset). The oldest $^{207}Pb/^{206}Pb$ age of 84.0 ± 4.6 Ma for the normally discordant fraction M2 is considered to be a minimum estimate for early monazite growth during prograde metamorphism. The reversely discordant fraction, M3, with a $^{207}Pb/^{235}U$ age of 70.8 Ma is considered to be the maximum age of most recent monazite growth in this sample associated with prograde metamorphism. The nearly concordant monazite analysis, M1, is considered to be a fortuitous mix between young and old components.

The ages determined for this sample agree very well with those documented ~4km to the northwest by Crowley et al. (2000) in a migmatitic Ky-bearing pelitic schist collected ~0.5 km south of Mica Dam (sample 1; Table 3.1; Fig. 3.3). SHRIMP analyses demonstrated that monazite grains included within garnet rims grew at ca. 110 Ma, and monazite inclusions within kyanite, as well as matrix monazite grains, grew at ca. 84-73 Ma. These ages are thought to place a lower age constraint on the growth of garnet rims and kyanite porphyroblasts in this sample. Rims on matrix monazite yielded the youngest ages, ca. 64-61 Ma. The absence of these ages for monazite inclusions within kyanite and garnet suggest the rims on the matrix monazite grew following the latest peak of metamorphism. The data from Crowley et al. (2000) and this study strongly point to a protracted period of medium- to high-grade metamorphism in this area that lasted at least from ca. 110 Ma to 70 Ma, and possibly as young as 61 Ma.

DG38a – Ms-Grt-Ky-Bt pelitic schist (IDTIMS and SHRIMP)

Sample DG38a, a Ms-Grt-Ky-Bt pelitic schist with at least 20-30% tonlititic melt content was collected ~3.2 km northeast of Mud Glacier, within the Ky-zone on the east flank of the fan (Fig. 3.3b). All kyanite and most biotite grains are aligned within the shallow southwest dipping transposition foliation that is pervasive throughout the area (see Chapter 2; Map 2). Most of the monazite crystals identified using a polarizing microscope also appear to be aligned parallel to the foliation (Fig. 3.4j). Both garnet and kyanite porphyroblasts have textures indicative of resorption, and appear to have broken down to biotite and quartz with or without plagioclase (Fig. 3.4j-k). Some of the garnets have cores with inclusion trails surrounded by inclusion-free, homogeneous rims, indicating there has been more than one episode of garnet growth. Multiple episodes of garnet growth are supported by the observations that garnet is found as inclusions within kyanite, but is also found to have overgrown it (Fig. 3.4k). Although not observed in this sample, retrograde chlorite is found nearby, <500 m to the north, as a late replacement of garnet.

The IDTIMS analyses of four single-grain monazite fractions plot in close proximity to the concordia curve between ca. 123 to 103 Ma (Fig. 3.6a). Fractions M2 and M4 are reversely discordant and plot just above the concordia curve (-2.3% and –4.1% discordant, respectively), whereas M5 and M3 are normally discordant and plot just below the concordia curve (2.6% and 3.7% discordant, respectively). A linear regression through the data produces a lower intercept (L.I.) of 107 ± 4.5 Ma and an upper intercept (U.I.) of 161 ± 20 Ma. The intercept ages seem to agree well with other age constraints in the region, but are considered spurious because the chemical maps of monazites for DG38a indicate complex and irregular chemical domains, suggestive of multiple age domains within single monazite crystals (Fig. 3.6e). Thus, the likelihood of bulk mixing of multiple age domains with varying degrees of unsupported ^{206}Pb make it difficult or impossible to correctly interpret the IDTIMS data even when manipulated using linear regression techniques.

In situ SHRIMP analysis confirmed the existence of multiple intracrystal age domains.

The Y maps generally provided the best indication of growth and/or recrystallization domains (see Chapter 4). The exact mechanism of monazite growth and/or replacement responsible for these domains remains unclear (i.e., resorption-reprecipitation, overgrowth, or recrystallization). Consequently, the general terms “growth” or “crystallization” will be used.

At least three, and possibly five ages of monazite crystallization were identified by the SHRIMP analyses (Figs. 3.6b-d). The oldest ages have a weighted mean $^{208}Pb/^{232}Th$ age of 138.7 ± 4.5 Ma that includes five SHRIMP spots on four monazites (see Fig. 3.6d, below the $^{238}U/^{206}Pb$ axis of the Tera-Wasserburg plot). These ages corresponded to the darkest Y domains with the lowest Y concentration, located in the core portion of the analyzed monazites (Mnz2, 9, and10); except for Mnz12, which has a younger 75.9 ± 1.2 Ma, high Y zone in the core partly surrounded by the older, lowest Y domain (Fig. 3.6e). However, the high Y core is interpreted to be part of the same high Y domain found rimming this monazite. In this crystal, the third dimension must be considered. The central high Y portion likely represents a lobe of the younger rim that extended down in the z-direction into the plane (x-y) of the image (cf. Fig. 13 of Pyle and Spear, 2002).

The second oldest domain of the monazite grains analyzed has a weighted mean $^{208}Pb/^{232}Th$ age of 126.1 ± 2.2 Ma based on a total of three spots within three monazites. This corresponds with the zones that have the second lowest Y concentration (Mnz1, 8, and 9 of Fig. 3.6e). This domain is interpreted to be distinct from the older, lowest Y core described above because in Mnz9 there is a sharp, truncated boundary between the younger (125.6 ± 1.9 Ma) intermediate Y domain and the older (144.4 ± 2.2 Ma) lower Y core that appears to have been significantly resorbed. Also, the SHRIMP spots are clearly situated within their respective Y zones (Fig. 3.6e, Mnz9), leaving little doubt that these are robust ages for separate growth domains.

The youngest domain in all the monazites analyzed is associated with the discordant, high Y rims, except for Mnz4 (Fig. 3.6e), which is almost completely composed of this high Y domain. The limited preservation of small, isolated patches of low Y concentration in Mnz4 suggest that resorption and/or recrystallization of this domain was nearly complete; this may have also been a prominent process in other samples in which the oldest monazite domain, ca. 144-135 Ma, was not detected (see below). The high Y domains appear to range in age from ca. 107 to 76 Ma (Fig. 3.6e). However, the weighted mean $^{208}Pb/^{232}Th$ age of 76.9 ± 3.6 Ma for five spots on four monazites is considered to be the best approximation for this domain, i.e., Group 3 in Fig. 3.6d. The older ages are likely the result of slight overlap into older, adjacent domains. This is clearly the case for spot 3 of Mnz9 which is 107 ± 4 Ma (Fig. 3.6e), and possibly for spot 2 of Mnz1 which is 91.2 ± 1.4 Ma (Fig. 3.6e). However, the ca. 86 Ma age of spot 2 for Mnz2 appears to be entirely within the high Y rim (Fig. 3.6e). This may suggest that the high Y rim is indeed older than ca. 77 Ma in some of the monazite crystals, or that the spot penetrated the older Y domain in z-direction. However, incursion of an older domain in the z-direction is considered unlikely because of the restricted depth of the spots (~ 2 µm), but it cannot be completely ruled out. The identified age domains were correlated with a series of prograde and retrograde reactions (Chapter 4), and have been used to provide absolute timing constraints on a P-T-t path for this sample that is interpreted to have diachronously evolved from pre-144 Ma to 73 Ma (Fig. 3.10b).

DG225 – Ms-Grt-Ky-Bt pelitic schist (IDTIMS and SHRIMP)

This sample comes from a migmatitic Ms-Grt-Ky-Bt pelitic schist collected at Warsaw Mountain, in the Ky-zone within the eastern flank of the fan (Fig. 3.3b). In outcrop, the leucosome is highly strained, showing evidence of dismemberment due to shearing as well as Type 2 and Type 3 fold interference patterns (Ramsay, 1967). In thin section (Fig.3.4l-m), the textures and fabrics observed are very similar to those described for DG38a, with kyanite, biotite, and muscovite aligned within the moderate to shallow southwest dipping transposition foliation, S_2. Kyanite and garnet grains show evidence of having been variably resorbed, and elongate garnets concordant with S_2 have inclusion-rich cores surrounded by inclusion-free rims. Most monazite grains are subhedral, and occur primarily as inclusions in biotite and along biotite grain boundaries.

Four single-grain monazite fractions analyzed by IDTIMS have minor normal discordance (4.2 to 5.5%; Table 3.3) and lie on a chord near the concordia curve (Fig. 3.7a). Their $^{207}Pb/^{206}Pb$ ages range between ca. 102-90 Ma; a discordia line yielded an imprecise U.I. of 119 ± 45 Ma. SHRIMP analyses confirmed the existence of multiple age domains within the monazite grains of this sample. Seven spot analyses on three monazites yielded ages between 104-62 Ma, which were initially divided into two age groups (Fig. 3.7b-d). The spots within the interior domains of the monazite crystals have a weighted $^{208}Pb/^{232}Th$ mean age of 97.6 ± 4.7 Ma (Fig. 3.4d), with an age range between 103.9 ± 1.6 Ma and 92.2 ± 1.4 Ma. However, based on the Th maps, as opposed to the Y maps, the interior domain may be further subdivided into two groups; an older ca. 103 Ma, higher Th domain, and a younger ca. 93 Ma, lower Th domain. The other age domain consisted of a single spot within the rim of Mnz6 (Fig. 3.7e) that produced a

$^{208}Pb/^{232}Th$ age of 61.9 ± 1.0. These data are interpreted to represent the timing of diachronous and possibly episodic monazite growth during prograde metamorphism from ca. 104-92.2 Ma, followed by a rim overgrowth that likely grew during retrograde metamorphism related to decompression (?) at ca. 62 Ma.

DG216 – Bt-Grt-St-Ms pelitic schist (IDTIMS and SHRIMP)

Sample DG216 comes from a Bt-Grt-St-Ms pelitic schist that was collected on the shore of Redrock Harbour within the Ky-St-zone situated in the east flank of the fan (Fig. 3.3b). It should be noted that kyanite was not observed in either hand sample or thin section.

In thin section (Fig. 3.4n-o), quartz inclusion trails within cores of staurolite and garnet define an interior fabric (S_i), that is oriented at a high angle to the external foliation, S_e, equated with S_2. It is likely that S_i represents an early stage in the development of S_2, but S_2 continued to develop following initial M_1 garnet and staurolite growth, such that S_2 is now oriented at a high angle to S_i. The anhedral M_1 cores are overgrown by uniform, inclusion-free, euhedral rims, M_2, that appear to truncate most of the S_e foliation, which has been crenulated by F_3 (Fig. 3.4n), suggesting that some of the staurolite and garnet recrystallization occurred during or after D_3. However, the deflection of biotite and muscovite around the staurolite at the bottom of Fig. 3.4n near the scale bar suggests D_3 continued to develop following M_2.

Monazite grains were difficult to identify in thin section, and were quite sparse and hard to distinguish in the mineral separates for this sample due to the abundance of staurolite crystals that have the same magnetic properties as monazite. The few monazite grains that were identified had a peculiar slight greenish-yellow hue, which was not observed in any of the monazites separated from higher-grade samples. Two single-grain fractions analyzed by IDTIMS are normally discordant (8.6% and 9.2%), with $^{207}Pb/^{206}Pb$ ages of 127.1 ± 3.4 Ma and 126.6 ± 7.0 Ma (Table 3.3). Again, SHRIMP analyses demonstrated that the monazites contained at least three and possibly four age domains (Fig. 3.8b-d; Table 3.4). The chemical maps for Th and Y display a progressive decrease in concentration of these elements from core to mantle, and then a slight increase toward the rim (Fig. 3.8e). Although the chemical zoning is diffuse, the five SHRIMP analyses on three monazite crystals strongly suggest that they contain at least three age domains. The high Y-Th interior has a mean $^{208}Pb/^{232}Th$ age of 127.6 ± 8.3 Ma, surrounded by a younger, lower Y-Th mantle that is 114.2 ± 1.7 Ma, which is rimmed by intermediate Y-Th monazite that is 81.8 ± 2.9 Ma.

The two interior age domains identified are interpreted to represent metamorphic monazite grown during prograde metamorphism at this locality from ca. 128-114 Ma. The gradual shift in both the Y and Th concentration is likely due to the growth of other metamorphic minerals, such as garnet, that can significantly affect the availability of these elements, especially Y (see Chapter 4; Bea and Montero, 1999; Foster et al., 2000; Pyle et al., 2001; Foster et al., 2002; Pyle and Spear, 2002, 2003; Zhu and O'Nions, 1999a). The rim overgrowth is likely related to retrograde metamorphism that resulted in the growth of crosscutting chlorite observed in this sample (Figs. 3.4o and 3.10).

DG254 – Ms-St-Ky-Grt-Bt pelitic schist (IDTIMS and SHRIMP)

Located within the Ky-St-zone on the east flank of the fan, DG254 was sampled from a migmatitic Ms-St-Ky-Grt-Bt pelitic schist that has ~15% leucosome. Alignment of muscovite, kyanite and biotite laths define the transposition foliation, S_2, that dips ~30° to the southwest. In thin section, staurolite is highly resorbed and appears to be have been replaced primarily by quartz, biotite and garnet. Kyanite commonly appears as subhedral laths that are aligned within the foliation and deflected around garnet porphyroclasts (Fig. 3.4p-q). Cores within garnet contain helicitic quartz inclusion trails, S_i, that range from being concordant to highly discordant with S_e, i.e., S_2. The inclusion trails were variably crenulated during initial garnet growth, to the point that some of the trails in certain garnet porphyroblasts were completely reoriented parallel with S_2. A thin inclusion-free rim is found on most garnet porphyroblasts, around which the foliation and some chlorite grains are deflected. Most of the monazite growth in this sample is interpreted to have postdated that of biotite and muscovite. This is based on textures showing evidence of forceful impingement of monazite grain boundaries into the biotite and muscovite (Fig. 3.4q), and the preferential growth of monazite in cracks when it is found as an included mineral.

Three single-grain, clear yellow, anhedral monazite fractions plus one multigrain fraction were analyzed by IDTIMS. The data are normally discordant between 4.7% to 17.7% (Table 3.3), and plot in a tight cluster just beneath the concordia curve at ca. 62 Ma (Fig. 3.9a). Their $^{207}Pb/^{206}Pb$ ages range between 75.0 ± 6.2 to 64.6 ± 4.5 Ma (Table 3.3). These data indicate that there must have been some age mixing within the monazite crystals analyzed. However, the older monazite component must have been negligible as compared to the younger component since the data tightly cluster immediately below the concordia curve at 62 Ma (Fig. 3.9a), otherwise a more significant spread would be expected. The chemical maps did reveal some zoning in the monazite grains from this sample, especially in the Th maps (Fig. 3.9e), which suggested there was a low Th core surrounded by a higher Th rim. However, the SHRIMP analyses were unable to provide evidence for individual age domains within the Th zones described above (Fig. 3.9b-d; Table 3.4). Four spots on two monazite crystals yielded $^{208}Pb/^{232}Th$ ages that range between 56.9-55.5 Ma, resulting in a very tight cluster just above the concordia curve at 56 Ma in U-Th-Pb concordia space (Fig. 3.9c). In U-Pb concordia space, analyses 2-2 and 3-2 appear to be normally discordant below the concordia curve (Fig. 3.9b), suggesting that they may include a slightly older monazite component not present in the other two spots, 2-1 and 3-1. However, since this does not manifest itself in the U-Th-Pb concordia diagram, which uses the most precise U-Th-Pb ratios, the normal discordance is likely attributable to the imprecision imparted by the ^{204}Pb correction on the $^{207}Pb/^{235}U$ ratios. As such, the weighted mean of the $^{208}Pb/^{232}Th$ ages of 56.3 ± 0.9 Ma is interpreted to be the best approximation of timing for the most recent monazite growth in this sample.

The reasons why the older monazite component indicated by the IDTIMS analyses was not detected by the *in situ* SHRIMP analyses remains enigmatic. This may be due to the limited number of SHRIMP analyses for this sample (i.e., four); perhaps the older age domains would have been detected if a greater number of monazite crystals had been analyzed. However, the monazites analyzed by the SHRIMP were picked from the same magnetic fraction as those analyzed by IDTIMS, all of which indicated an older age component. Possibly, the discrepancy between the IDTIMS and SHRIMP analyses is due instead to the difference in the analytical precision achieved by the two techniques. Perhaps the monazite grains in this sample were so severely overprinted at 56 Ma that the SHRIMP was not able to detect the trace of the older component preserved within.

Whereas, the greater analytical precision provided by the IDTIMS analyses facilitated the recognition of this older monazite component. Based on the above data, these monazites are inferred to have grown during a period that spanned from at least ca. 75 to 56 Ma, which may represent points along both the prograde (ca. 75-65 Ma = IDTIMS $^{207}Pb/^{206}Pb$ ages) and retrograde (ca. 56 Ma = SHRIMP weighted mean age) P-T-t path of this sample (Fig. 3.10e).

3. 6. Discussion

U-Th-Pb geochronologic data attained by IDTIMS and *in situ* SHRIMP analyses of metamorphic monazite from pelitic schists significantly refine the timing of metamorphism associated with the development of the Selkirk fan within the northern Selkirk Mountains. The data demonstrate that metamorphism in the axis (Domain 2) and east flank of the fan (Domain 3) was strongly diachronous, ranging in age from at least 144 to 56 Ma. An attempt has been made to place the geochronologic data within P-T-t space (Fig. 3.10), but are considered a qualitative first order approximation because geothermobarometry studies on the dated samples were not carried out. Nevertheless, there is a certain degree of confidence in the placement of ages because it is based on textural observations in thin section, and a comparison of chemical maps of the analyzed monazite grains with monazite inclusions within kyanite and garnet (see Chapter 4). In addition, *in situ* analyses of monazite crystals included within kyanite and garnet of a sample from the base of Fred Laing Ridge along Highway 23 (Sample 1 of Crowley et al., 2000), corroborate the Early to Late Cretaceous growth of kyanite and garnet as suggested in the P-T-t diagrams of Fig. 3.10. Future investigations will be conducted to test these interpretations.

The new age constraints provided by this study agree well with those provided in the northern Monashee Mountains to the west, and thus, appear to reconcile the apparent geochronologic contradiction between the northern Selkirk Mountains and northern Monashee Mountains as discussed earlier in the Introduction section of Chapter 2. In addition, the Cretaceous-Tertiary metamorphism elucidated in this study is interpreted to have overprinted a pre-existing Middle Jurassic assemblage (Chapter 2). The U-Th-Pb isotopic data associated with the Middle Jurassic assemblage is no longer preserved within the east flank of the fan at the latitude of this study, but is preserved within the lower grade, higher structural levels of the west flank (Domain 1). In the east flank, the absence of the Middle Jurassic ages is interpreted to be the consequence of the intense medium- to high-grade Cretaceous-Tertiary overprint. The processes of resorption and recrystallization that would accompany such an overprint, as demonstrated by some of the monazites imaged in this study (e.g., DG38a, Mnz's 4, 9, 10 of Fig. 3.6), may have completely erased or reset the Jurassic isotopic systems of these monazites. Support for this interpretation also comes from the Middle Jurassic ages, ca. 163 Ma, documented by Crowley et al. (2000) for metamorphic monazite within the northern Monashee Mountains ~7-20 km to the north. The lithostratigraphy, and northeast vergent folds and transposition foliation are considered to be part of the same package of rocks found within the east flank of the fan examined in this study. The Middle Jurassic ages documented by Crowley et al. are confined to areas of relatively lower metamorphic grade (i.e., Bt-Grt grade), and presumably higher structural level as compared to the Ky-Sil grade rocks examined in this study. Thus, the Cretaceous-Tertiary overprint appears to be mostly confined to the deeper structural levels that experienced the highest metamorphic pressures and temperatures. However, there is evidence of a Cretaceous overprint in the west flank of the study area, albeit to a much lesser extent; a thin ca. 92 Ma metamorphic rim was found on an igneous zircon from a deformed ca. 170 Ma dike (CT07, Chapter 2, p.32) near the Bigmouth pluton. Also, unpublished $^{40}Ar/^{39}Ar$ cooling ages (M. Colpron, 1997, pers. comm.; Table 3.1) for muscovite and biotite within the west flank of this study area suggest Early to Late Cretaceous heating and subsequent cooling through their respective closure temperatures of 350ºC and 300ºC (Hanes, 1991). This overprint was not detected further south in the Illecillewaet synclinorium, where Colpron et al. (1996) documented Middle Jurassic cooling ages for hornblende, muscovite and biotite (Table 3.1). This discrepancy and the patchy preservation of Middle Jurassic ages in the northern Monashee Mountains is not fully understood, but is most likely a function of structural level (e.g., Reid, 2003; Chapter 2), such that the intensity of the Cretaceous overprint increases with depth. Other factors such as variable conduction-advection of heat from deeper structural levels, asymmetry of isogradic surfaces (Ghent et al., 1980) and hydrothermal perturbations (e.g., Digel et al., 1999) may also have had a significant influence.

The data imply that the mineral assemblage and associated transposition foliation represent composite metamorphic and structural features that were likely developed initially in the Middle Jurassic, and were either progressively or episodically overprinted during the Cretaceous, and that the overprint was more pronounced at deeper levels. Future work in this region should include a detailed study that investigates the component of the mineral assemblages that is related to Jurassic versus Cretaceous metamorphism. Also, in light of this data, the series of metamorphic isograds for the region needs to be reexamined, because they were established based on mapping of metamorphic assemblages that were assumed to have formed during one event in the Middle Jurassic (e.g., Wheeler, 1965; Leatherbarrow, 1981). The relatively simple configuration of isograds that parallel each other across the region (Fig. 3.3, Map 2), which includes structural levels that were apparently exhumed and quenched at disparate times, seems fortuitous.

What does this imply with regard to the thermo-mechanical processes responsible for the observed configuration of isotopic ages, metamorphic isograds, and structures? Presumably in the Middle Jurassic, the strata of the eastern flank were initially buried, deformed and metamorphosed within upper crustal levels. Perhaps, as the fan continued to develop and migrate eastward during the Cretaceous, a significant portion of the east flank was taken to deeper levels, and remained there until exhumation in the Late Cretaceous-Early Tertiary. During this protracted period of time the Middle Jurassic transposition foliation and associated metamorphic assemblage would have been progressively or episodically reactivated and recrystallized because the original foliation surfaces would represent pre-existing planes of weakness that Cretaceous strain would naturally exploit.

Alternatively, the deepest levels exposed in the east flank may represent rocks that were originally located significantly east of the initial position of the fan and were not buried until the Cretaceous. In this scenario, as the fan expanded eastward rocks would be buried or underplated (cf. Brown, 2003), metamorphosed and exhumed within the east flank at progressively younger times. If this is correct we should expect to see the initial burial and heating ages become younger eastward, but this was not clearly demonstrated in the data set for the east flank. However, this expectation may be overly simplistic considering the complex three-dimensional geometry that likely characterized this lower crustal zone (cf. Ghent et al., 1980). Also, it is difficult to predict the convoluted burial-exhumation paths rocks may have followed during distributed ductile strain (e.g., Jamieson et al., 1996, 1998), channel flow (e.g., Beaumont et al., 2001), or out-of-sequence deformation.

Clearly, uncertainties remain with regard to the thermo-mechanical processes involved in the evolution of the Selkirk fan. Perhaps some combination of both scenarios discussed above was responsible for the observed distribution of metamorphic ages in this region. Nevertheless, it is clear that previously proposed tectonic models for the development of the Selkirk fan need to be significantly revised. A conceptual model is presented in Chapter 5 that attempts to reconcile these data.

3. 7. Conclusions

The integration of U-Pb IDTIMS, *in situ* U-Th-Pb SHRIMP analyses, and chemical mapping of pelitic monazite significantly refined the timing of metamorphism associated with the development of the Selkirk fan within the northern Selkirk Mountains of the southern Canadian Cordillera. The data also reconcile an apparent geochronologic contradiction between the northern Selkirk Mountains and adjacent northern Monashee Mountains to the west. The age constraints provided by this study demonstrate that metamorphism in the axis and east flank of the Selkirk fan was strongly diachronous, ranging in age from at least 144 to 56 Ma. The Cretaceous-Tertiary metamorphic and structural elements documented in the east flank may have overprinted pre-existing Middle Jurassic structures (ca. 172-167 Ma, Chapter 2) and the associated metamorphic assemblage, which have been identified within higher structural levels of the fan. The degree of overprinting appears to have been a function of structural level, and is interpreted to have been most intense in the deepest levels of the east flank where the isotopic evidence associated with the Middle Jurassic event is absent.

This study may have far reaching implications with regard to metamorphic and deformation processes that were active in other orogenic belts with similar tectonic features. Most specifically, the development of a middle to lower crustal zone that continuously remained at depth for up to ~100 M.y. has neither been previously identified nor modeled (e.g., Jamieson et al., 1996, 1998; Beaumont et al., 2001). Perhaps, this suggests that without the benefit of *in situ* U-Th-Pb analyses, chemical mapping and integration of regional data sets, the apparent protracted nature of the metamorphic and deformation processes identified in this study may have been overlooked in other orogens. Alternatively, this may be a feature unique to the Cordilleran orogen.

Table 3.1. Summary of Previous U-Th-Pb Age Constraints for Metamorphism in the Northern Selkirk Mountains, British Columbia[a]

Sample	Lithology[b]	Textures and Fabrics[c]	Age Constraints[d]	Location UTM
Crowley et al. (2000) northernmost Selkirk Mountain – East flank of fan				
1	Migmatitic Ms-Grt-Ky-Bt schist; Lower Pelite unit of the Windermere Supergroup (SG)	S_{1+2} defined by aligned Ky, Bt, and Ms, which wraps around Grt; Grt has internal foliation discordant to S_{+2}	IDTIMS analyses spread out b/w ca. 77-70 Ma strongly suggest age mixing; SHRIMP spot ages of ca. 113-109 Ma for Mnz inclusions in Grt rim, and 83-73 Ma for Mnz inclusions in Ky; Spot ages of ca. 84-73 Ma for cores of matrix Mnz and ca. 64-61 Ma for rims	HWY 23, 0.5 km south of Mica Dam E393200 N5770350
3	Migmatitic Grt-Bt-Ky schist; Lower Pelite unit of the Windermere SG	Bt highly chloritized; Elongate Mnz w/in S_{1+2} along Bt, Qtz, and Ky grain boundaries	Three IDTIMS analyses plot on or near concordia with $^{207}Pb/^{235}U$ ages b/w ca. 132 to 124 Ma; A fourth analysis is normally discordant w/ a $^{207}Pb/^{235}U$ age of ca. 126 Ma. Analyzed Mnz are interpreted as a mixture of domains that grew before and after 132 and 124 Ma	HWY 23 at Potlach Creek E393200 N5770800
26	Migmatitic Grt- Bt-Ms-Ky schist; Lower Pelite unit of the Windermere SG	Large, elongate Mnz grains lie w/in S_{1+2}, mostly as inclusions in Bt, and along Bt, Qtz, Ky grain boundaries	Mnz w/ complex zoning, indicating multiple age domains; Four reversely discordant IDTIMS analyses = ca. 112-93 Ma; Three normally discordant analyses = 111-98 Ma w/ $^{207}Pb/^{206}Pb$ ages = 136-101 Ma; One concordant fraction has a $^{207}Pb/^{235}U$ age of ca. 94 Ma	HWY 23, ~2km south of Mica Cr. Village E392500 N5760000
Marchildon (1999) Bigmouth pluton (BMP) – West flank of fan				
BMP	Kfs-megacrystic, Hbl-Bt bearing, Qtz-monzonite	Coarse grained; weak foliation defined by aligned Kfs and Hbl; transposed xenoliths found near margin	Discordant Zrn w/ Precambrian xenocrystic cores produced imprecise lower intercept of ca. 157 Ma, interpreted as age of syn- tectonic pluton and M_1 metamorphism; Ttn ca. 139 Ma interpreted as time of thermal resetting of Ttn during M_2 metamorphism	mid-east part of the pluton E401700 N5741100
Shaw (1980) Adamant pluton (AP) – Southwest corner of pluton within west flank of fan				
Group C	Hyp-Aug core enclosed by Bt-Hbl granodiorite	Bt-Hbl granodiorite w/ weak F_2 and S_2 fabric; pluton interpreted to be pre-tectonic	Zrn age of ca. 169 Ma interpreted as time of metamorphic recrystallization of outer zone of pluton, which is thought to be late D_2 and pre-D_3	SW corner of the pluton E421885 N5729200
Colpron (1997, written communication) Argonaut Pass-Goldstream pluton-Long Creek stock-Adamant pluton – West flank of fan				
Argonaut Pass	Bt-Ms-Qtz schist of the Lardeau Group	Not Avail.; minerals assumed to be aligned within the regional NE-dipping foliation (S_2)	$^{40}Ar/^{39}Ar$ Ms cooling age = 76 ± 0.8 Ma (Tc = 350 ± 50°C; Hanes, 1991) Bt cooling age = 76 ± 0.7 Ma (Tc = 300 ± 50°C; Hanes, 1991)	~4 km west of Argonaut Pass E396000 N5718600
Goldstream mine	Black phyllite of the Lardeau Group	Not Available	$^{40}Ar/^{39}Ar$ Ms cooling age = 97 ± 0.9 Ma	Goldstream mine E401300 N5720000

[a]Summary is presented from north to south. [b]Mineral abbreviations after Kretz (1983); only major rock forming minerals listed. [c]Texture and fabric description as provided by author of each study. [d]Quoted monazite (Mnz) IDTIMS ages based on $^{207}Pb/^{235}U$ ratio, SHRIMP ages based on $^{208}Pb/^{232}Th$ ratio; Zircon (Zrn) and titanite (Tnt) ages are based on the $^{206}Pb/^{238}U$ ratio. [e]The Kfs $^{40}Ar/^{39}Ar$ cooling ages not included for Colpron et al. (1996)

Table 3.1. (concluded)

Sample	Lithology[b]	Textures and Fabrics[c]	Age Constraints[d]	Location UTM
Colpron (1997, written communication) cont.				
Hitchhiker Peak	Upper Pelite unit of Windermere SG	Not Available	$^{40}Ar/^{39}Ar$ Ms cooling age = 75 ± 0.9 Ma; Bt cooling age 90 ± 0.9 Ma; older Bt age interpreted to be the result of excess Argon	Hitchhiker Peak E421000 N5726500
Goldstream pluton area	Qtz grit of Lardeau Group	Not Available	$^{40}Ar/^{39}Ar$ Ms cooling age = 101 ± 1 Ma; nearly the same age as the U-Pb zircon age of 104 ± 1.6 Ma (Logan and Friedman, 1997)	Near north contact Goldstream pluton E394750 N5718700
Sorcerer Creek	Laminated phyllite, Upper pelite of Windermere SG	Not Available	$^{40}Ar/^{39}Ar$ Ms cooling age = 143 ± 1 Ma	Sorcerer Creek area E421400 N5710800
Colpron et al. (1996)[e] Illecillewaet Synclinorium – West flank of fan				
423 and 370b Fang pluton	Hbl-Bt Qtz-monzonite with Kfs-megacrysts	Coarse-grained; no apparent foliation; foliated (S_2) xenoliths near margin; surface traces of SW vergent folds and faults appear to be deflected around margin of the pluton	$^{40}Ar/^{39}Ar$ - Sample 423 – Hbl cooling age = 169 ± 1.3 Ma (Tc = 500 ± 50°C, Hanes, 1991); Bt cooling age = 167 ± 0.7 Ma; Sample 370b – Ms cooling age = 168 ± 0.7 Ma; interpreted late syn-kinematic pluton emplacement prior to the cessation of SW vergent deformation and regional metamorphism; the cooling ages are interpreted to indicate rapid exhumation during the latest stages of SW vergent deformation	Fang pluton Sample 423 E436575 N5681849 Sample 370b E435444 N5684467
271 Tangier	Tangier stock; Same as Fang pluton	Same as Fang pluton (above)	$^{40}Ar/^{39}Ar$ - Sample 271 Hbl cooling age = 171 ± 2.4 Ma; Bt cooling age = 165 ± 0.9 Ma; Same interpretation as for Fang pluton.	Tangier stock E441527 N5682017
319b Corbin stock	Hbl-Bt granodiorite w/ Kfs phenocrysts	Medium-grained; truncates strat. and structures; no tectonic foliation; magmatic banding parallel to margins	$^{40}Ar/^{39}Ar$ - Sample 319b Hbl cooling age = 176 ± 1.9 Ma; Bt cooling age = 156 ± 1.1 Ma; same interpretation for Fang pluton and Tangier stock to the west, except that the younger Bt cooling age may indicate Corbin stock was exhumed later and possibly at a slower rate	Corbin stock E446605 N5680358
401c Lanark stock	Same as Corbin stock	Same as Corbin stock, except there is no magmatic banding	$^{40}Ar/^{39}Ar$ - Sample 401c Hbl cooling age = 168 ± 0.9 Ma; Bt cooling age = 131 ± 1.2 Ma; Sample 403 Ms cooling age = 157 ± 1 Ma; the younger Bt and Ms cooling ages for Lanark stock, the easternmost intrusive analyzed in the Illecillewaet synclinorium, further supports the idea of more rapid exhumation rates from west to east	Lanark stock Sample 401c E451177 N5676037 Sample 403 E451451 N5676009
Brown et al. (1992) Fang and Pass Creek Plutons – West flank of fan				
RB 21 Fang pluton	Kfs-megacrystic, Hbl-Bt Qtz-monzonite	See sample 423 above, except deflection of structures around the pluton attributed to D_3 strain	Igneous Zrn with xenocrystic cores (≥1950 Ma) crystallized ca. 168 ± 2 Ma, interpreted as pluton age that post-dates peak metamorphism and D_2 deformation, but pre-dates D_3	Fang pluton E436708 N5684600
R502 Pass Cr. pluton	Same as Fang pluton (above)	Same as Fang pluton (above)	Concordant Ttn at 168 ± 3 Ma interpreted as age for post-tectonic (D_2) pluton following the peak of metamorphism; possibly pre-dates D_3	Pass Creek pluton E419250 N5692230

Table 3.2. This Study: U-Th-Pb Age Constraints on Metamorphism, Northern Selkirk Mountains, British Columbia

Sample	Lithology[b]	Textures and Fabrics	Age Constraints[c]	Location UTM
Domain 2: Transition zone (fan axis) – French Glacier and Argonaut Mountain				
DG01	Migmatitic Ms-Grt-Sil-Bt schist; Upper Pelite unit of the Windermere Supergroup	S_2 defined by aligned Bt-Ms; Grt very resorbed, commonly replaced by mats of Sil on Bt substrate; Sil randomly oriented	IDTIMS – two fraction just above the concordia curve at **ca. 92 Ma**, interpreted to approximate timing of Sil overprint, which post-dated initial S_2 development in the Middle Jurassic (See chapter 2)	French Glacier E415159 N5735272 Elevation 1825 m
DG70b	Migmatitic Grt-Sil-Bt-Ms schist; Pelite unit, possibly of Lardeau Group	S_2 defined by aligned Bt-Ms; Grt strongly resorbed, usually replaced by mats of Sil on Bt substrate; Sil randomly oriented	IDTIMS – five fractions with varying degrees of reverse discordance that range in age between **ca. 100-95 Ma**, interpreted to approximate timing of Sil-grade metamorphism	Argonaut Mountain E410710 N5738202 Elevation 2450 m
Domain 3: East Flank – Mud Glacier area				
DG23	Migmatitic Ms-Grt-Sil-Bt schist; SPA unit of the Windermere Supergroup	S_2 defined by Bt, but also crosscut by it; late euhedral Ms crosscuts S_2; Grt very resorbed; Coarse and fine Sil crosscut S_2; Large, elongate Mnz lie within S_2, mostly as inclusions in Bt, and along Bt grain boundaries	IDTIMS – four fraction with slight reverse discordance that range in age between **ca. 94-92 Ma**, interpreted to approximate timing of Sil-grade metamorphism	~3 km southwest of Mud Glacier E392500 N5760000 Elevation 2160 m
DG38a	Migmatitic Ms-Grt-Ky-Bt schist with up to 30% melt; SPA unit of the Windermere Supergroup	S_2 defined by Bt-Ms-Ky; Grt-Ky variably resorbed; Grt has inclusions in core surrounded by inclusion-free rim; most Mnz lie w/in S_2, mostly as inclusions in Bt, and along Bt grain boundaries	IDTIMS – four Mnz fractions with slight reverse and normal discordance range in age between **ca. 123-103 Ma** SHRIMP – sixteen *in situ* analyses on seven Mnz produced ages ranging between **144-76 Ma**; ages separated into three groups based on the mean $^{208}Pb/^{232}Th$ ages for domains of relative Y enrichment or depletion, such that **ca. 139 Ma = low Y domain, 126 Ma = intermediate Y domain, and 77 Ma = high Y rim**; interpreted to approximate timing of episodes of prograde metamorphism	~3.3 km northeast of Mud Glacier E405249 N5758404 Elevation 2020 m

[a]Summary is presented in approximate geographic order from west to east across the fan
[b]Mineral abbreviations after Kretz (1983); only optically identified major rock forming minerals listed
[c]Quoted monazite (Mnz) ages are based on $^{207}Pb/^{235}U$ (IDTIMS) or $^{208}Pb/^{232}Th$ (SHRIMP) isotopic ratios, unless otherwise noted

Table 3.2. (concluded)

Domain 3: East Flank – Fred Laing Ridge, Warsaw Mountain, Redrock Harbour and Townsends Ridge

Sample	Lithology[b]	Textures and Fabrics[c]	Age Constraints[d]	Location UTM
DG206	Migmatitic Ms-Grt-Ky-Bt schist, with up to 40% melt; SPA unit of the Windermere Supergroup	S_2 defined by Bt-Ms-Ky; Grt-Ky variably resorbed; Grt has inclusions in core surrounded by inclusion-free rim; many Grt are oblate concordant with S_2; Mnz are subhedral inclusions in Bt, and along grain boundaries	IDTIMS – four Mnz fractions with variable reverse and normal discordance lie in a chord near the concordia curve with $^{207}Pb/^{235}U$ ages between 79.9-70.8 Ma; the oldest $^{207}Pb/^{206}Pb$ age for fraction M2 with normal discordance is 84.0 Ma; an imprecise U.I. for a discordia chord yields an age of 155 ± 210 Ma, but is considered speculative; **ca. 84 Ma** is interpreted to be minimum age for the oldest Mnz growth; **ca. 70.8 Ma** is thought to be timing of most recent Mnz growth	Fred Laing Ridge E395660 N5767735 Elevation 2120 m
DG225	Migmatitic Ms-Grt-Ky-Bt schist, ~30-40% melt; Lower Pelite unit of the Windermere Supergroup	S_2 defined by Bt-Ms-Ky; Grt-Ky variably resorbed; Grt has inclusions in core surrounded by inclusion-free rim; many Grt are oblate concordant with S_2; most Mnz are subhedral inclusions in Bt, and along Bt grain boundaries	IDTIMS – four Mnz fractions with minor normal discordance (4.2-5.5 %) lie on a chord near the concordia curve with $^{207}Pb/^{235}U$ ages between **96.3-86.6 Ma**; the $^{207}Pb/^{206}Pb$ ages range between **101.9-90.4 Ma**; an imprecise U.I. for a discordia chord yields 119 ± 45 Ma SHRIMP – seven *in situ* analyses on three Mnz yield ages of **103.9-61.9 Ma,** separated into two groups based on the mean $^{208}Pb/^{232}Th$ ages for domains of relative Y enrichment or depletion, **ca. 98 Ma = intermediate Y domain, and 62 Ma = low Y rim**, approximate timing of prograde and retrograde metamorphism, respectively	Warsaw Mountain E401527 N5764073 Elevation 2315m
DG216	Bt-Grt-St-Ms schist; Lower Pelite unit of the Windermere Supergroup	S_2 is preserved as Qtz inclusion trails (S_i) within M_1cores of Grt and St, overgrown by homogenous, inclusion-free M_2 rims; external foliation, S_e, occurs at a high angle to S_i; S_e has been crenulated by F_3	IDTIMS – two Mnz fractions are normally discordant with $^{207}Pb/^{206}Pb$ ages ranging between **127.1-126.6 Ma**; SHRIMP – five *in situ* analyses on three Mnz yielded ages between **131.3-81.1 Ma**; separated into three age groups based on the mean $^{208}Pb/^{232}Th$ ages for domains of relative Y-Th enrichment or depletion, **ca. 128 Ma = core, 114 Ma = mantle, and 81 ± 1 Ma = rim**; two older ages thought to constrain timing of prograde metamorphism, while the younger rim likely grew during retrograde metamorphism	Redrock Harbour E406140 N5771380 Elevation 750m
DG254	Ms-St-Ky-Grt-Bt schist; Lower Pelite unit of the Windermere Supergroup	Ms-Ky-Bt aligned within S_2; inclusion trails, S_i, in Grt cores are both typically perpendicular with S_e, i.e. S_2, ; inclusion trails often crenulated with axial planes // to S_e; inclusion free Grt rims crosscut S_e	IDTIMS – four Mnz fractions are normally discordant with $^{207}Pb/^{206}Pb$ ages ranging between 75.0-64.6 Ma; **75 Ma** interpreted to be minimum age of Mnz growth associated with prograde metamorphism SHRIMP – four *in situ* analyses on two Mnz yielded $^{208}Pb/^{232}Th$ ages between **56.9-55.5 Ma,** tightly clustered immediately above the concordia curve in a U-Th-Pb concordia diagram, with a weighted mean $^{208}Pb/^{232}Th$ age of **56.3 ± 0.9 Ma**; may be timing of last gasp of high-grade metamorphism prior to regional extensional faulting	Townsends Ridge E426849 N5752933 Elevation 2110m

Table 3.3. U-Pb IDTIMS Analytical Data for Northern Selkirk Mountains, British Columbi

Fraction[a]	Wt.[b] (µg)	U (ppm)	Pb*[c] (ppm)	$\frac{^{206}Pb}{^{204}Pb}$[d]	Pb[e] (pg)	^{208}Pb (%)[f]	$\frac{^{206}Pb}{^{238}U}$[g]	$\frac{^{207}Pb}{^{235}U}$[g]	$\frac{^{206}Pb}{^{238}U}$[h] (Ma)	$\frac{^{207}Pb}{^{235}U}$[h] (Ma)	Corr.[i] Coeff.	$\frac{^{207}Pb}{^{206}Pb}$[h]	$\frac{^{207}Pb}{^{206}Pb}$[g] (Ma)	Disc.[j] (%)
DG01 Ms-Grt-Sil-Bt Pelitic Schist							**Domain 2: French Glacier**							
M2 105-149	5	957	202	606	7	93.7	0.014625 ± 0.90 %	0.09468 ± 1.60 %	93.6 ± 1.7	91.9 ± 2.8	0.78	0.04696 ± 1.05 %	47.0 ± 50.1	-100.0
M3 105-149	5	2529	270	727	16	87.6	0.014556 ± 0.78 %	0.09405 ± 1.33 %	93.2 ± 1.4	91.3 ± 2.3	0.51	0.04686 ± 1.16 %	42.1 ± 55.3	—
A* <74	3	1215	104	1669	12	4.0	0.085508 ± 0.28 %	1.40648 ± 0.33 %	528.9 ± 2.8	891.7 ± 3.9	0.86	0.11930 ± 0.17 %	1945.7 ± 6.0	75.7
C* 74-149	5	534	82	1473	16	9.2	0.144401 ± 0.20 %	2.31679 ± 0.16 %	869.5 ± 3.3	1217.4 ± 1.3	0.52	0.11636 ± 0.18 %	1901.1 ± 6.5	57.9
DG70b Ms-Grt-Sil-Bt Pelitic Schist							**Domain 2: Argonaut Mountain**							
M1 74-105	3	4280	199	1075	12	69.8	0.015463 ± 0.63 %	0.10205 ± 0.79 %	98.9 ± 1.2	98.7 ± 1.5	0.67	0.04787 ± 0.59 %	92.6 ± 28.0	-6.8
M4 74-105	3	3168	134	967	10	63.8	0.015686 ± 0.35 %	0.10309 ± 0.68 %	100.3 ± 0.7	99.6 ± 1.3	0.55	0.04767 ± 0.57 %	82.7 ± 27.2	-21.4
M5 105-149	5	6599	242	3046	10	63.0	0.014956 ± 0.17 %	0.09771 ± 0.27 %	95.7 ± 0.3	94.7 ± 0.5	0.64	0.04738 ± 0.20 %	68.4 ± 9.7	-40.1
M6 74-105	2	7258	284	2343	6	64.4	0.015382 ± 0.14 %	0.10216 ± 0.27 %	98.4 ± 0.3	98.8 ± 0.5	0.51	0.04817 ± 0.23 %	107.5 ± 10.8	8.5
M7 74-105	3	3465	163	844	12	70.5	0.015308 ± 0.26 %	0.10002 ± 0.86 %	97.9 ± 0.5	96.8 ± 1.6	0.30	0.04739 ± 0.82 %	68.9 ± 39.0	-42.4
DG23 Grt-Sil-Bt Pelitic Schist							**Domain 3: Southwest of Mud Glacier**							
M2 105-149	9	3513	196	868	35	76.0	0.014743 ± 0.28 %	0.09724 ± 0.47 %	94.3 ± 0.5	94.2 ± 0.9	0.50	0.04784 ± 0.41 %	91.1 ± 19.5	-3.5
M4 105-149	2	15727	747	2192	13	72.5	0.014437 ± 0.29 %	0.09441 ± 0.36 %	92.4 ± 0.5	91.6 ± 0.6	0.76	0.04743 ± 0.23 %	71.0 ± 11.1	-30.4
M5 105-149	7	4890	205	4345	7	68.0	0.014868 ± 0.19 %	0.09494 ± 0.22 %	95.1 ± 0.4	92.1 ± 0.4	0.70	0.04631 ± 0.16 %	14.0 ± 7.7	—
M6 105-149	2	13865	675	4383	6	72.8	0.014607 ± 0.13 %	0.09648 ± 0.18 %	93.5 ± 0.3	93.5 ± 0.3	0.68	0.04790 ± 0.13 %	94.4 ± 6.3	1.0
DG38a Ms-Grt-Ky-Bt Pelitic Schist							**Domain 3: Northeast of Mud Glacier**							
M2 +202	28	4280	194	2568	48	67.5	0.016239 ± 0.56 %	0.10758 ± 0.57 %	103.8 ± 1.2	103.7 ± 1.1	0.98	0.04805 ± 0.10 %	101.6 ± 4.9	-2.5
M3 +202	25	4954	238	5874	26	63.5	0.019337 ± 0.18 %	0.12956 ± 0.19 %	123.5 ± 0.4	123.7 ± 1.1	0.95	0.04859 ± 0.06 %	128.2 ± 2.9	3.7
M4 +202	20	5801	231	3913	30	63.4	0.016062 ± 0.39 %	0.10627 ± 0.40 %	102.7 ± 0.8	102.5 ± 0.8	0.98	0.04799 ± 0.08 %	98.7 ± 4.0	-4.1
M5 +202	17	6710	288	5209	24	64.1	0.017032 ± 0.29 %	0.11332 ± 0.30 %	108.9 ± 0.6	109.0 ± 0.6	0.94	0.04826 ± 0.10 %	111.8 ± 4.8	2.6
DG206 Ms-Grt-Ky-Bt Pelitic Schist							**Domain 3: Fred Laing Ridge**							
M1 149-202	16	10649	293	2120	57	63.3	0.011148 ± 0.10 %	0.07293 ± 0.13 %	71.5 ± 0.1	71.5 ± 0.2	0.73	0.04745 ± 0.09 %	71.8 ± 4.3	0.4
M2 149-202	32	6932	205	2576	68	61.9	0.012442 ± 0.13 %	0.08182 ± 0.14 %	79.7 ± 0.2	79.9 ± 0.2	0.75	0.04769 ± 0.10 %	84.0 ± 4.6	5.1
M3 149-202	29	7663	199	2255	70	61.0	0.011076 ± 0.11 %	0.07217 ± 0.14 %	71.0 ± 0.1	70.8 ± 0.2	0.76	0.04726 ± 0.09 %	62.1 ± 4.3	-14.4
M4 149-202	10	16349	400	2604	46	57.4	0.011506 ± 0.16 %	0.07537 ± 0.17 %	73.7 ± 0.2	73.8 ± 0.2	0.86	0.04751 ± 0.09 %	74.8 ± 4.2	1.5

Table 3.3. (concluded)

Fraction[a]	Wt.[b] (µg)	U (ppm)	Pb*[c] (ppm)	$^{206}Pb/^{204}Pb$[d]	Pb[e] (pg)	^{208}Pb (%)[f]	$^{206}Pb/^{238}U$[g]	$^{207}Pb/^{235}U$[g]	$^{206}Pb/^{238}U$[h] (Ma)	$^{207}Pb/^{235}U$[h] (Ma)	Corr.[i] Coeff.	$^{207}Pb/^{206}Pb$[h]	$^{207}Pb/^{206}Pb$[g] (Ma)	Disc.[j] (%)
DG225 Ms-Grt-Ky-Bt Pelitic Schist							**Domain 3: Warsaw Mountain**							
M1 149-202	43	6367	228	3571	193	64.3	0.015056 ± 0.54 %	0.09976 ± 0.59 %	96.3 ± 1.0	96.6 ± 1.1	0.94	0.04805 ± 0.20 %	101.9 ± 9.5	5.5
M2 149-202	39	4566	163	3034	142	65.7	0.013530 ± 0.11 %	0.08921 ± 0.13 %	86.6 ± 0.2	90.4 ± 4.1	0.74	0.04782 ± 0.09 %	90.4 ± 4.1	4.2
M3 149-202	27	6208	225	3054	139	64.5	0.014202 ± 0.09 %	0.09384 ± 0.12 %	90.9 ± 0.2	91.1 ± 0.2	0.87	0.04792 ± 0.06 %	95.3 ± 2.9	4.6
M4*105-149	91	5170	176	2706	423	63.8	0.013592 ± 0.11 %	0.08966 ± 0.14 %	87.0 ± 0.2	87.2 ± 0.2	0.89	0.04784 ± 0.07 %	91.4 ± 3.1	4.8
DG216 Bt-Grt-St-Ms Pelitic Schist							**Domain 3: Redrock Harbour**							
M2 149-202	14	7144	364	4931	23	67.6	0.018203 ± 0.11 %	0.12190 ± 0.12 %	116.3 ± 0.3	116.8 ± 0.3	0.80	0.04857 ± 0.07 %	127.1 ± 3.4	8.6
M3 149-202	16	4460	186	4741	17	60.9	0.018008 ± 0.21 %	0.12057 ± 0.18 %	115.1 ± 0.5	115.6 ± 0.4	0.72	0.04856 ± 0.15 %	126.6 ± 7.0	9.2
DG254 Ms-Grt-St-Ky-Bt Pelitic Schist							**Domain 3: Townsends Ridge**							
M1 +202	38	4321	98	1200	130	61.7	0.009639 ± 0.15 %	0.06314 ± 0.22 %	61.8 ± 0.2	62.2 ± 0.3	0.81	0.04751 ± 0.13 %	75.0 ± 6.2	17.7
M2 +202	43	4997	112	2404	84	61.3	0.009598 ± 0.13 %	0.06260 ± 0.20 %	61.6 ± 0.2	61.7 ± 0.2	0.90	0.04730 ± 0.10 %	64.6 ± 4.5	4.7
M3 +202	25	6347	145	2474	61	61.7	0.009651 ± 0.12 %	0.06297 ± 0.14 %	61.9 ± 0.1	62.0 ± 0.2	0.78	0.04732 ± 0.09 %	65.6 ± 4.2	5.6
M4*149-202	47	4944	113	2572	85	62.0	0.009632 ± 0.06 %	0.06288 ± 0.11 %	61.8 ± 0.1	61.9 ± 0.1	0.79	0.04735 ± 0.07 %	66.7 ± 3.2	7.3

[a]M1-M6 fraction code for single-grain monazite analysis; M4* fraction code for multigrain monazite analysis; A* fraction code for multigrain zircon analysis; +74-105, size range in µm.
[b]Wt. = Weights, estimated from grain size measurements; uncertainty is 2 µg. [c]Radiogenic Pb. [d]Measured ratio, corrected for spike and Pb fractionation of 0.09 ± 0.03%/a.m.u.
[e]Total common Pb in analysis, corrected for spike and fractionation. [f]Radiogenic ^{208}Pb, expressed as percentage of total radiogenic Pb. [g]Corrected for Pb and U laboratory blank where 208/204:207/204:206/204 = 19.01:15.64:38.23:1, and common Pb (Stacey-Kramers model Pbcomposition equal to interpreted age of analysis); errors are one standard error of the mean in percent. [h]Corrected for common Pb and laboratory blank; errors are two standard errors of the mean in Ma. [i]Corr. Coeff. = Correlation Coefficient.
[j]Disc. = Discordance in percent; values are not reported when less than -100.

Table 3.4. SHRIMP U-Th-Pb Analytical Data for Northern Selkirk Mountains, British Columbia

Spots[a]	U (ppm)	Th (ppm)	Th/U	Pb*[b] (ppm)	^{204}Pb (ppb)	$^{206}Pb/^{204}Pb$	$^{208}Pb/^{232}Th$[c]	$^{206}Pb/^{238}U$[c]	$^{207}Pb/^{235}U$[c]
DG38a	**Ms-Grt-Ky-Bt pelitic schist**							***Domain 3: East flank of fan***	
M1.1c	16972	116552	6.87	953	67	4403	0.00631 ± 0.00010	0.02018 ± 0.00037	0.13181 ± 0.00293
M1.2r	17886	100243	5.60	629	33	6661	0.00452 ± 0.00007	0.01442 ± 0.00026	0.09834 ± 0.00285
M2.1c	15792	112385	7.12	965	52	5651	0.00669 ± 0.00010	0.02148 ± 0.00039	0.14430 ± 0.00361
M2.2r	17623	110604	6.28	627	46	4525	0.00425 ± 0.00007	0.01364 ± 0.00025	0.08621 ± 0.00248
M4.1	15819	132005	8.34	635	16	10848	0.00393 ± 0.00006	0.01258 ± 0.00023	0.08846 ± 0.00325
M4.2	15190	102313	6.74	522	54	3040	0.00391 ± 0.00006	0.01256 ± 0.00022	0.08176 ± 0.00215
M8.1c	13545	74316	5.49	647	56	4110	0.00624 ± 0.00010	0.01971 ± 0.00035	0.13072 ± 0.00381
M8.2r	22064	97160	4.40	539	50	4410	0.00360 ± 0.00006	0.01171 ± 0.00021	0.07497 ± 0.00265
M9.1c	15404	126280	8.20	1107	35	8590	0.00717 ± 0.00011	0.02258 ± 0.00043	0.15398 ± 0.00391
M9.2m	27170	106203	3.91	1058	87	5256	0.00624 ± 0.00010	0.01959 ± 0.00035	0.12939 ± 0.00282
M9.3r	17890	98687	5.52	731	69	3730	0.00533 ± 0.00008	0.01675 ± 0.00030	0.10900 ± 0.00312
M10.1c	13247	95330	7.20	843	9	27933	0.00696 ± 0.00011	0.02180 ± 0.00039	0.15351 ± 0.00391
M10.2r	17375	107257	6.17	553	63	2902	0.00388 ± 0.00006	0.01212 ± 0.00022	0.07890 ± 0.00447
M12.1c	11988	96584	8.06	448	33	3781	0.00376 ± 0.00006	0.01197 ± 0.00022	0.07893 ± 0.00338
M12.2m	16097	101479	6.30	922	91	3298	0.00686 ± 0.00010	0.02171 ± 0.00039	0.14022 ± 0.00426
M12.3m	22341	109505	4.90	1082	67	6222	0.00680 ± 0.00010	0.02157 ± 0.00039	0.14022 ± 0.00333
DG225	**Grt-Ky-Ms-Bt pelitic schist**							***Domain 3: East flank of fan***	
M1.1c	37346	72705	1.95	837	79	6336	0.00492 ± 0.00008	0.01555 ± 0.00028	0.10367 ± 0.00223
M1.2m	18008	119938	6.66	757	93	2572	0.00481 ± 0.00007	0.01549 ± 0.00028	0.09872 ± 0.00290
M3.1c	21602	149768	6.93	995	122	2514	0.00515 ± 0.00008	0.01643 ± 0.00030	0.10381 ± 0.00269
M3.2m	21091	114955	5.45	734	63	4182	0.00457 ± 0.00007	0.01445 ± 0.00027	0.09651 ± 0.00288
M6.1r	17790	100968	5.68	431	69	2209	0.00307 ± 0.00005	0.00993 ± 0.00018	0.06454 ± 0.00219
M6.2m	25375	152158	6.00	1038	107	3298	0.00503 ± 0.00008	0.01622 ± 0.00029	0.10534 ± 0.00307
M6.3c	18334	103550	5.65	670	77	3116	0.00465 ± 0.00007	0.01516 ± 0.00028	0.10130 ± 0.00550
DG216	**Ms-Grt-St-Bt pelitic schist**							***Domain 3: East flank of fan***	
M1.1c	14309	105533	7.38	838	110	2269	0.00631 ± 0.00010	0.02026 ± 0.00037	0.12696 ± 0.00599
M2.1r	12820	47335	3.69	449	31	6645	0.00567 ± 0.00009	0.01846 ± 0.00033	0.12279 ± 0.00373
M2.2c	10580	132891	12.56	962	53	3678	0.00652 ± 0.00010	0.02137 ± 0.00041	0.14775 ± 0.00492
M3.1c	10352	139693	13.49	946	86	2115	0.00619 ± 0.00009	0.02026 ± 0.00037	0.12638 ± 0.00405
M3.2r	9282	50107	5.40	285	30	3410	0.00402 ± 0.00006	0.01279 ± 0.00024	0.08462 ± 0.00334
DG254	**Ms-Grt-St-Ky-Bt pelitic schist**							***Domain 3: East flank of fan***	
M2.1c	14006	70140	5.01	283	67	1627	0.00275 ± 0.00004	0.00900 ± 0.00016	0.05541 ± 0.00202
M2.2r	22137	117780	5.32	472	51	3442	0.00280 ± 0.00004	0.00917 ± 0.00017	0.06147 ± 0.00181
M3.1c	14259	81797	5.74	318	69	1649	0.00278 ± 0.00004	0.00922 ± 0.00017	0.05673 ± 0.00246
M3.2c	27835	137848	4.95	573	21	10323	0.00282 ± 0.00004	0.00928 ± 0.00017	0.06493 ± 0.00165

[a]Spots are denoted as follows: M1.1 = monazite and spot number; c = core, m = mantle and r = rim indicates the location of the spot in a zoned crystal when applicable, genetic origin is not implied. [b]Radiogenic Pb.
[c]Corrected for common Pb according to procedure outlined by Stern and Berman (2000); uncertainties are reported at 1σ and are calculated by numerical propagation of all known sources of error; $^{207}Pb/^{206}Pb$ ages that are ≤0Ma are reported as 0 Ma.

Table 3.4. (concluded)

Spots[a]	$^{207}Pb^{c}/^{206}Pb$	$^{208}Pb^{c}/^{232}Th$ (Ma)	$^{206}Pb^{c}/^{238}U$ (Ma)	$^{207}Pb^{c}/^{235}U$ (Ma)	Corr.[d] Coeff.	$^{207}Pb^{c}/^{206}Pb$ (Ma)	Disc.[e] (%)
DG38a Ms-Grt-Ky-Bt pelitic schist							
M1.1c	0.04736 ± 0.0005	127.1 ± 1.9	128.8 ± 2.3	125.7 ± 2.6	0.88	67.6 ± 25.6	-91
M1.2r	0.04945 ± 0.0010	91.2 ± 1.4	92.3 ± 1.7	95.2 ± 2.6	0.71	169.1 ± 48.8	45
M2.1c	0.04873 ± 0.0007	134.7 ± 2.1	137.0 ± 2.5	136.9 ± 3.2	0.80	135.0 ± 36.1	-2
M2.2r	0.04583 ± 0.0009	85.7 ± 1.3	87.4 ± 1.6	84.0 ± 2.3	0.72	0.0 ± 0.0	——
M4.1	0.05101 ± 0.0015	79.3 ± 1.2	80.6 ± 1.4	86.1 ± 3.0	0.59	241.2 ± 70.2	67
M4.2	0.04722 ± 0.0008	78.9 ± 1.2	80.5 ± 1.4	79.8 ± 2.0	0.76	60.3 ± 40.7	-33
M8.1c	0.04810 ± 0.0010	125.7 ± 1.9	125.8 ± 2.2	124.8 ± 3.4	0.71	104.3 ± 50.0	-21
M8.2r	0.04644 ± 0.0013	72.6 ± 1.1	75.0 ± 1.3	73.4 ± 2.5	0.61	21.3 ± 66.1	——
M9.1c	0.04947 ± 0.0007	144.4 ± 2.2	143.9 ± 2.7	145.4 ± 3.5	0.82	170.2 ± 34.8	15
M9.2m	0.04791 ± 0.0005	125.6 ± 1.9	125.0 ± 2.2	123.6 ± 2.5	0.89	95.0 ± 24.3	-32
M9.3r	0.04720 ± 0.0010	107.4 ± 1.6	107.1 ± 1.9	105.1 ± 2.9	0.72	59.2 ± 47.1	-81
M10.1c	0.05106 ± 0.0008	140.3 ± 2.1	139.1 ± 2.5	145.0 ± 3.5	0.78	243.6 ± 37.3	43
M10.2r	0.04720 ± 0.0024	78.3 ± 1.2	77.7 ± 1.4	77.1 ± 4.2	0.44	59.3 ± 118.0	-31
M12.1c	0.04784 ± 0.0017	75.9 ± 1.2	76.7 ± 1.4	77.1 ± 3.2	0.54	91.4 ± 84.3	16
M12.2m	0.04683 ± 0.0011	138.1 ± 2.1	138.5 ± 2.5	133.2 ± 3.8	0.68	40.8 ± 52.9	——
M12.3m	0.04715 ± 0.0006	136.9 ± 2.1	137.6 ± 2.4	133.2 ± 3.0	0.82	57.0 ± 32.4	——
DG225 Ms-Grt-Ky-Bt pelitic schist							
M1.1c	0.04836 ± 0.00046	99.1 ± 1.6	99.5 ± 1.8	100.2 ± 2.1	0.90	116.9 ± 22.7	15
M1.2m	0.04622 ± 0.00096	97.0 ± 1.5	99.1 ± 1.8	95.6 ± 2.7	0.71	11.4 ± 47.1	——
M3.1c	0.04582 ± 0.00074	103.9 ± 1.6	105.1 ± 1.9	100.3 ± 2.5	0.78	0.0 ± 0.0	——
M3.2m	0.04844 ± 0.00103	92.2 ± 1.4	92.5 ± 1.7	93.6 ± 2.7	0.71	120.8 ± 51.1	24
M6.1r	0.04713 ± 0.00124	61.9 ± 1.0	63.7 ± 1.2	63.5 ± 2.1	0.64	55.8 ± 61.7	-14
M6.2m	0.04711 ± 0.00097	101.5 ± 1.6	103.7 ± 1.9	101.7 ± 2.8	0.71	54.7 ± 48.6	-90
M6.3c	0.04848 ± 0.00236	93.8 ± 1.5	97.0 ± 1.8	98.0 ± 5.1	0.45	122.5 ± 115.0	21
DG216 Ms-Grt-St-Bt pelitic schist							
M1.1c	0.04546 ± 0.00187	127.2 ± 2.0	129.3 ± 2.4	121.4 ± 5.4	0.50	0.0 ± 0.0	——
M2.1r	0.04825 ± 0.00108	114.2 ± 1.7	117.9 ± 2.1	117.6 ± 3.4	0.69	111.4 ± 53.6	-5.9
M2.2c	0.05013 ± 0.00126	131.3 ± 2.0	136.3 ± 2.6	139.9 ± 4.4	0.66	201.2 ± 59.3	32.2
M3.1c	0.04524 ± 0.00109	124.7 ± 1.9	129.3 ± 2.3	120.8 ± 3.7	0.66	0.0 ± 0.0	——
M3.2r	0.04799 ± 0.00157	81.1 ± 1.3	81.9 ± 1.5	82.5 ± 3.1	0.57	98.8 ± 78.5	17.1
DG254 Ms-Grt-St-Ky-Bt pelitic schist							
M2.1c	0.04464 ± 0.00132	55.5 ± 0.9	57.8 ± 1.1	54.8 ± 2.0	0.60	0.0 ± 0.0	——
M2.2r	0.04863 ± 0.00101	56.5 ± 0.9	58.8 ± 1.1	60.6 ± 1.7	0.72	129.9 ± 49.5	50.5
M3.1c	0.04461 ± 0.00165	56.1 ± 0.9	59.2 ± 1.1	56.0 ± 2.4	0.53	0.0 ± 0.0	——
M3.2c	0.05074 ± 0.00080	56.9 ± 0.9	59.6 ± 1.1	63.9 ± 1.6	0.79	229.1 ± 36.6	63.4

[d]Corr. Coeff. = Correlation Coeficient. [e]Discordance = 100 x [1-($^{206}Pb/^{238}U$ age)/($^{207}Pb/^{206}Pb$ age)];
values are not quoted when < -100.

Figure 3.1. (a) Morphogeologic belts of the Canadian Cordillera. (b) Tectonic assemblage map of southeastern Omineca belt (modified after Wheeler and McFeely, 1991) showing lithologic map units of autochthonous Monashee complex (North American basement) and overlying Selkirk allochthon. Box outlined in the top left of the figure represents the location of Fig. 3.3. A-B is line of section for cross section Fig. 3.2. ADP = Adamant pluton; AS = Albert stock; BMP = Bigmouth pluton; BR = Battle Range batholith; CS = Clachnacudainn Slice; FP = Fang pluton; GP = Goldstream pluton; GS = Goldstream Slice; IS = Illecillewaet Slice; KB = Kuskanax batholith; PC = Pass Creek pluton.

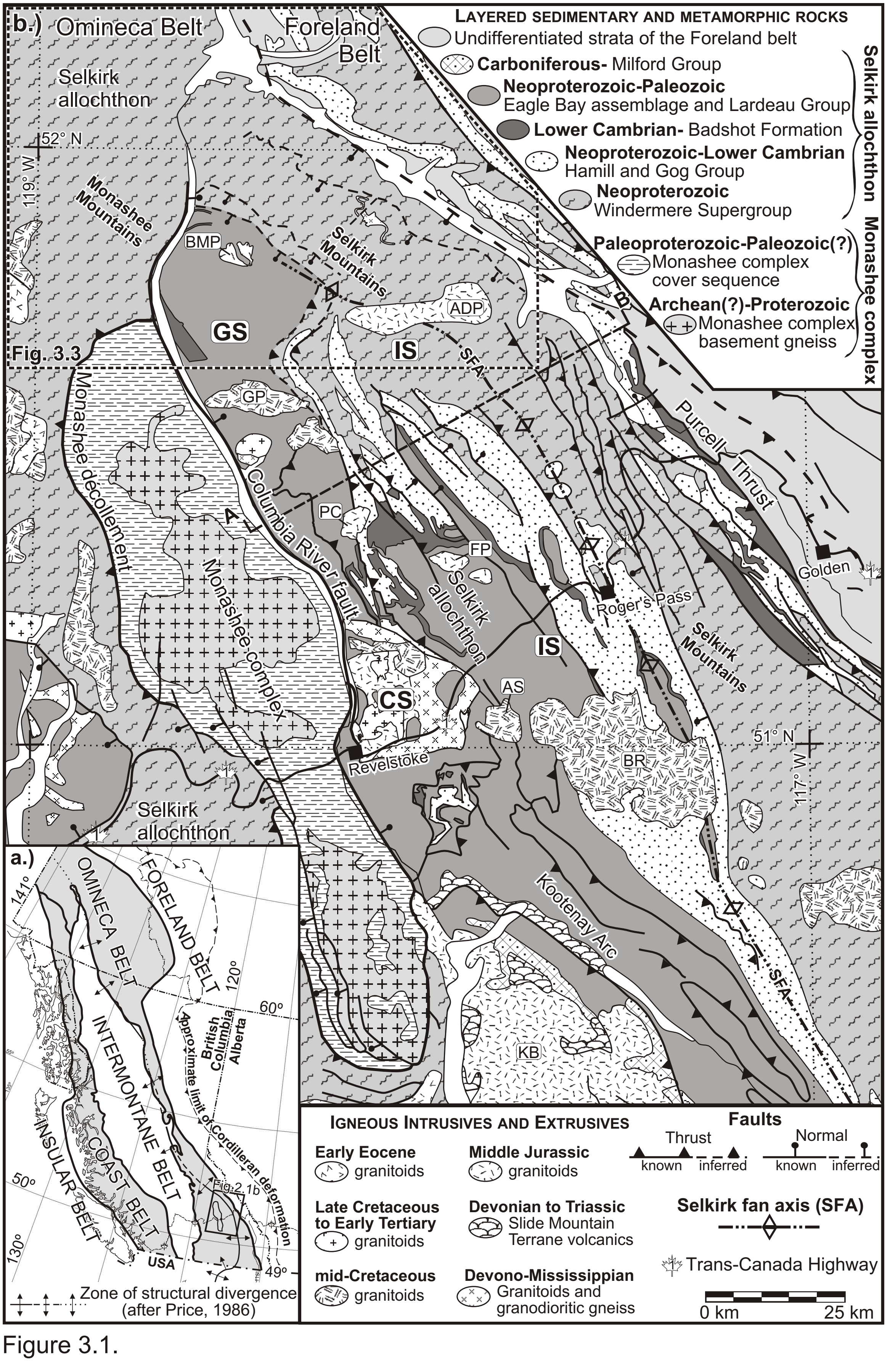
b.)
Omineca Belt
Foreland Belt
Selkirk allochthon
52° N
119° W
Monashee Mountains
Selkirk Mountains
BMP
GS
ADP
IS
SFA
Fig. 3.3
GP
Monashee decollement
Columbia River fault
Monashee complex
PC
FP
Selkirk allochthon
Roger's Pass
Golden
Purcell Thrust
Selkirk Mountains
CS
AS
BR
51° N
117° W
Revelstoke
Selkirk allochthon
Kootenay Arc
SFA
KB
LAYERED SEDIMENTARY AND METAMORPHIC ROCKS
Undifferentiated strata of the Foreland belt
Carboniferous- Milford Group
Neoproterozoic-Paleozoic
Eagle Bay assemblage and Lardeau Group
Lower Cambrian- Badshot Formation
Neoproterozoic-Lower Cambrian
Hamill and Gog Group
Neoproterozoic
Windermere Supergroup
Selkirk allochthon
Paleoproterozoic-Paleozoic(?)
Monashee complex cover sequence
Archean(?)-Proterozoic
Monashee complex basement gneiss
Monashee complex
a.)
141°
OMINECA BELT
FORELAND BELT
120°
60°
British Columbia
Alberta
Approximate limit of Cordilleran deformation
INTERMONTANE BELT
COAST BELT
INSULAR BELT
50°
Fig. 2.1b
130°
USA
49°
Zone of structural divergence
(after Price, 1986)
IGNEOUS INTRUSIVES AND EXTRUSIVES
Early Eocene granitoids
Middle Jurassic granitoids
Late Cretaceous to Early Tertiary granitoids
Devonian to Triassic Slide Mountain Terrane volcanics
mid-Cretaceous granitoids
Devono-Mississippian Granitoids and granodioritic gneiss
Faults
Thrust
known
inferred
Normal
known
inferred
Selkirk fan axis (SFA)
Trans-Canada Highway
0 km
25 km

Figure 3.1.

Figure 3.2. Generalized regional cross section of the Selkirk fan along section line A-B of Fig. 3.1 (modified after Brown et al., 1993). CRF = Columbia River fault; MD = Monashee décollement; PT = Purcell thrust.

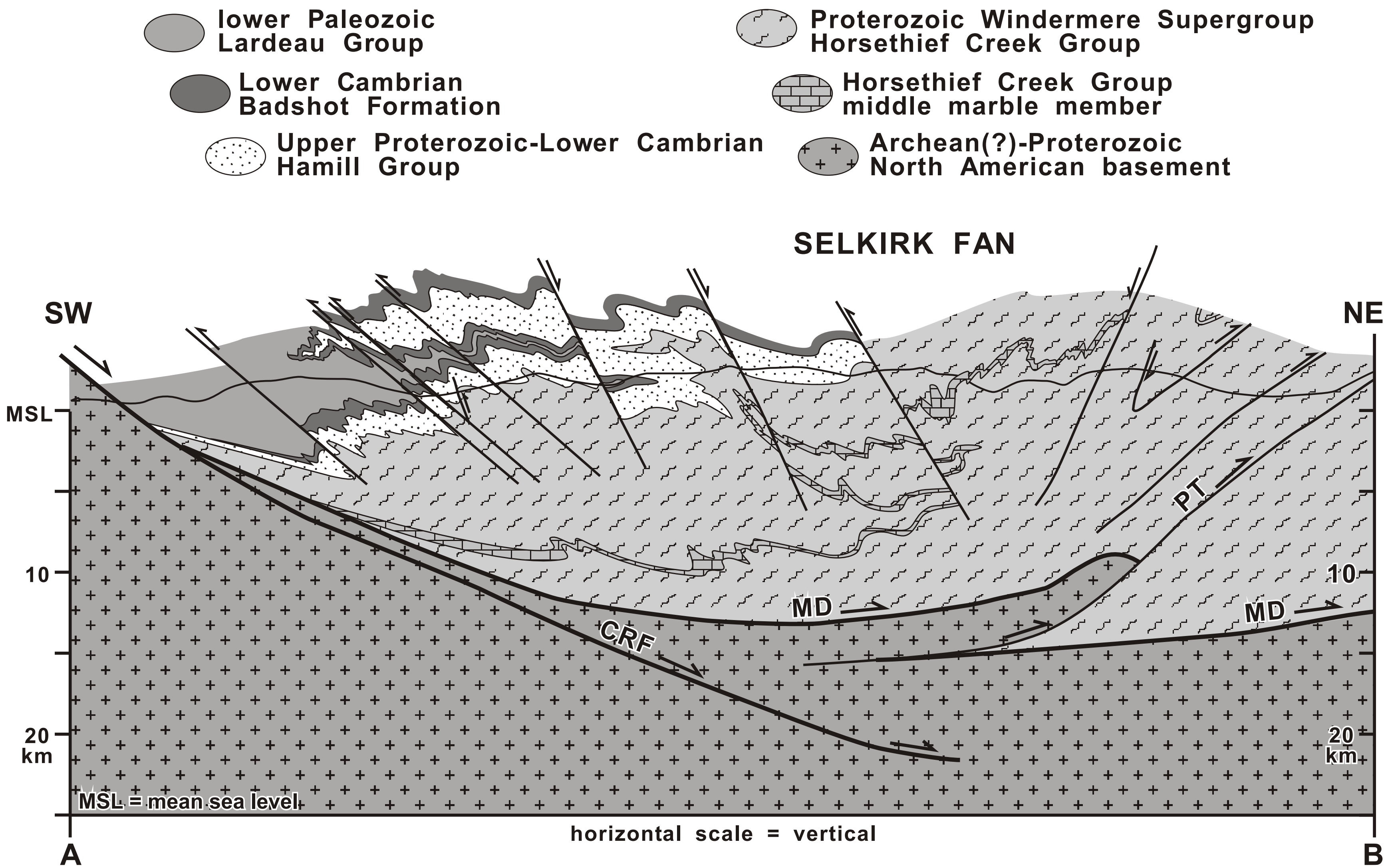

lower Paleozoic
Lardeau Group
Lower Cambrian
Badshot Formation
Upper Proterozoic-Lower Cambrian
Hamill Group
Proterozoic Windermere Supergroup
Horsethief Creek Group
Horsethief Creek Group
middle marble member
Archean(?)-Proterozoic
North American basement
SELKIRK FAN
SW
NE
MSL
10
20
km
PT
MD
MD
CRF
10
20
km
MSL = mean sea level
horizontal scale = vertical
A
B

Figure 3.2

Figure 3.3. (a) Inset delineates the domains discussed in the text, the general orientation of structures in each domain, and the location of cross section lines of Fig. 3.11. (b) Generalized geologic map of the northern Selkirk Mountains illustrating lithostratigraphy, regional metamorphic isograds, and major structures. Compiled from mapping by Brown (1991), Brown and Tippett (1978), Colpron et al. (1995), Leatherbarrow (1981), Marchildon (1999), Perkins (1983), Poulton and Simony, (1980), Raeside and Simony (1983), Scammell (1993), Simony et al. (1980), and Wheeler (1965). Geochronologic sample locations are shown. A-A', B-B', C-C', D-D', and E-E' represent the lines of cross sections drawn in Fig. 3.11. Abbreviations: ADP = Adamant pluton; ADM = Adamant Mountain; AM = Argonaut Mountain; AP = Argonaut Pass; BMP = Bigmouth pluton; BCF = Birch Creek fault; BMF = Bigmouth fault; FG = French glacier; MC = Mica Creek village; MCD = Mica Creek dam; MD = Monashee décollement; MN = Mount Nagle; MSF = Mount Sir Sanford; NEF = Northeastern fault; RP = Remillard Peak; TM = Trident Mountain; TR = Townsends Ridge. Abbreviations for metamorphic zones (e.g., Chl, Bt, Grt) based on mineral abbreviations after Kretz (1983).

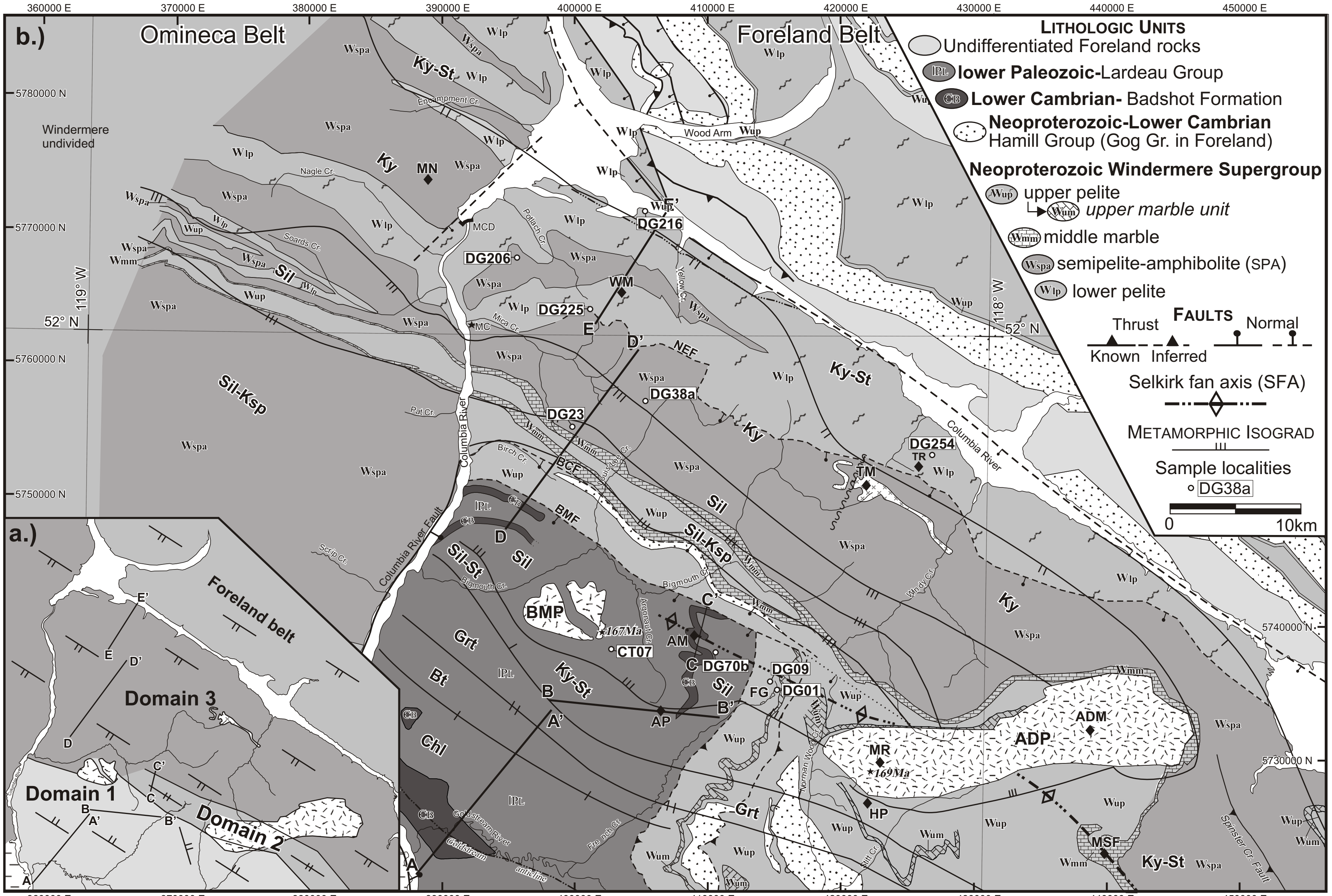

b.)
Omineca Belt
Foreland Belt
Windermere undivided
a.)
Foreland belt
Domain 3
Domain 1
Domain 2
LITHOLOGIC UNITS
Undifferentiated Foreland rocks
lower Paleozoic-Lardeau Group
Lower Cambrian- Badshot Formation
Neoproterozoic-Lower Cambrian
Hamill Group (Gog Gr. in Foreland)
Neoproterozoic Windermere Supergroup
upper pelite
upper marble unit
middle marble
semipelite-amphibolite (SPA)
lower pelite
FAULTS
Thrust
Normal
Known
Inferred
Selkirk fan axis (SFA)
METAMORPHIC ISOGRAD
Sample localities
DG38a
0
10km
Columbia River
Columbia River Fault
Wood Arm
BMP
ADP
167Ma
169Ma

Figure 3.3

Figure 3.4a-g. Photomicrographs of thin sections for the geochronology samples DG01, DG70b and DG23. (a) DG01 – garnet is almost completely resorbed within a mat of sillimanite that has grown on a biotite substrate. Sillimanite appears to be partly aligned within S_2, which is crenulated by F_3. (b) DG01 - example of a homogenous garnet rim surrounding a poikiloblastic core; the rim has also overgrown a mat of sillimanite. (c) DG01 – example of a monazite that has impinged upon the grain boundary of a biotite lath that is also overgrown by randomly oriented sillimanite. (d) DG70b – randomly oriented sillimanite that has overgrown both biotite and quartz. Monazite in the center of the photomicrograph appears to have grown within a mat of sillimanite. (e) DG70b – inclusion-free garnet rim overgrew both biotite and sillimanite. (f) DG23 – shows the concordance of the long axes of elongate monazite grains with the S_2 transposition foliation that is defined by the alignment of biotite and muscovite. (g) DG23 - strongly resorbed garnet porphyroblast that has been replaced by biotite, quartz and sillimanite. Monazite in mid-upper part of photomicrograph is enclosed entirely within biotite.

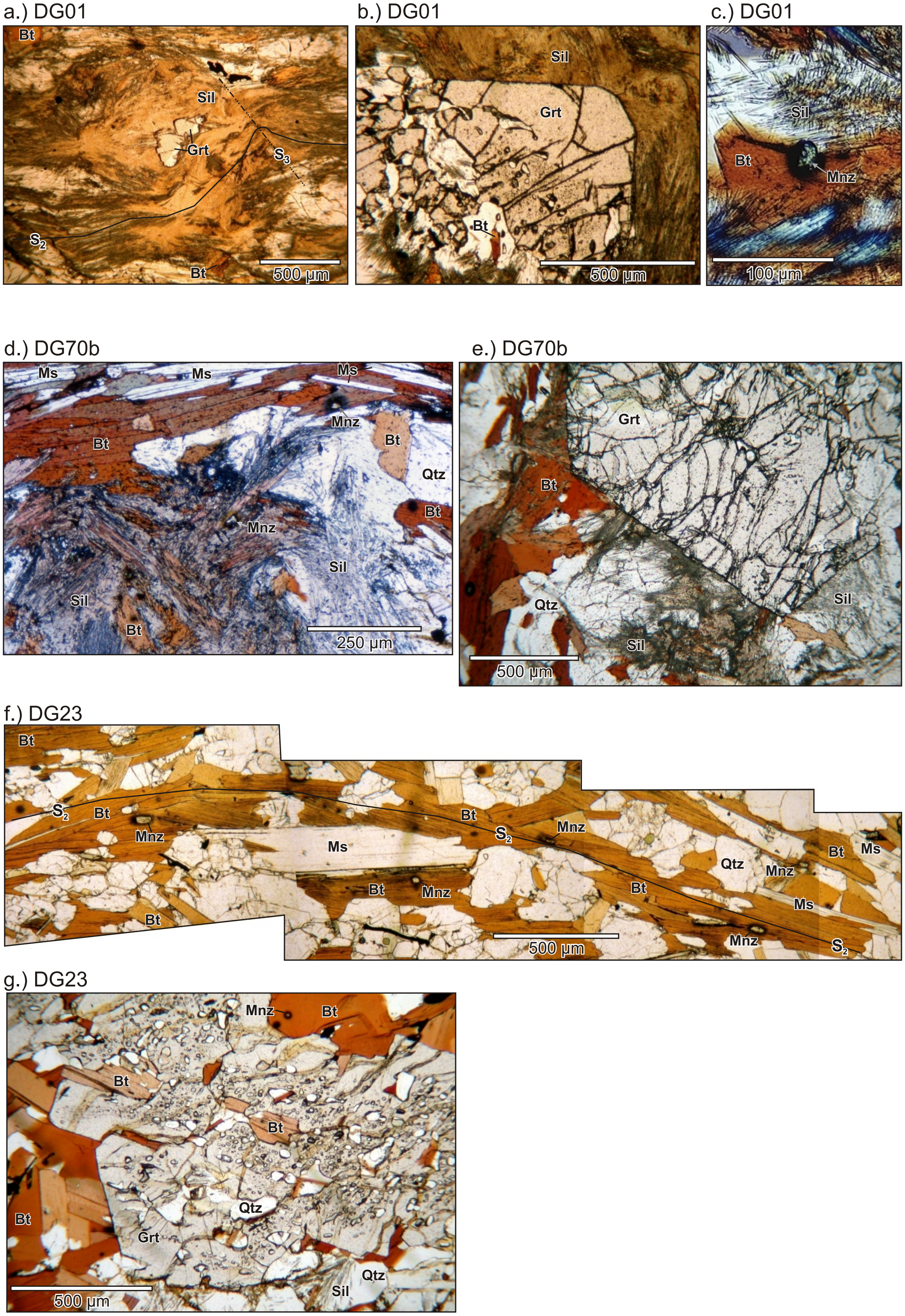
a.) DG01
Bt
Sil
Grt
S3
S2
Bt
500 µm
b.) DG01
Sil
Grt
Bt
500 µm
c.) DG01
Sil
Bt
Mnz
100 µm
d.) DG70b
Ms
Ms
Ms
Mnz
Bt
Bt
Qtz
Bt
Mnz
Sil
Sil
Bt
250 µm
e.) DG70b
Grt
Bt
Qtz
Sil
Sil
500 µm
f.) DG23
Bt
S2
Bt
Mnz
Ms
Bt
S2
Mnz
Bt
Ms
Qtz
Mnz
Bt
Mnz
Bt
Ms
Bt
Mnz
S2
500 µm
g.) DG23
Mnz
Bt
Bt
Bt
Bt
Qtz
Grt
Qtz
Sil
500 µm

Figure 3.4a-g.

Figure 3.4h-m. Photomicrographs of thin sections for the geochronology samples DG206, DG38a and DG225. (h) DG206 – alignment of kyanite, biotite and muscovite defines S_2. In the mid-upper portion of the photomicrograph, monazite has grown along a muscovite grain boundary that has embayed into the adjacent biotite lath. (i) DG206 – shows the alignment of biotite, muscovite, and oblate garnet within S_2. The homogeneous rims of the oblate garnets appear to have grown only along the long axes, suggesting that their shape is the result of preferential growth of the garnet rims parallel with the plane of flattening. (j) DG38a - two monazite grains in the center of the photo are aligned within the S_2 foliation, indicating they were present during the development of the foliation in DG38a. (k) Photomicrograph of the same thin section, demonstrating the resorption features of both kyanite and garnet, as well as garnet inclusions within kyanite. Note that the garnet in the mid-left portion of the photo has inclusion trails within the core surrounded by an inclusion-free rim that appears to obtrude into the nearby kyanite. (l) DG225 – photomicrograph displays significantly resorbed kyanite and garnet. S_2 defined by alignment of kyanite, biotite and muscovite. Also, garnet has an oblate shape that is concordant with S_2, similar to the garnets described above for DG206 (i). (m) DG225 – examples of monazite inclusions within biotite, mid-left, and kyanite, mid-right.

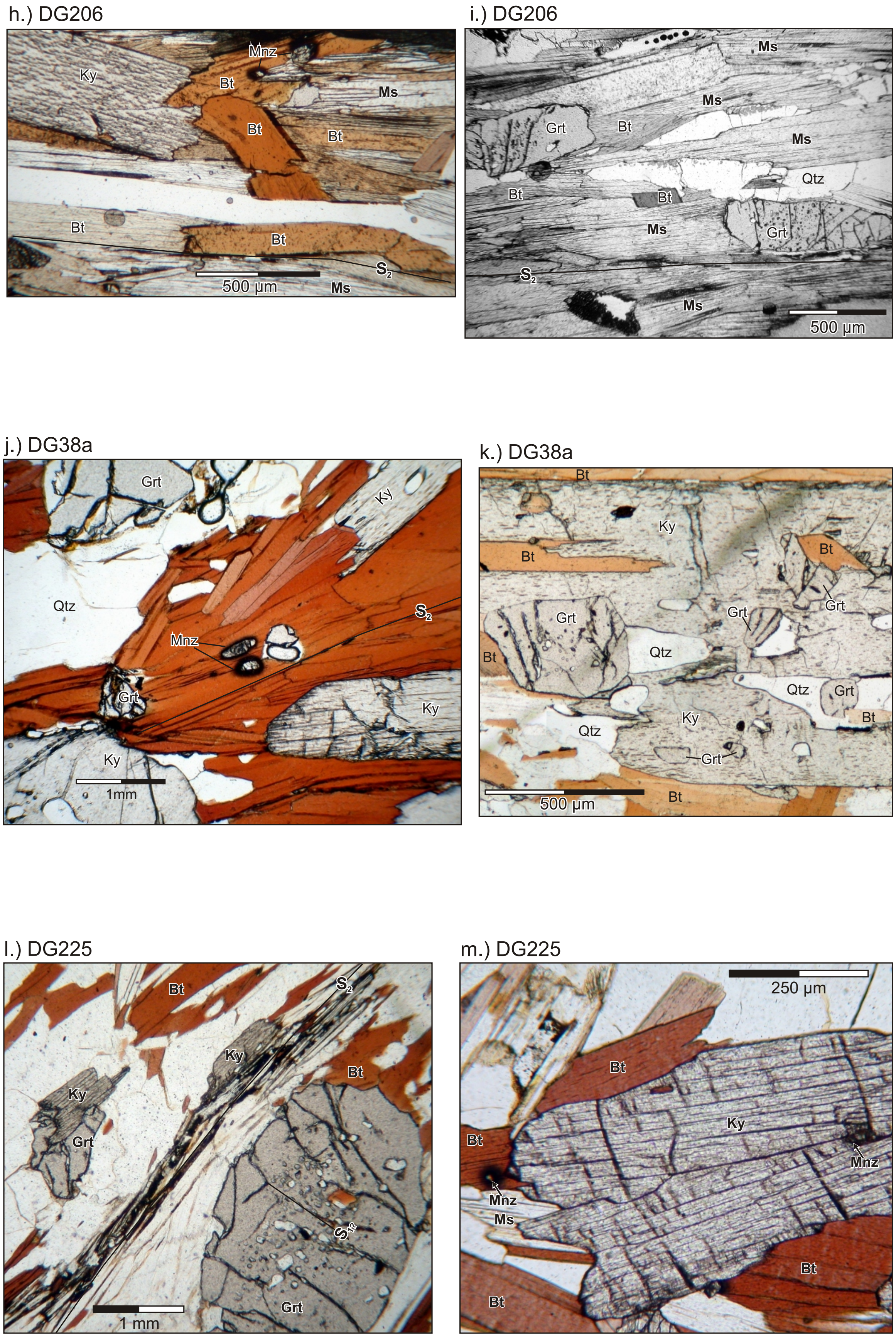
h.) DG206
Mnz
Ky
Bt
Ms
Bt
Bt
Bt
Bt
S2
500 µm
Ms
i.) DG206
Ms
Ms
Grt
Bt
Ms
Qtz
Bt
Bt
Ms
Grt
S2
Ms
500 µm
j.) DG38a
Grt
Ky
Qtz
S2
Mnz
Grt
Ky
Ky
1mm
k.) DG38a
Bt
Ky
Bt
Bt
Grt
Grt
Grt
Bt
Qtz
Qtz
Grt
Ky
Bt
Qtz
Grt
500 µm
Bt
l.) DG225
Bt
S2
Ky
Bt
Ky
Grt
S1?
Grt
1 mm
m.) DG225
250 µm
Bt
Ky
Bt
Mnz
Mnz
Ms
Bt
Bt

Figure 3.4h-m

Figure 3.4n-q. Photomicrographs of thin sections for the geochronology samples DG216 and DG 254. (n) and (o) DG216 – an earlier foliation that either represents S_1 or S_2 is preserved as quartz inclusion trails (S_i) within M_1 staurolite (n) and garnet cores (o). The external foliation, S_2, defined by the alignment of biotite and muscovite occurs at a high angle to S_I. The development of S_2 is interpreted to have continued following the initial episode of garnet and staurolite growth. In (n), the anhedral M_1 staurolite core is overgrown by a uniform, inclusion-free, euhedral rim, M_2, that appears to truncate most of the external S_2 foliation, which has been crenulated by F_3, suggesting that some of the staurolite recrystallization occurred during or after F_2 and F_3. However, the deflection of biotite and muscovite around the staurolite at the bottom near the scale bar suggests that F_3 continued to develop, in part, following M_2. (p) DG254 – S_2 is defined by the alignment of kyanite and biotite; most kyanite laths have been strongly resorbed. In the upper-right portion of the photomicrograph, an inclusion-free garnet rim truncates S_2. Retrograde chlorite has replaced part of the lower right margin of this garnet. (q) DG254 – shows an example of the forceful impingement of monazite into adjacent muscovite and biotite grain boundaries, which is typical of monazite in DG254.

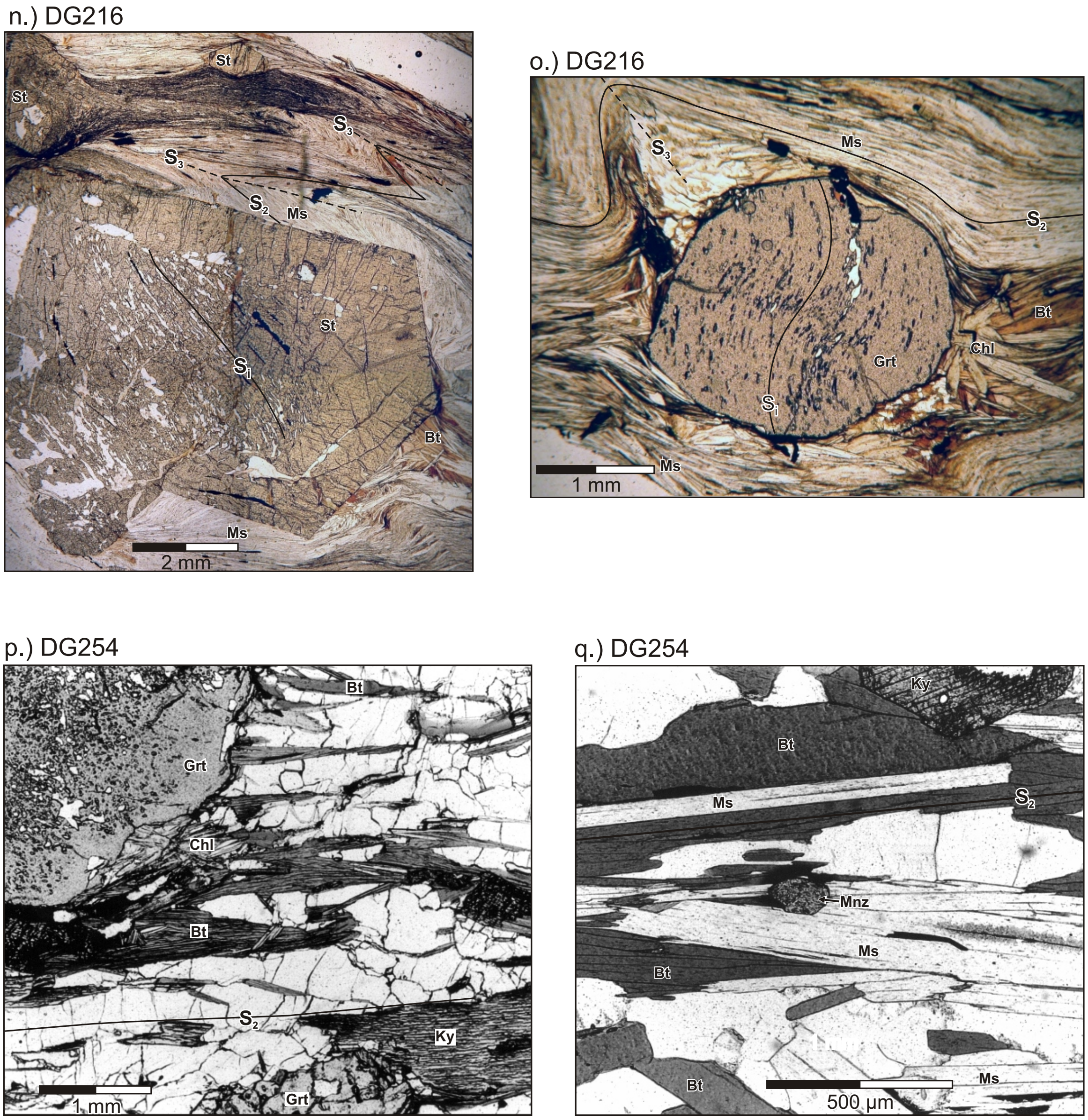
n.) DG216
St
St
S_3
S_3
S_2
Ms
St
S_i
Bt
Ms
2 mm
o.) DG216
S_3
Ms
S_2
Bt
Chl
Grt
S_i
Ms
1 mm
p.) DG254
Bt
Grt
Chl
Bt
S_2
Ky
Grt
1 mm
q.) DG254
Ky
Bt
Ms
S_2
Mnz
Ms
Bt
Bt
Ms
500 µm

Figure 3.4n-q

Figure 3.5. U-Pb concordia diagram for samples (a) DG01, (b) DG70b, (c) DG23 and (d) DG206 that were analyzed by IDTIMS. Each sample includes representative BSE images of monazite interiors that provide insight into chemical domains that may or may not correlate with age domains.

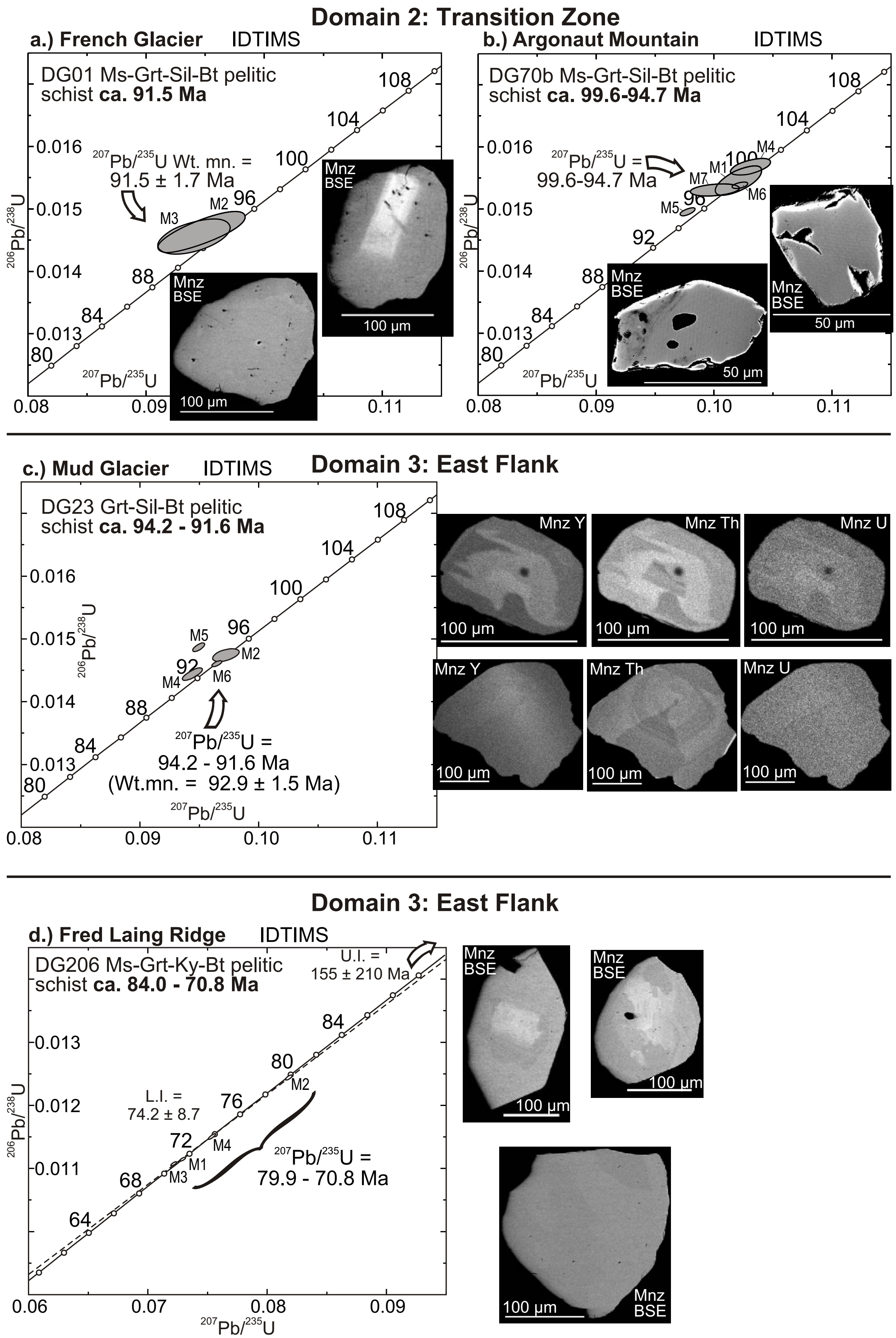

Domain 2: Transition Zone
a.) French Glacier IDTIMS
DG01 Ms-Grt-Sil-Bt pelitic schist ca. 91.5 Ma
207Pb/235U Wt. mn. = 91.5 ± 1.7 Ma
M3
M2
Mnz BSE
100 µm
b.) Argonaut Mountain IDTIMS
DG70b Ms-Grt-Sil-Bt pelitic schist ca. 99.6-94.7 Ma
207Pb/235U = 99.6-94.7 Ma
M1
M4
M5
M6
M7
50 µm
c.) Mud Glacier IDTIMS
Domain 3: East Flank
DG23 Grt-Sil-Bt pelitic schist ca. 94.2 - 91.6 Ma
207Pb/235U = 94.2 - 91.6 Ma (Wt.mn. = 92.9 ± 1.5 Ma)
Mnz Y
Mnz Th
Mnz U
d.) Fred Laing Ridge IDTIMS
DG206 Ms-Grt-Ky-Bt pelitic schist ca. 84.0 - 70.8 Ma
U.I. = 155 ± 210 Ma
L.I. = 74.2 ± 8.7
207Pb/235U = 79.9 - 70.8 Ma
206Pb/238U
207Pb/235U

Figure 3.5.

Figure 3.6. IDTIMS and SHRIMP U-Pb and U-Th-Pb concordia plots for sample DG38a. (a) U-Pb concordia diagram for the IDTIMS analyses. (b) U-Pb concordia diagram for the SHRIMP analyses. (c) U-Th-Pb concordia diagram for the SHRIMP analyses. (d) Tera-Wasserburg plot of the SHRIMP analyses, which is used to help distinguish the age domains identified within the monazites. The mean $^{208}Pb/^{232}Th$ ages for each "group" that is equated to be an age domain, is included beneath the Tera-Wasserburg plot; these are considered the best estimation of the age of each "group". (e) BSE and Y, Th and U chemical map images for each analyzed monazite, accompanied by a gray value profile for each of the Y maps (white line in Y map displays location of profile). Light gray values equate to higher Y concentrations. Spot locations for SHRIMP analyses have been superimposed on the Y maps of the analyzed monazite based on the BSE images acquired following the SHRIMP analyses. The numbers within the each spot correspond to the respective SHRIMP analysis for that monazite.

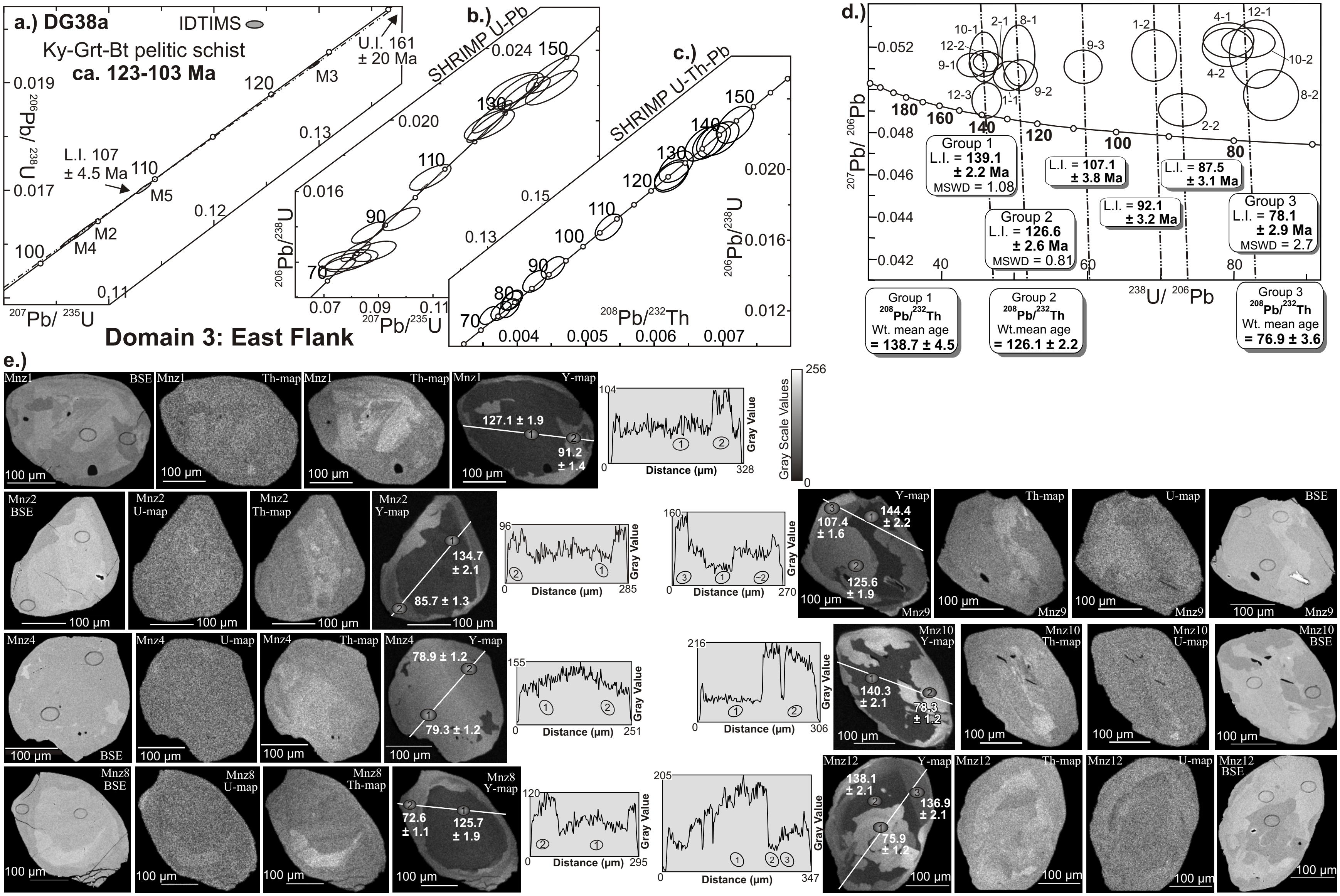
a.) DG38a
IDTIMS
Ky-Grt-Bt pelitic schist
ca. 123-103 Ma
U.I. 161
± 20 Ma
L.I. 107
± 4.5 Ma
b.)
SHRIMP U-Pb
c.)
SHRIMP U-Th-Pb
d.)
Group 1
L.I. = 139.1
± 2.2 Ma
MSWD = 1.08
Group 2
L.I. = 126.6
± 2.6 Ma
MSWD = 0.81
L.I. = 107.1
± 3.8 Ma
L.I. = 92.1
± 3.2 Ma
L.I. = 87.5
± 3.1 Ma
Group 3
L.I. = 78.1
± 2.9 Ma
MSWD = 2.7
Group 1 208Pb/232Th Wt. mean age = 138.7 ± 4.5
Group 2 208Pb/232Th Wt.mean age = 126.1 ± 2.2
Group 3 208Pb/232Th Wt. mean age = 76.9 ± 3.6
Domain 3: East Flank
e.)
Gray Scale Values
Distance (μm)
Gray Value

Figure 3.6

Figure 3.7. IDTIMS and SHRIMP U-Pb and U-Th-Pb concordia plots for sample DG225. (a) U-Pb concordia diagram for the IDTIMS analyses. (b) U-Pb concordia diagram for the SHRIMP analyses. (c) U-Th-Pb concordia diagram for the SHRIMP analyses. (d) Tera-Wasserburg plot of the SHRIMP analyses, which is used to help distinguish the age domains identified within the monazites. The mean $^{208}Pb/^{232}Th$ ages for each "group" that is equated to be an age domain, is included beneath the Tera-Wasserburg plot. (e) BSE and Y, Th and U chemical map images for each analyzed monazite, accompanied by a gray value profile for each of the Y maps (white line in Y map displays location of profile). Light gray values equate to higher Y concentrations. Spot locations for SHRIMP analyses have been superimposed on the Y and Th maps of the analyzed monazite based on the BSE images acquired following the SHRIMP analyses. The numbers within the each spot correspond to the respective SHRIMP analysis for that monazite.

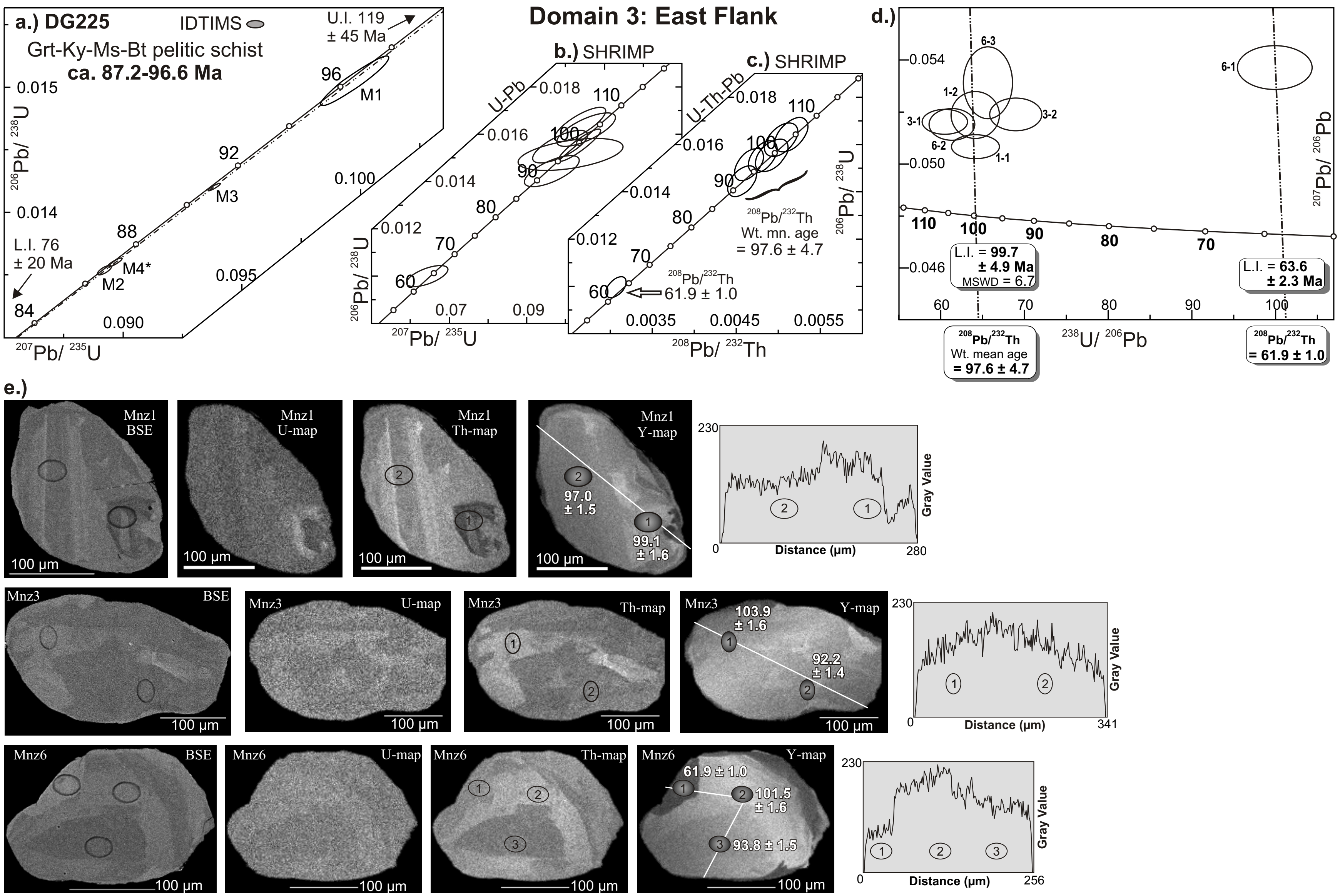
Domain 3: East Flank
a.) DG225
IDTIMS
Grt-Ky-Ms-Bt pelitic schist
ca. 87.2-96.6 Ma
U.I. 119
± 45 Ma
L.I. 76
± 20 Ma
M1
M2
M3
M4*
b.) SHRIMP
U-Pb
c.) SHRIMP
U-Th-Pb
208Pb/232Th
Wt. mn. age
= 97.6 ± 4.7
208Pb/232Th
61.9 ± 1.0
d.)
L.I. = 99.7
± 4.9 Ma
MSWD = 6.7
L.I. = 63.6
± 2.3 Ma
208Pb/232Th
Wt. mean age
= 97.6 ± 4.7
208Pb/232Th
= 61.9 ± 1.0
e.)
Mnz1 BSE
Mnz1 U-map
Mnz1 Th-map
Mnz1 Y-map
97.0 ± 1.5
99.1 ± 1.6
Mnz3 BSE
Mnz3 U-map
Mnz3 Th-map
Mnz3 Y-map
103.9 ± 1.6
92.2 ± 1.4
Mnz6 BSE
Mnz6 U-map
Mnz6 Th-map
Mnz6 Y-map
61.9 ± 1.0
101.5 ± 1.6
93.8 ± 1.5
100 µm
Gray Value
Distance (µm)

Figure 3.7

Figure 3.8. IDTIMS and SHRIMP U-Pb and U-Th-Pb concordia plots for sample DG216. (a) U-Pb concordia diagram for the IDTIMS analyses. (b) U-Pb concordia diagram for the SHRIMP analyses. (c) U-Th-Pb concordia diagram for the SHRIMP analyses. (d) Tera-Wasserburg plot of the SHRIMP analyses, which is used to help distinguish the age domains identified within the monazites. The mean $^{208}Pb/^{232}Th$ ages for each "group" that is equated to be an age domain, is included beneath the Tera-Wasserburg plot. (e) BSE and Y, Th and U chemical map images for each analyzed monazite, accompanied by a gray value profile for each of the Y maps (white line in Y map displays location of profile). Light gray values equate to higher Y concentrations. Spot locations for SHRIMP analyses have been superimposed on the Y and Th maps of the analyzed monazite based on the BSE images acquired following the SHRIMP analyses. The numbers within the each spot correspond to the respective SHRIMP analysis for that monazite.

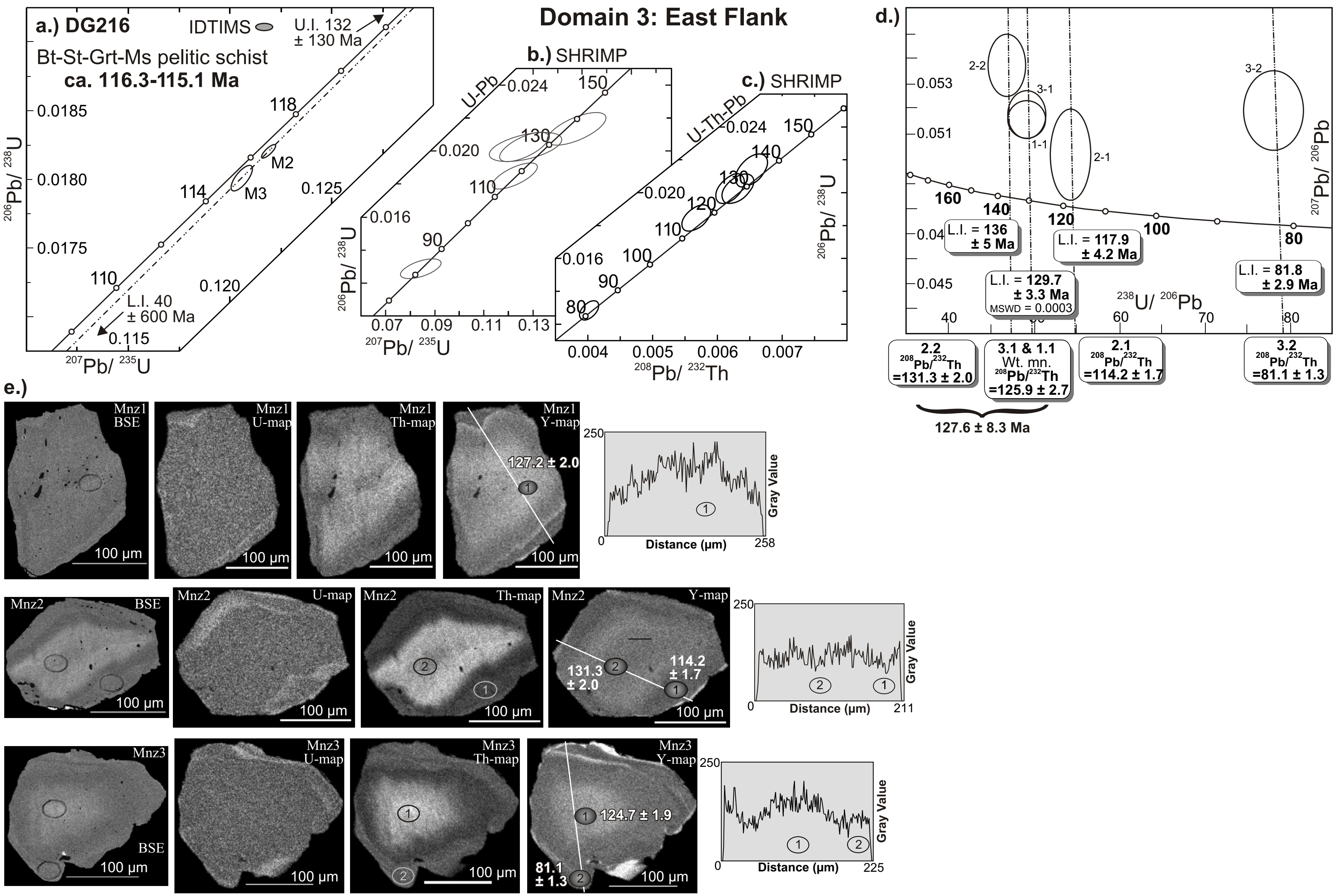

Domain 3: East Flank
a.) DG216
IDTIMS
Bt-St-Grt-Ms pelitic schist
ca. 116.3-115.1 Ma
U.I. 132
± 130 Ma
L.I. 40
± 600 Ma
M2
M3
b.) SHRIMP
U-Pb
c.) SHRIMP
U-Th-Pb
d.)
L.I. = 136
± 5 Ma
L.I. = 117.9
± 4.2 Ma
L.I. = 129.7
± 3.3 Ma
MSWD = 0.0003
L.I. = 81.8
± 2.9 Ma
2.2
$^{208}Pb/^{232}Th$
=131.3 ± 2.0
3.1 & 1.1
Wt. mn.
$^{208}Pb/^{232}Th$
=125.9 ± 2.7
2.1
$^{208}Pb/^{232}Th$
=114.2 ± 1.7
3.2
$^{208}Pb/^{232}Th$
=81.1 ± 1.3
127.6 ± 8.3 Ma
e.)
127.2 ± 2.0
131.3
± 2.0
114.2
± 1.7
124.7 ± 1.9
81.1
± 1.3
Distance (µm)
Gray Value

Figure 3.8

Figure 3.9. IDTIMS and SHRIMP U-Pb and U-Th-Pb concordia plots for sample DG254. (a) U-Pb concordia diagram for the IDTIMS analyses. (b) U-Pb concordia diagram for the SHRIMP analyses. (c) U-Th-Pb concordia diagram for the SHRIMP analyses. (d) Tera-Wasserburg plot of the SHRIMP analyses, which is used to help distinguish the age domains identified within the monazites. The mean $^{208}Pb/^{232}Th$ age for the SHRIMP analyses is included beside the lower intercept of the linear regression within the Tera-Wasserburg plot. (e) BSE and Y, Th and U chemical map images for each analyzed monazite, accompanied by a gray value profile for each of the Y maps (white line in Y map displays location of profile). Light gray values equate to higher Y concentrations. Spot locations for SHRIMP analyses have been superimposed on the Y and Th maps of the analyzed monazite based on the BSE images acquired following the SHRIMP analyses. The numbers within the each spot correspond to the respective SHRIMP analysis for that monazite.

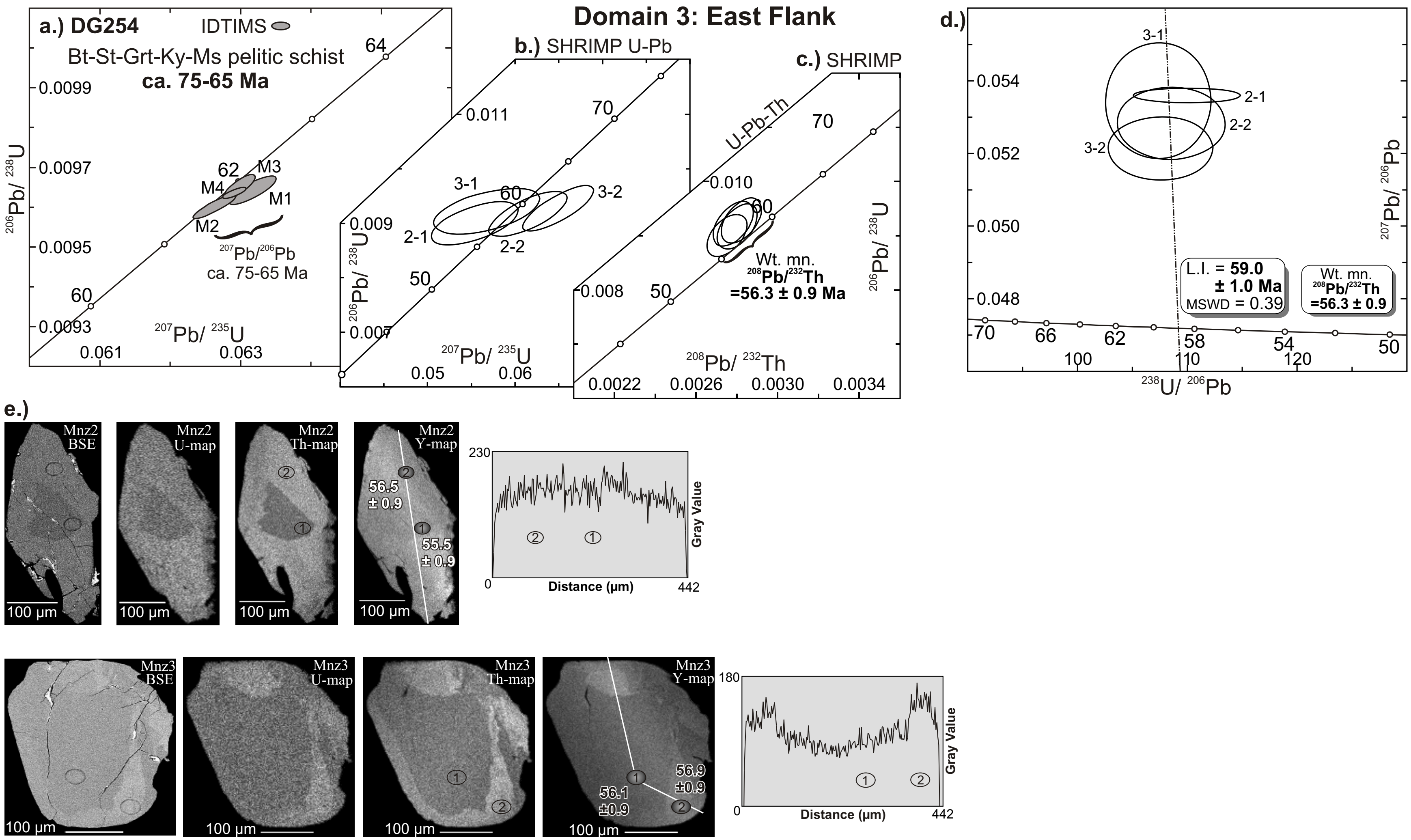
Domain 3: East Flank
a.) DG254
IDTIMS
Bt-St-Grt-Ky-Ms pelitic schist
ca. 75-65 Ma
^{206}Pb/ ^{238}U
0.0099
0.0097
0.0095
0.0093
64
62
60
M4
M3
M1
M2
^{207}Pb/^{206}Pb
ca. 75-65 Ma
^{207}Pb/ ^{235}U
0.061
0.063
b.) SHRIMP U-Pb
0.011
0.009
0.007
70
60
50
3-1
3-2
2-1
2-2
^{206}Pb/ ^{238}U
^{207}Pb/ ^{235}U
0.05
0.06
c.) SHRIMP
U-Pb-Th
0.010
0.008
70
60
50
Wt. mn.
^{208}Pb/^{232}Th
=56.3 ± 0.9 Ma
^{206}Pb/ ^{238}U
^{208}Pb/ ^{232}Th
0.0022
0.0026
0.0030
0.0034
d.)
0.054
0.052
0.050
0.048
3-1
2-1
2-2
3-2
L.I. = 59.0
± 1.0 Ma
MSWD = 0.39
Wt. mn.
^{208}Pb/^{232}Th
=56.3 ± 0.9
^{207}Pb/ ^{206}Pb
70
66
62
58
54
50
100
110
120
^{238}U/ ^{206}Pb
e.)
Mnz2 BSE
Mnz2 U-map
Mnz2 Th-map
Mnz2 Y-map
56.5 ± 0.9
55.5 ± 0.9
100 µm
230
0
Gray Value
Distance (µm)
442
Mnz3 BSE
Mnz3 U-map
Mnz3 Th-map
Mnz3 Y-map
56.1 ±0.9
56.9 ±0.9
180
0
Gray Value
Distance (µm)
442

Figure 3.9

Figure 3.10. The approximate P-T conditions and corresponding U-Th-Pb age constraints for the metamorphic samples analyzed in this study have been projected into the NaKFMASH petrogenetic grid of Spear et al. (1999). The P-T conditions have been inferred based on the metamorphic assemblage identified in each sample, and also on the geothermobarometric constraints provided by Leatherbarrow (1981) and Ghent et al. (1979, 1982, and 1983). (a) The small grey arrows point to the approximate P-T region that is interpreted to correspond with timing constraints for the samples DG01, DG23, DG70b and DG206 from Domains 2 and 3. (b-e) P-T-t paths inferred for samples of Domain 3. Attaching absolute timing constraints to points along the P-T-t path for these samples was made possible by integrating *in situ* SHRIMP analyses with the x-ray elemental maps of monazite crystals. The dark grey arrow represents the last part of the prograde path, and the light grey arrow corresponds to the retrograde path. The dotted portion of the P-T-t path is the part of the prograde path for which there are no timing constraints, and little or no metamorphic data. In (b), the circled numbers represent specific metamorphic reactions proposed in Chapter 4 (p. 185-192).

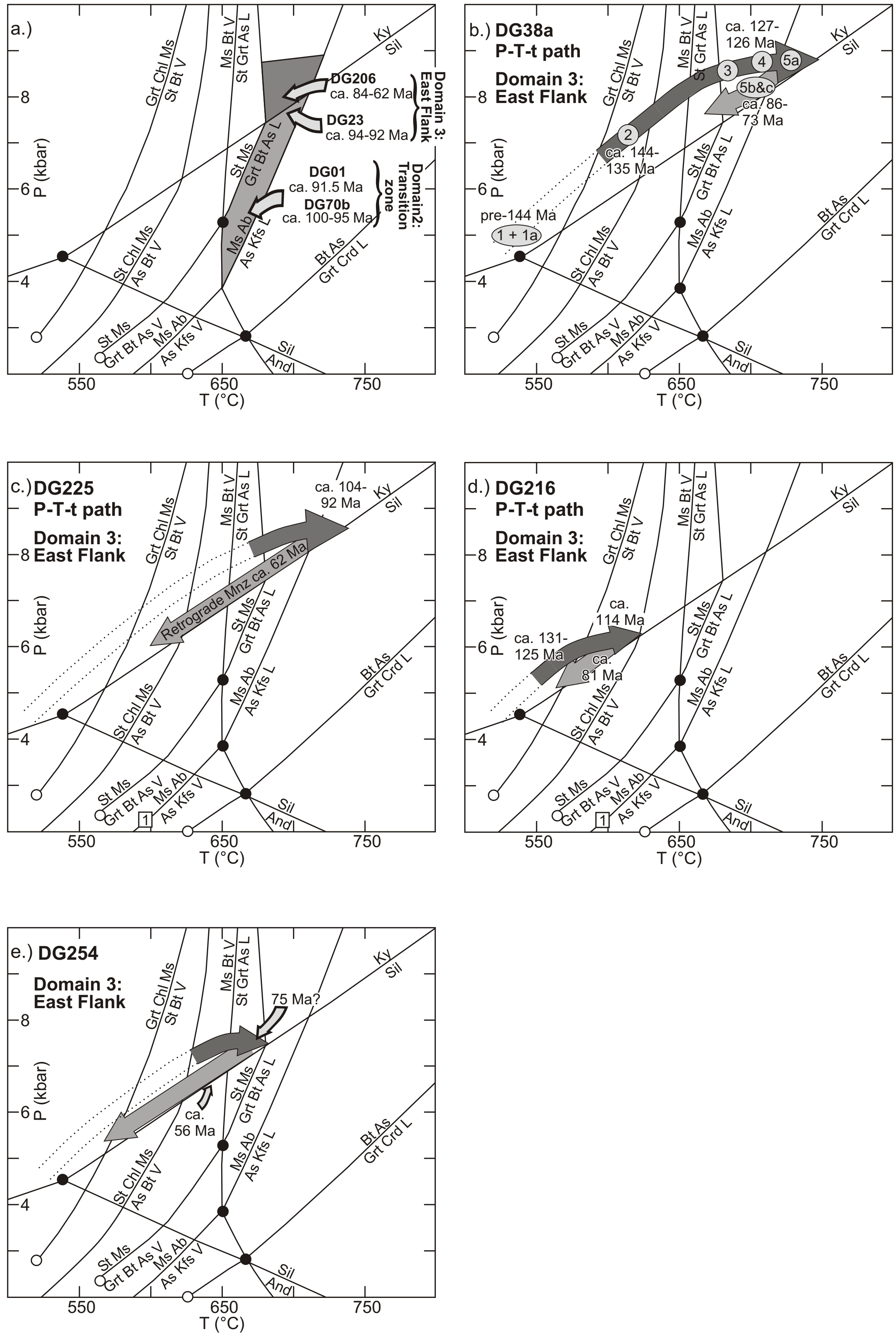
a.)
b.) DG38a
P-T-t path
Domain 3:
East Flank
c.) DG225
P-T-t path
Domain 3:
East Flank
d.) DG216
P-T-t path
Domain 3:
East Flank
e.) DG254
Domain 3:
East Flank
DG206
ca. 84-62 Ma
DG23
ca. 94-92 Ma
Domain 3:
East Flank
DG01
ca. 91.5 Ma
DG70b
ca. 100-95 Ma
Domain2:
Transition
zone
ca. 127-
126 Ma
ca. 86-
73 Ma
ca. 144-
135 Ma
pre-144 Ma
1 + 1a
2
3
4
5a
5b&c
ca. 104-
92 Ma
Retrograde Mnz ca. 62 Ma
ca.
114 Ma
ca. 131-
125 Ma
ca.
81 Ma
75 Ma?
ca.
56 Ma
Ky
Sil
And
Grt Chl Ms
St Bt V
Ms Bt V
St Grt As L
St Ms
Grt Bt As L
St Chl Ms
As Bt V
Ms Ab
As Kfs L
Bt As
Grt Crd L
St Ms
Grt Bt As V
Ms Ab
As Kfs V
1
P (kbar)
T (°C)
4
6
8
550
650
750

Figure 3.10

Figure 3.11. Composite structural cross section that transects the studied area, illustrating the geometry of the fan modified after Brown and Tippett (1978), Colpron et al. (1995), Perkins (1983), and Simony et al. (1980). Section lines are located in Fig. 3.3. U-Th-Pb geochronologic constraints for timing of metamorphism have been projected along strike into the line of section.

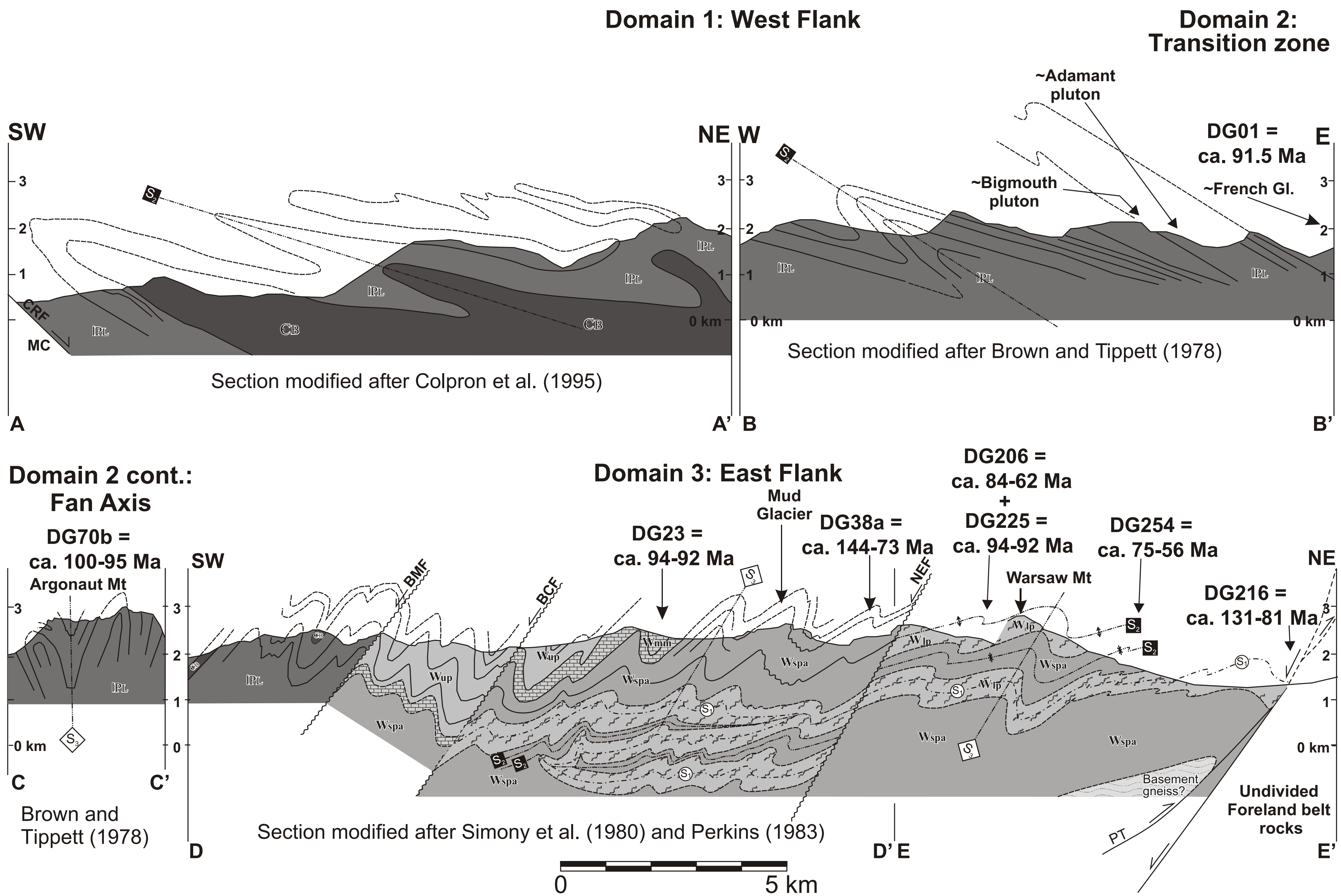

Domain 1: West Flank
Domain 2:
Transition zone
SW
NE
W
E
~Adamant
pluton
~Bigmouth
pluton
DG01 =
ca. 91.5 Ma
~French Gl.
CRF
MC
Section modified after Colpron et al. (1995)
Section modified after Brown and Tippett (1978)
A
A'
B
B'
Domain 2 cont.:
Fan Axis
DG70b =
ca. 100-95 Ma
Argonaut Mt
0 km
C
C'
Brown and
Tippett (1978)
Domain 3: East Flank
SW
NE
BMF
BCF
DG23 =
ca. 94-92 Ma
Mud
Glacier
DG38a =
ca. 144-73 Ma
NEF
DG206 =
ca. 84-62 Ma
+
DG225 =
ca. 94-92 Ma
Warsaw Mt
DG254 =
ca. 75-56 Ma
DG216 =
ca. 131-81 Ma
Basement
gneiss?
Undivided
Foreland belt
rocks
PT
Section modified after Simony et al. (1980) and Perkins (1983)
D
D'
E
E'
0
5 km

Figure 3.11

CHAPTER 4

CORRELATIONS BETWEEN CHEMICAL AND AGE DOMAINS IN MONAZITE, AND METAMORPHIC REACTIONS INVOLVING MAJOR PELITIC PHASES: AN INTEGRATION OF IDTIMS AND SHRIMP GEOCHRONOLOGY WITH Y-TH-U X-RAY MAPPING

Abstract

Chemical mapping and *in situ* U-Th-Pb analyses reveal the link between age domains and zones of relative yttrium (Y) depletion or enrichment within monazites correlated with metamorphic reactions involving garnet. Small-fraction Isotope Dilution Thermal Ionization Mass Spectrometry (IDTIMS) and Sensitive High Resolution Ion Microprobe (SHRIMP) techniques were utilized to measure U-Th-Pb in metamorphic monazite from pelitic rocks of the southern Canadian Cordillera. The IDTIMS data commonly demonstrated a 2 to 25 Ma range in U-Pb ages of monazites from a single sample. This is difficult to reconcile using conventional regression techniques due to complexities such as excess ^{206}Pb or bulk mixing of discrete age domains. Consequently, *in situ* analyses (~30 μm diameter) were carried out using the GSC SHRIMP II. Prior to SHRIMP analysis, the internal morphologies of the monazites were imaged using back-scattered electron (BSE) imaging and X-ray elemental mapping for Y, Th, and U. This revealed complex zoning in many of the monazites. The Y maps generally provided the best indication of growth or recrystallization domains, and were critical for targeting SHRIMP analyses because these relationships were not always clear in BSE, U, and Th images. Moreover, the Y domains consistently correlated with distinct age domains, with up to three or more in some crystals. These data clearly illustrate the cause of age dispersion within the analyzed monazite grains, and demonstrate the ubiquity of multiple age domains in metamorphic monazite that may be irreconcilable or misinterpreted when using conventional dating techniques such as IDTIMS.

Recent studies have investigated the interaction between accessory minerals such as monazite and major pelitic phases throughout a metamorphic event, and more specifically the partitioning of Y between these phases. They have established that garnet exerts considerable control over the Y budget available during metamorphism in pelitic rocks. Monazite appears to be sensitive to the availability of Y, as reflected internally in preserved Y zones; data from this study appear to support these interpretations. Thus, precise ages of Y domains within monazite provided by *in situ* SHRIMP analyses may be correlated with metamorphic reactions involving garnet, and may be assigned to points along the P-T path.

4. 1. Introduction

In this study, chemical mapping and *in situ* U-Th-Pb analyses reveal the link between age domains and zones of relative yttrium (Y) depletion or enrichment within monazite that are correlated with metamorphic reactions involving major pelitic minerals, especially garnet.

Previous studies have demonstrated that monazite (Ce, La, Th, PO_4) is perhaps the most useful radiogenic mineral for providing metamorphic age constraints in amphibolite- to granulite-facies terranes (e.g., Parrish, 1990, and references therein). This is because of monazite's common occurrence (Overstreet, 1967), high concentrations of radiogenic Pb versus low common Pb (Heaman and Parrish, 1991), and resistance to thermally-induced volume Pb diffusion (e.g., DeWolf et al., 1993; Smith and Giletti, 1997; Zhu et al., 1997; Braun et al., 1998; Cocherie et al., 1998; Crowley and Ghent, 1999; Zhu and O'Nions, 1999b; Cherniak et al., 2002). However, the interpretation of U-Th-Pb ages is often made difficult by a number of complexities that affect the isotopic systematics of monazite. For instance, unsupported ^{206}Pb in young monazite (Schärer, 1984), samples with significant age dispersion (Foster et al., 2002, and references therein), and hydrothermal alteration (Poitrasson et al., 1996, 2000) can render conventional IDTIMS U-Pb data sets meaningless or result in erroneous conclusions. Even when innovative *in situ* dating techniques were utilized (e.g., DeWolf et al., 1993; Harrison et al., 1995; Zhu et al., 1997; Cocherie et al., 1998), ambiguities persisted because the assignment of monazite ages to specific points along the P-T path of a metamorphic assemblage remained equivocal. Moreover, there continued to be uncertainty as to what part of the metamorphic cycle was actually dated, such as prograde versus retrograde, heating versus cooling, or a hydrothermal event. Clearly, the determination of the involvement of monazite production and/or consumption in metamorphic reactions is of paramount importance.

Fortunately, a number of investigations have improved our understanding of monazite paragenesis. These include systematic studies of monazite occurrence in pelitic assemblages over a broad range of metamorphic grade (e.g., Smith and Barreiro, 1990; Kingsbury et al., 1993; Ferry, 2000; Rubatto et al., 2001), and insights into metamorphic reactions involving monazite based on textural observations, accessory assemblages, and thermodynamic considerations (e.g., Bingen et al., 1996; Pan, 1997; Ferry, 2000; Foster et al., 2000, 2002; Pyle and Spear, 2000a, 2002, 2003). These studies have elucidated the interaction between accessory monazite and major phases throughout a metamorphic event, and more specifically the partitioning of Y between these phases (e.g., Bea and Montero, 1999; Foster et al., 2000; Pyle et al., 2001; Foster et al., 2002; Pyle and Spear, 2002, 2003). They have established that garnet exerts considerable control over the Y budget available during metamorphism in pelitic rocks. Monazite growth appears to be sensitive to the availability of Y, as reflected internally in zones of relative Y enrichment and depletion. As such, constraining the ages of these Y zones should provide detailed chronologic information that can be applied to the P-T evolution of a metamorphic assemblage. This concept was investigated by Foster et al. (2002) using laser ablation multicollector inductively coupled plasma mass spectrometry (LA-MC-ICPMS) and electron microprobe (EMP) chemical analyses. However, for Mesozoic and younger monazites the sensitivity of the LA-MC-ICPMS required rastering of the beam over a substantial area and depth (x-y-z = ~60 x 50 x 15 μm) of the monazite, usually across Y zone boundaries. Nevertheless, they were able to demonstrate the link between Y zones and age domains, and propose correlations with metamorphic reactions involving garnet.

This study builds upon the innovative contributions discussed above by integrating Y, Th, and U chemical mapping of monazite with high precision *in situ* SHRIMP U-Th-Pb analyses. Two important distinctions regarding this study are worth noting at this point: 1) The chemical maps were generated prior to the *in situ* SHRIMP analyses, not after as was the case for most other similar studies. 2) The SHRIMP spots were limited to ~30 μm diameter and ~2 μm depth. This approach provided the best chance to date specific Y zones without inadvertent overlap with adjacent domains. The results presented below indicate that distinct zones of relative Y depletion or enrichment in metamorphic monazite correspond with age domains. Finally, an attempt is made to correlate the dated Y domains with prograde and retrograde metamorphic reactions involving major pelitic phases and monazite (Foster et al., 2000; Pyle and Spear, 2000b; Foster et al., 2002; Pyle and Spear, 2002, 2003; Fig. 4.10).

4. 2. Geologic Setting

The study area is composed of Late Proterozoic to Paleozoic metasedimentary and metavolcanic rocks of the northern Selkirk Mountains, situated in the Omineca belt, which is the metamorphic and plutonic hinterland of the Canadian Cordillera (Figs. 4.1a and 4.2). These rocks were initially deposited along the western paleo-margin of the North American craton (Monger et al., 1982). During Middle Jurassic to Paleocene contraction these rocks were displaced northeastward ~250-300 km (e.g., Price and Mountjoy, 1970; Brown et al., 1993; Parrish, 1995) as part of the Selkirk allochthon (Read and Brown, 1981). During this time the allochthon is interpreted to have experienced protracted and diachronous internal deformation and metamorphism (Parrish, 1995). Subsequent Tertiary normal faulting along the Columbia River and Okanagan Valley fault systems has dissected and exposed all levels of the allochthon.

The complexly deformed rocks within the northern Selkirk Mountains comprise at least three generations of superposed folding that have been metamorphosed at low to high-grade (Brown and Tippett, 1978; Simony et al., 1980; Perkins, 1983). Bounding the eastern flank of this region is the southern Rocky Mountain trench, which is part of an orogen-scale tectonic lineament that trends northeast-southwest for more than 2300 km along the strike of the Canadian Cordillera. A zone of structural divergence from east to west across the northern Selkirk Mountains defines a regional-scale structure (Fig. 4.1b), termed the Selkirk Fan (Wheeler, 1963, 1965; Price and Mountjoy, 1970; Brown and Tippett, 1978). The structural style of the eastern flank of the northern Selkirk Mountains consists of moderate, southwest dipping faults, fold axial planes, and transposition foliation. Shallow, northeast dipping structures characterize the western flank of the region, which is partly situated in the immediate hanging wall of the Columbia River fault (Fig. 4.2), a NW-striking, crustal-scale, Eocene normal-sense shear zone (Parrish et al., 1988). This fault separates upper-amphibolite-facies footwall rocks of the Monashee complex that includes autochthonous North American basement (see Armstrong et al., 1991; Parkinson, 1991; Crowley, 1999) from greenschist-facies rocks of the Selkirk allochthon within the Selkirk Mountains.

4.2.1. Metamorphism

Sillimanite- and Sil-Kfs[1]-grade rocks core the central part of the study area, and are

[1] Mineral abbreviations according to Kretz (1983)

flanked on either side by progressively lower grade assemblages (Fig. 4.2). In many locations, complex textural relationships characteristic of polyphase metamorphism (cf. Chapter 3; Marchildon, 1999) have made it difficult to characterize the stable assemblage. Nonetheless, a set of northwest trending regional isograds (Fig. 4.2), parallel to the structural grain of the region have been established based on the appearance or disappearance of index minerals chlorite, biotite, garnet, staurolite, kyanite, and sillimanite in pelites (Leatherbarrow and Brown, 1978; Leatherbarrow, 1981; Simony et al., 1980). The lowest grade Chl-in assemblage is located in the west flank of the studied area, in the immediate hanging wall of the Columbia River fault (Fig. 4.2). Northeastward, the metamorphic grade increases progressively to Sil-Kfs-melt near the fan axis, and then decreases to Ky-St-grade adjacent to the southern Rocky Mountain Trench (SRMT, Fig. 4.2).

The peak metamorphic pressures and temperatures estimated for the region vary from west to east. On the basis of geothermobarometry, Leatherbarrow (1981) documented that in the southwest flank of the fan, in the vicinity of French Glacier (Fig. 4.2), peak pressures and temperatures were 5 kbar and 500-550 °C (St-Ky-zone). To the northeast within the Sil-Kfs-zone, pressures were estimated to have reached 7 kbar and temperatures as high as 650 °C. Geothermobarometric studies to the north in the Mica Creek area agree well with those of Leatherbarrow. Ghent et al. (1979, 1982, and 1983) estimated peak conditions of 540 to 700 °C and 5.6 to 7.2 kbar (lower P-T estimates for Ky-St-zone, higher for Sil-Kfs-zone).

4.2.2. Previous Timing Constraints

Prior to this study there was an apparent contradiction in the isotopic age constraints applied to the structures and metamorphic isograds of the northern Selkirk and Monashee Mountains, which are mapped as continuous features across the Columbia River (e.g., Simony et al., 1980; Fig. 4.2). In the northern Selkirk Mountains, Middle to Late Jurassic age constraints for deformation and metamorphism were provided by U-Pb and $^{40}Ar/^{39}Ar$ ages for plutons sampled exclusively within the west flank of the fan (e.g., Shaw, 1980a; Brown et al., 1992; Colpron et al., 1996; a summary is provided in Chapters 2 and 3, Tables 2.1 and 3.1). However, in the adjacent northern Monashee Mountains (Fig. 4.2), U-Pb and $^{40}Ar/^{39}Ar$ data indicate that a significant episode of deformation and metamorphism occurred in the Early to Late Cretaceous (Sevigny et al., 1989; Scammell, 1993; Digel et al., 1998; Crowley et al., 2000). Furthermore, geochronologic data of Crowley et al. (2000) from the northernmost Selkirk Mountains, near Mica Creek Village (Fig. 4.2), strongly suggest there was a significant component of Cretaceous strain and metamorphism. To reconcile this contradiction additional geochronologic data from this study have been used to constrain the timing of deformation (Chapter 2) and metamorphism (Chapter 3) across the width of the northern Selkirk Mountains. An important contribution of this chapter is to provide added confidence in the accuracy of the proposed metamorphic age constraints.

4. 3. Analytical Methods

Geochronologic methods included U-Pb IDTIMS and U-Th-Pb SHRIMP analyses accompanied by backscattered electron (BSE) imaging, and high-resolution Y-Th-U X-ray maps of metamorphic monazite from eight pelitic samples. A detailed study of one sample, DG38a, is considered in this chapter; monazites from this sample provided the greatest variety of chemical and age domains. A thorough treatment of all eight metapelitic samples is presented in Chapter 3.

U-Pb IDTIMS geochronology at Carleton University followed procedures outlined by Parrish et al. (1987). Mineral separates were obtained by standard crushing, grinding, Rogers Gold™ table, heavy liquid, and Frantz™ magnetic separation techniques. When possible, the clearest, crack- and inclusion-free crystals were selected for analysis. Teflon® microcapsules (Parrish, 1987) were used for mineral dissolution with a mixed ^{233}U-^{235}U-^{205}Pb tracer (Parrish and Krough, 1987). Ion exchange column chemistry (Parrish et al., 1987) facilitated U-Pb element separation. U-Pb isotopes were analyzed using a multicollector mass spectrometer (Finnagan MAT 261 as described by Roddick et al., 1987), and estimation of errors was based on numerical error propagation (Roddick, 1987). Decay constants used are those recommended by Steiger and Jagër (1977). Discordia lines through analyses were calculated using a modified (York, 1969) regression (Parrish et al., 1987). Typically, procedural U blanks were less than 5 pg and Pb blanks less than 10 pg. Common Pb corrections were made assuming model Pb compositions derived from the growth curves of Stacey and Kramers (1975).

Ion microprobe analyses of monazite grains in a polished mount using the SHRIMP II at the Geological Survey of Canada (GSC) in Ottawa were carried out according to the methods outlined by Stern (1997), Stern and Sanborn (1998), and Stern and Berman (2000). A full description of the SHRIMP II instrument may be found in Stern (1997), Williams (1998) and De Laeter and Kennedy (1998). Monazites and zircons from samples dated in this study were set in an araldite resin grain mount. The mount was polished using 9, 6, and 1 μm diamond polishing compound to reveal grain centers, and coated with 5.8-6.0 nm of Au (99.9999%). BSE and cathodoluminescence (CL) images were obtained at the GSC using a Cambridge Instruments S360 scanning electron microscope operating at 20 kV accelerating potential and using an electron beam current of 2-5 nA. In addition, kyanite, garnet, and staurolite mineral separates from three samples, including DG38a (kyanite and garnet only), were mounted, polished, and imaged by BSE. This approach provided access to a greater number porphyroblasts that may contain monazite inclusions relative to analysis of individual thin sections. Despite lacking the textural information provided by EMP analysis of a polished thin section, textural evidence for the grain mount could be indirectly furnished from thin section observations using a polarizing microscope. Chemical maps of Y, Th, and U of selected monazites from both grain mounts were made using a Cameca SX-50 electron microprobe at the University of Massachusetts according to procedures outlined by Williams et al. (1999). High resolution X-ray maps of Y, Th, and U were produced using a high sample current (>200 nA), small step sizes (~0.5 μm), and rastering the electron beam. Obtaining chemical maps of monazite prior to SHRIMP II analyses is unique to this study, and proved to be very effective for elucidating age domains within the analyzed monazite.

Target locations for U-Th-Pb SHRIMP analysis on selected monazites were chosen using the images acquired from the techniques described above. Targeted areas were sputtered using a mass-filtered O_2^- primary beam operating in Kohler illumination mode to effect even sputtering. All samples were analyzed using the K120 Kohler aperture setting, which yielded an approximate beam diameter of 22 x 31 μm. For monazite, the primary beam current was ~2-2.3 nA for both standards and unknowns. The operational mass resolution (1% peak height) over the course of the analyses was 5550-5700.

Instrumental bias in the measured Pb/U and Pb/Th ratios was corrected by an empirically-derived calibration of the linear relationships between $^{206}Pb^+/UO^+$ vs. UO_2^+/UO^+, determined on natural monazite standards (GSC samples 3345 and 4170). Isotopic ratios were corrected for common Pb using ^{204}Pb. However, for SHRIMP data the ^{204}Pb correction can impart significant error on the calculated age due to extremely low ^{204}Pb counts (see Stern, 1997). The propagation of the statistical error associated with this presumably has the most impact on the $^{207}Pb/^{235}U$ age, because of low ^{207}Pb counts in Mesozoic or younger minerals. This may cause an "artificial" disagreement between the calculated $^{207}Pb/^{235}U$ age and the other isotopic systems. Thus, for monazite the $^{208}Pb/^{232}Th$ chronometer is considered most accurate because it includes the highest Pb counts, and is apparently unaffected by isotopic disequilibrium (i.e., unsupported ^{206}Pb). In the following sections and figures, quoted ages rely on the $^{208}Pb/^{232}Th$ chronometer unless otherwise noted. Errors assigned to SHRIMP U-Th-Pb ages were determined using numerical propagation of all known sources of error as outlined by Stern (1997), Stern and Sanborn (1998), and Stern and Berman (2000).

4. 4. Results

Monazite U-Th-Pb data for a medium-grade metapelitic sample, DG38a, from the northern Selkirk Mountains are reported below and presented in Figs. 4.3-4.9 (see Tables 3.3 and 3.4 of Chapter 3 for IDTIMS and U-Th-Pb SHRIMP analytical data). BSE images and Y, Th, and U maps are provided for each monazite analyzed, and are accompanied by a conventional U-Pb concordia plot (Wetherill, 1956; errors for ellipses are presented at two standard errors, 2σ). The monazites were imaged by BSE before and after the SHRIMP analyses. However, only the post-SHRIMP BSE images are included which illustrate the location of each SHRIMP spot. The BSE images were used to superimpose the SHRIMP spot locations onto the Y maps in Figs. 4.4-4.7 and 4.9. The numbers within each spot correspond to the respective SHRIMP analysis for that monazite (Table 3.4, Chapter 3). Figures 4.4-4.7 also include the $^{208}Pb/^{232}Th$ SHRIMP age beside each spot (errors are quoted at 1σ in Ma). In addition, each Y image has a corresponding gray value pixel profile that has been included to further illustrate the contrast between Y zones. The plots provide a means to qualitatively assess the Y concentrations within the zones to facilitate comparisons. In the following sections, references to element concentrations (e.g., Y concentration) are based on the original, unadjusted gray pixel values of the X-ray maps. This is considered a reasonable qualitative approach for estimating and comparing Y zone concentrations (M. Jercinovic EMP lab UMASS, 2002, pers. comm.). Some of the Y images have been adjusted slightly for contrast and brightness to enhance the zoning, but only after the gray value plots were created. Figure 4.8 is an exception. In this figure, the gray value plots correspond to Y zones that were adjusted and normalized based on the gray value intensity of zones within Mnz9. This is discussed in more detail below (p. 182).

In Fig. 4.7, the SHRIMP data are plotted in a Tera-Wasserburg diagram (Tera and Wasserburg, 1972; errors presented at 2σ), in which the $^{207}Pb/^{206}Pb$ ratio uncorrected for common Pb is plotted against the uncorrected $^{238}U/^{206}Pb$ ratio. Linear regressions were fit through data that clustered in distinguishable groups. The age for a particular group was determined using the lower intercept of the regression line with the concordia curve. The upper end of the chord was anchored at the common $^{207}Pb/^{206}Pb$ composition representing the approximate age of each group using Stacey-Kramers (1975) model growth curves[2]. In theory, the ages derived from the lower intercepts of the regressions avoid the potentially large uncertainty imposed by the ^{204}Pb correction for common Pb. Also, the Tera-Wasserburg plots provide a means to assess the common Pb component in the monazite analyzed, since the farther the ellipse plots away from the concordia curve, the larger the common Pb component (see Stern, 1997). Although the calculated ages may be affected by variable amounts of unsupported ^{206}Pb, the Tera-Wasserburg plot helps to highlight the age domains within DG38a, as well as within individual monazite crystals.

4.4.1. DG38a – Ms-Grt-Ky-Bt pelitic schist

Sample DG38a comes from a Ms-Grt-Ky-Bt pelitic schist[3], with at least 20-30% melt content. All kyanite and most biotite are aligned within the shallow southwest dipping transposition foliation that is pervasive throughout the area. Most of the monazite grains identified using a polarizing microscope appear to be aligned parallel to the foliation (Fig. 4.3c). Both garnet and kyanite have textures indicative of resorption, and appear to have broken down to biotite and quartz with or without plagioclase (Fig. 4.3c). Some of the garnets have cores with inclusion trails surrounded by inclusion-free, homogeneous rims (Fig. 4.3d), indicating there has been more than one episode of garnet growth. Although not observed in this sample, retrograde chlorite is found nearby (<500 m) as a late replacement of garnet.

The IDTIMS analyses of single-grain monazite fractions plot in close proximity to the concordia curve between ca. 123 to 103 Ma (Fig. 4.3a). Fractions M2 and M4 are

---

[2] It was not necessary to know the exact ^{207}Pb/^{206}Pb ages when calculating the Stacey-Kramer common Pb composition because there is <1% variation in the common ^{207}Pb/^{206}Pb ratio for Jurassic-Cretaceous ages.
[3] Minerals are listed by increasing modal abundance.

reversely discordant and plot just above the concordia curve (-2.3% and –4.1% discordant, respectively; negative values assigned to reverse discordance), conversely, M5 and M3 are normally discordant and plot just below the concordia curve (2.6% and 3.7% discordant, respectively). A linear regression through the data produces a lower intercept (L.I.) of 107 ± 4.5 Ma and an upper intercept (U.I.) of 161 ± 20 Ma. The intercept ages seemed to agree well with other age constraints in the region, but are considered spurious for the following reasons: 1) The L.I. is obviously older than the youngest monazites, M4 and M2, a result of a linear regression through reversely discordant data. 2) The discordia chord plots very close to the concordia curve. This imparts substantial error on the upper intercept age because the low angle intersection of the chord with the concordia curve magnifies the error that is associated with the chord. 3) BSE images of monazite grains for DG38a indicate complex and irregular chemical domains, suggestive of multiple age domains within single monazite crystals (inset Fig. 4.3a). Thus, the likelihood of bulk mixing of multiple age domains with varying degrees of unsupported ^{206}Pb make it difficult or impossible correctly interpret the IDTIMS data, even when they are manipulated using linear regression techniques.

In situ SHRIMP analysis confirmed the existence of multiple intracrystal age domains. Prior to the SHRIMP analyses, BSE imaging and X-ray elemental mapping for Y, Th, and U revealed complex zoning in many of the monazites. The Y maps generally provided the best indication of growth and/or recrystallization domains, and were critical for targeting SHRIMP analyses because these relationships were not always clear in BSE, U, and Th images. The exact mechanism of monazite growth and/or replacement responsible for these domains remains unclear (i.e., resorption-reprecipitation, overgrowth, or recrystallization). Consequently, the general terms “growth” or “crystallization” will be used in the following sections to represent all possible means of growth and/or replacement, except when the inferred mechanism is specifically stated.

At least three, and possibly five, ages of monazite crystallization were identified when the Y images were used to target the SHRIMP analyses (Figs. 4.4 - 4.7). The oldest ages have a weighted mean $^{208}Pb/^{232}Th$ age of 138.7 ± 4.5 Ma that includes five SHRIMP spots on four monazites (see Fig. 4.7b, below $^{238}U/^{206}Pb$ axis of the Tera-Wasserburg plot). These ages correspond to the lowest Y domains located in the core portion of the analyzed monazites (Mnz2, 9, and10 of Figs. 4.4 and 4.6, respectively) with one exception; Mnz12, has a younger (75.9 ± 1.2 Ma), high Y zone in the core partly surrounded by the older, lowest Y domain (Fig. 4.6). However, the high Y core is interpreted to be part of the high Y domain found rimming this monazite. In this crystal, the third dimension must be considered. The central high Y portion likely represents a lobe of the younger rim that extends down in the z-direction into the plane (x-y) of the image (cf. Pyle and Spear, 2002).

The second oldest domain of the monazites in DG38a has a weighted mean $^{208}Pb/^{232}Th$ age of 126.1 ± 2.2 Ma based on three spots on monazite from three samples (Fig. 4.7b). This corresponds with the zones that have the second lowest Y concentration (Mnz1, 8, and 9 of Figs. 4.4, 4.5, and 4.6, respectively). This domain is interpreted to be distinct from the older, lowest Y core described above because in Mnz9 there is a sharp, truncated boundary between the younger (125.6 ± 1.9 Ma), intermediate Y domain and the older (144.4 ± 2.2 Ma) lower Y core that appears to have been significantly resorbed. Also, the SHRIMP spots are clearly situated within their respective Y zones (Fig. 4.6), leaving little doubt that these are robust ages for separate growth domains.

The youngest domain in all the monazites is associated with the discordant, high Y rims, except for Mnz4 (Fig. 4.5), which is almost completely composed of this high Y domain. The limited preservation of small, isolated patches of low Y concentration in Mnz4 suggest that resorption and/or recrystallization of this domain was nearly complete. The high Y domains appear to range in age from ca. 107 to 76 Ma (Figs. 4.4-4.7). However, the weighted mean $^{208}Pb/^{232}Th$ age of 76.9 ± 3.6 Ma for five spots on four monazites is considered to be the best approximation for this domain, i.e., Group 3 in Fig. 4.7b. The older ages are likely the result of slight overlap into older, adjacent age domains. This is clearly the case for spot 3 of Mnz9 which is 107 ± 4 Ma (Fig. 4.6), and possibly for spot 2 of Mnz1, which is 91.2 ± 1.4 Ma (Fig. 4.4). However, the ca. 86 Ma age of spot 2 for Mnz2 appears to be entirely within the high Y rim (Fig. 4.4). This may suggest that the high Y rim is indeed older than ca. 77 Ma in some of the monazites, or that the spot penetrated the older Y domain in z-direction. However, incursion of an older domain in the z-direction is considered unlikely because of the restricted depth of the spots (~ 2 μm), but it cannot be completely ruled out.

Of the three main age groups described above, Groups 1 and 2 appear to have overlap between the gray value intensities (e.g., Mnz1 and Mnz2, Fig. 4.4) and the spot ages assigned to both groups (e.g., spots 2-1 of Group 1 and 1-1 of Group2 in the Tera-Wasserburg plot, Fig. 4.7b). Also, a scan of the gray value plots in Figs. 4.4-4.7 indicate that the gray value intensities, in other words Y concentrations, for the domains belonging to a specific “Group” are not very uniform. For instance, the gray values of the high Y rims assigned to Group 3 vary from 96 (Mnz2) to 205 for (Mnz12). Perhaps this reflects the scale of chemical equilibrium and elemental transport between garnet and monazite at different locations within the rock. However, this could only be assessed using quantitative analyses of the Y domains within the monazite and garnet of this sample. Notwithstanding, in Fig. 4.8, an attempt is made to asses the validity of the ages and corresponding Y zones attached to each Group by normalizing the gray pixel intensities of the Y maps to those in Mnz9, because only Mnz9 clearly displays all three domains. A unifying feature for all the monazites are the high Y rims, which were adjusted for brightness and contrast to match the gray value of the high Y rim in Mnz9. The consistent pattern in the gray value plots that accompany each Y map in Fig. 4.8 strongly indicates that there are indeed three distinct Y domains, corresponding to mean gray values (mgv's) of ~40, ~80, and ~140. Although not as rigorous as quantitative EMP analysis, the approach used in Fig. 4.8 lends further support to the interpretation of three major periods of monazite growth at ca. 139 Ma, 126 Ma, and 77 Ma, which correlate with low, medium, and high Y domains, respectively.

4. 5. Discussion

4.5.1. Why do Y maps provide the best indication of age domains?

The images provided by the Y maps consistently provided the best indication of age domains within the metamorphic monazite. Although many of the zones revealed within the BSE images closely approximated those in the Y maps, some BSE images appeared more complicated and/or lacked the definition provided by the Y maps (Figs. 4.4 – 4.7). Other studies have documented the lack of correlation between BSE images and age domains determined using *in situ* techniques (e.g., SHRIMP in Rubatto et al., 2001; EMP in Cocherie et al., 1998). The above observations may be attributed to the process involved in the generation of BSE images, where the production of backscattered electrons varies directly with atomic number; in general, higher atomic number elements appear brighter than lower atomic number elements. Discrimination of "chemical domains" by BSE imaging of minerals such as monazite arises from the differences in average atomic number within the crystal (cf. Stern and Sanborn, 1998). Since monazite typically contains several thousand ppm Th with a high atomic number (Z = 90), the zoning in BSE images should strongly reflect the Th distribution. However, the zoning may also be significantly influenced by the distribution of other elements such as U (Z = 92; 100's to 1000's ppm), and possibly Ce (Z = 58) and La (Z = 57). Thus, the domains revealed in BSE imaging may represent a composite image of superimposed chemical zones of more than one element, which is more visually complicated and less discrete compared to those found in an image generated from the analysis specifically for Y.

The zones and boundaries observed in the Th and U images tend to have less definition or were absent when compared to the sharp zoning produced by the Y maps (Figs. 4.4 – 4.7). This is primarily an analytical artifact related to the detector collection efficiency for X-rays of Th and U versus those of Y (see Goldstein et al., 1981, Chapter 5.2.2). The quantum efficiency for detecting X-rays with a wavelength (λ) close to 4 angstroms (Å; i.e., U = 3.910 Å, Th = 4.138 Å, as determined by Bearden, 1964) drops sharply to ~40% efficiency compared to X-rays with λ of 6.5 Å (Y = 6.449 Å) that have ~80% detection efficiency. This accounts for the lack of resolution in the Th and U maps when compared to the Y maps in this study. However, this does account for the lack of correlation between age domains and chemical zones in the Th and U maps. For instance, in Mnz2, 8, 9, and 10 (Figs. 4.4-4.6) the age domains identified based on zoning within the Y maps could not be similarly correlated with zones in the U and Th maps. Williams et al. (1999) have also demonstrated an inconsistent relationship between age domains and zoning within Th and U chemical maps. They presented Th, U, and Pb maps of monazites with complex zoning, but did not find a consistent correspondence with age domains.

The cation sites preferentially occupied by Th and U versus Y likely account for their observed non-correlative nature regarding their distribution within a monazite crystal, and their correspondence, or lack thereof, with age domains (e.g., this study; Pyle et al., 2001). However, this is still poorly understood. In monazite, all three elements occupy 9-fold coordination sites (e.g., Yunxiang et al., 1995), are relatively abundant (1000's ppm to many %, e.g., Bea, 1996; Zhu and O'Nions, 1999a; Pyle et al., 2001), and have similar ionic radii (U = 1.05 Å, Th = 1.09 Å, Y = 1.08 Å; Shannon, 1976). However, the difference in valence between Y^{3+} and $U^{4+}$and Th^{4+} does have an influence on both the lattice sites and the stoichiometry of coupled substitutions that accommodate the incorporation or removal of these elements during recrystallization processes (e.g., Bingen et al., 1996; Poitrasson et al., 1996, 2000). Another important and related factor is the influence other major and accessory minerals have on the availability of these light rare earth elements (LREE) during monazite production. Unfortunately, the influence of other minerals on the availability of Th (e.g., allanite, thorite, thorianite) and U (e.g., zircon, uraninite, epidote) for incorporation into metamorphic monazite is not well understood, especially for medium to high-grade samples. Conversely, a growing body of evidence strongly suggests that garnet exerts considerable control over the Y budget during metamorphism because it is a major Y sink (e.g., Bea and Montero, 1999; Foster et al., 2000, 2002; Pyle et al., 2001; Pyle and Spear, 2002, 2003). Consequently, reactions involving the production and consumption of monazite are sensitive to this, and are reflected internally in preserved Y zones.

Pyle and Spear (2002, 2003) have proposed a number of metamorphic reactions involving both major and accessory phases based on Gibbs method modeling using differential thermodynamics. Yttrium zones within monazite similar to those found in this study were correlated with reactions that involved garnet, monazite, and xenotime. Using the concepts and metamorphic reactions put forward by Pyle and Spear (2002, 2003), the age domains identified in the monazites of this study are tentatively correlated with metamorphic reactions that involve similar mineral assemblages (see Fig. 10). It should be noted that reactions proposed by Pyle and Spear involved assemblages metamorphosed at lower pressures (~4 kbar) relative to those interpreted for this study (5-7 kbar). Consequently, the metamorphic reactions proposed for the upper amphibolite facies assemblages that include Ky-Grt-Bt-Ms and melt reflect the pressure difference, such that DG38a is interpreted to have evolved primarily within the kyanite stability field rather than the sillimanite stability field.

4.1.1. Constraining the age of metamorphic reactions involving monazite

The correlation of monazite age domains with metamorphic reactions is facilitated, in part, by thin section observations and by comparison of Y maps for monazite analyzed by the SHRIMP with Y maps of monazite included in garnet and kyanite (Fig. 4.9). Regrettably, only two monazite inclusions in kyanite and garnet were found. It is questionable whether the two inclusions are representative of the entire monazite population included within garnet and kyanite of this sample. Notwithstanding, they at least provide additional evidence that can be used to reasonably infer metamorphic reactions that may correlate with the age domains. The reactions proposed in the following discussion are summarized in Fig. 4.10.

Figure 4.9 illustrates that the Y concentrations within the monazite inclusions are uniform and mostly homogeneous (Fig. 4.9a and b), presumably, because they were armored within kyanite and garnet, and were thus protected from involvement with subsequent metamorphic reactions. Also, the monazite included within garnet appears to be fairly euhedral, and quite restricted in size (<15 μm). The monazite separates in grain mount selected for SHRIMP analysis are interpreted as matrix monazite because they have multiple, irregularly shaped chemical domains, and are >>100μm in diameter. This is interpreted to be the end result of variable growth and consumption processes involving matrix monazites that were able to participate in the metamorphic reactions experienced by DG38a (cf. Foster et al., 2000; Pyle and Spear, 2003).

The monazite included within garnet of Fig. 4.9a has a relatively high Y concentration with a total mgv of 158 ± 3 (1σ) that decreases progressively from a value of 175 ± 1 in the core to 108 ± 2 in the rim. When compared to the Y zoning found in Mnz9, only the high Y rim of Mnz9 with a mgv of 141 ± 3 comes close (Fig. 4.9c). However, the monazite included within the garnet is found in the core of the garnet, and presumably grew prior to the formation of the high Y rim on Mnz9, which is interpreted to have grown near the end of the metamorphic cycle (see below). Also, the restricted grain size is characteristic of monazite that grew early in the prograde metamorphism of a pelitic assemblage (i.e., Grt to St-grade; e.g., Rubatto et al., 2001; Pyle and Spear, 2002). In this study, the absence of relatively older, high Y cores in the matrix monazites analyzed suggests that any high Y monazites produced concomitant with the one included in the garnet core of Fig.4.9a were completely consumed or recrystallized during subsequent metamorphic reactions. Two slightly modified reactions from Pyle and Spear (2003) are proposed below to account for this scenario. Pyle and Spear concluded that the presence or absence of xenotime (YPO_4) during the production of monazite and garnet has a significant influence on the amount of Y incorporated into these minerals, as well as their stability. In the first reaction, high Y monazite and garnet are produced in the presence of xenotime via:

$$\mathrm{Bt + Chl + Qtz + Pl + Xno} \rightleftharpoons \mathrm{Ms + Ap + Mnz_{[high\ Y]} + Grt_{[high\ Y]} + H_2O} \qquad [1]$$

With further heating and after the supply of xenotime has been exhausted, the consumption of monazite occurs producing relatively low Y garnet:

$$\mathrm{Bt + Chl + Qtz + Pl + Mnz_{[high\ Y]}} \rightleftharpoons \mathrm{Ms + Ap + Grt_{[low\ Y]} + H_2O} \qquad [1a]$$

From this point on, xenotime is assumed to be absent from subsequent reactions that are proposed below. Support for this may be drawn from the observation that no xenotime was identified in thin section or as inclusions in the kyanite and garnet of DG38a imaged by BSE.

Although [1a] involves the consumption of relatively high Y monazite, low Y garnet is produced because a substantial portion of the whole rock Y budget is already locked up in the garnet cores produced during reaction [1]. Thus, reactions [1] and [1a] result in the production and then nearly complete consumption of high Y monazite, respectively, concomitant with the growth of high Y garnet cores that are overgrown by low Y garnet rims, respectively (Pyle and Spear, 2003; Fig. 4.10).

In Figs. 4.9b and c there is a striking similarity between Y concentrations for the monazite included in kyanite and the low Y core in Mnz9. The mgv for both is the same within error, which is 44 ± 1 for the monazite included in kyanite and 42 ± 1 for low Y core of Mnz9. The low Y monazite is therefore interpreted to have grown prior to the initial production of kyanite accompanied by the consumption of the low Y garnet rim produced in reaction [1a], such that:

$$Grt_{[low\ Y]} + Chl + Ms + Ap \rightleftharpoons St + Bt + Pl + Mnz_{[low\ Y]} + Qtz \qquad [2]$$

Reaction [2] is constrained to be as old as 144.4 ± 2.2 Ma (i.e., $^{208}Pb/^{232}Th$ SHRIMP age for low Y core of Mnz9 in Fig. 4.6).

The intermediate Y composition of the younger, ca. 126 Ma monazite domain mantling the low Y core in Mnz9 (Figs. 4.6 and 4.9) is not present in either of the two monazite inclusions of kyanite and garnet. In Mnz9, the significant embayment of the older low Y core by the intermediate Y zone indicates that reactions involving monazite at this time involved either resorption - reprecipitation or encroachment by recrystallization fronts. The consumption of the low Y monazite core may have occurred during the reaction,

$$St + Pl + Ms + Qtz + Mnz_{[low\ Y]} \rightleftharpoons Grt_{[low\ Y]} + Ky + Bt + Ap + H_2 0 \qquad [3]$$

which would result in the addition of low Y garnet. The absence of staurolite in DG38a indicates that [3] is a discontinuous reaction with respect to staurolite. The Fe/Mg composition of these pelitic rocks is not considered to be a factor controlling the absence or presence of staurolite, because staurolite is found in increasing quantity in the same package of rocks further to the east in progressively lower-grade rocks. According to the NaKFMASH petrogenetic grid of Spear et al. (1999), the minimum P-T constraints for the staurolite-out reaction are ~7.4 kbar and 675 °C. Once staurolite was used up, the renewed growth of monazite with intermediate Y composition may have progressed by the reactions proposed by Pyle and Spear (2003) for near isobaric heating:

$$\text{Grt} + \text{Ms} + \text{Ap} \rightleftharpoons \text{Ky} + \text{Bt} + \text{Mnz}_{[\text{intermediate Y}]} \qquad [4]$$

The youngest, ca. 77 Ma domain for all the analyzed monazites belongs to the high Y rims. Approximately 18 km to the northwest, within the same Ky-zone rocks (Fig. 4.2), Crowley et al. (2000) produced U-Th-Pb SHRIMP spot ages of ca. 83-73 Ma for monazite inclusions in kyanite from a migmatitic Ms-Grt-Ky-Bt schist (Sample 1 of Crowley et al.). The range of ages produced by Crowley et al. closely match the ca. 86-73 Ma ages for the high Y rims of monazites from sample DG38a, excluding spot 2 of Mnz1 and spot 3 of Mnz9 due to interpreted overlap with older age domains. The data suggest that kyanite growth, or at least the last episode of kyanite growth, may have post-dated ca. 73 Ma. However, the one monazite that was found included in kyanite of DG38a (Fig. 4.9b) has a uniform low Y composition, and is thus lacking the high Y rim and irregular zones found in matrix monazite grains (e.g., Mnz9). It is possible that the kyanite in DG38a overgrew and included the monazite of Fig. 4.9b just before the formation of the high Y rims. If Mnz2 of Fig. 4.4 had been included in kyanite in the same fashion, it would have also been revealed as a uniform inclusion with the same gray value as the monazite in Fig. 4.9b, and the core of Mnz9. Perhaps if more monazite inclusions were found within the kyanite porphyroblasts of this sample, some would have had a high Y rim that was ca. 77 Ma.

Pyle and Spear (2003) described monazite grains with high Y rims that were interpreted to have formed upon cooling following the peak of metamorphism (~740º C, 3.5 kbar), which produced the assemblage Crd-Kfs-Grt-melt at the expense of Sil-Bt-Qtz-

Mnz ± Xno (reaction [4] of Pyle and Spear). Subsequent melt crystallization during cooling reversed the direction of this reaction, which resulted in the formation of the high Y rims on monazite. Foster et al. (2000) also interpreted high Y rims on monazite grains to have formed during the breakdown of garnet, probably during decompression. The peak kyanite-bearing assemblage of DG38a with 20-30% melt content may be interpreted as the higher-pressure equivalent to the reaction proposed by Pyle and Spear. According to the NaKFMASH petrogenetic grid of Spear et al. (1999), at higher pressures of ≥8 kbar, and similar temperatures of >700º C, cordierite is not present within the kyanite stability field, and thus reaction [4] of Pyle and Spear (2003) may be written as:

$$\text{Ky} + \text{Bt} + \text{Qtz} + \text{Pl} + \text{Mnz} \rightleftharpoons \text{Grt} + \text{Kfs} + \text{Melt} \qquad [5a]$$

The pressures of ≥8 kbar and temperatures of >700º C predicted for this assemblage using the grid of Spear et al. (1999) are higher than the average estimates provided by Ghent et al. (1979, 1982, 1983) or Leatherbarrow (1981). However, P-T estimates for sample 7-8 of Ghent et al. (1982) near Warsaw Mt., and nearest DG38a, yielded a P-T of 8.3 kbar and 740° C. This P-T on the Spear et al. petrogenetic grid is on the high temperature side of the Ms-out melting reaction, which would account for the substantial production of melt observed in DG38a. Even if a lower P-T is assigned to DG38a, melt may have been produced if there was excess water in the system provided by previous prograde dehydration reactions (see Spear et al., 1999) that shifted the Ms-out melt reaction to a lower P-T.

Upon cooling, the melt produced in [5a] began to crystallize, which reversed the reaction, and resulted in the renewed production of monazite:

$$\text{Grt} + \text{Kfs} + \text{Melt} \rightleftharpoons \text{Ky} + \text{Bt} + \text{Qtz} + \text{Pl} + \text{Mnz} \qquad [5b]$$

Further cooling led to final melt crystallization and the production of cross cutting muscovite, which has also been observed in DG38a. Interestingly, Spear et al. (1999) anticipate a lack or absence of K-feldspar in the final assemblage, which is characteristic of DG38a. Spear et al. conclude that the liberated potassium produced during prograde muscovite consumption was initially incorporated into the melt. Production of retrograde muscovite is expected in place of K-feldspar if the melt cools on a P-T path that passes above the invariant point IP1'' of Spear et al. (IP1'' is defined by the intersection of reactions 1, 2, and 3 of Spear et al., 1999; P-T = ~3.8 kbar and 650° C).

Reactions [5a] and [5b] may account for the assemblage and textures in DG38a, as well as the inclusion of young ca. 83-73 Ma monazites in kyanite documented by Crowley et al. (2000) to the northwest. In addition, at the location of DG38a, continued melt crystallization may have resulted in further resorption of kyanite accompanied by production of high Y monazite. Pyle and Spear (2003) presented a supplementary reaction for continued melt crystallization following reaction [5b] in which monazite was formed and sillimanite was consumed. Substituting kyanite for sillimanite, this reaction may be written as:

$$\mathrm{Ky} + \mathrm{Melt} \rightleftharpoons \mathrm{Qtz} + \mathrm{Pl} + \mathrm{Ms} + \mathrm{Mnz}_{[\mathrm{high\ Y}]} \qquad [5c]$$

In [5b] and [5c], the necessary elements for monazite growth (i.e., PO_4, Ce, La, Th, Y) via melt crystallization must have been acquired initially from the consumption of monazite during melt production in reaction [5a]. The sequestering of incompatible elements like Y within the melt during crystallization may have resulted in the formation of the higher Y rims on the matrix monazite during the late stage of melt crystallization. Support for reactions [4], [5a], [5b] and [5c] is gained from the textures observed in thin section that demonstrate both kyanite and garnet have been significantly resorbed (Fig. 4.3c and d), and that some garnets appear to replace kyanite while other garnets appear to be included within kyanite (Fig. 4.3d).

Admittedly, the reactions proposed in this paper have two obvious shortfalls. The first is that they are based mainly on precise *in situ* SHRIMP analyses that were coupled with qualitative observations, such as textural evidence in thin section, Y maps, and the shape of Y zones. Without quantitative analyses of the Y concentrations for the zones in monazite and garnet that can be considered in the context of thermodynamic modeling, the reactions proposed in this study can only be considered as speculative.

The second shortfall, is the lack of consideration given to Th, a major constituent of monazite, and the accesory minerals involved in the contribution or depletion of Th throughout a metamorphic event. It is quite likely that Th-silicates (e.g., allanite, thorite, huttonite), other Th-phosphates (e.g., cheralite), and Th-oxides (thorianite), play an important role with respect to the Th budget during metamorphism (see Bea and Montero, 1999, and references therein). However, this role is still poorly understood with regard to specific metamorphic reactions, especially for assemblages that come from upper amphibolite- to granulite-facies rocks. A detailed examination of this is beyond the scope of this study, but should be considered in future investigations.

4. 6. Conclusions

The most significant contribution of this study is the clear link that has been established between Y zones of relative depletion or enrichment in metamorphic monazite and age domains as revealed by chemical mapping coupled with *in situ* SHRIMP analyses. The Y maps provided the best indication of growth and/or recrystallization domains, and were critical for targeting SHRIMP analyses because these relationships were not always clear in BSE, U, and Th images. Moreover, the Y domains consistently correlated with distinct age domains, with up to three or more in some crystals that ranged in age between ca. 144-73 Ma. These data clearly demonstrate that multiple age domains within metamorphic monazite are the cause of the age dispersion produced in the IDTIMS analyses. As such, this study adds to a growing body of evidence that points to the ubiquity of multiple age domains within single monazite crystals from medium to high-grade metamorphic terranes. This has significant implications for previous studies that relied upon conventional geochronological techniques such as isotope dilution and linear regressions through discordant data to date metamorphic monazite. Problems related to bulk mixing of multiple age domains combined with isotopic complexities such as unsupported ^{206}Pb may be irreconcilable or erroneously interpreted. Obviously, future studies should bear this in mind when deciding on an approach to date monazite for the purposes of constraining metamorphic/thermal events.

The recognition of the link between age domains and Y zones in monazite also has important implications for correlating the ages with major metamorphic reactions. Recent studies have investigated the interaction between accessory and major phases in pelites throughout a metamorphic event, and more specifically the partitioning of Y between phases such as garnet, monazite, and xenotime (e.g., Bea and Montero, 1999; Foster et al., 2000, 2002; Pyle et al., 2001; Pyle and Spear, 2002, 2003). They have established that garnet exerts considerable control over the Y budget available during metamorphism in pelitic rocks. Monazite crystallization is sensitive to the availability of Y, and is reflected internally in preserved Y zones; data from this study appear to support these interpretations. As such, the precise ages of Y domains within monazite provided by *in situ* SHRIMP analyses were tentatively correlated with metamorphic reactions involving garnet. However, these reactions lack rigorous thermodynamic modeling associated with quantitative measurements of Y, and are therefore considered speculative. Nevertheless, they provide testable hypotheses that can be considered in a more regional context, and have created a framework around which future studies can be shaped.

Figure 4.1. (a) Morphogeologic belts of the Canadian Cordillera (modified after Wheeler and McFeely, 1991). Physiographic boundaries according to Mathews (1986): MM = Monashee Mountains; SM = Selkirk Mountains; PM = Purcell Mountains. A-B represents line of section for (b). (b) Regional cross section illustrating the geometry of the Selkirk fan in the northern Selkirk Mountains (modified after Brown et al., 1993).

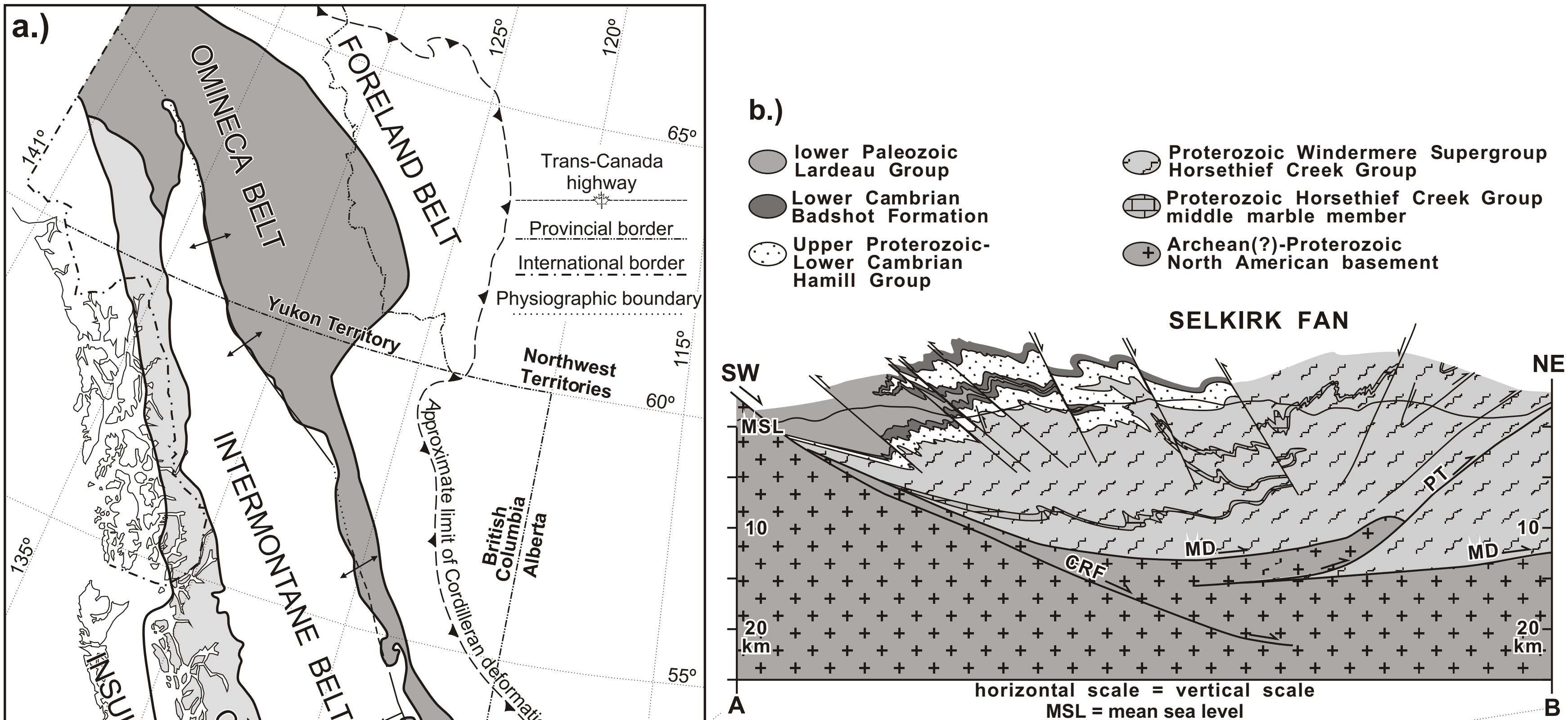

a.)
OMINECA BELT
FORELAND BELT
INTERMONTANE BELT
COAST BELT
INSULAR BELT
Trans-Canada highway
Provincial border
International border
Physiographic boundary
Yukon Territory
Northwest Territories
British Columbia
Alberta
Approximate limit of Cordilleran deformation
Fig.4.2
Calgary
Canada
USA
SRMT
MM
SM
PM
A
B
141°
135°
130°
125°
120°
115°
65°
60°
55°
50°
49°
Zone of structural divergence
(after Price, 1986)
b.)
lower Paleozoic Lardeau Group
Lower Cambrian Badshot Formation
Upper Proterozoic-Lower Cambrian Hamill Group
Proterozoic Windermere Supergroup Horsethief Creek Group
Proterozoic Horsethief Creek Group middle marble member
Archean(?)-Proterozoic North American basement
SELKIRK FAN
SW
NE
MSL
PT
MD
CRF
10
20 km
horizontal scale = vertical scale
MSL = mean sea level
A
B

Figure 4.1

Figure 4.2. Generalized geologic map of the northern Selkirk Mountains illustrating lithostratigraphy, regional metamorphic isograds, major structures and location for sample DG38a. Compiled from mapping by Brown (1991), Brown and Tippett (1978), Colpron et al. (1995), Leatherbarrow (1981), Marchildon (1999), Perkins (1983), Poulton and Simony, (1980), Raeside and Simony (1983), Scammell (1993), Simony et al. (1980), and Wheeler (1965). Location for sample DG38a within the studied area has also been included. Abbreviations: ADM = Adamant Mountain; ADP = Adamant pluton; AM = Argonaut Mountain; AP = Argonaut Pass; BCF = Birch Creek fault; BMF = Bigmouth fault; BMP = Bigmouth pluton; CRF = Columbia River fault; FG = French glacier; MC = Mica Creek village; MD = Monashee décollement; MN = Mount Nagle; MR = Mount Remillard; MSF = Mount Sir Sanford; NEF = Northeastern fault; TM = Trident Mountain. Mineral abbreviations for metamorphic zones after Kretz (1983).

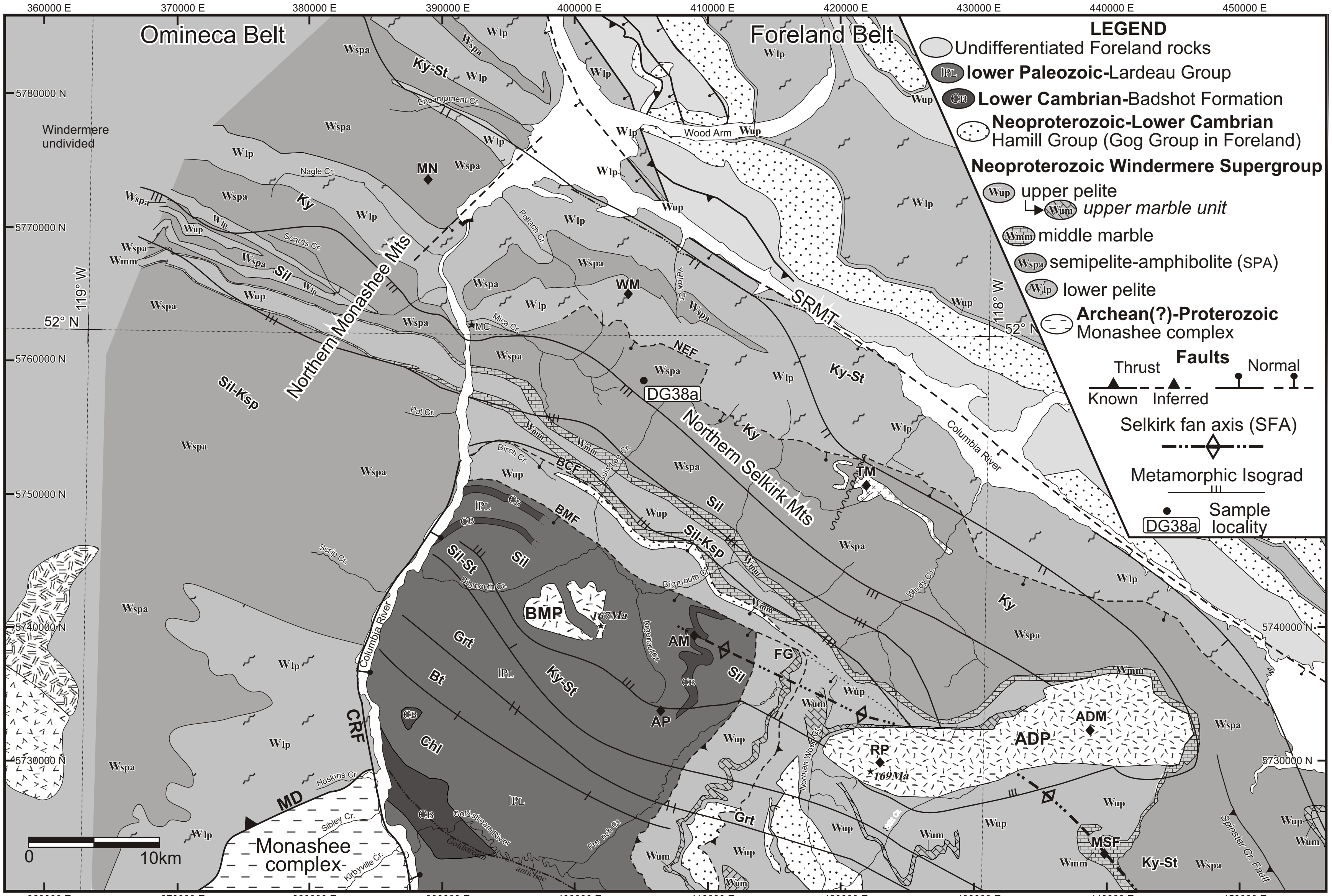
Omineca Belt
Foreland Belt
LEGEND
Undifferentiated Foreland rocks
lower Paleozoic-Lardeau Group
Lower Cambrian-Badshot Formation
Neoproterozoic-Lower Cambrian
Hamill Group (Gog Group in Foreland)
Neoproterozoic Windermere Supergroup
upper pelite
upper marble unit
middle marble
semipelite-amphibolite (SPA)
lower pelite
Archean(?)-Proterozoic
Monashee complex
Faults
Thrust
Normal
Known
Inferred
Selkirk fan axis (SFA)
Metamorphic Isograd
Sample locality
DG38a
Windermere undivided
Northern Monashee Mts
Northern Selkirk Mts
SRMT
NEF
BCF
BMF
CRF
MD
FG
MSF
BMP
ADP
167Ma
169Ma
MN
WM
TM
AM
AP
RP
ADM
Monashee complex
Columbia River
Wood Arm
52° N
119° W
118° W
0
10km
Sil-Ksp
Ky-St
Sil-St
Sil
Ky
Grt
Bt
Chl

Figure 4.2.

Figure 4.3. (a) IDTIMS U-Pb concordia plot for DG38a illustrating the spread of single crystal monazite fractions in close proximity to the concordia curve. A discordia line was fitted using a linear regression, but the upper and lower intercepts (U.I. and L.I., respectively) are considered to be geologically meaningless (see text for details). Inset BSE images of monazite grains from DG38a reveal chemical zoning that is indicative of multiple age domains within single crystals. (b) SHRIMP U-Pb concordia plot illustrating the range of *in situ* spot ages for different domains within analyzed monazites of DG38a, confirming the presence of multiple ages of monazite growth within single crystals. (c) Photomicrograph of DG38a, a Ms-Grt-Ky-Bt + melt pelitic schist (Note: Ms is not present in this part of the thin section). Two monazite grains in the center of the photo are aligned within the foliation of DG38a, indicating they were present during the development of the foliation in DG38a. Presumably, dating these monazite grains would provide age constraints for the formation of foliation in DG38a. However, this interpretation is complicated due to the presence of multiple age domains within single crystals. These domains are interpreted to represent episodic periods of recrystallization and/or overgrowth attributed to monazite's involvement in the metamorphic reactions that have affected DG38a. (d) Photomicrograph of the same thin section, demonstrating the resorption features of both kyanite and garnet, as well as the garnet inclusions within kyanite. Note that the garnet in the mid-left portion of the photo has inclusion trails within the core surrounded by an inclusion-free rim that appears to obtrude into the nearby kyanite.

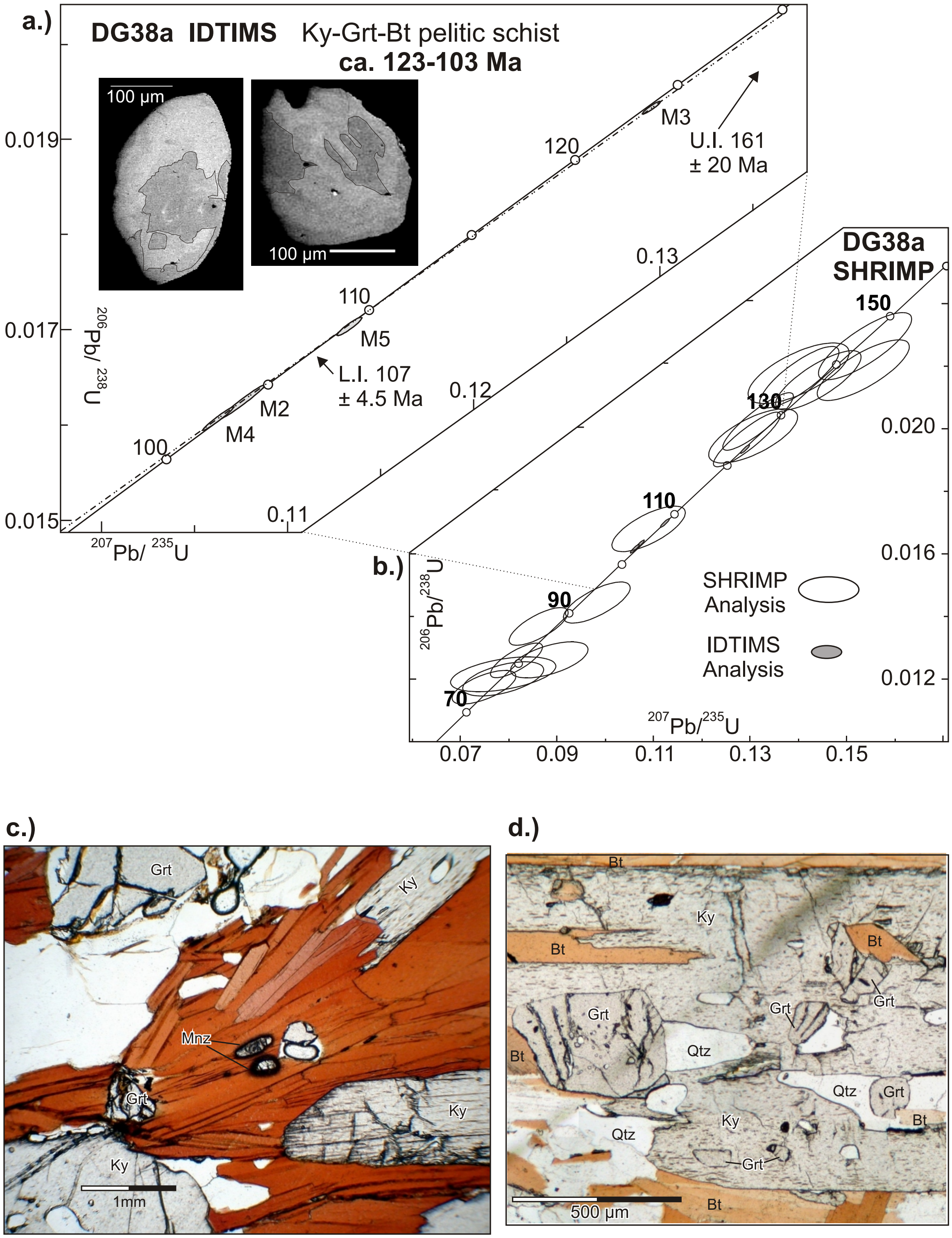
a.)
DG38a IDTIMS Ky-Grt-Bt pelitic schist
ca. 123-103 Ma
100 µm
100 µm
U.I. 161
± 20 Ma
L.I. 107
± 4.5 Ma
M3
M5
M2
M4
100
110
120
0.019
0.017
0.015
0.11
0.12
0.13
^{206}Pb/ ^{238}U
^{207}Pb/ ^{235}U
b.)
DG38a
SHRIMP
150
130
110
90
70
0.020
0.016
0.012
0.07
0.09
0.11
0.13
0.15
^{206}Pb/^{238}U
^{207}Pb/^{235}U
SHRIMP
Analysis
IDTIMS
Analysis
c.)
Grt
Ky
Mnz
Grt
Ky
Ky
1mm
d.)
Bt
Ky
Bt
Bt
Grt
Grt
Grt
Bt
Qtz
Qtz
Grt
Bt
Qtz
Ky
Grt
Bt
500 µm

Figure 4.3.

Figure 4.4. BSE images, Y, Th, and U maps, respectively, of monazites 1 and 2 of sample DG38a that were analyzed by the SHRIMP. The Y domains were used as a guide to target the SHRIMP analyses. BSE images of the analyzed monazites illustrate the locations of the SHRIMP spots. The locations of the spots were then transposed onto the Y maps to demonstrate their positions relative to the Y chemical domains. The numbers within the spots correspond to the SHRIMP analyses. Also associated with each Y map is a gray value profile that demonstrates the relative Y concentration in each domain. The brighter domains that correspond to higher numbers on the y-axis reflect higher Y concentrations. The U-Pb concordia plot includes the spot analyses for each monazite analyzed (errors for ellipses presented at 2σ). Notation for each spot represents the monazite number followed by the spot number, i.e., M1-1 equals Mnz1, spot 1. Figures 4.5-4.7 have a similar setup.

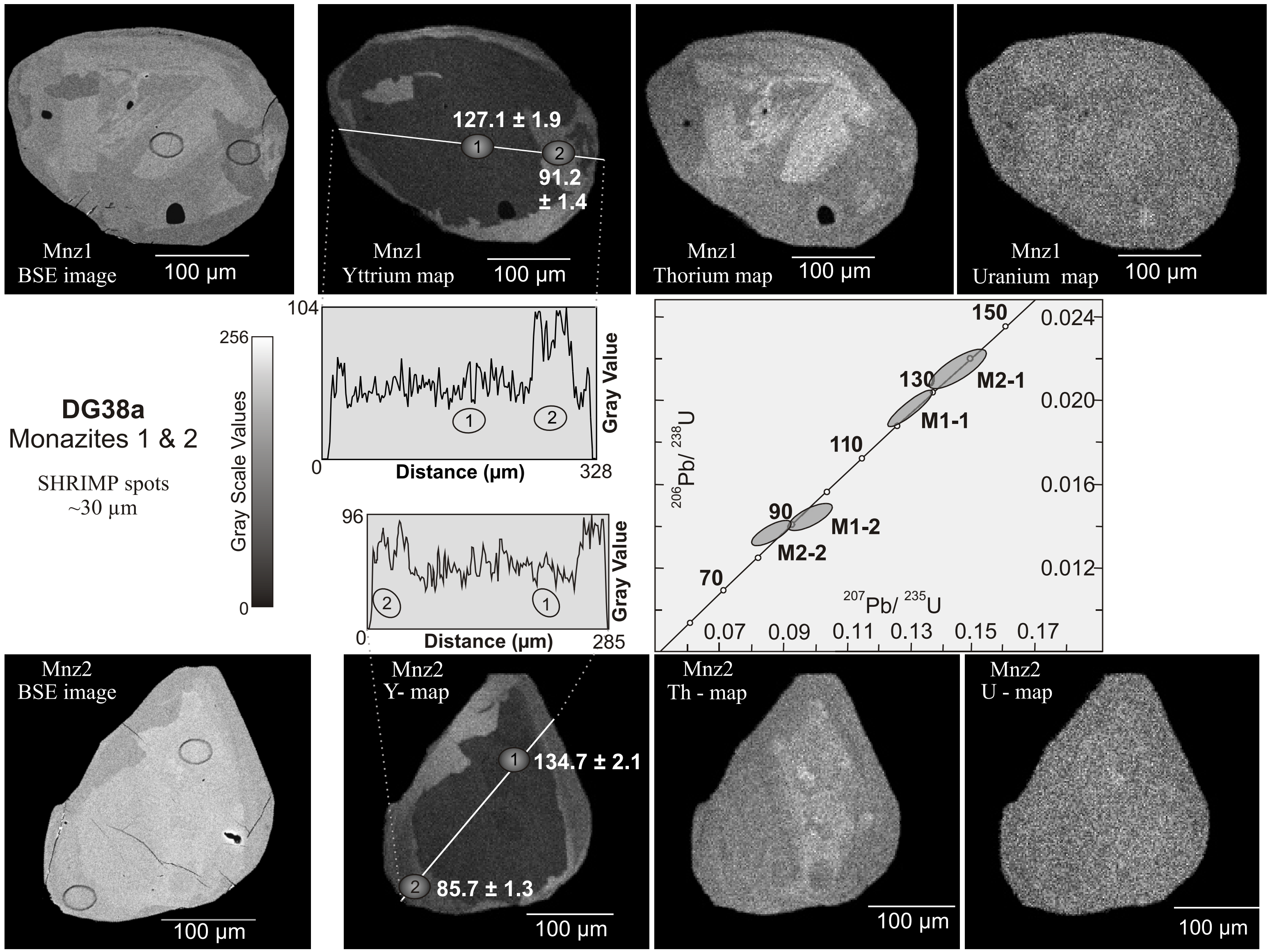
Mnz1
BSE image
100 μm
127.1 ± 1.9
91.2
± 1.4
Mnz1
Yttrium map
100 μm
Mnz1
Thorium map
100 μm
Mnz1
Uranium map
100 μm
DG38a
Monazites 1 & 2
SHRIMP spots
~30 μm
Gray Scale Values
256
0
104
0
Distance (μm)
328
Gray Value
96
0
Distance (μm)
285
Gray Value
150
130
110
90
70
M2-1
M1-1
M1-2
M2-2
0.024
0.020
0.016
0.012
^{206}Pb/ ^{238}U
^{207}Pb/ ^{235}U
0.07
0.09
0.11
0.13
0.15
0.17
Mnz2
BSE image
100 μm
Mnz2
Y- map
134.7 ± 2.1
85.7 ± 1.3
100 μm
Mnz2
Th - map
100 μm
Mnz2
U - map
100 μm

Figure 4.4

Figure 4.5. BSE images, Y, Th, and U maps, respectively, of monazites 4 and 8 of sample DG38a that were analyzed by the SHRIMP. The open ellipses in the U-Pb concordia plot represent analyses of the monazites shown in the previous figure, and shaded ellipses are for analyses of monazites 4 and 8.

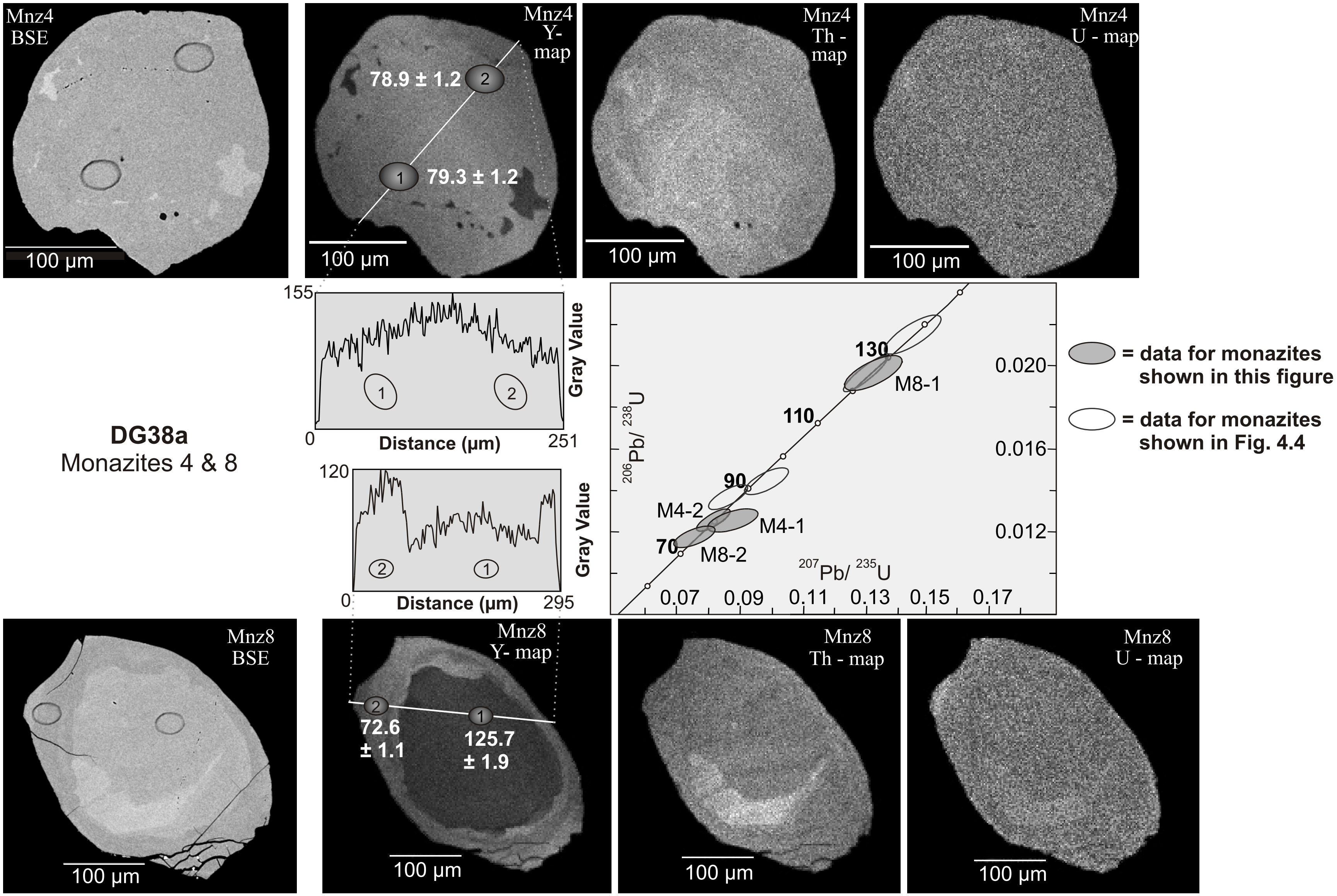
Mnz4
BSE
100 µm
Mnz4
Y-map
78.9 ± 1.2
79.3 ± 1.2
100 µm
Mnz4
Th - map
100 µm
Mnz4
U - map
100 µm
DG38a
Monazites 4 & 8
155
Gray Value
0
Distance (µm)
251
120
Gray Value
0
Distance (µm)
295
130
110
90
70
M8-1
M4-2
M4-1
M8-2
$^{206}Pb/^{238}U$
$^{207}Pb/^{235}U$
0.020
0.016
0.012
0.07
0.09
0.11
0.13
0.15
0.17
= data for monazites shown in this figure
= data for monazites shown in Fig. 4.4
Mnz8
BSE
100 µm
Mnz8
Y- map
72.6 ± 1.1
125.7 ± 1.9
100 µm
Mnz8
Th - map
100 µm
Mnz8
U - map
100 µm

Figure 4.5

Figure 4.6. BSE images, Y, Th, and U maps, respectively, of monazites 9 and 10 of sample DG38a. The open ellipses in the concordia plot represent analyses of the monazites shown in the previous figures, and shaded ellipses are for analyses of monazites 9 and 10.

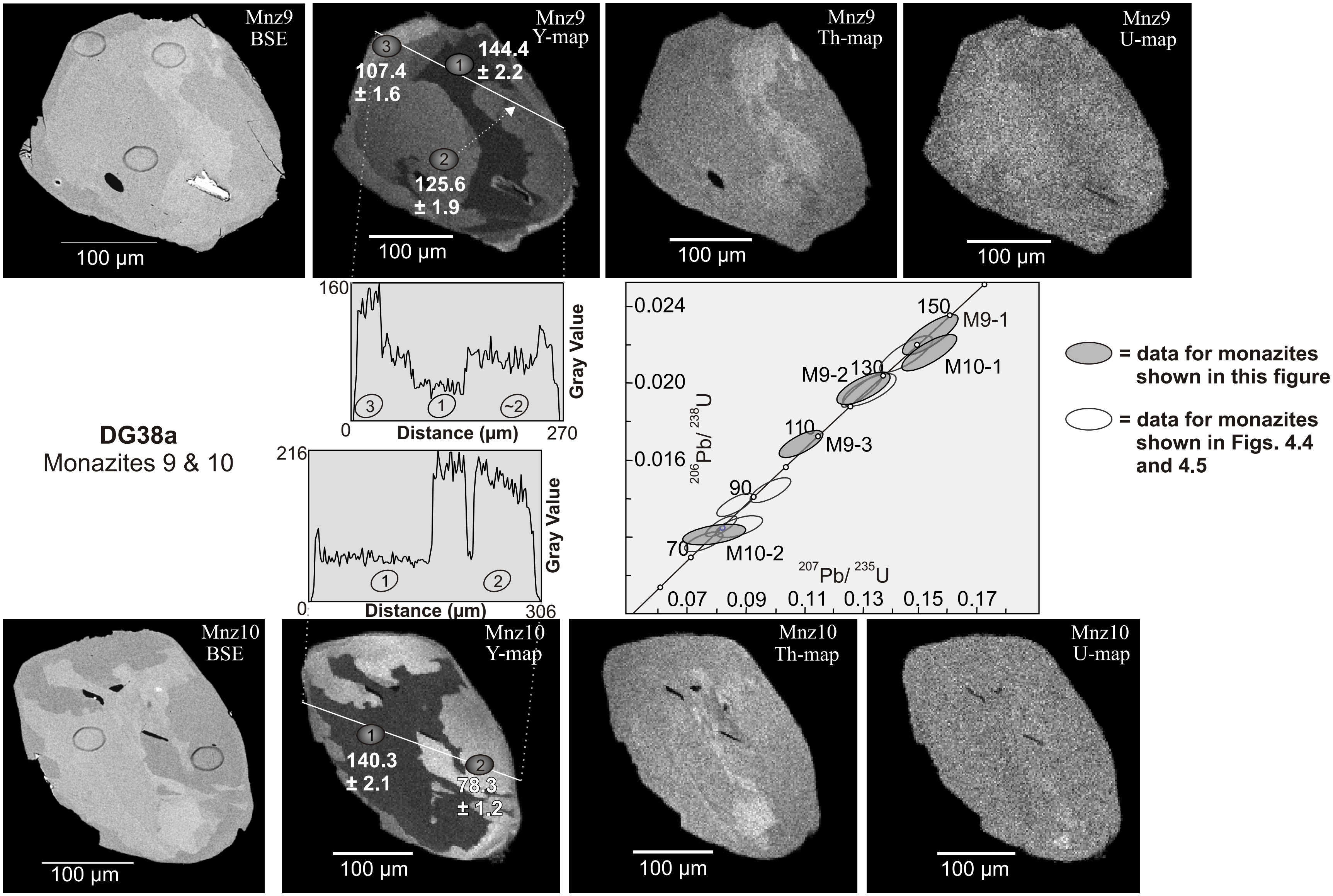

Mnz9
BSE
100 µm
Mnz9
Y-map
3
107.4
± 1.6
1
144.4
± 2.2
2
125.6
± 1.9
100 µm
Mnz9
Th-map
100 µm
Mnz9
U-map
100 µm
160
Gray Value
0
Distance (µm)
270
3
1
~2
DG38a
Monazites 9 & 10
216
Gray Value
0
Distance (µm)
306
1
2
0.024
0.020
0.016
206Pb/238U
207Pb/235U
0.07 0.09 0.11 0.13 0.15 0.17
150
130
110
90
70
M9-1
M10-1
M9-2
M9-3
M10-2
= data for monazites shown in this figure
= data for monazites shown in Figs. 4.4 and 4.5
Mnz10
BSE
100 µm
Mnz10
Y-map
1
140.3
± 2.1
2
78.3
± 1.2
100 µm
Mnz10
Th-map
100 µm
Mnz10
U-map
100 µm

Figure 4.6

Figure 4.7. (a) BSE images, Y, Th, and U maps, respectively, of monazite 12 of sample DG38a. The open ellipses in the concordia plot represent analyses of the monazites shown in the previous figures, and shaded ellipses are for analyses of monazite 12. (b) The Tera-Wasserburg (T-W) plot illustrates the various age domains within monazites of DG38a. In the T-W plot, the $^{207}Pb/^{206}Pb$ ratio uncorrected for common Pb is plotted against the uncorrected $^{238}U/^{206}Pb$ analyses (errors presented at 2σ). Ages for each group of data are provided by the intercept of a linear regression through the data with the concordia curve. Please refer to the Results section 4.4 (p. 77-78) for a more detailed description of the plot and the methods used to determine the intercept ages. The weighted (Wt.) mean of the $^{208}Pb/^{232}Th$ ages for each group is included below the T-W plot for comparison; the $^{208}Pb/^{232}Th$ ages are considered the most accurate.

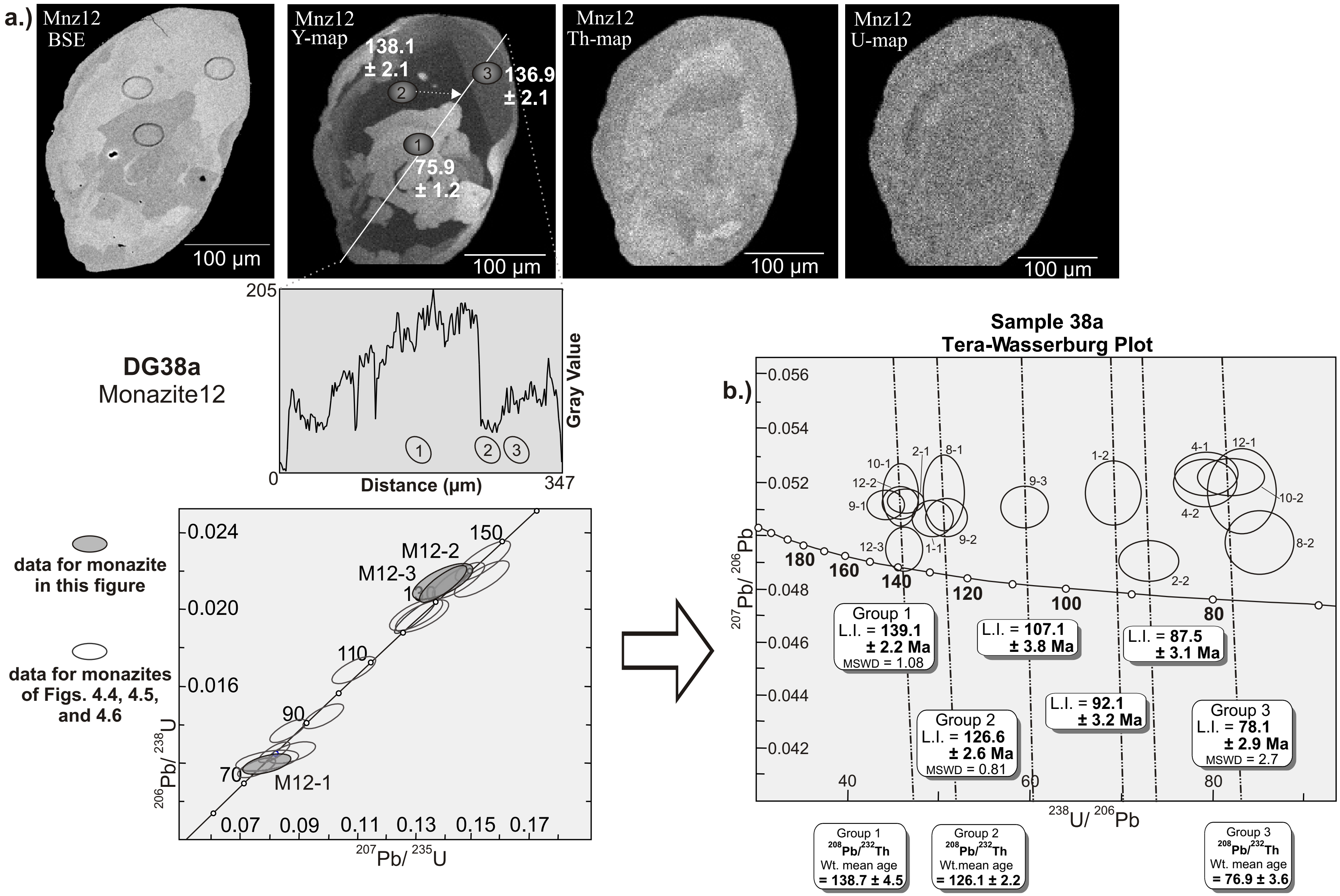

a.)
Mnz12
BSE
100 µm
Mnz12
Y-map
138.1
± 2.1
136.9
± 2.1
75.9
± 1.2
1
2
3
100 µm
Mnz12
Th-map
100 µm
Mnz12
U-map
100 µm
205
0
347
Distance (µm)
Gray Value
DG38a
Monazite12
data for monazite in this figure
data for monazites of Figs. 4.4, 4.5, and 4.6
M12-2
M12-3
M12-1
150
110
90
70
0.024
0.020
0.016
0.07 0.09 0.11 0.13 0.15 0.17
^{206}Pb/ ^{238}U
^{207}Pb/ ^{235}U
Sample 38a
Tera-Wasserburg Plot
b.)
0.056
0.054
0.052
0.048
0.046
0.044
0.042
^{207}Pb/ ^{206}Pb
180
160
140
120
100
80
40
60
80
^{238}U/ ^{206}Pb
10-1
2-1
8-1
12-2
9-1
12-3
1-1
9-2
9-3
1-2
4-1
12-1
4-2
10-2
8-2
2-2
Group 1
L.I. = 139.1
± 2.2 Ma
MSWD = 1.08
L.I. = 107.1
± 3.8 Ma
L.I. = 87.5
± 3.1 Ma
Group 2
L.I. = 126.6
± 2.6 Ma
MSWD = 0.81
L.I. = 92.1
± 3.2 Ma
Group 3
L.I. = 78.1
± 2.9 Ma
MSWD = 2.7
Group 1
^{208}Pb/^{232}Th
Wt. mean age
= 138.7 ± 4.5
Group 2
^{208}Pb/^{232}Th
Wt.mean age
= 126.1 ± 2.2
Group 3
^{208}Pb/^{232}Th
Wt. mean age
= 76.9 ± 3.6

Figure 4.7

Figure 4.8. Y maps of each monazite were normalized for brightness and contrast using the Y map of Mnz9, the only monazite that contained all three identified age domains. The gray values for each monazite were re-plotted in their respective gray value profiles. A comparison of the gray value intensities illustrated in the profiles demonstrates that the Y zones can be separated into three major groups that correspond with the three major age domains identified. The Y domains with the lowest average gray value of ~40 correspond with the oldest age domain, ca. 139 Ma, which is the Wt. mean of the $^{208}Pb/^{232}Th$ ages (see Fig. 4.7b). The Y domains with an intermediate average gray value of ~80 correspond with the second oldest age domain, ca. 126 Ma. The domain with the highest gray value, ~140, corresponds to the youngest age domain, ca. 77 Ma. Note: ellipses within each Y map represent the location and number of the SHRIMP spot analyses.

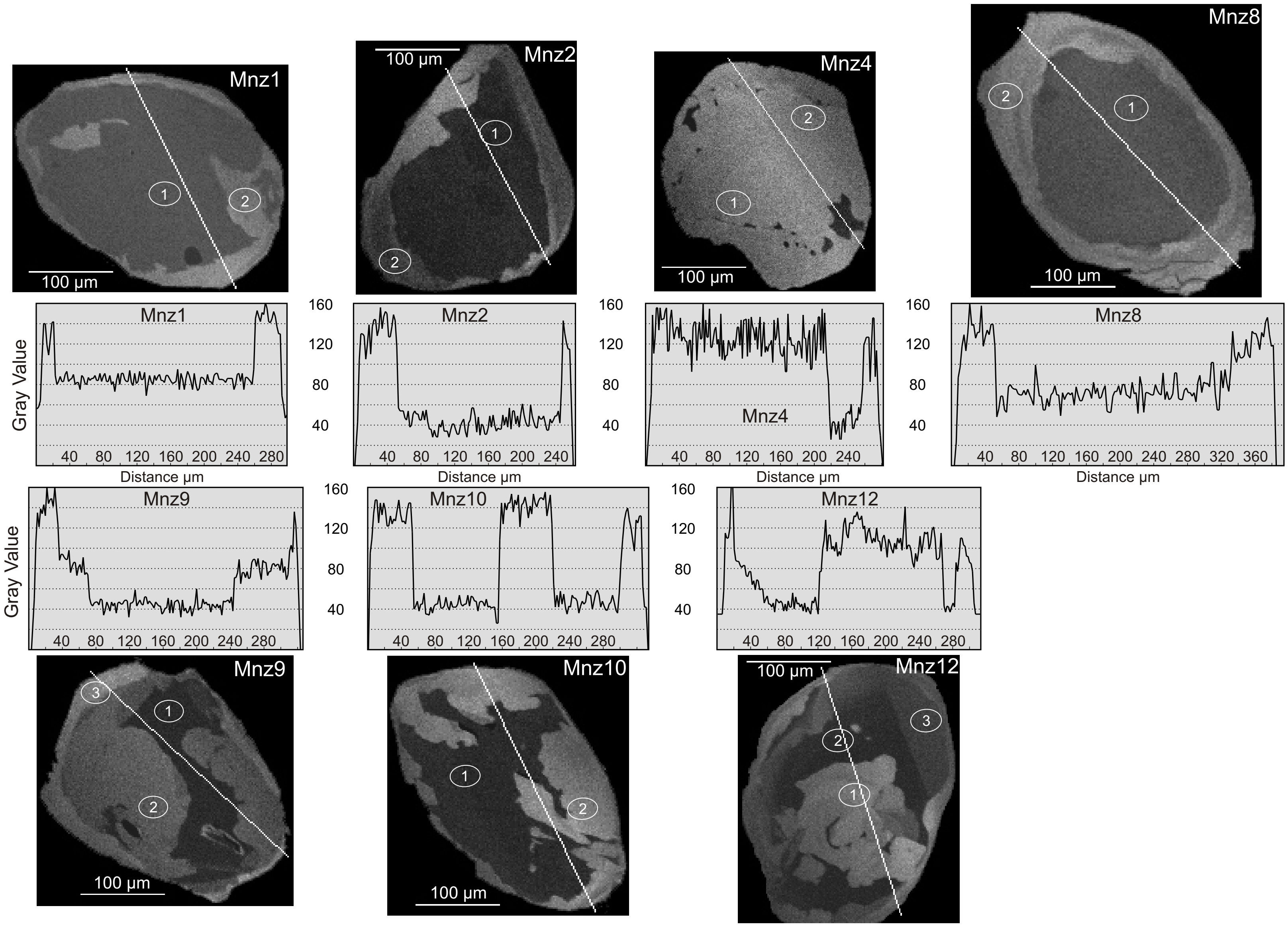
Mnz1
100 µm
Mnz2
100 µm
Mnz4
100 µm
Mnz8
100 µm
Gray Value
Distance µm
160
120
80
40
40 80 120 160 200 240 280
40 80 120 160 200 240
40 80 120 160 200 240 280 320 360
Mnz9
Mnz10
Mnz12
100 µm

Figure 4.8.

Figure 4.9. Comparison of Y maps and their gray scale values for monazite inclusions in garnet and kyanite with matrix monazite (Mnz9) in sample DG38a. (a) Monazite inclusion found in the core of a garnet displays a fairly uniform Y concentration, with a mean gray value (mgv) of ~158 that progressively decreases from 175 in the core to 108 toward the rim. Zones of similar Y concentration were not found in the matrix monazites that were analyzed, suggesting that preservation of monazites with a similar Y content likely occur only as inclusions armored by garnet. (b) The monazite included within kyanite also has a uniform Y concentration, with a mgv of ~44, which matches very closely with the mgv of ~42 found in the oldest portions of the Mnz9. (c) Y map of Mnz9. This is considered to be a matrix monazite due to the multiple, irregularly shaped zoning patterns and relatively large size (~320 x 240 μm) compared to the monazite inclusions within garnet (a) and kyanite (b).

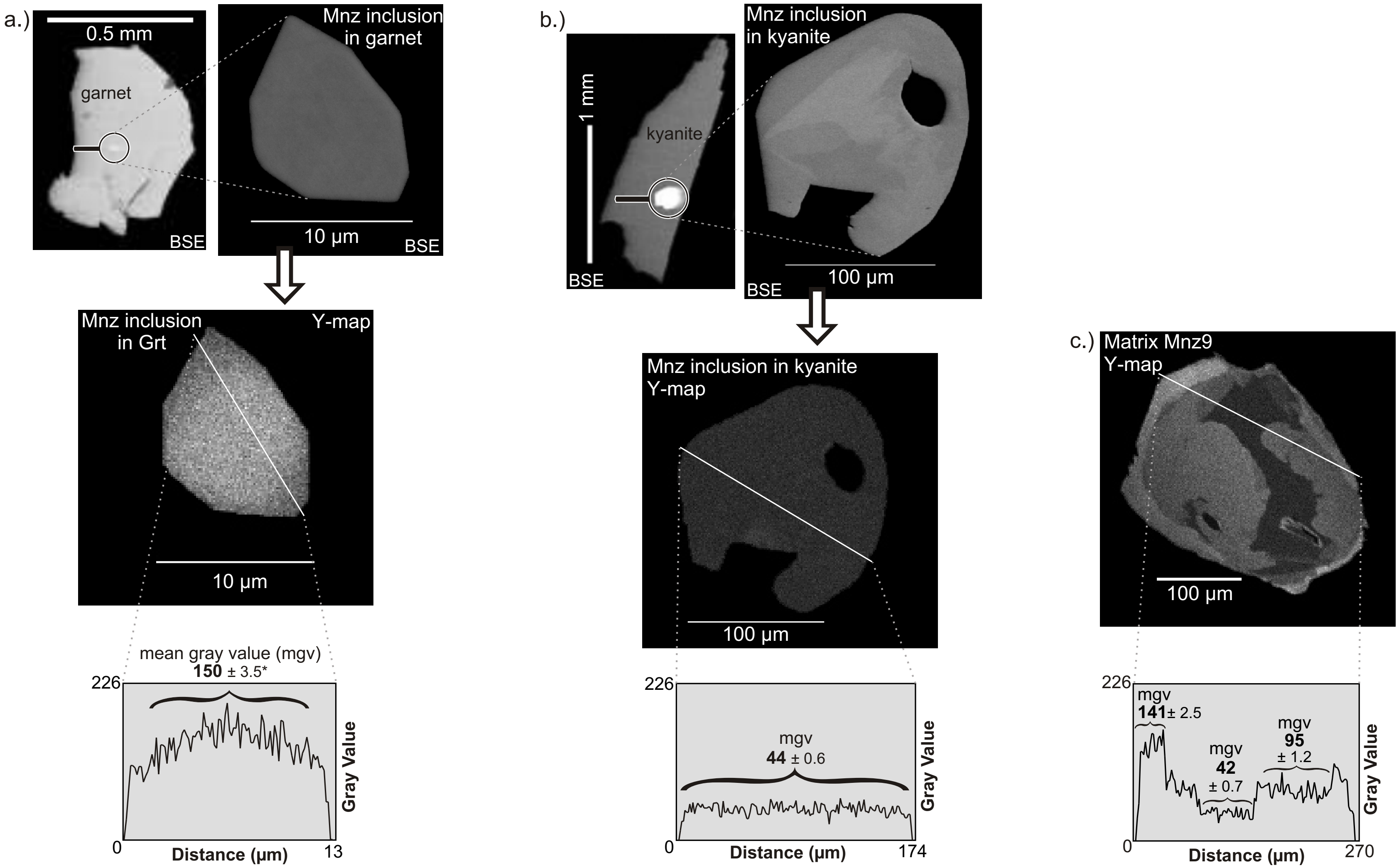

*Errors expressed as one standard error of the mean.

Figure 4.9.

Figure 4.10. (a) Y map for Mnz9 with SHRIMP spot locations and associated $^{208}Pb/^{232}Th$ ages. Numbered circles correspond to metamorphic reactions listed in (b). (b) Schematic representation of metamorphic history interpreted for monazite, garnet, and kyanite of DG38a. (c) Possible metamorphic reactions and their timing constraints that correspond with the production and consumption of monazite, garnet and kyanite. (d) Pressure-Temperature-time path proposed for DG38a with the notation for each of the metamorphic reactions and their approximate timing constraints. The dark grey arrow represents the last part of the prograde path, based on the textures observed in thin section and the chemical maps, as well as the geothermobarometric constraints provided by the previous studies of Leatherbarrow (1981) and Ghent et al. (1979, 1982, and 1983). The light grey arrow corresponds to the beginning of the retrograde path. The dotted portion of the P-T-t path represents the Jurassic part of the prograde path for which there are no timing constraints, and little or no metamorphic data; it is simply extrapolated down from reaction [2]. NaKFMASH petrogenetic grid is from Spear et al. (1999). Numbered squares correspond to melting reactions associated with univariant curves assigned by Spear et al. to the NaKFMASH grid; the intersection of these curves define invariant point IP1''. Mineral abbreviations after Kretz (1983). As = aluminosilicate; L = liquid; V = vapor.

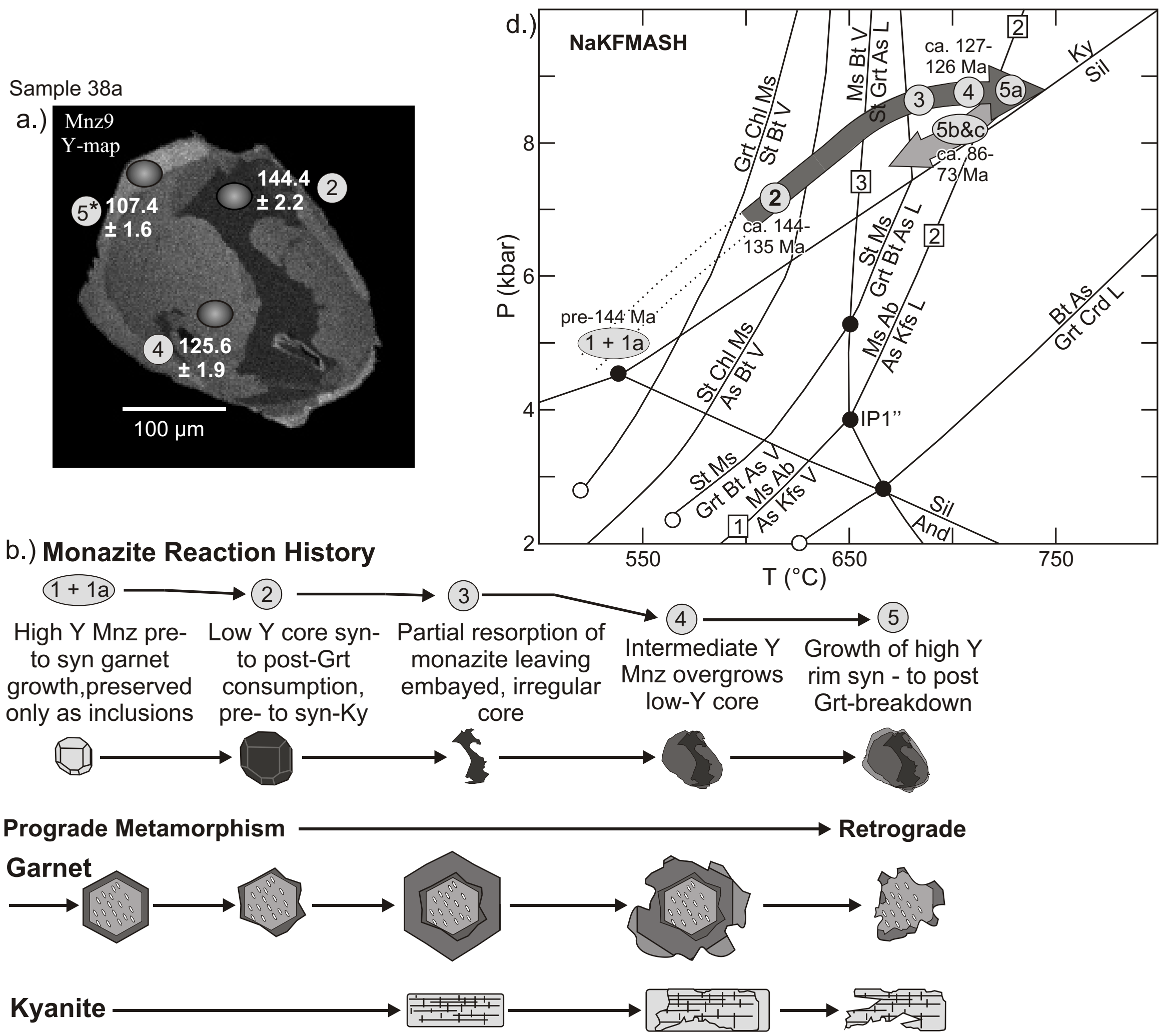

c.) Possible reactions responsible for the production and consumption of monazite (Mnz) throughout prograde and retrograde metamorphism of sample DG38a

pre-144 Ma

1 **High Y Mnz producedby:**

$$\text{Bt + Chl + Qtz + Plg + Xno} \rightleftharpoons \text{Ms + Ap + Mnz}_{[\text{high Y}]} + \text{Grt}_{[\text{high Y}]} + \text{H}_2\text{0} \quad [1]$$

1a **Mnz is consumed once Xno is exhausted, producing relatively low Y Grt:**

$$\text{Bt + Chl + Qtz + Plg + Mnz} \rightleftharpoons \text{Ms + Ap + Grt}_{[\text{low Y}]} + \text{H}_2\text{0} \quad [1a]$$

2 **The low Y rim of the Grt is consumed during the production of low Y Mnz:**

$$\text{Grt}_{[\text{low Y}]} + \text{Chl + Ms + Ap} \rightleftharpoons \text{St + Bt + Plg + Mnz}_{[\text{low Y}]} + \text{Qtz} \quad [2]$$ **ca. 144-135 Ma**

3 **Consumption of both St and Mnz involved in production of Grt:**

$$\text{St + Plg + Ms + Qtz + Mnz}_{[\text{low Y}]} \rightleftharpoons \text{Grt}_{[\text{low Y}]} + \text{Ky + Bt + Ap + H}_2\text{O} \quad [3]$$

4 **Ky and Grt are consumed during production of intermediate Y Mnz:**

$$\text{Grt + Ms + Ap} \rightleftharpoons \text{Ky + Bt + Mnz}_{[\text{intermdiate Y}]} \quad [4]$$ **ca. 127- 126 Ma**

5* **Melt crystallization upon cooling leads to consumption of Ky and Grt, and production of high Y Mnz:**

$$\text{Ky + Bt + Qtz + Pl + Mnz} \rightleftharpoons \text{Grt + Kfs + Melt} \quad [5a]$$

ca. 86-73 Ma

$$\text{Grt + Kfs + Melt} \rightleftharpoons \text{Ky + Bt + Qtz + Pl + Mnz}_{[\text{high Y}]} \quad [5b]$$

$$\text{Ky + Melt} \rightleftharpoons \text{Qtz + Pl + Ms + Mnz}_{[\text{high Y}]} \quad [5c]$$

*Note: spot age for high Y rim on Mnz9 is older than interpreted age range due to overlap into older intermediate Y domain

Figure 4.10

CHAPTER 5

TECTONIC EVOLUTION OF THE SELKIRK FAN, NORTHERN SELKIRK MOUNTAINS, SOUTHEASTERN CANADIAN CORDILLERA: A COMPOSITE MIDDLE JURASSIC – CRETACEOUS STRUCTURE

Abstract

In the southeastern Canadian Cordillera a zone of structural divergence marks the transition from the ductile deformation, metamorphism and plutonism of the Omineca belt to the "thin-skinned" deformation of the Foreland belt. Understanding the development of this zone is fundamental to elucidating the transition from hinterland to foreland tectonics in the Cordillera. In the Selkirk Mountains of southern British Columbia, a divergent, km-scale structure termed the Selkirk fan coincides with this zone of structural divergence. The fan strikes SE-NW for more than 120 km, consists of medium- to high-grade metamorphic rocks, and comprises at least three generations of superposed structures. Southwest verging F_2 folds with shallow dipping S_2 axial surfaces dominate the west flank of the fan. East of the fan axis F_2 and F_3 folds are northeast verging, and become increasingly overturned to the east near the Rocky Mountain Trench. The kinematic development of the Selkirk fan has been the focus of considerable debate, but most researchers concluded that fan formation occurred primarily in the Middle Jurassic. U-Th-Pb geochronologic data obtained by Isotope Dilution Thermal Ionization Mass Spectrometry (IDTIMS) and Sensitive High Resolution Ion Microprobe (SHRIMP) analyses indicate a more complex and protracted origin for the fan. The data demonstrate that the thermo-structural development and exhumation of the west flank of the fan occurred principally in the Middle Jurassic (ca. 172-167 Ma). In contrast, east of the fan axis significant Cretaceous deformation (104-84 Ma) and Cretaceous to Paleocene metamorphism (144-56 Ma) were superimposed on an early transposition fabric. This was followed by, or partly concomitant with Late Cretaceous to Early Tertiary exhumation.

A tectonic model is proposed in which the Selkirk fan developed within a critically tapered orogenic wedge that evolved diachronously in response to changing boundary conditions associated with periods of terrane accretion on the western margin of North America. During the Early to Middle Jurassic accretion of the Intermontane superterrane, a proto-F_{1-2} fan developed above a singularity where oceanic or marginal basin lithosphere was subducted eastward beneath continental lithosphere. Subsequently, the fan decoupled along a basal décollement system and was transferred northeastward, as rocks to the east were progressively incorporated into the orogenic wedge. The mid-Cretaceous accretion of the Insular superterrane resulted in rejuvenation of compressional forces. This gave rise to out-of-sequence deformation that thickened the tectonic pile to reestablish critical taper and the continued eastward propagation of folding and faulting within the foreland to the east.

5. 1. Introduction

In the southern Canadian Cordillera a zone of structural divergence corresponds with the eastward transition from distributed ductile deformation, low- to high-grade metamorphism and plutonism of the Omineca belt to the "thin-skinned" deformation of the Foreland belt (Eisbacher, 1974; Price, 1986; Fig 5.1a and b). Within the Selkirk Mountains of southern British Columbia, this zone coincides with the axis of a regional-scale structure termed the Selkirk fan (Wheeler, 1963, 1965; Price and Mountjoy, 1970; Brown and Tippett, 1978; Figs. 3.1b, 3.2). The fan is composed of low to high-grade metamorphic rocks, and comprises at least three generations of superposed structures (Brown and Tippett, 1978; Perkins, 1983; Chapter 2; Fig. 5.2). Understanding the development of the Selkirk fan is important to elucidating the transition from hinterland to foreland tectonics in the Cordillera.

Two principal models for the development of the fan have emerged (Figs. 5.3a and b). Brown et al. (1993) presented a finite-element model in which the fan developed in the Middle Jurassic above a singularity that marked the eastward subduction of oceanic lithosphere beneath continental lithosphere, analogous to the doubly vergent structures produced in the mechanical models of Malavieille (1984) and Willet et al. (1993). Following its initial development, the fan decoupled from above the singularity and was transferred eastward some 250-300 km along a basal décollement system. Alternatively, fan formation is thought to have occurred during a single protracted event (Price, 1979) that resulted from the tectonic wedging of allochthonous terrane between the North American cratonic basement and the overlying miogeoclinal cover (Price, 1986). Colpron et al. (1998) expanded on this model by including an inherited basement ramp that impeded the eastward transfer of deformation in the Middle Jurassic. The ramp caused the more proximal miogeoclinal sequence to internally deform via west-directed back thrusting and folding over top of more distal pericratonic rocks. In the Late Jurassic, once sufficient gravitational potential was attained, the orogenic pile overrode and cannibalized the ramp. This facilitated the propagation of structures with a northeastward vergence into the foreland to the east. Despite their differences, the models conclude that fan formation occurred primarily in the Middle Jurassic.

More recently, U-Th-Pb geochronologic data (Crowley et al., 2000; this study) obtained by Isotope Dilution Thermal Ionization Mass Spectrometry (IDTIMS) and Sensitive High Resolution Ion Microprobe (SHRIMP) analyses point to a complex and protracted origin for the Selkirk fan (Chapters 2 and 3; Gibson et al., 2003). It has been established that the fan is a composite tectonic feature composed of Middle Jurassic to Late Cretaceous-Early Tertiary structures and metamorphic assemblages (Chapters 2 and 3; Gibson et al., 2000, 2001 and 2002). These data require significant modification of previous tectonic models. Thus, a revised model is proposed that attempts to reconcile the findings of this study with documented geochronologic, structural and metamorphic data.

5. 2. Geologic Setting

The study area within the northern Selkirk Mountains (Figs. 5.1 and 5.4) is composed of metasedimentary and metavolcanic rocks that were originally deposited along the rifted western paleo-margin of the North American craton (see Gabrielse and Campbell, 1991 and references therein). During the Middle Jurassic to Paleocene contraction these rocks were telescoped and displaced ~250-300 km northeastward along a basal shear zone (Price and Mountjoy, 1970; Brown et al. 1993; Parrish, 1995), as part of the Selkirk allochthon (Read and Brown, 1981). During this time (ca. 100 M.y.), the allochthon is interpreted to have experienced protracted internal deformation and diachronous metamorphism (Parrish, 1995). Early Tertiary normal faulting along the Columbia River and Okanagan Valley fault systems has served to dissect and expose all levels of the allochthon, as well as exposing autochthonous Precambrian North American basement of the Monashee complex (see Armstrong et al., 1991; Parkinson, 1991; Crowley, 1999; Fig. 5.1b).

The eastern boundary of northern Selkirk Mountains is delineated by the southern Rocky Mountain trench, which is part of an orogen-scale tectonic lineament that trends >2300 km along the strike of the Canadian Cordillera. The trace of a major out-of-sequence, northeast verging Cretaceous contractional fault, the Purcell thrust, is mapped within the trench, but is transected and obscured at the latitude of this study by an en echelon series of down-to-the-west Tertiary normal faults (Simony et al., 1980). The western flank of the area is situated within the immediate hanging wall of the Columbia River fault, a crustal-scale, Eocene normal-sense shear zone (Read and Brown, 1981; Parrish et al., 1988). This northwest-striking fault separates upper-amphibolite-facies footwall rocks of the Monashee complex from greenschist-facies rocks within the Selkirk Mountains (i.e., Selkirk allochthon). The surface trace and magnitude of displacement of this fault dies out just south of 52ºN latitude at the confluence of Birch Creek and the Columbia River (Figs. 5.1 and 5.4; Map 2). North of Birch Creek, the northwest trending stratigraphy, structures and isograds of the region are mapped uninterrupted across the Columbia River into the northern Monashee Mountains (e.g., Simony et al., 1980; Raeside and Simony, 1983; Crowley et al., 2000; Figs. 5.1, 5.4 and 5.5; Map 2).

The lithostratigraphy within the east flank of the fan of the study area is composed primarily of a metamorphosed clastic turbidite sequence that belongs to the Late Proterozoic Windermere Supergroup (Wheeler, 1963 1965; Brown et al., 1977, 1978; Perkins, 1983). Near the fan axis and within the west flank of the fan, the Windermere Supergroup is conformably overlain, in ascending order, by the Eocambrian Hamill Group quartzites, the Lower Cambrian marbles of the Badshot Formation, and the carbonates, calc-silicates, metavolcanics and schists of the Lower Paleozoic Lardeau Group (Fig. 5.4; Map 2).

The structural style in the northern Selkirk Mountains is dominated by northwest-southeast trending folds and faults. The Selkirk fan comprises at least three generations of superposed structures (Figs. 5.3, 5.5 and 5.6). Assignment of fold generation is based on overprinting and geometric observations; no regional timing correlation is implied, especially across the fan. The first generation of deformation (D_1) is found primarily in the southwest flank of the fan. This includes a recumbent, km-scale, southwest verging isoclinal fold termed the Carnes nappe (Brown and Lane, 1988). Identification of this and other D_1 structures is complicated due to the pervasive and intense coaxial overprint of F_2 folds, which dominate the observable deformation at the outcrop scale across the fan. Second generation F_2 folds are generally isoclinal with axial planes parallel to the regional transposition foliation (S_2), which is defined by the alignment of metamorphic minerals. Porphyroblasts (e.g., garnet, staurolite) also overgrew S_2, thus metamorphism is interpreted to have been syn- to post-D_2 (e.g., Brown and Tippett, 1978; Leatherbarrow, 1981; Perkins, 1983). Within the west side of the fan, F_2 folds verge to the southwest with shallow dipping axial surfaces (S_2) that become steeper toward the fan axis. To the east, F_2 is coaxial with F_3, and both have southwest dipping axial surfaces that become progressively overturned northeastward near the Rocky Mountain Trench. The F_3 folds are interpreted to be late syn- to post-peak metamorphic (e.g., Brown and Tippett, 1978; Simony et al., 1980; Perkins, 1983), and are easily distinguished from F_2 because they refold the transposition foliation (S_2), and have a more upright and open geometry (i.e., close to tight). All of the above structures are transected by northwest trending, southwest dipping normal faults. Their cohesive nature and the presence of sheared-out leucosome suggest these faults were active within the ductile to brittle-ductile transition of the crust.

In the study area, a set of northwest trending regional isograds have been established based on the appearance or disappearance of minerals in pelitic rocks (Wheeler, 1965; Campbell, 1968; Ghent et al., 1977; Leatherbarrow and Brown, 1978; Simony et al., 1980; Leatherbarrow, 1981). In general, the isograds trend parallel to the structural grain of the region, except where they are at a high angle to the trace of F_2 structures south of the Bigmouth pluton (Figs. 5.4 and 5.5; Map 2). The lowest grade assemblages, Chl-in, are located in the west flank of the fan in the immediate hanging wall of the Columbia River fault (Fig. 5.4). The metamorphic grade progressively increases toward the fan axis where the assemblage Sil-Kfs-melt occurs (mineral abbreviations after Kretz, 1983), and then decreases to the northeast where Ky-St assemblages occur adjacent to the Rocky Mountain Trench (Fig. 5.4).

5. 3. Summary of Geochronology

U-Th-Pb geochronologic data obtained in this study by IDTIMS and SHRIMP analyses point to a complex and protracted origin for the Selkirk fan (see Chapters 2, 3 and 4). The data provided by monazite and zircon from pelitic schists, variably deformed and undeformed pegmatites, leucogranites, granodioritic dykes and plutons indicate that the structural and metamorphic development of the west flank of the fan occurred primarily in the Middle Jurassic, ca. 172-167 Ma (Chapter 2; Fig. 5.6). In contrast, east of the fan axis, significant Cretaceous deformation (104-84 Ma) and Cretaceous to Paleocene metamorphism (144-56 Ma) were superimposed on an early transposition fabric (Chapters 2 and 3; Fig. 5.6). This was followed by, or partly concomitant with Late Cretaceous to Early Tertiary exhumation.

In the study area, development of F_2 folds and the S_2 transposition fabric within the west flank of the fan has been constrained to ca. 172-163 Ma, with a minor thermal overprint at 91 Ma. Unpublished $^{40}Ar/^{39}Ar$ cooling ages for muscovite and biotite (M. Colpron, 1997, pers. comm.; see Table 3.1 of Chapter 3) also indicate a Cretaceous thermal overprint in the west flank at the latitude of this study. Based on analyses of hand samples and thin sections, the metamorphic assemblage in the west flank of the fan is interpreted to have developed primarily pre- to syn-F_2, and is therefore indirectly constrained to the Middle Jurassic. This is corroborated to the south in the Illecillewaet synclinorium where Colpron et al. (1996) demonstrated that the Middle Jurassic development of southwest vergent structures was associated with the thermal peak of metamorphism, which occurred at depths >20 km. Colpron et al. produced Middle Jurassic $^{40}Ar/^{39}Ar$ hornblende, muscovite and biotite cooling ages for these rocks, which indicated they were exhumed on the order of 10 km to upper crustal levels during this time. The lack of a discernable Cretaceous overprint within the Illecillewaet synclinorium may suggest that this area remained at higher structural levels relative to the north since

Middle Jurassic time, perhaps above the thermal aureole associated with deeper level rocks that were still hot and ductile in the Cretaceous.

To the east of the fan axis, the timing of F_2 and S_2 remains enigmatic. Dykes deformed by F_2 yield monazites that either grew or were totally recrystallized during the mid- to Late Cretaceous. The zircons from these dykes were so severely altered by metamictization and/or hydrothermal processes that they could not be analyzed (see Fig. 2.10g, Chapter 2). Perhaps if dateable zircons were found, they would provide evidence for Middle Jurassic deformation. For instance, ~5-10 km along strike to north of this study, Crowley et al. (2000) documented Middle Jurassic ages, ca. 173-163 Ma, for low-grade metamorphism (i.e., Bt-Grt grade), and the development of second generation northeast vergent structures and transposition foliation. This is very important because it demonstrates that northeast vergent F_2 and S_2 structures within the east flank of the fan were being formed as early as the Middle Jurassic, concomitant with the formation of southwest vergent F_2 and S_2 structures in the west flank of the fan.

Development of F_3 folds within the east flank of the fan is constrained to ca. 104-84 Ma (Chapter 2), which post dated earlier periods of metamorphism at ca. 144 Ma, but was outlasted by the latest episode of metamorphism, ca. 70-56 Ma (Chapter 3). These age constraints agree well with those documented within high-grade migmatitic kyanite and sillimanite schists of the adjacent northern Monashee Mountains (Sevigny et al., 1990; Scammell, 1993; Digel et al., 1998; Crowley et al., 2000), with the exception noted above for Crowley et al. (2000). The data clearly demonstrate a lack of Middle Jurassic ages preserved within the highest-grade assemblages. Perhaps rocks within the east flank that were buried to deeper structural levels and subjected to high-grade metamorphic conditions until the Late Cretaceous – Early Tertiary, were so thoroughly recrystallized and/or altered by hydrothermal processes that the isotopic evidence for Middle Jurassic deformation and metamorphism were essentially erased.

The timing constraints summarized above suggest that there was Middle Jurassic development of both southwest and northeast vergent structures and transposition foliation concomitant with low-grade (Chl-Bt-Grt) metamorphism. The Middle Jurassic tectonism appears to be preserved only in rocks that apparently remained at upper crustal levels, as reflected by their low-grade assemblages. Whereas rocks that were taken to deeper levels in the Cretaceous, such as those exposed within eastern flank of the fan, appear to have been progressively or episodically reworked and recrystallized until their exhumation in Late Cretaceous to Early Tertiary.

5. 4. A Conceptual Model for the Tectonic Development of the Selkirk Fan

Based on the data from this study together with results from previous studies in the adjoining regions to the north and south, a tectonic model for the development of the Selkirk fan is presented in Fig. 5.7a-d. The Selkirk fan is thought to have developed within an orogenic system with a critically tapered leading edge that evolved diachronously in response to changing boundary conditions associated with periods of terrane accretion on the western margin of North America. The model described herein elaborates upon the concepts presented by Brown et al. (1993, and references therein) and incorporates the principles of critical taper (e.g., Chapple, 1978; Davis et al., 1983; Williams et al., 1994).

The initial development of the Selkirk Fan is interpreted to have occurred in the Early to Middle Jurassic during the accretion of the Intermontane Superterrane (Fig. 5.7a).

During this time, a proto-fan began to develop in an accretionary wedge above the point where oceanic or marginal basin lithosphere was subducted beneath North America, analogous to the mechanical modeling of Malavieille (1984) and Willet at al. (1993). In this model, the North American lithosphere is considered to be have been moving westward toward the singularity, where it was incorporated into the asthenosphere.

Continued convergence in the Middle Jurassic led to the diachronous development of southwest vergent structures in the prowedge or west flank of the fan, and northeast vergent structures in the retrowedge or east flank of the fan (Fig. 5.7b). As a result, southwest vergent, km-scale F_1 nappes formed during the early stages of accretion were overprinted by F_2 folds in the prowedge, which developed synchronously with F_2 folds in the retrowedge. During this time the expanding retrowedge decoupled from the underlying lithosphere along a distributed basal shear system, leading to the northeastward propagation of deformation and translation of the fan axis. The northeastward thickening of the orogen resulted in the protracted evolution of a ductile thermo-mechanical layer within the lower crust of the retrowedge that migrated eastward with time. Rocks to the east were gradually underplated beneath the leading edge of the orogenic welt, where they were deformed, buried and heated at progressively younger times (see Brown, 2003). According to the models of Willet et al. (1993) and Williams et al. (1994), a stable plateau likely developed above the thermally weakened ductile lower crust, perhaps analogous to that currently envisaged for the Tibetan plateau of the Himalayas (e.g., Nelson et al., 1996). In the Late Jurassic, tectonic loading caused downward flexure of the crust to the east of the burgeoning orogen, which resulted in the initial deposition of foreland basin sediments, such as the Kimmeridgian age Passage beds of the Fernie Group (Price, 1994).

The subsequent accretion and obduction of the Insular Superterrane in the mid-Cretaceous, ca. 100 Ma, caused an increase in compressional forces acting upon the Cordilleran orogen. This gave rise to out-of-sequence deformation within the retrowedge of the fan that served to thicken the tectonic pile in order to reestablish critical taper (Fig. 5.7c). Medium- to high-grade rocks within the east flank of the fan were uplifted and exhumed along surfaces such as the Purcell thrust, which likely coincided with the superposition of F_3 in the mid- to Late Cretaceous. Once critical taper was reestablished, the out-of-sequence deformation abated, and further deformation was transferred to the foreland.

The onset of extension, which denuded and exhumed significant portions of the southern Omineca belt, occurred during the waning stages of compression in the Paleocene to Eocene time (Parrish et al., 1988; Fig. 5.7d). At the latitude of this study, the Selkirk fan was dropped to its current structural position along the Columbia River fault (CRF). West-directed extensional faults found within the east flank of the Selkirk fan (see Chapter 2) likely played a minor role in the placement of higher structural levels to the west against deeper levels to the east. Also, normal erosive processes have helped to expose higher-grade rocks within the axis and east flank (Fig. 5.4) because of the antiformal geometry that characterizes this part of the fan (Fig. 5.2).

5. 5. Discussion

The proposed model, which is similar in concept to that put forward by Brown et al. (1993), is favored because it better accommodates the protracted and composite nature of the Selkirk fan, as revealed by this study, within the broader tectonic framework of the Cordilleran orogen. Although not attempted in this communication, the tectonic wedging model proposed by Price (1986) and Colpron et al. (1998) would have to be significantly modified to accommodate the data presented in this study. However, this does not preclude the role of tectonic wedging. In fact, there may have been some degree of tectonic wedging, but likely at a more localized scale as opposed to a primary orogenic mechanism responsible for the protracted evolution of the Selkirk fan. For instance, the mechanics involved in tectonic wedging seem to be most appropriate for upper crustal rocks that deform by brittle processes. Over an extended period of time, the growth of the tectonic pile above the wedge would cause its overall mean ductility to significantly increase and the competency contrasts to greatly diminish, rendering the mechanics of the wedge ineffective. Also, an inconsistency with the model elaborated upon by Colpron et al. (1998) needs to be addressed. They argue that the top surface of the tectonic wedge was a southwest directed antithetic thrust termed the Standfast Creek fault (Fig. 5.3b), above which substantial southwest-directed backthrusting and folding occurred. However, Crowley and Brown (1994) concluded that there was minimal movement associated with the Standfast Creek fault because structures, metamorphic isograds and stratigraphy appear to be uninterrupted across it. Finally, seismic profiles provided by the Canadian LITHOPROBE project do not appear to image the presence of a tectonic wedge in the subsurface for this region (e.g., Cook et al., 1992; Cook, 1995).

Conversely, Colpron et al. (1998) questioned the viability of the model presented by Brown et al. (1993). Colpron et al. argued that if the Selkirk fan formed above a subduction zone in the Middle Jurassic, arc-related plutonism should have intruded the east flank of the fan before it was translated to the northeast. Presently, most Middle Jurassic intrusives are situated to the west of the fan axis, except for the Adamant pluton, which straddles the fan axis (Figs. 5.1 and 5.4). However, a number of factors could have led to the observed configuration of Middle Jurassic plutons. For instance, a moderate to steep angle of subduction would result in arc-plutonism focussed primarily within the prowedge of the fan (cf. Fig. 5.7a). Also, the fan may have decoupled and started to shunt northeastward prior to the onset of major arc-related plutonism, giving rise to pluton emplacement primarily in the prowedge. Notwithstanding, there may have been Middle Jurassic plutons situated in the upper crustal levels of the east flank, similar to what is currently found in the west flank, but subsequent exhumation related to uplift and erosion have stripped off the evidence.

Although the models presented by Brown et al. (1993), Price (1986) and Colpron et al. (1998) appear to be incompatible with each other, perhaps the apparent differences are a matter of scale rather than mechanical immiscibility. Future investigations involving techniques such as finite element modeling could test the coalescence of the concepts for these models.

Another concept not considered in this communication is the possibility that the thermo-mechanical evolution of the ductile lower crust involved mid- to lower crustal channel flow (Beaumont et al., 2001a and b). Although there are features similar to both models, such as the establishment of a plateau above a zone or “channel” of thermally weakened lower crust, there are noticeable differences that would have to be accounted for in the channel flow model parameters that would make it appropriate for the Cordillera. First, the diachronous nature of this zone, which appears to have evolved for

~100 M.y. from the Middle Jurassic to Tertiary, is more protracted than what has been considered thus far in the channel flow models (i.e., ≤75 .M.y.; Beaumont et al., 2001a, b). However, unpublished models have produced channels that have persisted for 100 M.y. or more (R. Jamieson, 2003, pers. comm.). Furthermore, for a similar coupled thermal-mechanical model, Jamieson et al. (1998, p. 49) described the formation of a 5-10 km thick zone of hot (700-750°C), weak lower crust “trapped beneath the actively deforming orogen”, that would not be exhumed until a subsequent tectonic episode. This seems to agree well with what is envisaged in this contribution.

A second deviation relates to the direction of flow and extrusion of the mid-crustal channel, which is typically toward the prowedge side of the orogen in the channel flow models, whereas in the Cordillera this would have to be toward the retrowedge. Also, the Canadian Cordillera appears to lack a focussed erosion-front that would serve to rapidly denude and facilitate extrusion of the channel. Lastly, the presence of coeval thrust- and normal sense distributed shear zones that mark the upper and lower boundaries of the extruded channel, analogous to the Main Central thrust (MCT) and the South Tibetan detachment (STD) in the Himalayas, respectively, have not been clearly identified. Perhaps, the lower boundary was the Monashee décollement, a transient basal thrust zone of east-directed distributed shear strain (e.g., Brown, 2003), and the upper, west-directed shear zone included the Okanagan Valley-Eagle River fault system (Brown and Gibson, 2003).

5. 6. Conclusions

The Selkirk fan within the northern Selkirk Mountains of the southern Omineca belt is part of an orogen-parallel zone of structural divergence extending the length of the

Canadian Cordillera. The kinematic development of this structure has been the topic of considerable debate, but researchers agreed that fan formation occurred primarily in the Middle Jurassic. New U-Th-Pb geochronologic data obtained by small-fraction IDTIMS and *in situ* SHRIMP analyses point to a complex and protracted origin for the Selkirk fan, requiring significant revision of previous models. Dated zircon and monazite from variably deformed leucocratic dykes, monzonitic plutons and pelitic schists indicate that the thermo-structural development and exhumation of the west flank of the fan occurred principally in the Middle Jurassic (ca. 173-167 Ma). In contrast, east of the fan axis significant Cretaceous deformation (104-84 Ma) and Cretaceous to Paleocene metamorphism (144-56 Ma) were superimposed on an early transposition fabric. This was followed by, or partly concomitant with Late Cretaceous to Early Tertiary exhumation. Thus, the Selkirk fan should be thought of as a composite structure of juxtaposed Middle Jurassic and Cretaceous features, rather than a singular fan that developed during one progressive event. A revised tectonic model has been proposed that attempts to reconcile these data with previously documented geochronologic, structural and metamorphic data.

During the Early to Middle Jurassic accretion of the Intermontane superterrane, a proto-F_{1-2} fan developed above a singularity where oceanic or marginal basin lithosphere was subducting eastward beneath continental lithosphere. Southwest verging structures developed within the prowedge (i.e., F_2 in west flank), immediately followed by or coeval with the development of northeast vergent structures in the retrowedge (i.e., F_2 in east flank). Subsequent decoupling of the fan above a basal thrust system allowed it to be carried northeastward toward the foreland. During this time, rocks to the east were progressively incorporated into a critically tapered retrowedge as it propagated northeastward. In general, this resulted in diachronous, eastward younging of medium to high-grade metamorphism and ductile deformation.

The mid-Cretaceous (ca. 100 Ma) accretion of the Insular Superterrane resulted in the rejuvenation of compressional forces acting upon the orogenic wedge. Out-of-sequence deformation, which included the Purcell thrust, served to thicken the tectonic pile to reestablish critical taper and continued deformation within the foreland. This was coeval with the development of mid- to Late Cretaceous (ca. 104-84 Ma), northeast vergent F_3 folds found primarily in the east flank of the fan. During this time, deep-seated rocks in the east flank of the fan were uplifted and exhumed relative to the western flank. This may have been accentuated latterly by a number of west-directed Tertiary extensional faults, as well as erosive processes that exhumed deeper levels within the core of an antiform that characterizes the axis and east flank of the fan.

Figure 5.1. (a) Morphogeologic belts of the Canadian Cordillera. (b) Tectonic assemblage map of the southeastern Omineca belt (modified after Wheeler and McFeely, 1991) showing lithologic map units of autochthonous Monashee complex (North American basement) and overlying Selkirk allochthon. Box outlined in the top left of the figure represents the location of Figs. 5.4 and 5.5. A-B is line of section for Fig. 5.2. ADP = Adamant pluton; AS = Albert stock; BMP = Bigmouth pluton; BR = Battle Range batholith; CS = Clachnacudainn Slice; FP = Fang pluton; GP = Goldstream pluton; GS = Goldstream Slice; IS = Illecillewaet Slice; KB = Kuskanax batholith; PC = Pass Creek pluton.

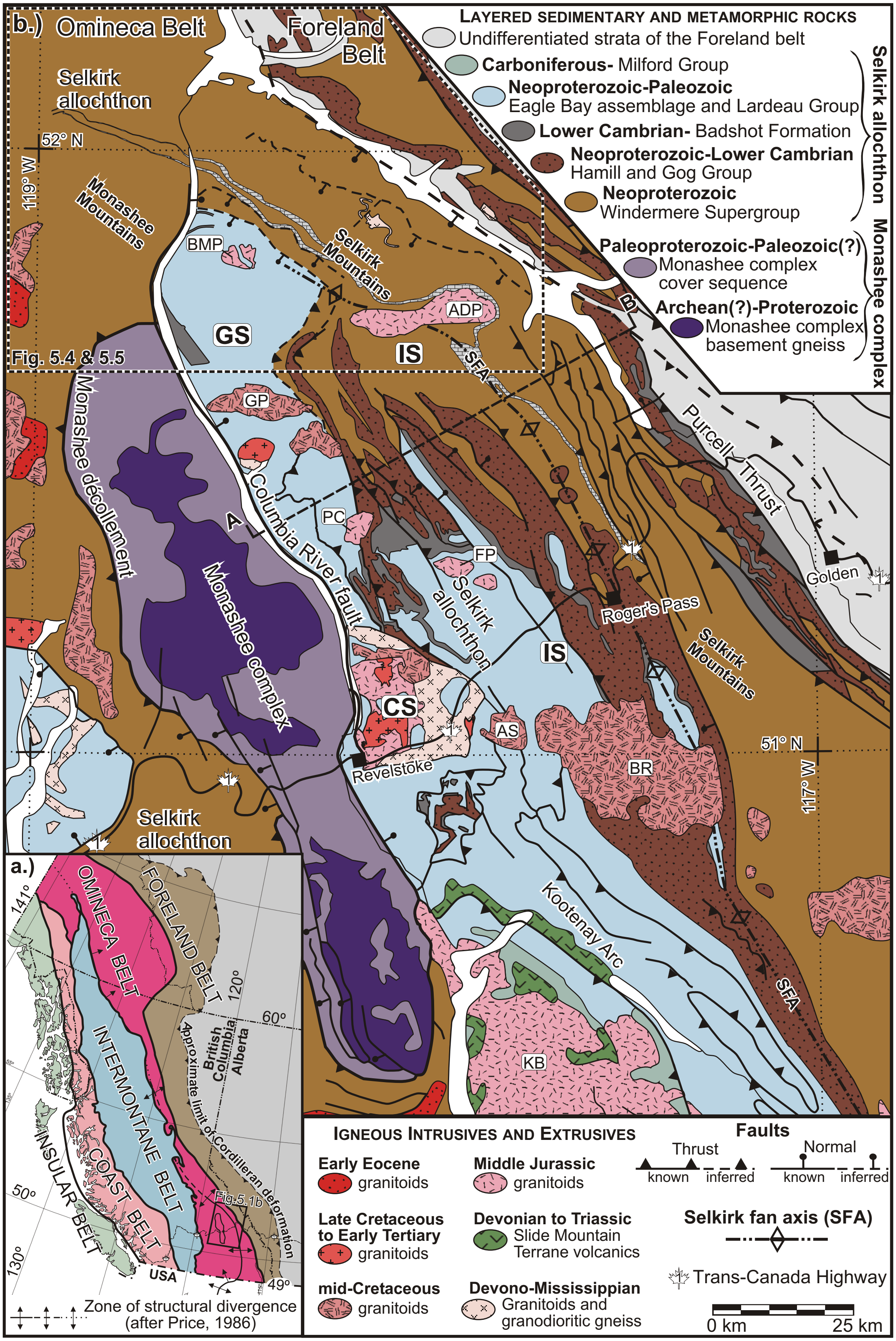
b.) Omineca Belt
Foreland Belt
Selkirk allochthon
52° N
119° W
Monashee Mountains
Selkirk Mountains
BMP
GS
ADP
IS
SFA
Fig. 5.4 & 5.5
GP
Monashee décollement
Columbia River fault
Monashee complex
A
B
PC
FP
Selkirk allochthon
Purcell Thrust
Golden
Roger's Pass
Selkirk Mountains
CS
AS
BR
51° N
117° W
Revelstoke
Selkirk allochthon
Kootenay Arc
KB
LAYERED SEDIMENTARY AND METAMORPHIC ROCKS
Undifferentiated strata of the Foreland belt
Carboniferous- Milford Group
Neoproterozoic-Paleozoic
Eagle Bay assemblage and Lardeau Group
Lower Cambrian- Badshot Formation
Neoproterozoic-Lower Cambrian
Hamill and Gog Group
Neoproterozoic
Windermere Supergroup
Selkirk allochthon
Paleoproterozoic-Paleozoic(?)
Monashee complex cover sequence
Archean(?)-Proterozoic
Monashee complex basement gneiss
Monashee complex
a.)
141°
OMINECA BELT
FORELAND BELT
120°
60°
British Columbia
Alberta
Approximate limit of Cordilleran deformation
INTERMONTANE BELT
COAST BELT
INSULAR BELT
50°
130°
Fig.5.1b
USA
49°
Zone of structural divergence (after Price, 1986)
IGNEOUS INTRUSIVES AND EXTRUSIVES
Early Eocene granitoids
Late Cretaceous to Early Tertiary granitoids
mid-Cretaceous granitoids
Middle Jurassic granitoids
Devonian to Triassic Slide Mountain Terrane volcanics
Devono-Mississippian Granitoids and granodioritic gneiss
Faults
Thrust
known
inferred
Normal
known
inferred
Selkirk fan axis (SFA)
Trans-Canada Highway
0 km
25 km

Figure 5.1.

Figure 5.2. Generalized regional cross section of the Selkirk fan for section line A-B of Fig. 5.1 (modified after Brown et al., 1993).

CRF = Columbia River fault; MD = Monashee décollement; PT = Purcell thrust.

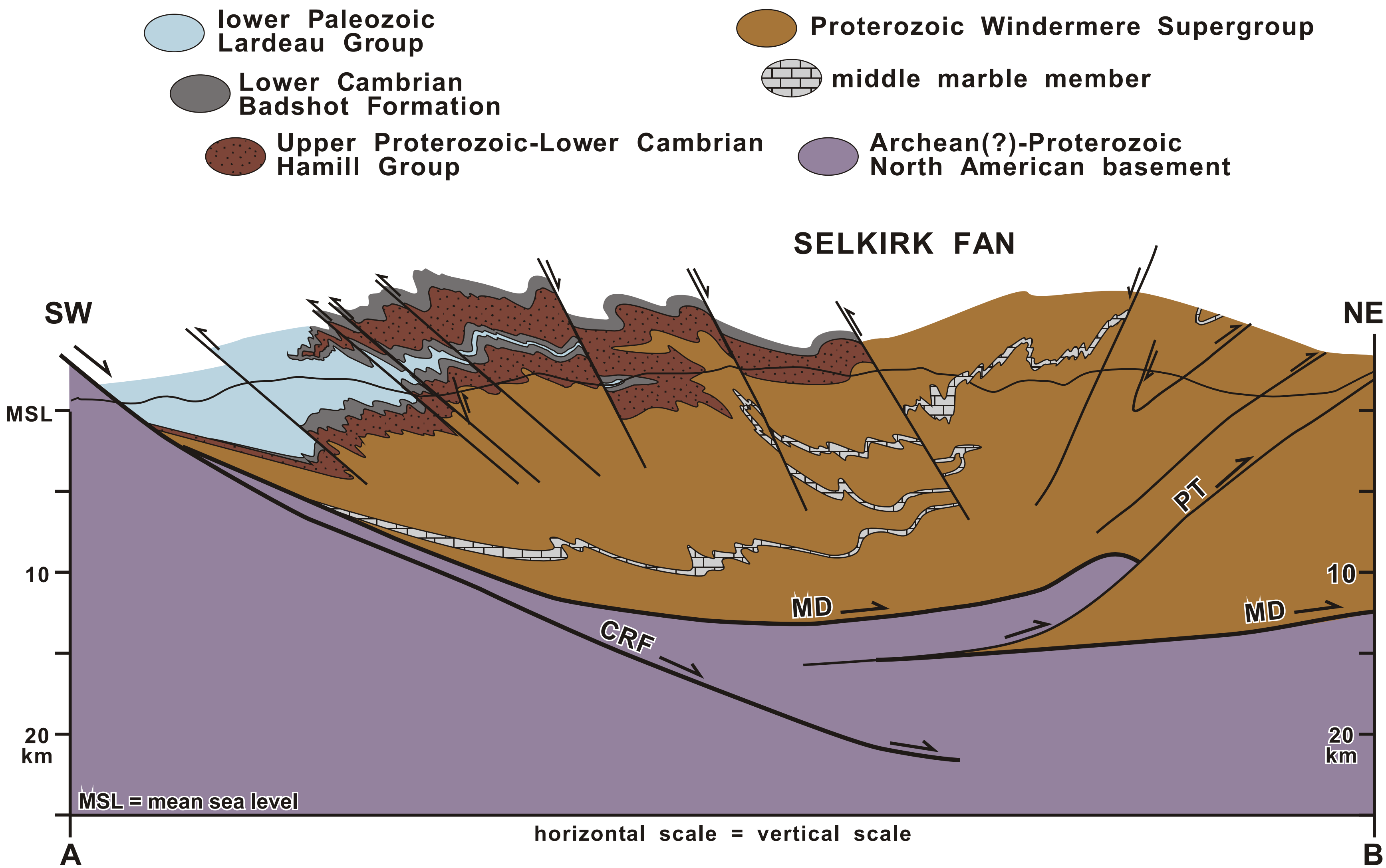
lower Paleozoic
Lardeau Group
Lower Cambrian
Badshot Formation
Upper Proterozoic-Lower Cambrian
Hamill Group
Proterozoic Windermere Supergroup
middle marble member
Archean(?)-Proterozoic
North American basement
SELKIRK FAN
SW
NE
MSL
10
20
km
MD
CRF
PT
MSL = mean sea level
horizontal scale = vertical scale
A
B

Figure 5.2

Figure 5.3. Two principal tectonic models for the formation of the Selkirk fan.

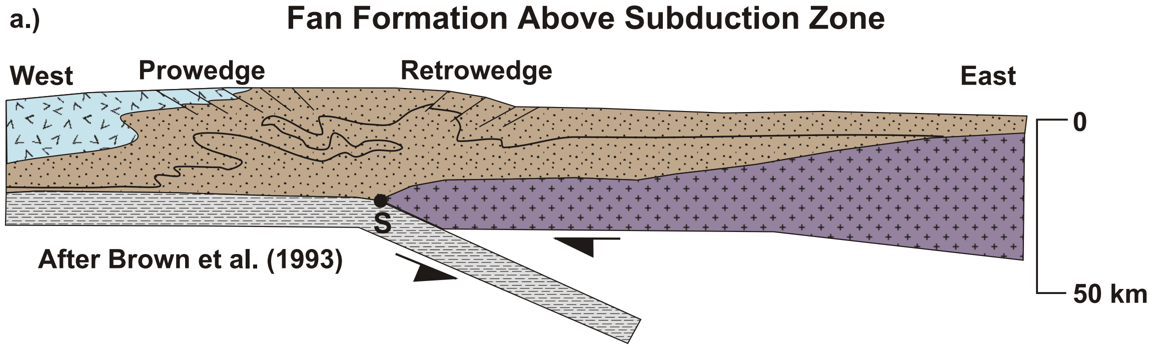

Early to Middle Jurassic accretion and obduction of Intermontane Superterrane

Singularity (S) represents point of detachment and underthrusting of oceanic lithosphere beneath continental lithosphere

Middle Jurassic development of southwest verging folds and faults in prowedge, northeast verging structures in retrowedge above singularity

Fan becomes detached and is carried passively along basal thrust toward foreland

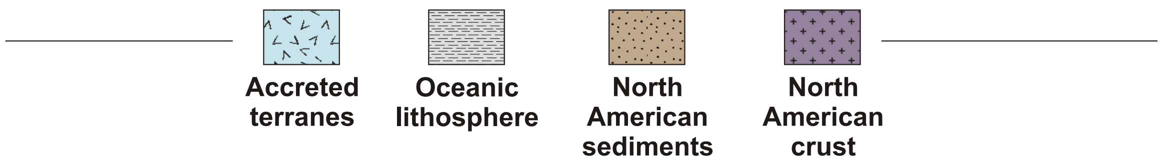

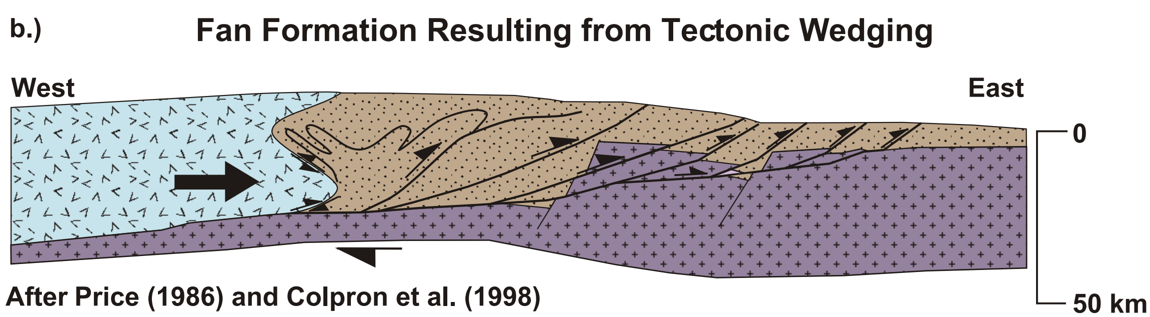

Early to Middle Jurassic accretion and obduction of Intermontane Superterrane

Middle Jurassic tectonic wedging of allochthonous terrane between the North American basement and the overlying miogeoclinal cover resulted in backfolding and thrusting of cover rocks toward the southwest

A basement ramp inherited from Late Proterozoic rifting impeded the eastward propagating front of southwest verging structures above the wedge in the Middle Jurassic

In the Late Jurassic the wedge overrode and cannibalized the ramp after attaining sufficient gravitational potential, resulting in the eastward propagation of northeastward verging deformation into the foreland

Figure 5.3

Figure 5.4. Generalized geologic map of the northern Selkirk Mountains illustrating lithostratigraphy, regional metamorphic isograds and major structures. Compiled from mapping by Brown (1991), Brown and Tippett (1978), Colpron et al. (1995), Leatherbarrow (1981), Marchildon (1999), Perkins (1983), Poulton and Simony (1980), Raeside and Simony (1983), Scammell (1993), Simony et al. (1980), and Wheeler (1965). Geochronologic sample locations within the studied area have also been included. Abbreviations: ADP = Adamant pluton; ADM = Adamant Mountain; AM = Argonaut Mountain; AP = Argonaut Pass; BMP = Bigmouth pluton; BCF = Birch Creek fault; BMF = Bigmouth fault; CRF = Columbia River fault; FG = French glacier; MC = Mica Creek village; MD = Monashee décollement; MN = Mount Nagle; MSF = Mount Sir Sanford; NEF = Northeastern fault; RP = Remillard Peak; TM = Trident Mountain. Mineral abbreviations for metamorphic zones after Kretz (1983).

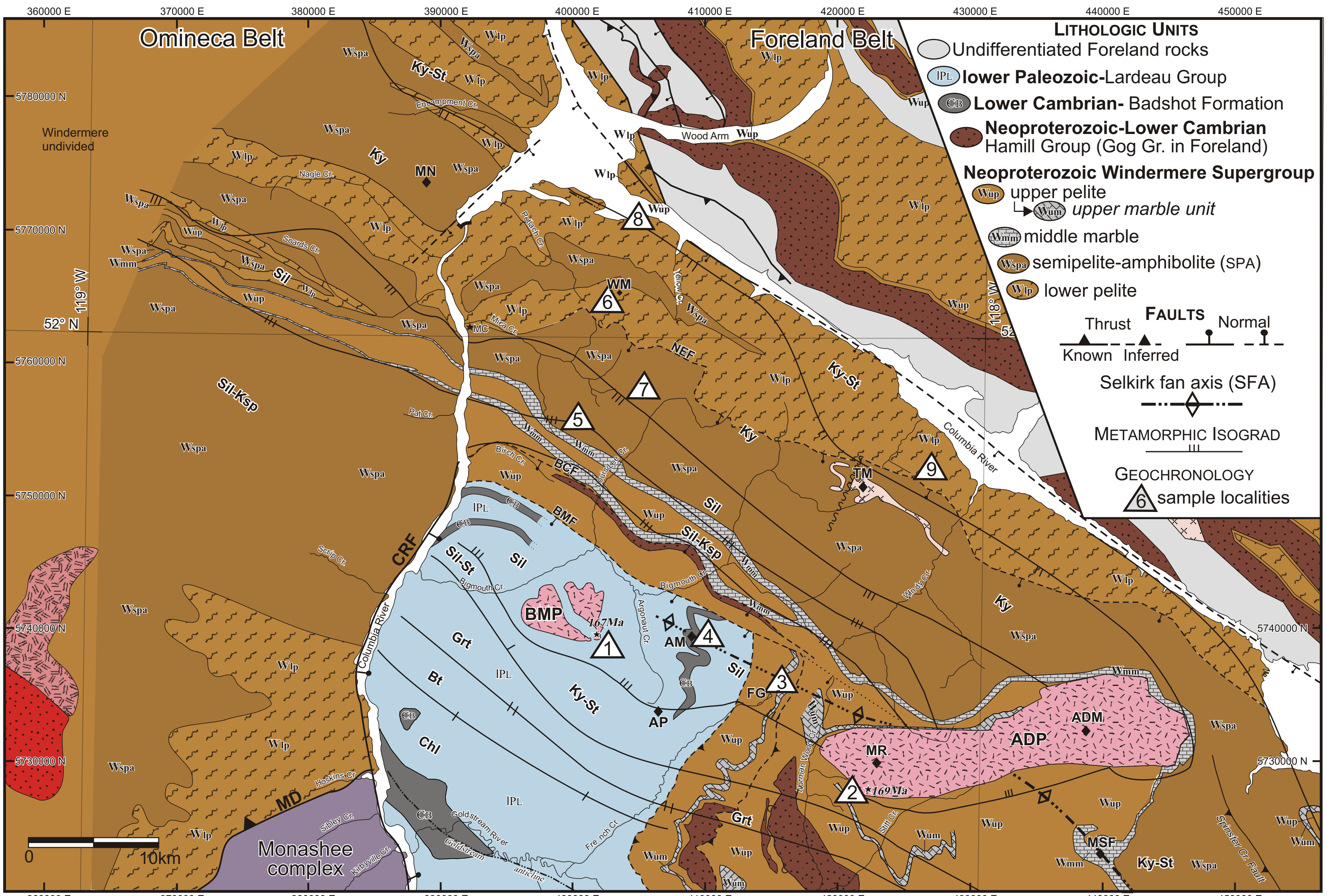

Omineca Belt
Foreland Belt
Lithologic Units
Undifferentiated Foreland rocks
lower Paleozoic-Lardeau Group
Lower Cambrian- Badshot Formation
Neoproterozoic-Lower Cambrian
Hamill Group (Gog Gr. in Foreland)
Neoproterozoic Windermere Supergroup
upper pelite
upper marble unit
middle marble
semipelite-amphibolite (SPA)
lower pelite
Faults
Thrust
Normal
Known
Inferred
Selkirk fan axis (SFA)
Metamorphic Isograd
Geochronology
sample localities
Windermere undivided
Monashee complex
Columbia River
Wood Arm
BMP
ADP
167Ma
169Ma
CRF
BCF
BMF
NEF
MD
MSF
Sil-Ksp
Sil-St
Ky-St
Ky
Sil
Grt
Bt
Chl
MN
WM
MC
TM
AM
AP
FG
MR
ADM
52° N
119° W
118° W
0
10km
360000 E
370000 E
380000 E
390000 E
400000 E
410000 E
420000 E
430000 E
440000 E
450000 E
5780000 N
5770000 N
5760000 N
5750000 N
5740000 N
5730000 N

Figure 5.4.

Figure 5.5. Generalized structure map of the northern Selkirk and Monashee Mountains showing the axial surface traces of F_1, F_2 and F_3. Compiled from Brown and Tippett (1978), Colpron et al. (1995), Perkins (1983), and Simony et al. (1980). A-A', B-B', C-C', D-D', and E-E' represent the lines of cross sections drawn in Fig. 5.6. Abbreviations: ADP = Adamant pluton; ADM = Adamant Mountain; AM = Argonaut Mountain; AP = Argonaut Pass; BMP = Bigmouth pluton; BCF = Birch Creek fault; BMF = Bigmouth fault; CRF = Columbia River fault; FG = French glacier; MC = Mica Creek village; MD = Monashee décollement; MN = Mount Nagle; MSF = Mount Sir Sanford; NEF = Northeastern fault; RP = Remillard Peak; TM = Trident Mountain.

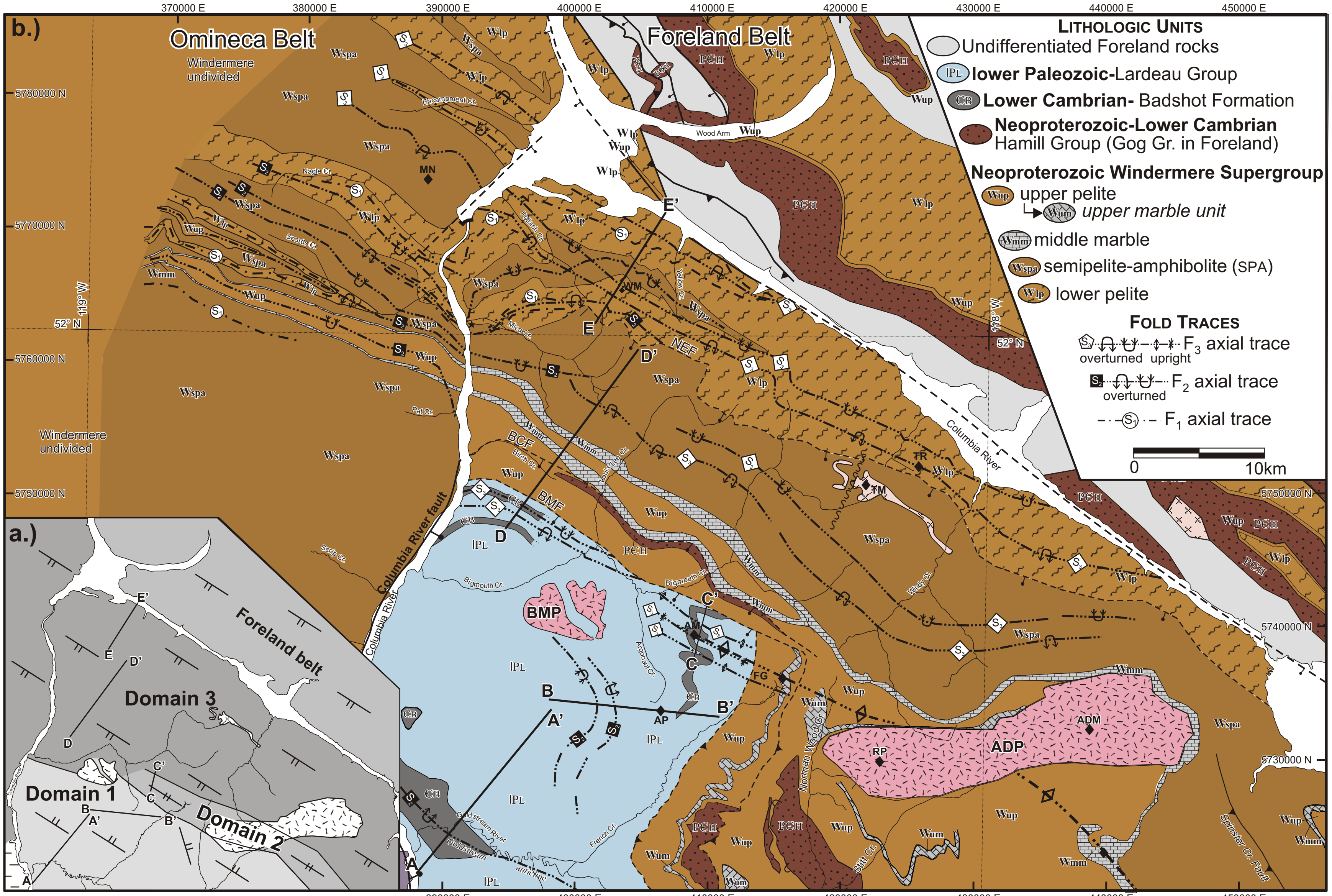
b.)
Omineca Belt
Foreland Belt
Windermere undivided
a.)
Domain 1
Domain 2
Domain 3
Foreland belt
LITHOLOGIC UNITS
Undifferentiated Foreland rocks
lower Paleozoic-Lardeau Group
Lower Cambrian- Badshot Formation
Neoproterozoic-Lower Cambrian Hamill Group (Gog Gr. in Foreland)
Neoproterozoic Windermere Supergroup
upper pelite
upper marble unit
middle marble
semipelite-amphibolite (SPA)
lower pelite
FOLD TRACES
overturned upright F3 axial trace
F2 axial trace overturned
F1 axial trace
0 10km
Columbia River fault
Columbia River
Goldstream River
Goldstream anticline
Wood Arm
Spinster Cr. Fault
BMP
ADP
BCF
BMF
NEF
370000 E
380000 E
390000 E
400000 E
410000 E
420000 E
430000 E
440000 E
450000 E
5780000 N
5770000 N
5760000 N
5750000 N
5740000 N
5730000 N
52° N
119° W
118° W

Figure 5.5.

Figure 5.6. Composite structural cross section that transects the studied area, illustrating the geometry of the fan, modified after Brown and Tippett (1978), Colpron et al. (1995), Perkins (1983), and Simony et al. (1980). Section lines are located in Fig. 5.5. U-Th-Pb geochronologic constraints for timing of deformation (Chapter 2) and metamorphism (Chapter 3) have been projected along strike into the line of section.

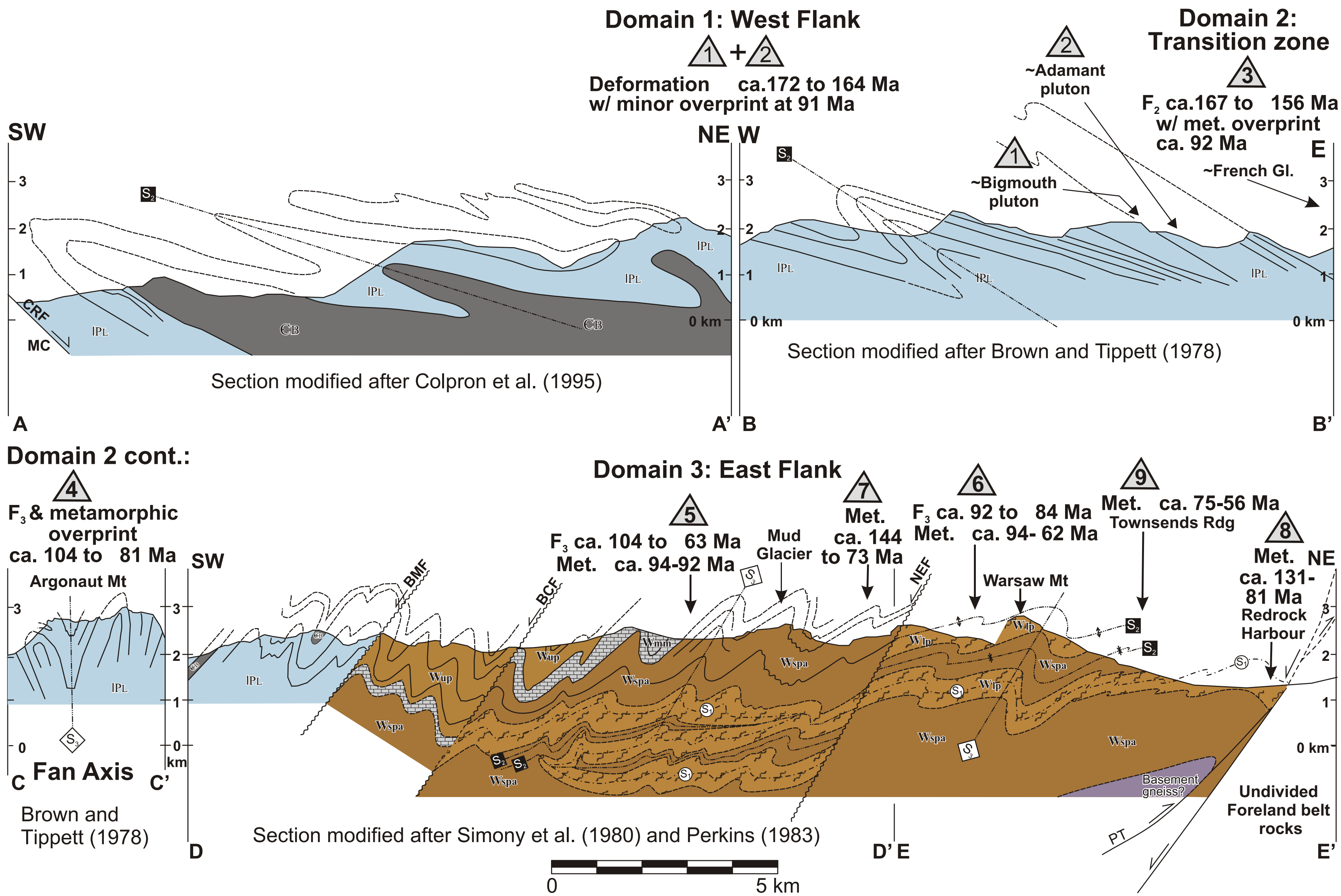
Domain 1: West Flank
1 + 2
Deformation ca.172 to 164 Ma
w/ minor overprint at 91 Ma
Domain 2:
Transition zone
3
F2 ca.167 to 156 Ma
w/ met. overprint
ca. 92 Ma
2
~Adamant
pluton
1
~Bigmouth
pluton
~French Gl.
SW
NE
W
E
S2
IPL
CB
CRF
MC
0 km
Section modified after Colpron et al. (1995)
Section modified after Brown and Tippett (1978)
A
A'
B
B'
Domain 2 cont.:
4
F3 & metamorphic
overprint
ca. 104 to 81 Ma
Argonaut Mt
S3
Fan Axis
C
C'
km
Brown and
Tippett (1978)
Domain 3: East Flank
5
F3 ca. 104 to 63 Ma
Met. ca. 94-92 Ma
Mud
Glacier
7
Met.
ca. 144
to 73 Ma
6
F3 ca. 92 to 84 Ma
Met. ca. 94- 62 Ma
9
Met. ca. 75-56 Ma
Townsends Rdg
8
Met.
ca. 131-
81 Ma
Redrock
Harbour
Warsaw Mt
BMF
BCF
NEF
Wup
Wmm
Wspa
Wlp
S1
S2
S3
Basement
gneiss?
Undivided
Foreland belt
rocks
PT
Section modified after Simony et al. (1980) and Perkins (1983)
D
D'
E
E'
0
5 km

Figure 5.6.

Figure 5.7. Conceptual tectonic model for the development of the Selkirk fan. (a) Incipient stages of accretion and obduction of the Intermontane Superterrane in the Early to Middle Jurassic resulted in formation of a proto-fan above the subduction zone similar to that modeled by Malavieille (1984) and Willet et al. (1993).

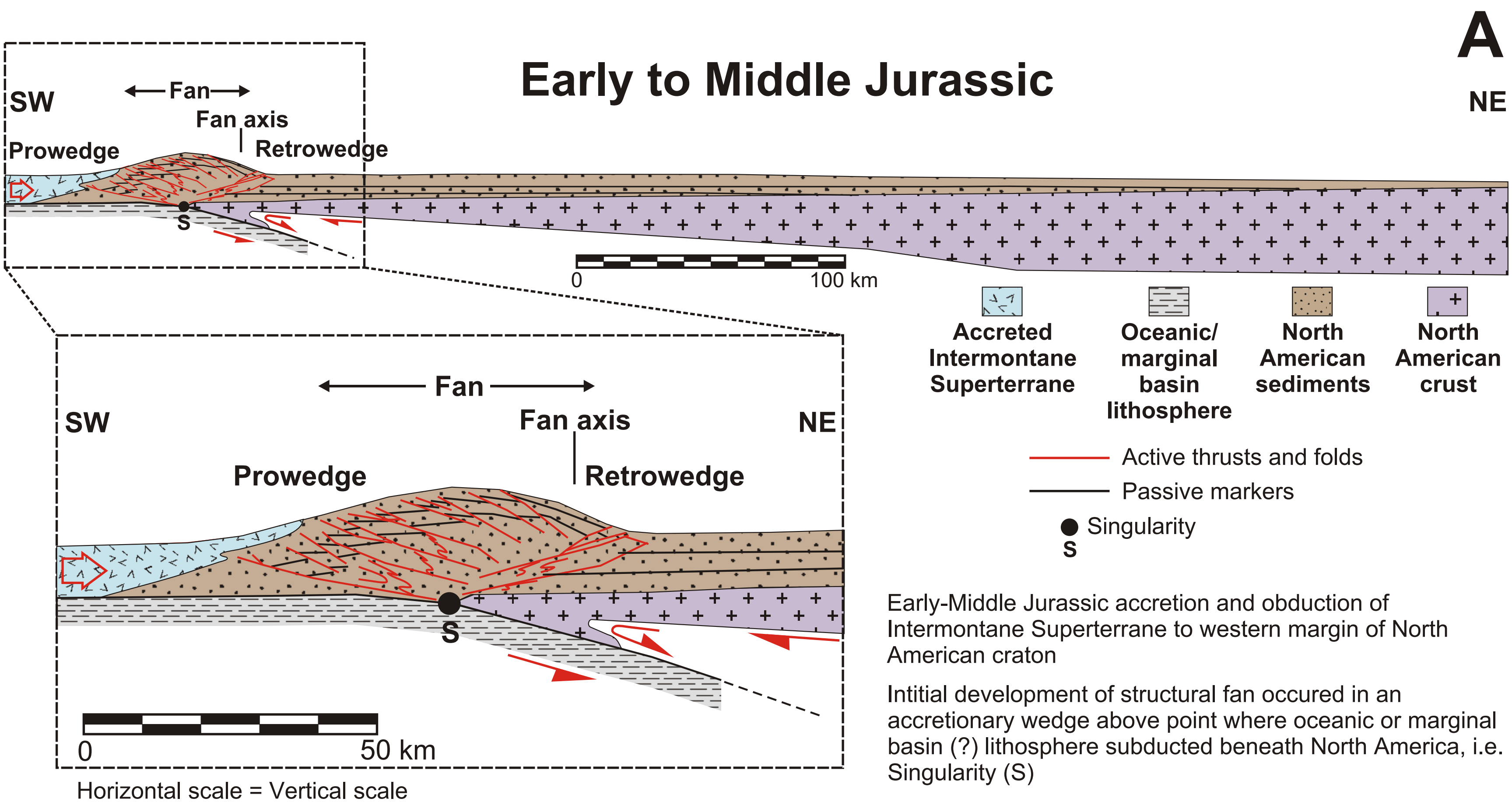
A
Early to Middle Jurassic
SW
Fan
Fan axis
Prowedge
Retrowedge
NE
S
0
100 km
Accreted Intermontane Superterrane
Oceanic/ marginal basin lithosphere
North American sediments
North American crust
Active thrusts and folds
Passive markers
Singularity
S
SW
Fan
Fan axis
NE
Prowedge
Retrowedge
S
0
50 km
Horizontal scale = Vertical scale
Early-Middle Jurassic accretion and obduction of Intermontane Superterrane to western margin of North American craton
Intitial development of structural fan occured in an accretionary wedge above point where oceanic or marginal basin (?) lithosphere subducted beneath North America, i.e. Singularity (S)

Figure 5.7a.

Figure 5.7. continued. (b) Continued convergence facilitated the expansion of the retrowedge, decoupling of the fan and its eastward translation along a basal thrust system. This was accompanied by eastward migration of a hot, ductile lower crustal zone, and establishment of an interior plateau.

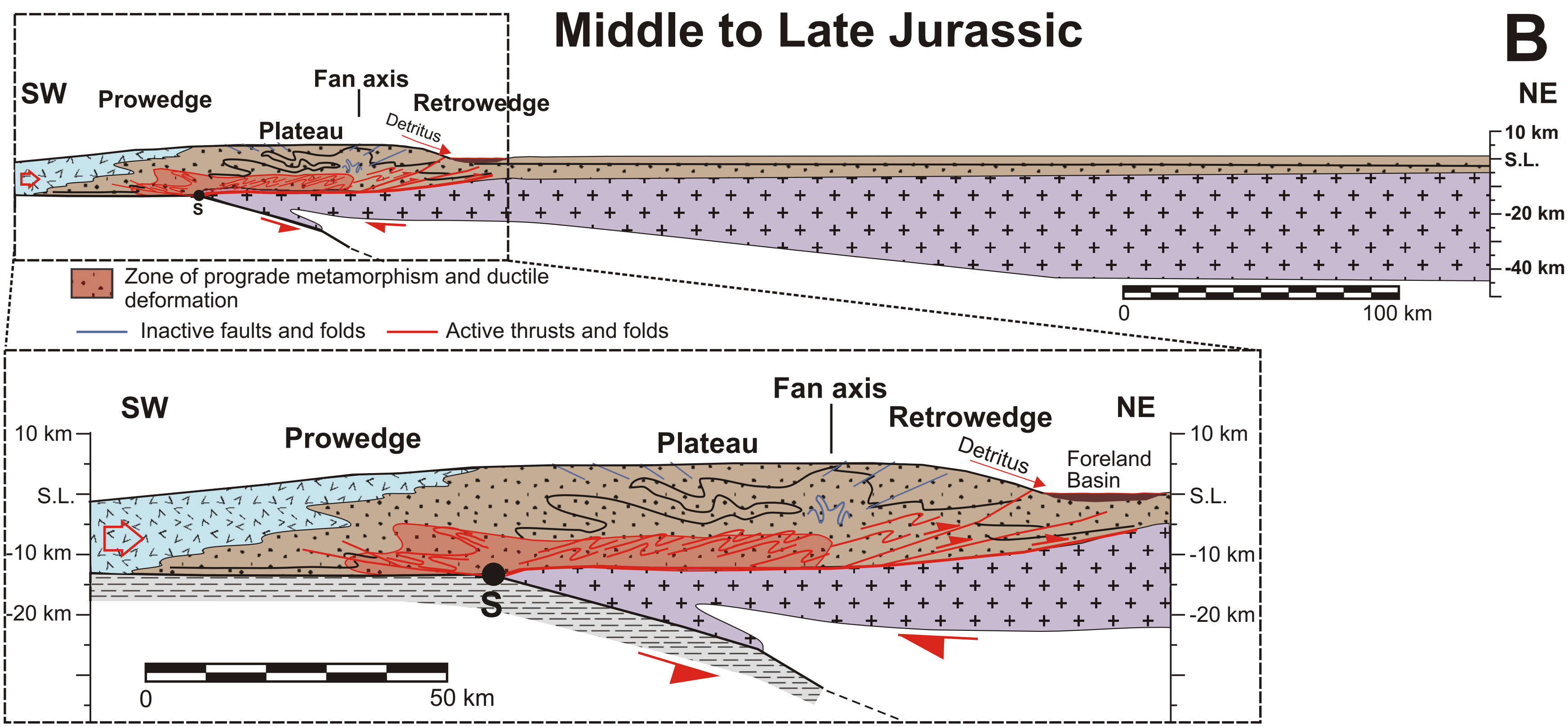

Continued Middle Jurassic convergence and growth of fan resulted in development of large-scale nappes (F_1) followed by detachment of retrowedge base, and northeastward propagation of deformation and translation of the fan axis

Continued deformation resulted in a pervasive overprint by F_2 folds coeval with prograde metamorphism; a stable plateau was established over a relatively hot, weak lower crust

Progressive northeastward thickening of the wedge lead to diachronous heating of the lower crust accompanied by ductile deformation; both became younger to the northeast and with depth

In the Late Jurassic, tectonic loading caused flexure of the crust to the east, resulting in the initial deposition of foreland basin sediments (e.g. Passage beds of Fernie Group; Price, 1994)

Figure 5.7b.

Figure 5.7. continued. (c) Out-of-sequence deformation in the leading edge of the retrowedge was necessary to reestablish critical taper during the mid-Cretaceous accretion of the Insular Superterrane. Deeper-seated rocks in the east flank of the fan were uplifted and exhumed relative to higher structural levels within the west flank of the fan.

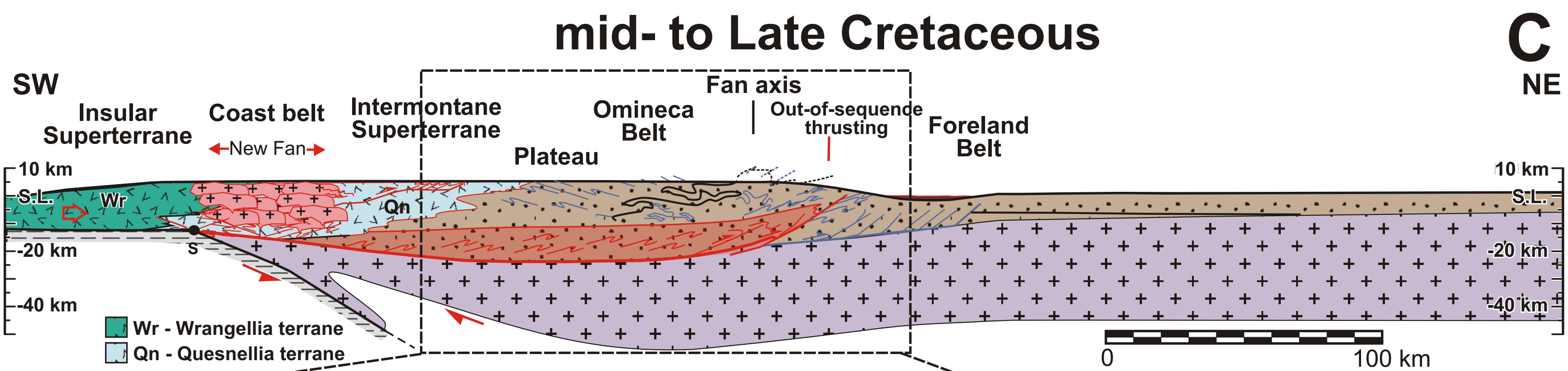

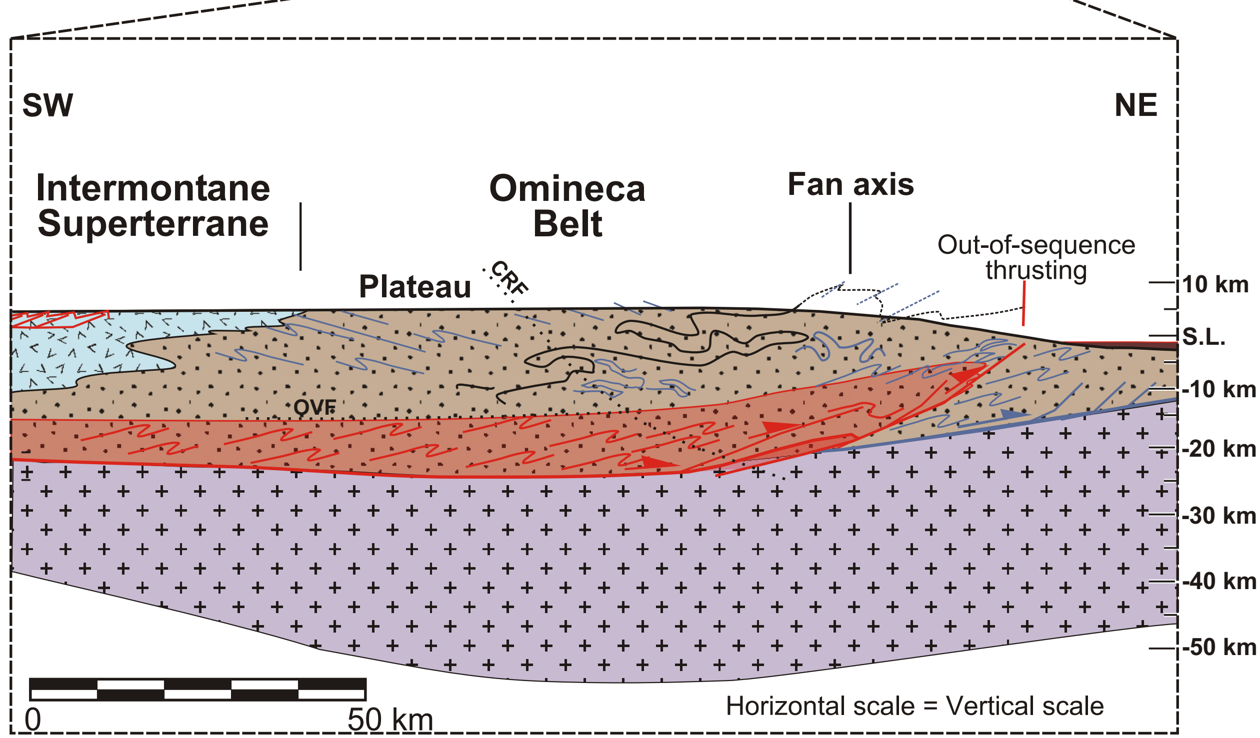

Mid-Cretaceous accretion of the Insular Superterrane increased the compressional forces acting on the orogenic wedge

Out-of-sequence thrusting (e.g. Purcell thrust) and folding served to thicken tectonic pile in order to re-establish critical taper. Consequently, deeper level, higher grade rocks in the central and eastern flank of the Selkirk fan were uplifted and exhumed relative to the west flank

Once critical taper was reestablished, northeastward propagating deformation in the foreland resumes

A new fan develops within the Coast belt, which represents the accretionary boundary between the Insular and Intermontane Superterranes

Figure 5.7c.

Figure 5.7. concluded. (d) Generalized cross section that demonstrates the present day crustal features interpreted across the southern Canadian Cordillera at the approximate latitude of the current study (~51° N). The crustal section east of the Fraser River fault (FF) is modified after Brown et al. (1986), and Price and Mountjoy (1970), whereas the section west of the FF is modified after Clowes et al. (1995). A zone demarcated in red has been superimposed on the section in the lower panel to demonstrate the current position of known and inferred Cretaceous to Tertiary deformation and metamorphism. Subsurface after Brown et al. (1992), Cook (1986, 1995) and Cook et al. (1992).

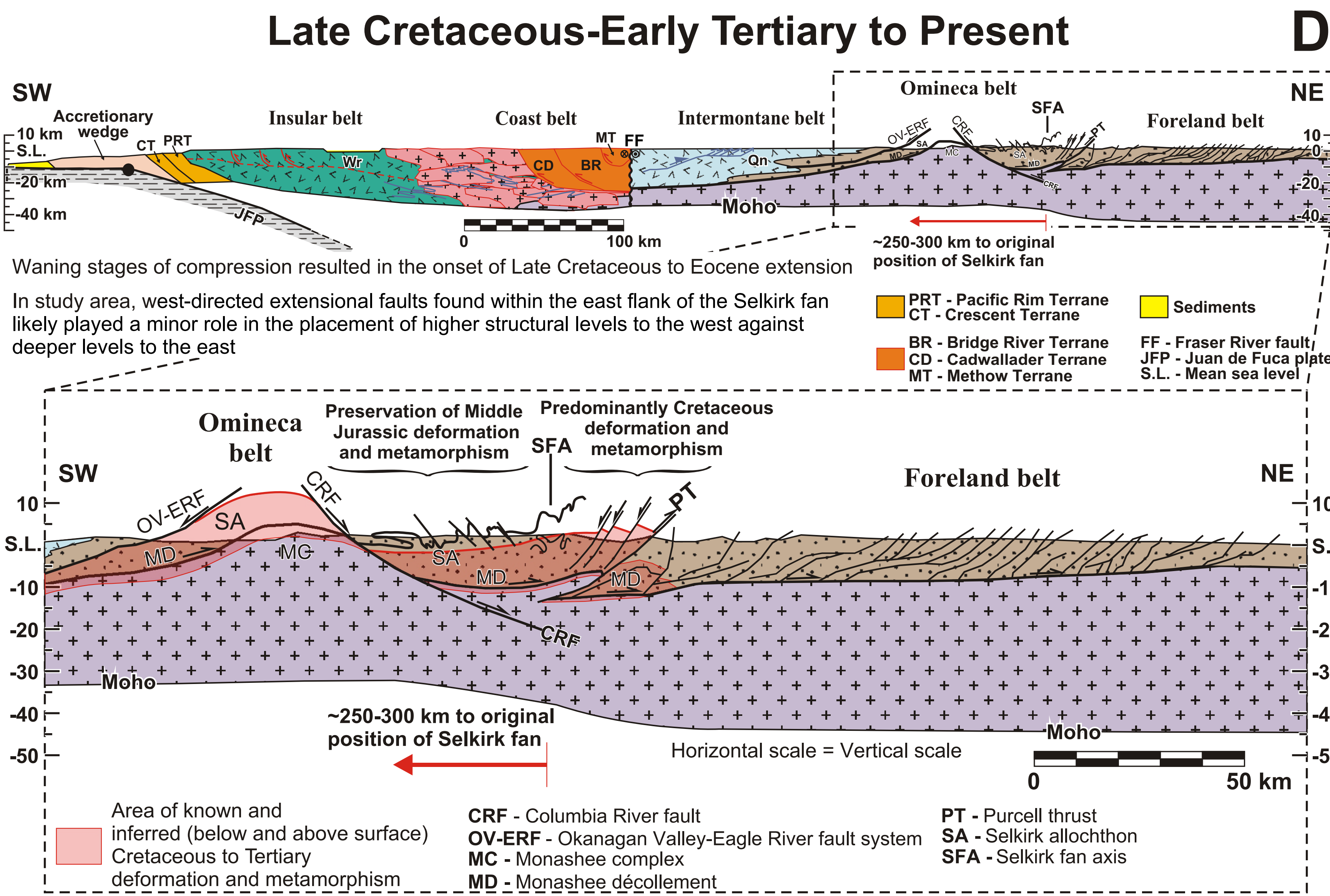

Late Cretaceous-Early Tertiary to Present
D
SW
NE
Accretionary wedge
Insular belt
Coast belt
Intermontane belt
Omineca belt
Foreland belt
10 km
S.L.
-20 km
-40 km
CT
PRT
Wr
CD
BR
MT
FF
Qn
JFP
Moho
OV-ERF
CRF
SFA
PT
SA
MC
MD
0
100 km
~250-300 km to original position of Selkirk fan
Waning stages of compression resulted in the onset of Late Cretaceous to Eocene extension
In study area, west-directed extensional faults found within the east flank of the Selkirk fan likely played a minor role in the placement of higher structural levels to the west against deeper levels to the east
PRT - Pacific Rim Terrane
CT - Crescent Terrane
Sediments
BR - Bridge River Terrane
CD - Cadwallader Terrane
MT - Methow Terrane
FF - Fraser River fault
JFP - Juan de Fuca plate
S.L. - Mean sea level
Omineca belt
Preservation of Middle Jurassic deformation and metamorphism
SFA
Predominantly Cretaceous deformation and metamorphism
Foreland belt
SW
NE
10
S.L.
-10
-20
-30
-40
-50
OV-ERF
SA
MD
MC
CRF
SA
MD
MD
PT
CRF
Moho
Moho
~250-300 km to original position of Selkirk fan
Horizontal scale = Vertical scale
0
50 km
Area of known and inferred (below and above surface) Cretaceous to Tertiary deformation and metamorphism
CRF - Columbia River fault
OV-ERF - Okanagan Valley-Eagle River fault system
MC - Monashee complex
MD - Monashee décollement
PT - Purcell thrust
SA - Selkirk allochthon
SFA - Selkirk fan axis

Figure 5.7d.

CHAPTER 6

SUMMARY OF CONCLUSIONS

The Selkirk fan within the northern Selkirk Mountains of the southern Omineca belt is part of an orogen-parallel zone of structural divergence extending the length of the Canadian Cordillera. Understanding its development is considered to be fundamental with regard to elucidating the transition from hinterland to foreland tectonics in the Cordillera. The kinematic development of this structure has been the topic of considerable debate, but researchers agreed that fan formation occurred primarily in the Middle Jurassic. However, the data presented in this thesis point to a more complex and protracted origin for the Selkirk fan, requiring significant revision of previous models. The following are a summary of conclusions reached in each chapter:

Chapter 2:

1. Geochronologic data provided by monazite and zircon from variably deformed leucocratic dykes and monzonitic-granodioritic plutons indicate that higher structural levels with an older deformation history in the west flank of the Selkirk fan were juxtaposed relative to lower levels that record a younger deformation history east of the fan axis. Thus, the Selkirk fan is a composite structure of Middle Jurassic and Cretaceous strain, rather than a singular fan that developed during one progressive event.
2. U-Th-Pb age constraints from the west flank of the fan indicate that structures developed principally in the Middle Jurassic between ca. ≥172 to 167 Ma.
3. In contrast, data from east of the fan axis demonstrate that there has been substantial Early to Late Cretaceous (ca. 104-84 Ma) deformation superimposed on an earlier

Middle Jurassic transposition fabric, and that significant exhumation did not occur until the Late Cretaceous-Early Tertiary.

4. A Late Cretaceous, ca. 92 Ma, overprint is interpreted to have affected west flank of the fan, but not enough to reset or erase the isotopic systems of the zircons analyzed.
5. The intensity of the Cretaceous overprint appears to be a function of structural level, such that the deepest levels that are exposed in the east flank of the fan at the latitude of this study produce only Cretaceous age constraints. Apparently the Middle Jurassic isotopic evidence in the deepest levels has been erased by processes that included recrystallization and hydrothermal alteration. Also, within the east flank there was likely significant reactivation of Middle Jurassic structures, and recrystallization of the associated transposition foliation during the Cretaceous.

Chapter 3:

1. The integration of U-Pb IDTIMS, *in situ* U-Th-Pb SHRIMP analyses, and chemical mapping of monazite from pelitic rocks significantly refined the timing of metamorphism associated with the development of the Selkirk fan.
2. The U-Th-Pb age constraints provided by this study demonstrate that metamorphism in the axis and east flank of the Selkirk fan was strongly diachronous, ranging in age from at least 144 to 56 Ma.
3. The Cretaceous-Tertiary metamorphic and structural elements within the east flank have overprinted pre-existing Middle Jurassic structures and the associated metamorphic assemblage that were identified within higher structural levels in the northern Monashee Mountains (Crowley et al., 2000), and within the west flank of the fan of this study. The degree of overprinting is a function of structural level, and is

interpreted to have been most intense in the deepest levels of the east flank such that the isotopic evidence associated with the Middle Jurassic metamorphism was essentially erased through processes of resorption, recrystallization, and hydrothermal alteration.

4. The protracted range of ages for the metamorphic assemblage in the east flank of the fan has far reaching implications with regard to mid- to lower crustal processes that were active during Cordilleran orogenesis. Most specifically, the data indicate the development of a hot middle to lower crustal zone that may have remained at depth for up to ~100 M.y.; this has not been previously identified or modeled (e.g., Jamieson et al., 1996, 1998; Beaumont et al., 2001). Perhaps without the benefit of *in situ* U-Th-Pb analyses, chemical mapping and integration of regional data sets, the apparent protracted nature of the middle to lower crustal processes associated with Cordilleran tectonism may have been overlooked in other orogens. Alternatively, this may be a feature unique to the Cordilleran orogen.

Chapter 4:

1. Chapter 4 presents a novel approach that couples chemical mapping for Y, Th and U in monazite with the *in situ* U-Th-Pb SHRIMP analyses. These techniques facilitated the establishment of the link between age domains and zones of relative Y depletion or enrichment within monazite that were correlated with metamorphic reactions involving garnet. The Y maps generally provided the best indication of growth or recrystallization domains, and were critical for targeting SHRIMP analyses.
2. The Y domains consistently correlated with distinct age domains, with up to three or more in some crystals. These data clearly illustrate the cause of age dispersion within

the analyzed monazites, and ubiquity of multiple age domains in metamorphic monazite from medium- to high-grade metamorphic terranes.

3. Precise SHRIMP ages of Y domains within monazite were correlated with metamorphic reactions involving garnet, and assigned to points along the P-T path. These interpretations were aided by work published in other studies that have investigated the interaction between accessory and major phases in pelites throughout a metamorphic event. More specifically, the partitioning of Y between phases such as garnet, monazite, and xenotime (e.g., Bea and Montero, 1999; Foster et al., 2000, 2002; Pyle et al., 2001; Pyle and Spear, 2002, 2003). These studies have established that garnet exerts considerable control over the Y budget available during metamorphism in pelitic rocks. Production and consumption of monazite is sensitive to the availability of Y, and is reflected internally in preserved Y zones. As such, SHRIMP analyses of these zones provide age constraints for the metamorphic reactions that involve monazite and the other major pelitic phases.

Chapter 5:

1. Based on the data produced in this study, a revised tectonic model is proposed in which the Selkirk fan developed within a critically tapered orogenic wedge that evolved diachronously in response to changing boundary conditions associated with periods of terrane accretion on the western margin of North America.
2. During the Early to Middle Jurassic accretion of the Intermontane Superterrane, a proto-F_{1-2} fan developed above a singularity where oceanic or marginal basin lithosphere was subducted eastward beneath continental lithosphere. Subsequently,

the fan decoupled along a basal shear zone, and was transferred northeastward as rocks to the east were progressively incorporated into the orogenic wedge.

3. The mid-Cretaceous accretion of the Insular Superterrane resulted in rejuvenation of compressional forces. This gave rise to out-of-sequence deformation that thickened the tectonic pile in order to reestablish critical taper. Once critical taper was reestablished, the out-of-sequence deformation abated, and further deformation was transferred eastward to the foreland.
4. The onset of extension, which denuded and exhumed significant portions of the southern Omineca belt, occurred during the waning stages of compression in the Paleocene to Eocene time (Parrish et al., 1988). At the latitude of this study, the Selkirk fan was dropped to its current structural position along the Columbia River fault (CRF). West-directed extensional faults found within the east flank of the Selkirk fan likely played a minor role in the placement of higher structural levels to the west against deeper levels to the east. Also, normal erosive processes have helped to expose higher-grade rocks within the axis and east flank because of the antiformal geometry that characterizes this part of the fan.

Outstanding Problems and Future Directions for Research:

1. The significance of the east-west orientation of the Adamant pluton such that it straddles both sides of the fan axis remains problematic (Map 2). The Adamant pluton is found in all three domains distinguished in this study, yet the analyzed zircons from the western portion of the pluton preserve Middle Jurassic ages. Perhaps zircons analyzed from the eastern part of the pluton would provide evidence of a significant Cretaceous overprint indicating that the west side was exhumed to higher levels prior

to the east due to differential uplift and rotation of the pluton. Future investigations within the Adamant pluton area are required to resolve this problem, especially around the eastern margin and surrounding country rock.

2. There is evidence for a Cretaceous thermal overprint within the west flank of the fan of the study area (see Chapter 2, p. 49), which is apparently not recorded along strike in rocks ~65 km to the south within the Illecillewaet synclinorium (Colpron et al., 1996). However, less than 20 km to the south and west, $^{40}Ar/^{39}Ar$ data for hornblende, muscovite and biotite from country rock of the Clachnacudainn complex and westernmost Illecillewaet synclinorium produced only Cretaceous to Early Tertiary cooling ages (Colpron et al. 1999). It should be noted that the hornblende, muscovite and biotite $^{40}Ar/^{39}Ar$ cooling ages provided by Colpron et al. (1996) were acquired from samples taken from various plutons in the region, not the country rock. Perhaps if the country rock in the rest of the Illecillewaet synclinorium area were analyzed, they too would reveal a Cretaceous overprint. It is also worth noting that the zircons from both the Adamant and Bigmouth plutons retain pristine crystallinity, whereas the zircon from the sampled dikes did not. These observations may be telling us something about the insulating effect that larger intrusive bodies have against overprinting metamorphic and/or hydrothermal events that would otherwise reset or alter the radiogenic isotopic systems of the minerals taken from the surrounding country rock.

3. The geochronologic data presented in Chapter 3 bring into question the exact nature and timing of metamorphic assemblages identified in the field and in thin section. The data imply that the mineral assemblage and associated transposition foliation

represent composite metamorphic and structural features that were likely developed initially in the Middle Jurassic, and were either progressively or episodically overprinted during the Cretaceous, and that the overprint was more pronounced at deeper levels. Throughout the region, the component of the assemblage that is related to Jurassic versus Cretaceous metamorphism needs to be investigated in detail. Also, in light of this data, the series of metamorphic isograds for the region needs to be reexamined because they were established based on mapping of metamorphic assemblages that were assumed to have formed during one event in the Middle Jurassic (e.g., Wheeler, 1965; Leatherbarrow, 1981).

4. In Chapter 4, the assignment of absolute age constraints to metamorphic reactions involving monazite and major pelitic minerals needs to be tested with quantitative thermobarometric data that can be applied in programs such as Gibbs method modeling.
5. The viability of the revised tectonic model for the development of the Selkirk fan should be further tested both in the field (e.g., reexamine timing of Purcell thrust, application of model to the north and south), and using finite element modeling. Also, the role of tectonic wedging has not been fully considered in this model. Consideration should be given to the possibility that tectonic wedging may have accompanied the development of structures produced in the model presented in Chapter 5, especially when using finite element modeling.
6. Lastly, the role of mid- to lower crustal channel flow has not been fully considered. Although, some tectonic features of the southern Canadian Cordillera appear to agree with what is predicted in the channel flow models, the dissimilar features need to be

accounted for when setting up the parameters for future models specific to the Cordillera (see Chapter 5, p. 228).

REFERENCES

Andrew, K. P. E., Höy, T. and Drobe, J. 1990. Stratigraphy and tectonic setting of the Archibald and Elise Formations, Rossland Group, Beaver Creek area, southeastern British Columbia (82F/4E). In:*Geologic fieldwork 1989.* British Columbia Ministry of Energy, Mines and Petroleum Resources. Paper 1990-1, p. 19-27.

Armstrong, R. L., Parrish, R. R., Van der Heyden, P., Scott, K., Runkle, D. and Brown, R. L. 1991. Early Proterozoic basement exposures in the southern Canadian Cordillera: core gneiss of Frenchman Cap, Unit I of the Grand Forks Gneiss, and the Vaseaux Formation. *Canadian Journal of Earth Sciences.* **28:** 1169-1201.

Bea, F. 1996. Residence of REE, Y, Th and U in Granites and Crustal Protoliths; Implications for the Chemistry of Crustal Melts. *Journal of Petrology.* **37:** 521-552.

Bea, F. and Montero, P. 1999. Behavior of accessory phases and redistribution of Zr, REE, Y, Th, and U during metamorphism and partial melting of metapelites in the lower crust: An example from the Kinzigite Formation of Ivrea-Verbano, NW Italy. *Geochimica et Cosmochimica Acta.* **63:** 113-1153.

Bearden, J. A. 1964. X-ray wavelengths. U.S. Atomic Energy Commission Oak Ridge, Tennessee. Report NYO 10586.

Beaumont, C., Jamieson, R. A., Nguyen, M. H. and Lee, B. 2001. Himalayan tectonics explained by extrusion of a low viscosity crustal channel coupled to focussed surface denudation. *Nature.* **414:** 738-742.

Bingen, B., Demaiffe, D. and Hertogen, J. 1996. Redistribution of Rare Earth Elements, Thorium, and Uranium over accessory minerals in the course of amphibolite to granulite-facies metamorphism - the role of apatite and monazite in orthogneisses from Southwestern Norway. *Geochimica et Cosmochimica Acta.* **60:** 1341-1354.

Braun, I., Montel, J., Marc and Nicollet, C. 1998. Electron microprobe dating of monazites from high-grade gneisses and pegmatites of the Kerala khondalite belt, southern India. *Chemical Geology.* **146:** p.65-85.

Brown, R. L. 1991. Geological Map and Cross Section, Downie Creek Map Area (82M/8), British Columbia: Geological Survey of Canada, Map 2414, scale 1:50 000.

Brown, R. L. 2003. Thrust belt accretion and hinterland underplating of orogenic wedges: an example from the Canadian Cordillera. In: *Thrust Tectonics and Petroleum Systems: AAPG Memoir* (edited by McClay, K. R.). American Association of Petroleum Geologists in press.

Brown, R. L., Beaumont, C. and Willett, S. D. 1993. Comparison of the Selkirk fan structure with mechanical models: implications for interpretation of the southern Canadian Cordillera. *Geology.* **21:** 1015-1018.

Brown, R. L. and Gibson, H. D. 2003. Comparison of Himalayan and Cordilleran tectonic processes. *In* Geological Association of Canada Annual Meeting, Vancouver, BC in press.

Brown, R. L. and Lane, L. S. 1988. Tectonic interpretation of west-verging folds in the Selkirk Allochthon of the southern Canadian Cordillera. *Canadian Journal of Earth Sciences.* **25:** 292-300.

Brown, R. L., Lane, L. S., Psutka, J. F. and Read, P. B. 1983. Stratigraphy and structure of the western margin of the northern Selkirk Mountains: Downie Creek Map area, British Columbia. In:*Current Research , Part A.* Geological Survey of Canada. Paper 83-1A, p. 203-206.

Brown, R. L., McNicoll, V. J., Parrish, R. R. and Scammell, R. J. 1992. Middle Jurassic plutonism in the Kootenay Terrane, northern Selkirk Mountains, British Columbia. In:*Radiogenic and Isotopic Studies: Report 5.* Geological Survey of Canada. Paper 91-2, p. 135-141.

Brown, R. L., Perkins, M. J. and Tippett, C. R. 1977. Structure and stratigraphy of the Big Bend area, British Columbia. In:*Report of Activities, Part A.* Geological Survey of Canada. Paper 77-1A, p. 273-275.

Brown, R. L. and Tippett, C. R. 1978. The Selkirk fan structure of the southeastern Canadian Cordillera. *Geological Society of America Bulletin.* **89:** 548-558.

Brown, R. L., Tippett, C. R. and Lane, L. S. 1978. Stratigraphy, facies changes, and correlations in the northern Selkirk Mountains, southern Canadian Cordillera. *Canadian Journal of Earth Sciences.* **15:** 1129-1140.

Campbell, R. B. 1968. Canoe River (83D), British Columbia: Geological Survey of Canada, Map 15-1967.

Carr, S. D. 1991. Three crustal zones in the Thor-Odin-Pinnacles area, southern Omineca Belt, British Columbia. *Canadian Journal of Earth Sciences.* **28:** 2003-2023.

Cherniak, D. J. and Watson, E. B. 2000. Pb diffusion in zircon. *Chemical Geology.* **172:** 5-24.

Cherniak, D. J., Watson, E. B., Grove, M. and Harrison, T. M. 2002. Pb diffusion in Monazite. *In* Geological Society of America Annual Meeting, Denver, CO. **34:** 311.

Clowes, R. M., Colin, A. Z., Amor, J. R. and Ellis, R. M. 1995. Lithospheric structure in the southern Canadian Cordillera from a network of seismic refraction lines. *Canadian Journal of Earth Sciences.* **32:** 1485-1513.

Cocherie, A., Legendre, O., Peucat, J. J. and Kouamelan, A. N. 1998. Geochronology of polygenetic monazites constrained by in situ electron microprobe Th-U-total lead determination: Implications for lead behaviour in monazite. *Geochimica et Cosmochimica Acta.* **62:** 2475-2497.

Colpron, M., Logan, J. M., Gibson, G. and Wild, C. J. 1995. Geology and Mineral Occurrences of the Goldstream River Area, Northern Selkirk Mountains (82M/9 and part of 10): British Columbia Ministry of Energy, Mines and Petroleum Resources, Map 1995-2, scale 1:50 000.

Colpron, M., Price, R. A. and Archibald, D. A. 1999. $^{40}Ar/^{39}Ar$ thermochronometric constraints on the tectonic evolution of the Clachnacudainn complex, southeastern British Columbia. *Canadian Journal of Earth Sciences.* **36:** 1989-2006.

Colpron, M., Price, R. A., Archibald, D. A. and Carmichael, D. M. 1996. Middle Jurassic exhumation along the western flank of the Selkirk fan structure: thermobarometric and thermochronometric constraints from the Illecillewaet synclinorium, southeastern British Columbia. *Geological Society of America Bulletin.* **108:** 1372-1392.

Colpron, M., Warren, M. J. and Price, R. A. 1998. Selkirk fan structure, southeastern Canadian Cordillera: tectonic wedging against an inherited basement ramp. *Bulletin of the Geological Society of America.* **110:** 1060-1074.

Connelly, J. N. 2001. Degree of preservation in igneous zonation in zircon as a signpost for concordancy in U/Pb geochronology. *Chemical Geology.* **172:** 25-39.

Cook, F. A. 1986. Seismic reflection geometry of the Columbia River fault zone and east margin of the Shuswap metamorphic complex in the Canadian Cordillera. *Tectonics.* **5:** 669-685.

Cook, F. A. 1995. The reflection Moho beneath the southern Canadian Cordillera. *Canadian Journal of Earth Sciences.* **32:** 1520-1530.

Cook, F. A., others and et al. 1992. Lithoprobe crustal reflection cross section of the southern Canadian Cordillera, 1. Foreland thrust and fold belt to Fraser River Fault. *Tectonics.* **11:** 12-35.

Crowley, J. L. 1999. U-Pb geochronologic constraints on Paleoproterozoic tectonism in the Monashee complex, Canadian Cordillera: Elucidating an overprinted geologic history. *Bulletin of the Geological Society of America.* **111:** 560-577.

Crowley, J. L. and Brown, R. L. 1994. Tectonic links between the Clachnacudainn terrane and Selkirk allochthon, southern Omineca Belt, Canadian Cordillera. *Tectonics.* **13:** 1035-1051.

Crowley, J. L., Brown, R. L. and Parrish, R. R. 2001. Diachronous deformation and a strain gradient beneath the Selkirk allochthon, northern Monashee complex, southeastern Canadian Cordillera. *Journal of Structural Geology.* **23:** 1103-1121.

Crowley, J. L. and Ghent, E. D. 1999. An electron microprobe study of the U-Th-Pb systematics of metamorphosed monazite: The role of Pb diffusion versus overgrowth and recrystallization. *Chemical Geology.* **157:** 285-302.

Crowley, J. L., Ghent, E. D., Carr, S. D., Simony, P. S. and Hamilton, M. A. 2000. Multiple thermotectonic events in a continuous metamorphic sequence, Mica Creek area, southeastern Canadian Cordillera. *Geological Materials Research.* e-journal. http://gmr.minsocam.org/papers/v2/v2n2/v2n2abs.html. p. 1-45.

Davis, D., Suppe, J. and Dahlen, F. A. 1983. Mechanics of fold-and- thrust belts and accretionary wedges. *Journal of Geophysical Research.* **88:** 1153-1172.

De Laeter, J. R. and Kennedy, A. K. 1998. A double focusing mass spectrometer for geochronology. *International Journal of Mass Spectrometry.* **178:** 43-50.

DeWolf, C. P., Belshaw, N. S. and O'Nions, R. K. 1993. A metamorphic history from micron-scale $^{207}Pb/^{206}Pb$ chronometry of Archean monazite. *Earth and Planetary Science Letters.* **120:** p.207-220.

Digel, S. G., Ghent, E. D., Carr, S. D. and Simony, P. S. 1998. Early Cretaceous kyanite-sillimanite metamorphism and Paleocene sillimanite overprint near Mount Cheadle, southeastern British Columbia: Geometry, geochronology, and metamorphic implications. *Canadian Journal of Earth Sciences.* **35:** 1070-1087.

Dodson, M. H. 1973. Closure Temperature in Cooling Geochronological and Petrological Systems. *Contributions to Mineralogy and Petrology.* **40:** 259-274.

Evans, C. S. 1933. Brisco-Dogtooth map-area, British Columbia. Geological Survey of Canada. Report 1932, Part AII, p. 106-176.

Ferry, J. M. 2000. Patterns of mineral occurrence in metamorphic rocks. *American Mineralogist.* **85:** 1573-1588.

Foster, G., Gibson, H. D., Parrish, R. R., Horstwood, M., Fraser, J. and Tindle, A. 2002. Textural, chemical and isotopic insights into the nature and behaviour of metamorphic monazite. *Chemical Geology.* **191:** 183-207.

Foster, G., Kinny, P., Vance, D., Prince, C. and Harris, N. 2000. The significance of monazite U-Th-Pb age data in metamorphic assemblages; a combined study of monazite and garnet chronometry. *Earth and Planetary Science Letters.* **181:** 327-340.

Fox, P. E. 1969. Petrology of Adamant Pluton, British Columbia. In:*Current Research.* Department of Energy, Mines and Resources. Paper 67-61, p. 1-101.

Franzen, J. 1974. Structural analysis in the Selkirk fan axis near Argonaut Mountain, southeastern British Columbia. Unpublished M.Sc. thesis, Carleton University, p. 55.

Fyles, J. T. 1964. Geology of the Duncan Lake area, Lardeau district, British Columbia. British Columbia Department of Mines and Petroleum Resources. Bulletin 49, p. 78.

Fyles, J. T. and Eastwood, G. E. P. 1962. Geology of the Ferguson Area, Lardeau District, British Columbia. British Columbia Ministry of Energy, Mines and Petroleum Resources. Bulletin 45, p. 1-92.

Gabrielse, H. and Campbell, R. B. 1991. Upper Proterozoic assemblages, Chapter 6. In: *Geology of the Cordilleran Orogen in Canada* (edited by Gabrielse, H. & Yorath, C. J.). *Geology of Canada*. Geological Survey of Canada. **No. 4:** 125-150.

Gerasimoff, M. D. 1988. The Hobson lake Pluton, Cariboo Mountains, and its significance to Mesozoic and Early Tertiary Cordilleran tectonics. Unpublished M.Sc. thesis, Queens University, p. 188.

Ghent, E. D., Knitter, C. C., Raeside, R. P. and Stout, M. Z. 1982. Geothermometry and geobarometry of pelitic rocks, upper kyanite and sillimanite zones, Mica Creek area, British Columbia. *The Canadian Mineralogist.* **20:** 295-305.

Ghent, E. D., Robbins, D. B. and Stout, M. Z. 1979. Geothermometry, geobarometry, and fluid compositions of metamorphosed calc-silicates and pelites, Mica Creek, British Columbia. *American Mineralogist.* **64:** 874-885.

Ghent, E. D., Simony, P. S. and Knitter, C. C. 1980. Geometry and Pressure-Temperature significance of the Kyanite-Sillimanite isograd in the Mica Creek area, British Columbia. *Contributions to Mineralogy and Petrology.* **74:** 67-73.

Ghent, E. D., Simony, P. S., Mitchell, W., Perry, D., Robbins, D. and Wagner, J. 1977. Structure and metamorphism in the southeast Canoe River area, British Columbia. In:*Report on Activities, Part C.* Geological Survey of Canada. Paper 77-1C, p. 13-17.

Ghent, E. D., Stout, M. Z. and Raeside, R. P. 1983. Plagioclase- clinopyroxene- garnet-quartz equilibria and the geobarometry and geothermometry of garnet amphibolites from Mica Creek, British Columbia. *Canadian Journal of Earth Sciences.* **20:** 699-706.

Gibson, H. D., Brown, R. L. and Carr, S. D. 2003. Tectonic evolution of the Selkirk fan: A composite Middle Jurassic - Cretaceous structure, northern Selkirk Mountains, southeastern Canadian Cordillera. *In* Geological Association of Canada Annual Meeting, Vancouver, BC in press.

Gibson, H. D., Brown, R. L., Carr, S. D. and Hamilton, M. A. 2001. Structural Evolution of the Selkirk Fan Structure, Northern Selkirk Mountains, southeastern Canadian Cordillera. *In* Geological Society of America Annual Meeting, Boston, MA. **33:** A327.

Gibson, H. D., Brown, R. L. and Parrish, R. R. 1999. Deformation-induced inverted metamorphic field gradients: An example from the southeastern Canadian Cordillera. *Journal of Structural Geology.* **21:** 751-767.

Gibson, H. D., Carr, S. D. and Brown, R. L. 2000. U-Pb geochronologic constraints on metamorphism and deformation within the northern Selkirk mountains, southeastern Canadian Cordillera. *In* GeoCanada 2000, Calgary, Alberta Abstract #986, Volume on CD.

Gibson, H. D., Carr, S. D., Hamilton, M. A. and Brown, R. L. 2002. Insights into the chemical and isotopic complexities of metamorphic monazite: integration of IDTIMS and SHRIMP geochronology with BSE and Y-Th-U X-ray mapping techniques. *In* Geological Society of America Annual Meeting, Denver, CO. **34:** 68.

Goldstein, J. I., Newbury, D. E., Echlin, P., Joy, D. C., Fiori, C. and Lifshin, E. 1981. Scanning electron microscopy and X-ray microanalysis : a text for biologists, materials scientists, and geologists. Plenum Press, New York.

Gradstein, F. M., Agterberg, F. P., Ogg, J. G., Hardenbol, J., van Veen, P., Thierry, J. and Huang, Z. 1994. A Mesozoic time scale. *Journal of Geophysical Research.* **99:** 24051-24074.

Hanchar, J. M. and Miller, C. F. 1993. Zircon zonation patterns as revealed by cathodoluminescence and backscattered electron images: implications for interpretation of complex crustal histories. *Chemical Geology.* **110:** 1-13.

Hanes, J. A. 1991. K-Ar and ^{40}Ar/^{39}Ar geochronology: methods and applications. In: *Applications of radiogenic isotope systems to problems in geology* (edited by Heaman, L. & Ludden, J. N.). *Short Course Handbook*. Mineralogical Association of Canada. **19:** 27-57.

Harland, W. B., Armstrong, R. L., Cox, A. V., Craig, L. E., Smith, A. G. and Smith, D. G. 1990. A geologic time scale 1989. Cambridge University Press, Cambridge, England.

Harrison, T. M., McKeegan, K. D. and LeFort, P. 1995. Detection of inherited monazite in the Manaslu leucogranite by ^{208}Pb/^{232}Th ion microprobe dating: crystallization age and tectonic implications. *Earth and Planetary Science Letters.* **133:** 271-282.

Heaman, L. and Parrish, R. 1991. U-Pb geochronology of accessory minerals. In: *Applications of Radiogenic Isotope Systems to Problems in Geology* (edited by Heaman, L. & Ludden, J. N.). *Short Course Handbook*. Mineralogical Association of Canada. **19:** 59-100.

Hobbs, B. E., Mean, W. D. and Williams, P. F. 1976. An outline of Structural Geology. John Wiley & Sons, Inc.

Höy, T. 1977. Stratigraphy and structure of the Kootenay Arc in the Riondel area, southeastern British Columbia. *Canadian Journal of Earth Sciences.* **14:** 2301-2315.

Jamieson, R. A., Beaumont, C., Fullsack, P. and Lee, B. 1998. Barrovian regional metamorphism: where's the heat? *Geological Society Special Publication.* **138:** 23-51.

Jamieson, R. A., Beaumont, C., Hamilton, J. and Fullsack, P. 1996. Tectonic assembly of inverted metamorphic sequences. *Geology.* **24:** 839-842.

Klepacki, D. W. 1985. Stratigraphy and structural geology of the Goat Range area, southeastern British Columbia. Unpublished Ph.D. thesis, Massachusetts Institute of Technology, p. 268.

Kretz, R. 1983. Symbols for rock-forming minerals. *American Mineralogist.* **68:** 277-279.

Krogh, T. E. 1982. Improved accuracy of U-Pb ages by the creation of more concordant systems using an air abrasion technique. *Geochimica et Cosmochimica Acta.* **46:** 637-649.

Leatherbarrow, R. W. 1981. Metamorphism of pelitic rocks from the northern Selkirk Mountains, southeastern British Columbia. Unpublished Ph.D. thesis, Carleton University, p. 218.

Leatherbarrow, R. W. and Brown, R. L. 1978. Metamorphism of the northern Selkirk Mountains, British Columbia. In:*Current Research, Part A.* Geological Survey of Canada. Paper 78-1A, p. 81-82.

Logan, J. M. and Colpron, M. 1995. Northern Selkirk Project - Geology of the Goldstream River area (82M/9 and parts of 82M/10). In:*Geological Fieldwork 1995-1.* British Columbia Geological Survey of Canada. Paper 1995-1, p. 215-241.

Logan, J. M., Colpron, M. and Johnson, B. J. 1996. Northern Selkirk Project, Geology of the Downie Creek Map area. In:*Geological Fieldwork 1995.* British Columbia Geological Survey of Canada. Paper 1996-1, p. 107-125.

Logan, J. M. and Friedman, R. M. 1997. U-Pb ages from the Selkirk allochthon, Seymour Arm map area, southeast British Columbia (82M/8 and 9). In:*Geological Fieldwork 1996.* British Columbia Geological Survey of Canada. Paper 1997-1, p. 17-23.

Malavieille, J. 1984. Modélisation expérimentale des chevauchements imbriqués: Application aux chaînes de montagnes. *Bulletin de la Société Géologique de France.* **26:** 129-138.

Marchildon, M. N. 1999. Petrologic studies of process interactions in metamorphic systems: deformation and metamorphism in the Selkirk allochthon orogenic wedge; And feedback mechanisms during reactive fluid flow. Unpublished Ph.D. thesis, University of British Columbia, p. 155.

Mathews, W. H. 1986. Physiography of the Canadian Cordillera: Geological Survey of Canada, Map 1701A, scale 1:5 000 000.

McDonough, M. R., Simony, P. S., Sevigny, J. H., Robbins, D. B., Raeside, R., Doucet, P., Pell, J. and Dechesne, R. G. 1992. Geology of Nagle Creek and Blue River, British Columbia (83D/2 and 83D/3): Geological Survey of Canada, Map 2512, scale 1:50 000.

Monger, J. W. H. and Price, R. A. 1979. Geodynamic evolution of the Canadian Cordillera - progress and problems. *Canadian Journal of Earth Sciences.* **16:** 770-791.

Monger, J. W. H., Price, R. A. and Tempelman-Kluit, D. J. 1982. Tectonic accretion and the origin of the two major metamorphic and plutonic welts in the Canadian Cordillera. *Geology.* **10:** 70-75.

Murphy, D. C. 1987. Suprastructure-infrastructure transition, east-central Cariboo Mountains, British Columbia: geometry, kinematics and tectonic implications. *Journal of Structural Geology.* **9:** 13-29.

Murphy, D. C., van der Heyden, P., Parrish, R. R., Klepacki, D. W., McMillan, W., Struik, L. C. and Gabites, J. 1995. New geochronological constraints on Jurassic deformation of the western edge of North America, southeastern Canadian Cordillera. In: *Jurassic magmatism and tectonics of the North American Cordillera* (edited by Miller, D. M. & Busby, C.). Geological Society of America. **Special Paper 299:** 159-171.

Nelson, K. D., Wenjin Zhao, Brown, L. D., Kuo, J., Che, J., Liu, X., Klemperer, S. L., Makovsky, Y., Meissner, R., Mechie, J., Kind, R., Wenzel, F., Ni, J., Nabelek, J., Leshou, C., Tan, H., Wei, W., Jones, A. G., Booker, J., Unsworth, M., Kidd, W. S. F., Hauck, M., Alsdorf, D., Ross, A., Cogan, M., Wu, C., Sandvol, E. and Edwards, M. 1996. Partially Molten Middle Crust Beneath Southern Tibet: Synthesis of Project INDEPTH Results. *Science.* **274:** 1684-1688.

Overstreet, W. C. 1967. The geological occurrence of monazite. In:*US geological survey professional paper.* US geological survey. 530, p. 327.

Pan, Y. M. 1997. Zircon- and monazite-forming metamorphic reactions at Manitouwadge, Ontario. *Canadian Mineralogist.* **35:** 105-118.

Parkinson, D. 1991. Age and isotopic character of early Proterozoic basement gneisses in the southern Monashee Complex, southeastern British Columbia. *Canadian Journal of Earth Sciences.* **28:** 1159-1168.

Parrish, R. R. 1987. An improved micro-capsule for zircon dissolution in U-Pb geochronology. *Chemical Geology.* **66:** 99-102.

Parrish, R. R. 1990. U-Pb dating of monazite and its application to geological problems. *Canadian Journal of Earth Sciences.* **27:** 1431-1450.

Parrish, R. R. 1995. Thermal evolution of the southeastern Canadian Cordillera. *Canadian Journal of Earth Sciences.* **32:** 1618-1642.

Parrish, R. R., Carr, S. D. and Parkinson, D. L. 1988. Eocene extensional tectonics and geochronology of the southern Omineca Belt, British Columbia and Washington. *Tectonics.* **7:** 181-212.

Parrish, R. R. and Krogh, T. E. 1987. Synthesis and purification of ^{205}Pb for U-Pb geochronology. *Chemical Geology.* **66:** 103-110.

Parrish, R. R., Roddick, J. C., Loveridge, W. D. and Sullivan, R. W. 1987. Uranium-lead analytical techniques at the geochronology laboratory, Geological Survey of Canada. In:*Radiogenic Age and Isotopic Studies: Report 1.* Geological Survey of Canada. Paper 87-2, p. 3-7.

Parrish, R. R. and Wheeler, J. O. 1983. A U- Pb zircon age from the Kuskanax batholith, southeastern British Columbia (Canada). *Canadian Journal of Earth Sciences.* **20:** 1751-1756.

Pattison, D. R. W. 1992. Stability of andalusite and sillimanite and the Al_2SiO_5 triple point: constraints from the Ballachulish aureole, Scotland. *Journal of Geology.* **100:** 423-446.

Pell, J. and Simony, P. 1987. New correlations of Hadrynian strata, south-central British Columbia. *Canadian Journal of Earth Sciences.* **24:** 302-313.

Perkins, M. J. 1983. Structural geology and stratigraphy, Big Bend of the Columbia river, Selkirk Mountains, British Columbia. Unpublished Ph.D. thesis, Carleton University, p. 238.

Pidgeon, R. T. 1992. Recrystallization of oscillatory zoned zircon: some geochronological and petrological implications. *Contributions to Mineralogy and Petrology.* **110:** 463-472.

Poitrasson, F., Bland, D. J. and Chenery, S. 1996. Contrasted monazite hydrothermal alteration mechanisms and their geochemical implications. *Earth and Planetary Science Letters.* **146:** 79-96.

Poitrasson, F., Chenery, S. and Shepherd, T. J. 2000. Electron microprobe and LA-ICP-MS study of monazite hydrothermal alteration: Implications for U-Th-Pb geochronology and nuclear ceramics. *Geochimica et Cosmochimica Acta.* **64:** 3283-3297.

Poulton, T. P. and Simony, P. S. 1980. Stratigraphy, sedimentology, and regional correlation of the Horsethief Creek Group (Hadrynian, Late Precambrian) in the northern Purcell and Selkirk Mountains, British Columbia. *Canadian Journal of Earth Sciences.* **17:** 1708-1724.

Price, R. A. 1979. The Selkirk fan structure of the southeastern Canadian Cordillera: Discussion. *Geological Society of America Bulletin.* **90:** 695-698.

Price, R. A. 1986. The southeastern Canadian Cordillera: thrust faulting, tectonic wedging, and delamination of the lithosphere. *Journal of Structural Geology.* **8:** 239-254.

Price, R. A. 1994. Chapter 2: Cordilleran tectonics and the evolution of the western Canada sedimentary basin. In: *Geological atlas of the western Canada sedimentary basin* (edited by Mossop, G. & Shetsin, I.) p. 13-24.

Price, R. A. and Mountjoy, E. W. 1970. Geological structure of the Canadian Rocky Mountains between Bow and Athabasca Rivers - A progress report. In: *Structure of the southern Canadian Cordillera* (edited by Wheeler, J. O.). Geological Association of Canada Special Paper. **Paper 6:** 7-25.

Pyle, J. M. and Spear, F. S. 2000a. Accessory-phase paragenesis in low-P migmatites, Chesham Pond nappe, SE new Hampshire. *In* Geological Society of America Annual Meeting. **32:** A297.

Pyle, J. M. and Spear, F. S. 2000b. An empirical garnet (YAG) - xenotime thermometer. *Contributions to Mineralogy and Petrology.* **138:** 51-58.

Pyle, J. M. and Spear, F. S. 2002. Formation, consumption, and compositional zoning of pelitic monazite and xenotime: Metamorphic whole-rock reaction controls. *Journal of Metamorphic Geology.* in prep.

Pyle, J. M. and Spear, F. S. 2003. Four generations of accessory-phase growth in low-pressure migmatites from SW New Hampshire. *American Mineralogist.* **88:** 338-351.

Pyle, J. M., Spear, F. S., Rudnick, R. L. and McDonough, W. F. 2001. Monazite-xenotime-garnet equilibrium in metapelites and a new monazite-garnet thermometer. *Journal of Petrology.* **42:** 2083-2107.

Raeside, R. P. and Simony, P. S. 1983. Stratigraphy and deformational history of the Scrip Nappe, Monashee Mountains, British Columbia. *Canadian Journal of Earth Sciences.* **20:** 639-650.

Ramsay, J. G. 1967. Folding and fracturing of rocks. McGraw Hill, New York.

Read, P. B. 1973. Petrology and structure of the Poplar Creek map-area, British Columbia. Geological Survey of Canada, p. 144.

Read, P. B. and Brown, R. L. 1979. Inverted stratigraphy and structures, Downie Creek, southern British Columbia. In:*Current Research, Part A.* Geological Survey of Canada. Paper 79-1A, p. 33-34.

Read, P. B. and Brown, R. L. 1981. Columbia River fault zone: southeastern margin of the Shuswap and Monashee complexes, southern British Columbia. *Canadian Journal of Earth Sciences.* **18:** 1127-1145.

Read, P. B. and Wheeler, J. O. 1976. Geology of Lardeau W/2 (82K W/2): Geological Survey of Canada, Open File Map 432, scale 1:125 000.

Reid, L. F., Heaman, L. M., Simony, P. S. and Pattison, D. R. M. 2003. Relationship between multiple phases of Mesozoic deformation and metamorphism in the

Cariboo Mountains, Omineca belt, central British Columbia. *In* Cordilleran Tectonics Workshop, Ottawa, Canada 29.

Roddick, J. C. 1987. Generalized numerical error analysis with applications to geochronology and thermodynamics. *Geochimica et Cosmochimica Acta.* **51:** 2129-2135.

Roddick, J. C., Loveridge, W. D. and Parrish, R. R. 1987. Precise U/Pb dating of zircon at the sub-nanogram Pb level. *Chemical Geology.* **66:** 111-121.

Rubatto, D., Williams, I. S. and Buick, I. S. 2001. Zircon and monazite response to prograde metamorphism in the Reynolds Range, central Australia. *Contributions to Mineralogy and Petrology.* **140:** 458-468.

Scammell, R. J. 1993. Mid-Cretaceous to Tertiary thermotectonic history of former mid-crustal rocks, southern Omineca belt, Canadian Cordillera. Unpublished Ph.D. thesis, Queen's University, p. 576.

Schärer, U. 1984. The effect of initial ^{230}Th disequilibrium on young U-Pb ages: the Makalu case, Himalaya. *Earth and Planetary Science Letters.* **67:** 191-204.

Sevigny, J. H., Parrish, R. R., Donelick, R. A. and Ghent, E. D. 1990. Northern Monashee Mountains, Omineca Crystalline Belt, British Columbia: Timing of metamorphism, anatexis, and tectonic denudation. *Geology.* **18:** 103-106.

Sevigny, J. H., Parrish, R. R. and Ghent, E. D. 1989. Petrogenesis of peraluminous granites, Monashee Mountains, southeastern Canadian Cordillera. *Journal of Petrology.* **30:** 557-581.

Shannon, R. D. 1976. Revised effective ionic radii and systematic studies of interatomic distances in halides and chalcogenides. *Acta Crystallographica.* **A32:** 751-767.

Shaw, D. 1980a. A concordant Uranium-Lead age for zircons in the Adamant Pluton, British Columbia. In:*Rb-Sr and U-Pb Isotopic Age Studies in Current Research, Part C.* Geological Survey of Canada. Paper 80-1C, p. 243-246.

Shaw, D. A. 1980b. Structural setting of the Adamant Pluton, Northern Selkirk Mountains, British Columbia. Unpublished Ph.D. thesis, Carleton University, p. 197.

Simony, P. S., Ghent, E. D., Craw, D., Mitchell, W. and Robbins, D. B. 1980. Structural and metamorphic evolution of the northeast flank of Shuswap complex, southern Canoe River area, British Columbia. *Geological Society of America Memoir 153.* 445-461.

Smith, H. A. and Barreiro, B. 1990. Monazite U-Pb dating of staurolite grade metamorphism in pelitic schists. *Contributions to Mineralogy and Petrology.* **105:** 602-615.

Smith, M. T., Gerhels, G. E. and Klepacki, D. W. 1992. 173 Ma U-Pb age of felsite sells (Kaslo River intrusives) west of Kootenay Lake, southeastern British Columbia. *Canadian Journal of Earth Sciences.* **29:** 531-534.

Spear, F. S., Kohn, M. J. and Cheney, J. T. 1999. P-T paths from anatectic pelites. *Contributions to Mineralogy and Petrology.* **134:** 17-32.

Stacey, J. S. and Kramer, J. D. 1975. Approximation of terrestrial lead isotope evolution by a two-stage model. *Earth and Planetary Science Letters.* **26:** 207-221.

Steiger, R. H. and Jäger, E. 1977. Subcommission on geochronology: convention on the use of decay constants in geo- and cosmochronology. *Earth and Planetary Science Letters.* **36:** 359-362.

Stern, R. A. 1997. The GSC Sensitive High Resolution Ion Microprobe (SHRIMP): analytical techniques of zircon U-Th-Pb age determinations and performance evaluation. In:*Rb-Sr and U-Pb Isotopic Age Studies in Current Research, Part C.* Geological Survey of Canada. Current Research 1997-F, p. 1-31.

Stern, R. A. and Berman, R. G. 2000. Monazite U-Pb and Th-Pb geochronology by ion microprobe, with an application to in situ dating of an Archean metasedimentary rock. *Chemical Geology.* **172:** 113-130.

Stern, R. A. and Sanborn, N. 1998. Monazite U-Pb and Th-Pb geochronology by high-resolution secondary ion mass spectrometry. In:*Radiogenic Age and Isotopic Studies: Report 11.* Geological Survey of Canada. Current Research 1998-F, p. 1-18.

Tera, F. and Wasserburg, G. J. 1972. U-Th-Pb systematics in three Apollo 14 basalts and the problem of initial Pb in lunar rocks. *Earth and Planetary Science Letters.* **14:** 281-304.

Tipper, H. W. 1984. The age of the Jurassic Rossland Group. In:*Current Research, Part A.* Geological Survey of Canada. Paper 84-1A, p. 631-632.

Van der Leeden, J. 1976. Stratigraphy, structure and metamorphism in the northern Selkirk Mountains southwest of Argonaut Mountain, southeastern British Columbia. Unpublished M.Sc. thesis, Carleton University, p. 105.

Vavra, G. 1990. On the kinematics of zircon growth and its petrogenetic significance: a cathodoluminescence study. *Contributions to Mineralogy and Petrology.* **106:** 90-99.

Walker, J. F. 1926. Geology and mineral deposits of Windermere map-area, British Columbia. Geological Survey of Canada. Memoir 148, p. 68.

Warren, M. J. 1997. Crustal extension and subsequent crustal thickening along the Cordilleran rifted margin of ancestral North America, western Purcell Mountains, southeastern British Columbia. Unpublished Ph.D. thesis, Queens University, p. 361.

Wetherill, G. W. 1956. Discordant uranium-lead ages. *American Geophysical Union Transactions.* **37:** 320-326.

Wheeler, J. O. 1963. Rogers Pass Map-area, British Columbia and Alberta (82N West Half). Geological Survey of Canada. Paper 62-32, p. 1-32.

Wheeler, J. O. 1965. Big Bend map-area, British Columbia. Geological Survey of Canada. Paper 64-32, p. 1-37.

Wheeler, J. O. and McFeely, P. 1991. Tectonic assemblage map of the Canadian Cordillera and adjacent parts of the United States of America: Geological Survey of Canada, Map 1712A, scale 1:2 000 000.

Willett, S., Beaumont, C. and Fullsack, P. 1993. Mechanical model for the tectonics of doubly vergent compressional orogens. *Geology.* **21:** 371-374.

Williams, C. A., Suppe, J., Connors, C., Dahlen, F. A. and Price, E. J. 1994. Effect of the brittle-ductile transition on the topography of compressive mountain belts on Earth and Venus. *Journal of Geophysical Research.* **99:** 19,947-19,974.

Williams, I. S. 1998. U-Th-Pb geochronology by ion microprobe. In: *Applications of Microanalytical Techniques to Understanding Mineralizing Processes* (edited by

McKibben, M., Shanks, W. C. & Ridley, W. I.). Reviews in Economic Geology. **7:** 1-35.

Williams, M. L., Jercinovic, M. J. and Terry, M. P. 1999. Age mapping and dating of monazite on the electron microprobe: Deconvoluting multistage tectonic histories. *Geology.* **27:** 1023-1026.

Woodsworth, G. J., Anderson, R. G. and Armstrong, R. L. 1991. Plutonic regimes. In: *Geology of the Cordilleran orogen in Canada* (edited by Gabrielse, H. & Yorath, C. J.). Geological Survey of Canada. **No. 4:** 491-531.

York, D. 1969. Least squares fitting of a straight line with correlated errors. *Earth and Planetary Science Letters.* **5:** 320-324.

Yunxiang, N., Hughes, J. M. and Mariano, A. N. 1995. Crystal chemistry of the monazite and xenotime structures. *American Mineralogist.* **80:** 21-26.

Zen, E. 1985. Implications of magmatic epidote-bearing plutons on crustal evolution in the accreted terranes of northwestern North America. *Geology.* **13:** 266-269.

Zen, E. and Hammarstrom, J. M. 1984. Magmatic epidote and its petrologic significance. *Geology.* **12:** 515-518.

Zhu, X. K. and O' Nions, R. K. 1999a. Monazite chemical composition: Some implications for monazite geochronology. *Contributions to Mineralogy and Petrology.* **137:** 351-363.

Zhu, X. K. and O' Nions, R. K. 1999b. Zonation of monazite in metamorphic rocks and its implications for high temperature thermochronology: A case study from the Lewisian terrain. *Earth and Planetary Science Letters.* **171:** 209-220.

Zhu, X. K., O'Nions, R. K., Belshaw, N. S. and Gibb, A. J. 1997. Significance of in situ SIMS chronometry of zoned monazite from the Lewisian granulites, northwest Scotland. *Chemical Geology.* **135:** 35-53.

APPENDIX 1

Minerals identified in thin section and hand specimen for geochronology samples

Sample	Unit, Lithology	Quartz[a]	Plagioclase	K-feldspar	Muscovite	Biotite	Chlorite	Garnet	Staurolite	Kyanite	Sillimanite	Calcite	Tourmaline	Hornblende	Pyroxene	Epidote	Apatite	Zircon	Monazite	Titanite
DG01	Pelite Lardeau Group	X 30	X 5		X 15	X 25		X 5			X 20						X	X	**X**	
DG02	Crosscutting, medium-grained, tonalite dike	X 40	X 35		X 5	X 15	X 5										X	X	**X**	
DG09	Folded (F_2), medium-grained, tonalite dike	X 45	X 40		X 10			X <5									X	**X**	**X**	
DG22b	Coarse-grained pegmatite	X 20	X 5	X 70	X <5								X <5				X	X	**X**	
DG22c	Folded (F_3) leucosome	X 45	X 25		X 5	X 20		X 5									X	**X**	**X**	
DG23	Semipelite-Amphibolite unit Mica Creek Succession	X 30	X 10		X 10	X 30		X 10			X 10						X	X	**X**	
DG38a	Semipelite-Amphibolite unit Mica Creek Succession	X 40	X 10		X 5	X 20		X 10		X 15							X	X	**X**	
DG69	Undeformed pegmatite	X 30	X 10	X 45	X 5	X <5		X 5					X <5				X	X	**X**	

[a]X = mineral identified; **X** = accessory mineral analyzed for geochronology; 25 = modal percent for rock forming minerals.

APPENDIX 1 cont.

Sample	Unit, Lithology	Qtz[b]	Pl	Kfs	Ms	Bt	Chl	Grt	St	Ky	Sil	Cal	Tur	Hbl	Px	Ep	Ap	Zrn	Mnz	Ttn
	Folded (F_3) pegmatite	X	X	X		X		X									X	X	**X**	
DG70b	Pelite	X	X		X	X		X			X		X				X	X	**X**	
	Lardeau Group	20	5		30	25		10			10									
DG116	Weakly deformed pegmatite	X	X	X	X	X	X										X	**X**		X
		40	5	45	5	<5	<5													
DG129	Leucogranitic crosscutting	X	X	X	X	X	X					X				X	X	**X**		
	dike	20	10	50	<5	5	<5					<5				<5				
DG150	Megacrystic Kfs, Hbl-Bt bearing	X	X	X		X								X		X		**X**		X
	Qtz-monzonite	35	25	15		10								5		10				
DG169	Bt-Hbl bearing granodiorite	X	X	X		X								X	X			**X**		X
		10	25	20		10								20	10					5
CT07	Intensely strained pegmatite	X	X	X	X									X			X	**X**		
	dike	50	15	25	10															
DG206	Semipelite-Amphibolite unit	X	X		X	X		X		X			X				X	X	**X**	
	Mica Creek Succession	25	20		15	15		10		10			5							
DG216	Lower Pelite unit	X			X	X	X	X	X				X				X	X	**X**	
	Mica Creek Succession	10			50	10	<5	15	15											
DG225	Lower Pelite unit	X	X		X	X		X		X							X	X	**X**	
	Mica Creek Succession	25	10		20	25		10		10										

[b]Mineral abbreviations after Kretz (1983).

APPENDIX 1 concluded.

Sample	Unit, Lithology	Qtz	Pl	Kfs	Ms	Bt	Chl	Grt	St	Ky	Sil	Cal	Tur	Hbl	Px	Ep	Ap	Zrn	Mnz	Ttn
DG231	Medium-grained, tonalite dike	X 45	X 40		X 15												X		**X**	
DG235	Qtz-rich granitoid	X 70	X 15		X 15					X <5							X		**X**	
DG246	Medium-grained Qtz-diorite dike	X 15	X 75		X 10												X	**X**	**X**	
DG254	Lower Pelite unit Mica Creek Succession	X 30	X 5		X 10	X 20	X <5	X 15	X 5	X 10							X	X	**X**	

APPENDIX 2.
Structural data collected during field research

Station No.	S2 Strike/Dip		L2 mineral lineation Plunge/Trend		F2 folds S2 axial plane Strike/Dip		F2 folds[a] L2 hinge line Plunge/Trend		F3 folds S3 axial plane Strike/Dip		F3 folds[a] L3 hinge line Plunge/Trend		F3 crenulation L3 intersection Plunge/Trend	
1	067	83	02	251									82	176
2	255	89	85	320										
3	076	80												
4	090	68											80	178
5	091	84												
7					087	80	76	269 (S)						
8					100	90	83	100 (M)						
10					090	88	67	250 (S)						
11	111	67												
12	072	82												
13	096	81												
15	159	85												
16	171	84	84	261										
17	306	84					82	110 (M)					52	260
18	120	81											84	255
19	173	85	82	085										
21	125	80	60	325					114	72	39	048 (M)		
22a,b	111	79	30	289					141	79	61	147 (S)		
22a,b	097	80	48	149										
22a,b	119	64												
22c	114	66							113	48	48	135 (M)		
23	112	75	40	285										
23	117	66	70	280										
24	084	75	67	250										

[a]Letter in brackets (S, Z, M) following hinge line orientation relates to fold asymmetry; asymmetry unknown when no letter is given.

APPENDIX 2 cont.
Structural data collected during field research

Station No.	S2 Strike/Dip		L2 mineral lineation Plunge/Trend		F2 folds S2 axial plane Strike/Dip		F2 folds[a] L2 hinge line Plunge/Trend		F3 folds S3 axial plane Strike/Dip		F3 folds[a] L3 hinge line Plunge/Trend		F3 crenulation L3 intersection Plunge/Trend
25	121	79											
26			35	290	126	72	60	144 (Z)	145	78	65	160 (S)	
27	119	62							089	87	78	118 (S)	
27	104	62	56	225					100	66	79	280	
27	085	80							250	79	69	240	
28	126	62	24	317									
28	127	65	34	275					104	85	20	282 (S)	
28	089	84											
28	091	84											
29	142	49	27	281	151	49	38	187 (M)	148	39	13	158 (S)	
29	136	39									36	260 (S)	
30	117	14	28	255									
30	132	50	22	287									
30	129	45	38	263									
30	105	50									61	164 (Z)	
30	142	60											
31	130	43	07	300	143	42	24	290 (M)					
33	115	83											
33	140	61											
35	110	37											
35	122	46	24	220					132	72	53	135 (Z)	
35	115	58											
36	079	40			086	52	13	081 (S)					
36	115	46											
37	111	44	23	266									

APPENDIX 2 cont.
Structural data collected during field research

Station No.	S2 Strike/Dip	L2 mineral lineation Plunge/Trend	F2 folds S2 axial plane Strike/Dip	F2 folds[a] L2 hinge line Plunge/Trend	F3 folds S3 axial plane Strike/Dip	F3 folds[a] L3 hinge line Plunge/Trend	F3 crenulation L3 intersection Plunge/Trend
38	102 42	16 286			120 55	43 138 (S)	
38	129 40				140 42	12 285 (S)	
39	081 29						
40	073 43				110 56	29 115 (S)	
40	084 24				123 50	18 113 (S)	
41	119 26						
42	117 29		130 20	30 228 (Z)			
42	116 21		102 21	25 232 (M)			
43	115 60						
43	115 47	06 134					
43	113 34						
43	142 29						
44	125 45	05 271					
44	111 38						
44	111 33						
45	104 38						
45	100 51						
45	104 56						
46	116 58						
46	116 61						
46	117 56						
46	122 57	37 257					
47	110 52						
48	125 57	48 250					
49	141 56						

APPENDIX 2 cont.
Structural data collected during field research

Station No.	S2 Strike/Dip	L2 mineral lineation Plunge/Trend	F2 folds S2 axial plane Strike/Dip	F2 folds[a] L2 hinge line Plunge/Trend	F3 folds S3 axial plane Strike/Dip	F3 folds[a] L3 hinge line Plunge/Trend	F3 crenulation L3 intersection Plunge/Trend
50	106 36						
50	109 37	33 254					
50	122 45						
51					325 34	31 070 (M)	
53	089 50						
54	075 48						
54	058 62						
55	056 23	09 105					
55	094 23						
55	082 20		107 39	26 135 (S)		08 052 (Z)	
55	074 19						
55	095 40						
55	065 42						
56	064 37						
56	065 54						
57	052 12						
57	061 39		012 36	22 082 (M)	088 30	10 115 (Z)	
57	040 63						
57	077 36						
58	306 36	13 104			016 30	25 118 (S)	
58	292 54				090 50	09 104	
59	081 80						
59	125 72	02 301			090 62	57 186 (S)	
60	049 30						
60	092 34						

APPENDIX 2 cont.
Structural data collected during field research

Station No.	S2 Strike/Dip		L2 mineral lineation Plunge/Trend		F2 folds S2 axial plane Strike/Dip		F2 folds[a] L2 hinge line Plunge/Trend		F3 folds S3 axial plane Strike/Dip		F3 folds[a] L3 hinge line Plunge/Trend		F3 crenulation L3 intersection Plunge/Trend	
61	101	16												
61	087	26												
61	094	24												
61	104	14												
61	125	39												
61	096	26												
62	069	27									25	170		
62	059	25												
63	075	55												
64	120	64	09	295										
65	070	35												
66	143	45			115	79	16	287	142	73	37	151 (M)		
67					077	90	50	257						
70	101	52												
70b	101	55												
71					122	61	34	289 (Z)	120	75	35	145 (S)		
72	305	81												
101	331	22												
102	345	51											25	035
104	329	47	29	352										
105	335	55			343	58	49	131 (S)						
106	240	89			036	74	46	048 (S)					75	352
109	251	78			240	76	09	252 (Z)					77	340
109	054	55												
110	060	64												

APPENDIX 2 cont.
Structural data collected during field research

Station No.	S2 Strike/Dip	L2 mineral lineation Plunge/Trend	F2 folds S2 axial plane Strike/Dip	F2 folds[a] L2 hinge line Plunge/Trend	F3 folds S3 axial plane Strike/Dip	F3 folds[a] L3 hinge line Plunge/Trend	F3 crenulation L3 intersection Plunge/Trend
111	093 60						
111	126 74						
111	102 75						
112	111 64						
112	109 64						
113	115 64						
115	348 26						
115	354 22						
115	004 26						
116	299 31						
116	296 30		332 44	32 010			
116	297 34						
116	300 30						
117	321 24						
117	329 31						
119	320 25						
122	304 30						
122	305 25						
123	298 22						
123	298 24						
124	265 20						
126	225 32						
126	234 30						
126	276 49						
126	274 44						

APPENDIX 2 cont.
Structural data collected during field research

Station No.	S2 Strike/Dip	L2 mineral lineation Plunge/Trend	F2 folds S2 axial plane Strike/Dip	F2 folds[a] L2 hinge line Plunge/Trend	F3 folds S3 axial plane Strike/Dip	F3 folds[a] L3 hinge line Plunge/Trend	F3 crenulation L3 intersection Plunge/Trend
127	223 25		268 41	11 300 (Z)			
127	248 33		268 22	17 008			
128	221 44						
129	047 40		256 43	19 062 (Z)			
129	157 18						
129	147 30						
130							
132	197 35		212 35	34 285 (S)			
134	210 14						
136	225 50						
138	235 40						
139	007 30		020 28	27 124 (S)			
139	004 21						
140	312 44	32 051					
140	310 35						
140	310 30	32 033					10 147
140	337 37						
141	336 33						
141	308 36						
142	344 61	45 049	323 48	25 110 (Z)			
142	342 57						
144	215 43						
145	200 69						
145	205 54						
147	348 40	21 062					

APPENDIX 2 cont.
Structural data collected during field research

Station No.	S2 Strike/Dip	L2 mineral lineation Plunge/Trend	F2 folds S2 axial plane Strike/Dip	F2 folds[a] L2 hinge line Plunge/Trend	F3 folds S3 axial plane Strike/Dip	F3 folds[a] L3 hinge line Plunge/Trend	F3 crenulation L3 intersection Plunge/Trend
147	350 23						
148	332 34						14 120
149	345 32						
151	148 82	29 317					
152	165 68		175 90	46 148 (M)			34 345
153	153 81	07 332	150 80	19 328 (S)			
154	310 64						10 316
154	307 59				326 46	25 353 (Z)	
154	328 27						
155	173 69	28 347					
156	331 79	39 339					
157	141 74	22 315					
158	151 80						
160	142 78					19 343	
161			311 45	15 323 (S)			
162	150 85						
162	149 82						
163	160 78		290 50	39 330 (M)			
163	172 77						
164	331 87						
165	345 80						
166	336 69						
167	316 66		315 74	50 127			
173	316 71	66 004					
174	259 67	54 331					

APPENDIX 2 cont.
Structural data collected during field research

Station No.	S2 Strike/Dip		L2 mineral lineation Plunge/Trend		F2 folds S2 axial plane Strike/Dip		F2 folds[a] L2 hinge line Plunge/Trend		F3 folds S3 axial plane Strike/Dip		F3 folds[a] L3 hinge line Plunge/Trend		F3 crenulation L3 intersection Plunge/Trend	
174	248	61												
177	358	33							338	35	26	054 (Z)		
180	120	71	36	292	115	60	40	125 (Z)	117	75	22	130 (M)	47	147
181									155	63	61	184 (S)		
182									143	90	65	315 (Z)		
183									108	76	26	112 (M)		
184									110	74	09	112 (M)		
185					289	48	20	344						
201	105	38												
202	122	20			125	25	10	141 (S)						
203	120	21	10	290										
205	118	33	04	125										
205	117	30												
206	120	35												
207	095	33												
207	103	22												
207	110	50												
208	075	24												
208	071	31	02	095										
208	111	24												
208	101	27												
208	090	43	16	121										
208	123	23												
208	116	26												
209													13	353

APPENDIX 2 cont.
Structural data collected during field research

Station No.	S2 Strike/Dip	L2 mineral lineation Plunge/Trend	F2 folds S2 axial plane Strike/Dip	F2 folds[a] L2 hinge line Plunge/Trend	F3 folds S3 axial plane Strike/Dip	F3 folds[a] L3 hinge line Plunge/Trend	F3 crenulation L3 intersection Plunge/Trend
210	103 11	06 111					
211	024 32						
211	043 39						
211	036 30						
212	124 42						
212	118 46						
212	143 27						
212	136 24						
212	127 28						
212	129 31						
213	122 08				025 21	04 122 (S)	
213	120 07						
213	121 07						
214	304 62						11 293
214	296 52				115 74	13 122 (Z)	
215	205 44				101 75	12 260 (Z)	
216	140 37						
216	152 49	32 224					
216	137 46	29 236					
216	135 31						
217	165 32						
217	171 33						
217	173 36						
218	322 32	31 025					
219	314 35						04 327

APPENDIX 2 cont.
Structural data collected during field research

Station No.	S2 Strike/Dip		L2 mineral lineation Plunge/Trend		F2 folds S2 axial plane Strike/Dip		F2 folds[a] L2 hinge line Plunge/Trend		F3 folds S3 axial plane Strike/Dip		F3 folds[a] L3 hinge line Plunge/Trend		F3 crenulation L3 intersection Plunge/Trend	
220	308	41	14	099										
221	329	29							319	57	06	307	23	088
222									310	73	12	129 (Z)		
223	311	50	46	070										
224	107	31	15	258	301	79	11	121			26	214		
225	098	48			123	47	42	236 (S)	101	56	30	298 (Z)		
226					113	54	18	139 (Z)						
229	116	39							108	57	30	280 (Z)		
229	116	52												
231	100	37												
232									100	21	10	270 (S)		
233	099	33												
233	100	58												
234	111	42												
235	107	52							129	54	38	149 (S)		
236									140	40	20	297 (Z)		
237	100	59	10	282										
237	106	52												
237	101	47												
238	093	54	16	282										
238	098	51												
239	098	36	10	110					358	62	37	150 (Z)		
239	093	41							309	13	13	120 (S)		
240	095	48												
240	094	40												

APPENDIX 2 cont.
Structural data collected during field research

Station No.	S2 Strike/Dip	L2 mineral lineation Plunge/Trend	F2 folds S2 axial plane Strike/Dip	F2 folds[a] L2 hinge line Plunge/Trend	F3 folds S3 axial plane Strike/Dip	F3 folds[a] L3 hinge line Plunge/Trend	F3 crenulation L3 intersection Plunge/Trend
241	107 53						
241	094 52						
242	095 20						
242	086 28	03 106					
242	085 24						
243	092 22				087 62	18 112 (S)	
243	096 41						
243	088 34						
244	095 45						
244	091 53						
244	098 44						
245	125 24	09 275					
246					143 78	57 266 (Z)	
247					135 76	31 276 (Z)	
248			145 55	27 271 (S)	149 49	19 280 (Z)	
249					136 78	06 306 (Z)	
250					128 52	08 300 (Z)	
251	123 47	13 269					
251	110 40	19 265					
251	108 36	07 267					
251	107 43	31 250					
251	129 35	26 264					
252	124 28						
253	085 17	06 268					
253	110 24						

APPENDIX 2 concluded.
Structural data collected during field research

Station No.	S2 Strike/Dip	L2 mineral lineation Plunge/Trend	F2 folds S2 axial plane Strike/Dip	F2 folds[a] L2 hinge line Plunge/Trend	F3 folds S3 axial plane Strike/Dip	F3 folds[a] L3 hinge line Plunge/Trend	F3 crenulation L3 intersection Plunge/Trend
254	116 34	02 240					
254	131 18						
254	089 24						
254	090 27						
255	110 20	08 270			110 32	08 273 (Z)	
256					134 36	07 290 (Z)	
257	130 24	19 257					
258	088 25						
259			138 41	07 319 (Z)	182 43	26 233 (S)	
260	144 39						
260	146 37	24 285					
260	143 38						
261	121 21	08 274	146 36	15 327 (S)	142 38	32 307 (Z)	
262					122 43	19 276 (M)	
263	162 28	15 285					
263	140 26						
264	087 23						
265	135 36				140 50	10 135 (M)	
266			176 40	34 258 (M)			
267	158 23						
268	144 24	15 285					
269	142 24						
270	140 37	17 292					
271	133 53						
271	132 45						

APPENDIX 3. U-Pb IDTIMS analytical data not presented in thesis

Fraction[a]		Wt.[b] (µg)	U (ppm)	Pb*[c] (ppm)	$\frac{^{206}Pb}{^{204}Pb}$[d]	Pb[e] (pg)	^{208}Pb (%)[f]	$\frac{^{206}Pb}{^{238}U}$[g]	$\frac{^{207}Pb}{^{235}U}$[g]	$\frac{^{206}Pb}{^{238}U}$[h] (Ma)	$\frac{^{207}Pb}{^{235}U}$[h] (Ma)	Corr.[i] Coef.	$\frac{^{207}Pb}{^{206}Pb}$[h]	$\frac{^{207}Pb}{^{206}Pb}$[g] (Ma)	Disc.[j] (%)
DG02 Crosscutting tonalite dike								**Domain 2: French Glacier**							
B	149-202	2	133	2	44	9	10.7	0.014639 ± 3.4 %	0.08694 ± 36.5 %	93.7 ± 6	84.7 ± 59	0.20	0.04307 ± 34.5 %	-163.3 ± 4800	—
D	149-202	2	572	9	161	9	12.5	0.014722 ± 0.5 %	0.10066 ± 3.6 %	94.2 ± 1	97.4 ± 7	0.04	0.04959 ± 3.3 %	175.8 ± 168	46.7
E	149-202	5	4	0.3	23	7	40.7	0.032497 ± 24.7 %	1.65728 ± 28.0 %	206.2 ± 100	992.3 ± 354	0.93	0.36988 ± 10.4 %	3790.9 ± 357	95.9
F	149-202	4	20	0.5	35	5	25.0	0.017774 ± 8.3 %	0.46072 ± 14.9 %	113.6 ± 19	384.8 ± 95	0.72	0.18799 ± 10.6 %	313.2 ± 401	96.6
H	149-202	2	10	2	41	4	49.9	0.074387 10.1 %	7.51967 ± 9.9 %	462.5 ± 91	2175.3 ± 177	0.97	0.73316 ± 2.6 %	4797.1 ± 78	93.3
DG09 Folded (F2) tonalite dike								**Domain 2: French Glacier**							
D*	<74	2	6592	151	11334	19	0.3	0.025301 ± 2.40 %	0.17225 ± 2.40 %	161.1 ± 7.6	161.4 ± 7.2	1.00	0.04938 ± 0.17 %	165.7 ± 8	2.9
DG15 Meta-volcanoclastic								**Domain 2: French Glacier**							
B*	105-149	6	93	3	124	10	8.7	0.030322 ± 1.06 %	0.23015 ± 6.10 %	192.6 ± 4.0	210.3 ± 23.0	0.49	0.05505 ± 5.65 %	414.3 ± 274	54.3
D*	<74	11	200	7	374	12	20.0	0.030913 ± 0.34 %	0.22990 ± 0.98 %	196.3 ± 1.3	210.1 ± 4.0	0.40	0.05394 ± 0.90 %	368.5 ± 41	47.4
E*	<74	9	266	8	350	13	15.7	0.027205 ± 0.28 %	0.20108 ± 1.40 %	173.0 ± 1.0	186.0 ± 5.0	0.38	0.05361 ± 1.32 %	354.6 ± 61	51.9
G*	<74	13	88	3	491	56	15.0	0.035871 ± 0.12 %	0.29004 ± 0.35 %	227.2 ± 0.5	258.6 ± 1.6	0.70	0.05864 ± 0.28 %	553.9 ± 12	
DG22c Folded leucosome								**Domain 3: Southwest of Mud Glacier**							
A	105-149	6	14	0.4	71	3	5.9	0.031371 ± 1.24 %	0.23840 ± 8.99 %	199.1 ± 4.8	217.1 ± 35.1	0.42	0.05512 ± 8.54 %	416.9 ± 434	53
E	149-202	8	5	0.2	53	3	13.3	0.050819 ± 1.50 %	0.53047 ± 9.57 %	319.5 ± 9.4	432.1 ± 67.4	0.48	0.07571 ± 8.95 %	1087.3 ± 408	72.3
F	105-149	6	10	0.4	46	5	7.6	0.039185 ± 3.57 %	0.68255 ± 9.13 %	247.8 ± 17.3	528.3 ± 75.2	0.58	0.12633 ± 7.63 %	2047.5 ± 298	89.5

[a] A fraction code for multigrain zircon analysis; D* fraction code for multigrain monazite analysis; +74-105, size range in µm.
[b] Wt. = Weights, estimated from grain size measurements; uncertainty is 2 µg. [c] Radiogenic Pb. [d] Measured ratio, corrected for spike and Pb fractionation of 0.09 ± 0.03%/a.m.u.
[e] Total common Pb in analysis, corrected for spike and fractionation. [f] Radiogenic ^{208}Pb, expressed as percentage of total radiogenic Pb. [g] Corrected for Pb and U laboratory blank where 208/204:207/204:206/204 = 19.01:15.64:38.23:1, and common Pb (Stacey-Kramers model Pbcomposition equal to interpreted age of analysis); errors are one standard error of the mean in percent. [h] Corrected for common Pb and laboratory blank; errors are two standard errors of the mean in Ma. [i] Corr. Coef. = Correlation Coefficient.
[j] Disc. = Discordance in percent; values are not reported when less than -100.